Stabilizing Metal-Alanes and Metal-Metal Multiple Bonds to Effect Small Molecule Transformations

A Thesis

SUBMITTED TO THE FACULTY OF

UNIVERSITY OF MINNESOTA

BY

Paul Alexander Rudd

IN PARTIAL FULFILLMENT OF THE REQUIREMENTS

FOR THE DEGREE OF

DOCTOR OF PHILOSOPHY

Professor Connie C. Lu

October, 2018

Acknowledgements

I have enjoyed my time in Minnesota, thanks in large part to my friends here. As an early member of a new group, I'm forever indebted to the people who helped guide me through my early years in the lab: the ladies of the McNeil group, Kristen, Elodie, and Emily; Keying, our sagacious postdoc; and, Kit, Deanna, and Aubrey, the first students to trek into the unknown. Of course, I've made many other friends along the way. Thanks to the rest of the Lu group, the Tolman, Que, and Ellis groups, who always made themselves available when we needed help.

I would also like to acknowledge my friends in the Joint Safety Team, which was worth it just to get to know the three Katies, Ian, Brian, Nick, Kelly, Anna, and everyone else.

I would also like to acknowledge the mentorship I have received, which has substantially influenced the course of my career. Professors Cora MacBeth and Justin Gallivan at Emory University (Atlanta, GA) played an instrumental role in my genesis as an inorganic chemist, even though Justin was ostensibly teaching a class on bio-organic chemistry. At Minnesota, I have to thank Prof. John Ellis—John has always been a good sport no matter what esoteric topic I've dropped by to bother him about, and his generous donation of 2,2,2-crypt (1 g) made a large part of chapters 4 and 5 possible. Additionally, much to the annoyance of my labmates, I've picked up John's love of pKa values. Professor Larry Que taught me to think more analytically, especially regarding what your experiments *do not* tell you. We will also never forget that "phosphines are not biologically relevant!" (It also turns out, however, this is an insufficient reason not to give an MPIG seminar.)

Lastly, I would like to thank Professor Connie Lu, who has taught me innumerable lessons both inside and outside of the lab. Her willingness to let us follow our own interesting projects was extremely liberating, and her patience when we got stuck was gratifying. Looking back, I don't think I could have picked a better advisor, which I believe that is the highest praise I can give.

Table of Contents

List of Tables

List of Figures

Chapter 1

Introduction

1.1 Bio-inspired Strategies for Small Molecule Activation

Nature has evolved innumerable enzymes to accomplish difficult chemical transformations, but one of the most impressive reactions is the biological fixation of dinitrogen (N_2) to generate ammonia (NH_3).[1, 2-5] This reaction is a multi-electron reduction of N_2, adding a net six protons and six electrons, cleaving the N-N bonds, and generating two equivalents of ammonia (Eq. 1). Critically, reduction occurs at ambient temperature and pressure, and multicellular life may not have arisen if the reaction conditions were necessarily substantially harsher. In contrast, industrial fixation occurs on solid-state catalyst beds and requires extremely high temperatures and pressures, often in excess of 300 °C and 90 atmospheres.[3, 6-8] The industrial synthesis of ammonia, referred to as the Haber-Bosch process, is tremendously optimized to recover both reagents and heat energy, and modern technology now achieves energy efficiencies greater than 90%.[6] This success allowed for the unprecedented agricultural expansion in the green revolution of the 1960s, which is responsible for nearly doubling the global population. Nevertheless, the large energetic cost of Haber-Bosch production of ammonia has been estimated between 1-3% of the world's energy usage, and efforts that reduce the energetic cost of this reaction are highly attractive.[3]

Eq. 1 $$N_2 + 8H^+ + 8e^- + 16MgATP \rightarrow 2NH_3 + H_2 + 16(MgADP + P_i)$$

Synthetically, chemists are interested in mimicking the homogeneous reduction of nitrogen to ammonia without the necessity of a protein superstructure or the harsh conditions practiced in pure inorganic systems.[3, 9, 10-21] The primary and secondary

coordination spheres of protein active sites often have subtle methods of tuning substrate binding and reactivity pathways, so it is unsurprising that only a handful of systems have been able to replicate this feat with small ligand scaffolds and no secondary coordination spheres with which to direct the reaction. Iron and molybdenum complexes have been particular targets of research,[12, 13, 22-24] due to their inclusion in the FeMo cofactor (FeMoco) responsible for biological fixation (Figure 1.1). FeMoco contains what is widely regarded as the most complex bio-organometallic active site known, as it contains two corner-sharing iron-sulfur cubanes capped by an eighth metal site with either iron, molybdenum, or vanadium.[1, 2, 25] The presence of eight metal sites is highly unusual, as most metalloprotein active sites utilize only one to three metals.[2] One potential reason for the number of metal sites is the ability to delocalize charge across the highly coupled metal sites, which has multiple benefits. First, it should allow for the storage of multiple reducing equivalents prior to dinitrogen binding. Second, the overall geometry changes between multiple cluster oxidation states can be minimized due to the extensive charge delocalization across the multi-metal site.[2]

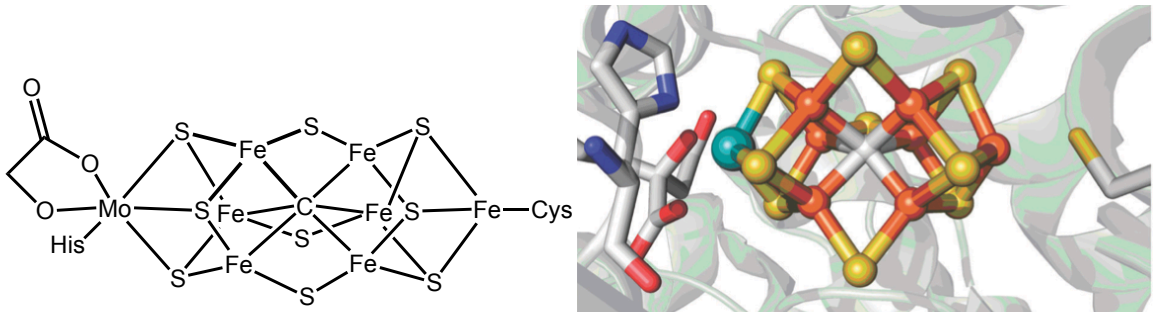

Figure 1.1 Diagrammatic representation of the iron-molybdenum cofactor (FeMoco) (left) and the solid-state X-ray structure (right). Atom colors: iron, orange; sulfur, yellow; molybdenum, teal; carbon, white; oxygen, red. The X-ray structure is copied from reference 6 and has been cropped.

The ability to add multiple electron equivalents is important, as the concerted addition of protons and electrons can substantially lessen the voltage required for substrate reduction. For dinitrogen, the addition of four protons and electrons eases the potential by nearly 700 mV relative to the two-electron reduction.[i] If all six protons and electrons can be transferred together, the electrochemical potential required drops by approximately one volt.[26]

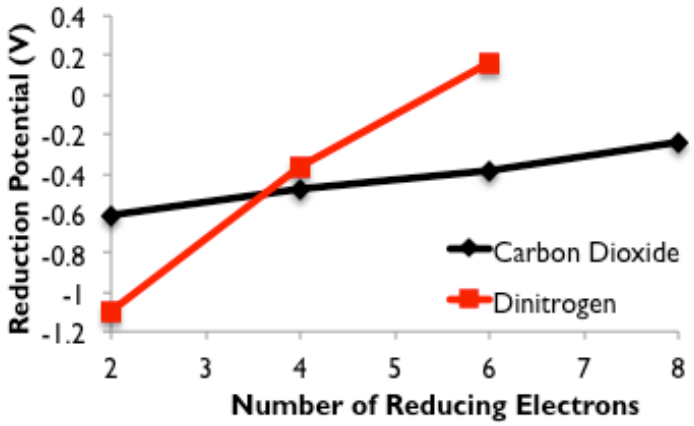

Figure 1.2 Electrochemical reduction potentials for N_2 and CO_2 (vs. NHE in H_2O)

Intriguingly, the cofactor is only minimally tethered to the protein through two amino acids at the corner sites. Initial crystallographic studies appeared to show an isolated, but highly protected, inorganic site with multiple low-coordinate iron sites.[27] The activity of the enzyme was initially attributed to the low coordination number at each iron site, though this explanation is unsatisfactory with respect to the high enzymatic selectivity. Indeed, an additional wrinkle was discovered in 2002, as an interstitial light

[i] Recent work strongly suggests that nitrogenase stores four electrons prior to initial binding and reduction of N_2. Due to the complexity in observing intermediates spectroscopically, though, these findings are controversial. For more detail, consult references 1 and 3.

atom was discovered in the center of the cluster (Figure 1.3).[28] This atom was later confirmed to be a carbide ligand, and its position is *trans* to multiple potential binding sites for dinitrogen.[29] Recent work has also established the general pathway of carbide insertion, though the precise details are still highly uncertain.[30]

Currently, no structurally faithful models of the FeMoco active site are known. However, chemists have extensively pursued functional models of this site based on monomolecular iron, molybdenum, and tungsten complexes. Early stoichiometric work by Chatt and coworkers demonstrated that dinitrogen reduction could be accomplished at a single molybdenum site, which was in accord with the then-accepted belief that the active metal was molybdenum.[ii]

[ii] Due to site mutagenesis studies, it is now believed that dinitrogen binding occurs at one of the "belt" iron atoms. It is unclear whether activation initially occurs via terminal dinitrogen binding to one site or bridging binding across two iron sites. The role of molybdenum is still unclear—in different species, the molybdenum site can be occupied by either iron or vanadium.

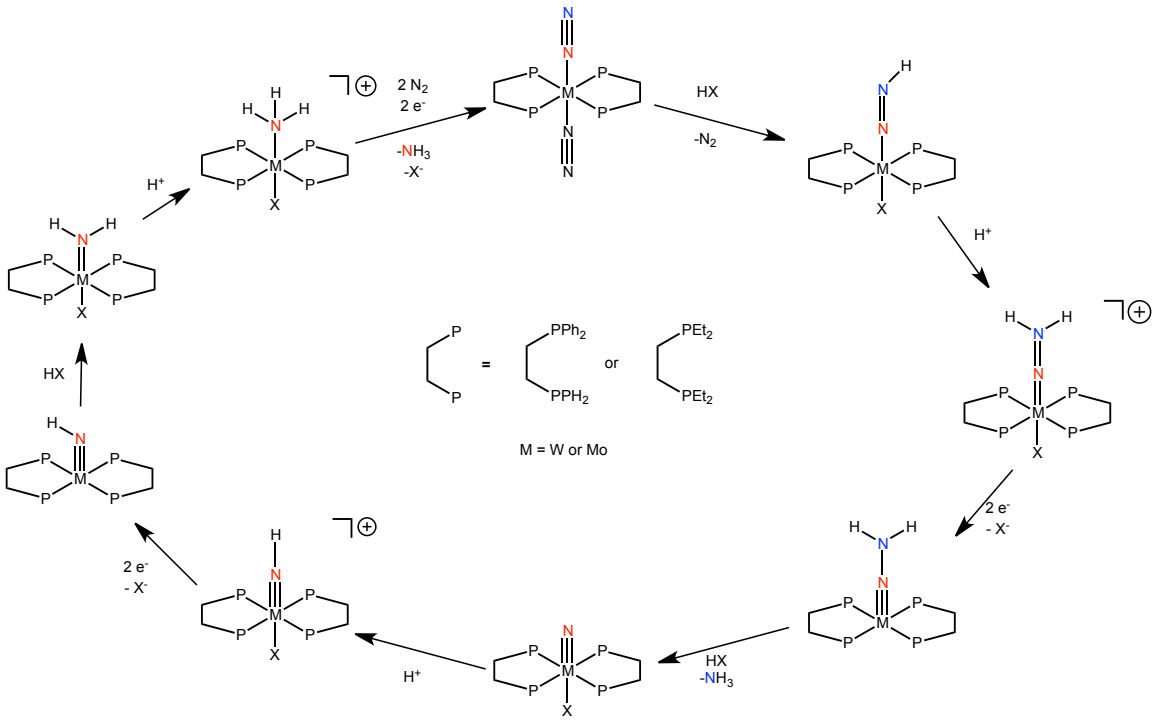

Figure 1.3 Diagrammatic representation of the Chatt cycle. X represents a halide. For clarity, the proximal (red) and distal (blue) nitrogen atoms have been highlighted.

The proposed cycle begins with an octahedral, formally zero-valent metal site with two diphosphine ligands and two dinitrogen ligands. Upon the addition of one equivalent of acid (HX, X = halide), the distal nitrogen atom (blue) is protonated and the N_2 unit is reduced to a diazenide, *i.e.*, $2e^-$ reduction at N_2. The two electrons come directly from the metal center, which expels one N_2 unit and coordinates the halide. Addition of another acid equivalent protonates the distal nitrogen atom, and reduction of this yields species by two electrons yields a hydrazido species. The N-N bond has now undergone a four-electron reduction, and the final N-N bond is broken upon protonation to generate the first equivalent of NH_3. The proximal nitrogen atom is retained as a metal-bound nitride. The metal-nitride then undergoes analogous protonations and reductions to

generate the second equivalent of ammonia, which dissociates when the metal returns to a zerovalent oxidation state. Upon the loss of the ammonia and halide ligands, two equivalents of dinitrogen bind. The full pathway is typically referred to as the Chatt cycle or the asymmetric/distal mechanism, as the distal nitrogen atom is functionalized and released prior to the functionalization of the proximal nitrogen atom.

In 2003, the Schrock group reported the first homogenous catalyst for this transformation, which occurred at a Mo center in a tripodal, trisamidoamine ligand framework.[12, 13, 31, 32] Unlike the Chatt chemistry, which starts with a zerovalent metal site, the Schrock cycle is initiated from a Mo^{III} center (Figure 1.4). The cycle of N_2 protonation and reduction is believed to follow the asymmetric pathway, and 7 of the 12 species involved in catalytic turnover have been identified or isolated. Notably, the Mo site must be extremely sterically hindered to prevent bimolecular pathways, which deactivate the catalyst. The catalytic cycle is extremely sensitive to reaction conditions, and the exact formulation of proton source, electron source, solvent, and reaction timing are critical.[12, 31] Even when fully optimized, this reaction yields only four turnovers.

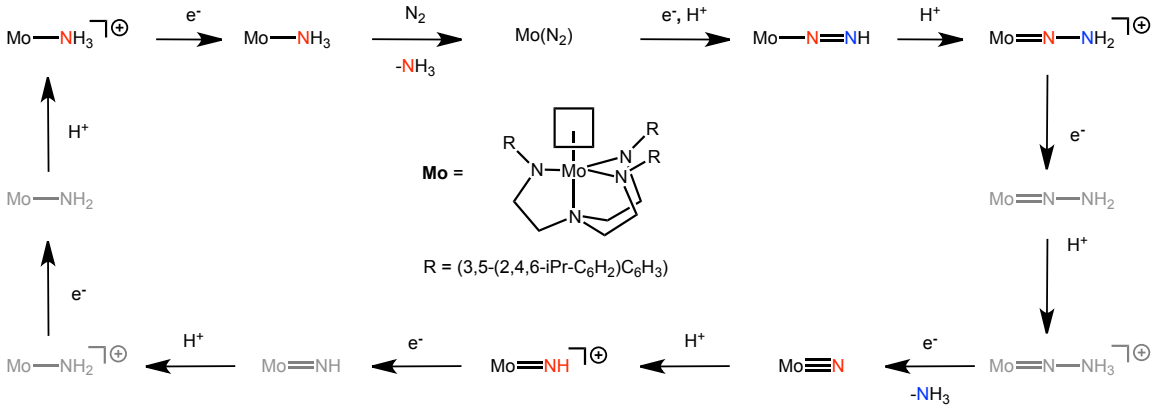

Figure 1.4 Proposed catalytic cycle for the reduction of dinitrogen at a trisamidoamine molybdenum complex. Gray intermediates have not been detected. For clarity, the proximal (red) and distal (blue) nitrogen atoms have been highlighted.

Nishibayashi and coworkers recently reported the most efficient catalyst to date, which forms up to twelve equivalents of ammonia per molybdenum site (Figure 1.6).[22, 24, 33] In this system, zerovalent molybdenum is bound by a bisphosphinopyridine ligand under an N_2 atmosphere to generate the complex shown in Figure 1.5. The Mo-N_2-Mo bridge is conserved in solution, as determined by ^{15}N NMR spectroscopy, and the infrared spectrum also confirms the retention of two terminally bound dinitrogen molecules.[22] Upon addition of excess protons and electrons, up to 12 equivalents of ammonia are formed per molybdenum site. Because five dinitrogen units are present in the precatalyst, it is ambiguous which N_2 unit is functionalized, but replacement of the *trans* N_2 ligands with *trans* CO ligands is known to completely deactivate the catalytic pathway. Monomolybdenum complexes, such as the diphosphines from Chatt's work, are completely inactive for the formation of ammonia.

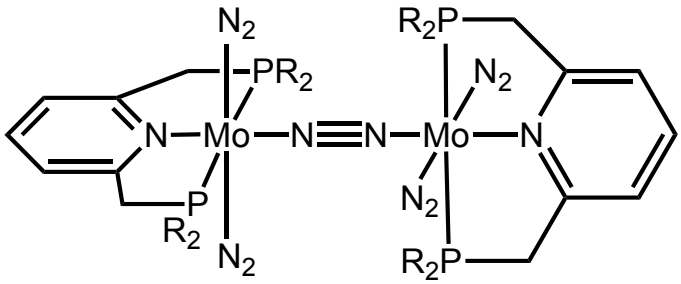

Figure 1.5 The zerovalent dimolybdenum precatalyst of Nishibayashi *et al.* In the most active complex, R = ^{t}Bu.

Though much synthetic work has focused on nitrogen reduction at the molybdenum site, recent work on nitrogenase has demonstrated that one or more of the iron sites bound to the interstitial carbide are likely to be the site of nitrogen binding. The Holland group has reported on several di-iron complexes with a bridging sulfide as a potential model for FeMoco iron sites (Figure 1.6).[34, 35] Unlike the terminal coordination seen at low-valent Mo sites, it has also been proposed that dinitrogen may bridge across two metal sites that are cooperatively responsible for accomplishing nitrogen reduction.

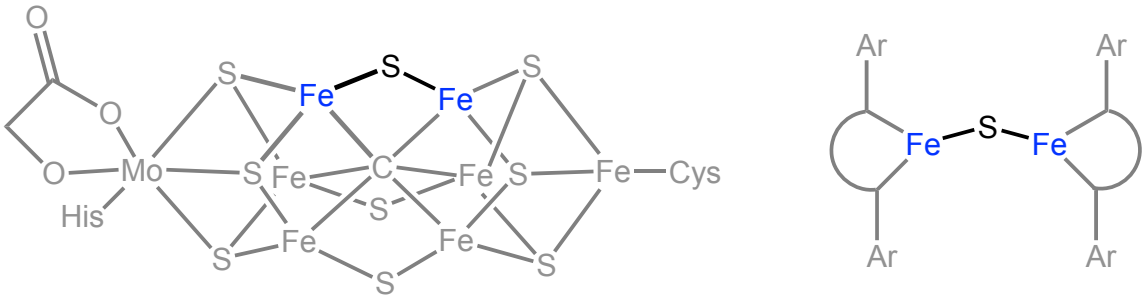

Figure 1.6 One representation for a partial structural model of FeMoco. Potential iron sites for N_2 binding at FeMoco are shown in blue (left), and this motif is highlighted in a simplified ligand framework (right). The semicircle cartoon represents a β-diketiminate.

The synthetic model complexes are observed to bind hydrazine and substituted hydrazine derivatives, and up to 1.7 equivalents of ammonia are produced under excess hydrazine.[35] The precise pathway for this reaction is unclear but strongly depends on the

presence of excess hydrazine. Additional studies to elucidate the mechanism of the reaction mechanism were hindered by the low solubility of the hydrazine adduct as well as the inability to isolate this complex on a preparative scale. The bridging nature of the hydrazine complex was confirmed crystallographically (Figure 1.7).[iii] For substituted hydrazine substrates, the respective primary amine is also obtained.[34]

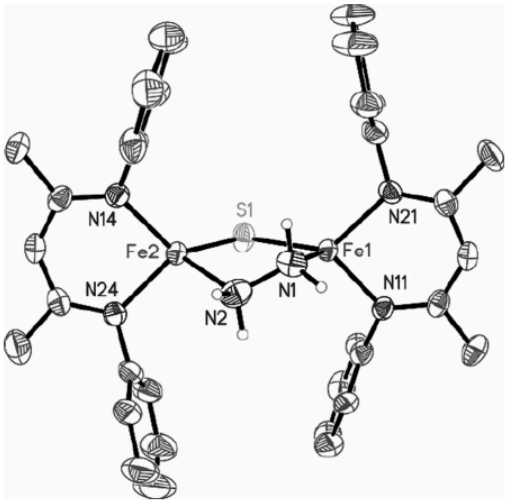

Figure 1.7 Solid-state structure of Holland's di-iron complex with bridging sulfide and hydrazine ligands. For clarity, aryl substituents and a hydrogen-bonded molecule have been omitted. This figure is copied without alteration from reference 42.

The Holland group has also demonstrated complete cleavage of N-N bonds with iron β-diketiminate complexes.[11] β-diketiminate complexes, often referred to as nacnac ligands, enforce a low-coordinate geometry at metal sites. Metallation of iron or cobalt with a bulky nacnac, followed by reduction under an N_2 atmosphere, has been shown to

[iii] Single crystals of this species were actually grown as a hydrogen-bonded adduct of DBU, 1,8-Diazabicyclo[5.4.0]undec-7-ene. Solution-state measurements indicate that DBU is not associated in solution. Confirmation via single crystal diffraction studies appears to have been fortuitous, as bulk crystals could not be obtained under various conditions.

generate 3-corodinate metal complexes that bind in a κ_2 manner and spontaneously coordinate dinitrogen, which bridges across two metal sites.[9] The bridging dinitrogen is significantly activated as determined by the crystallographic N-N distance and Raman stretching frequency; spectroscopically, it is assigned as the diazenide N_2^{2-}. In bulky nacnac systems, further activation has not been reported. When the nacnac is less sterically hindering, metallation and reduction under an N_2 atmosphere induces complete cleavage of the N-N bond, generating two bridging nitride species across three iron sites (Figure 1.8).[11] A fourth iron site is present but does not exhibit magnetic coupling. The lessened steric bulk is presumed to allow for closer interaction of multiple metal sites, facilitating N_2 reduction. The potassium counter-ion is also believed to be important, as it may induce a partial polarization of the N_2 bond responsible for easing the reduction potential. The crystalline nitride species is stable at −40 °C, but recent reports have noted that this species actually undergoes nitrogen loss under certain conditions.

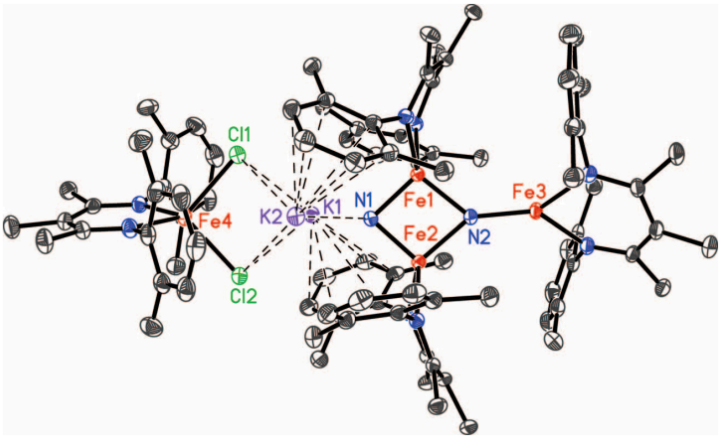

Figure 1.8 Solid-state crystal structure of Holland's tetra-iron dinitride species. This figure is copied without alteration from reference 15.

Within the last several years, the Peters group has proposed that iron in trigonal phosphine systems may provide a functional model for nitrogenase (Figure 1.9).[18, 19, 21, 36-38] The function of the central carbide is still unknown, but it seems reasonable to suggest that it might act as a *trans* ligand for a terminal dinitrogen ligand. Research in this area has focused on the synthesis of a ligand that differs only with respect to central element E, in an otherwise invariant ligand system. The studies on E = Si, B, and C have thus far been reported, and *both* the B and C ligands are shown to catalyze the reduction of N_2 to NH_3 with 7 and 4 turnovers, respectively.[19, 21]

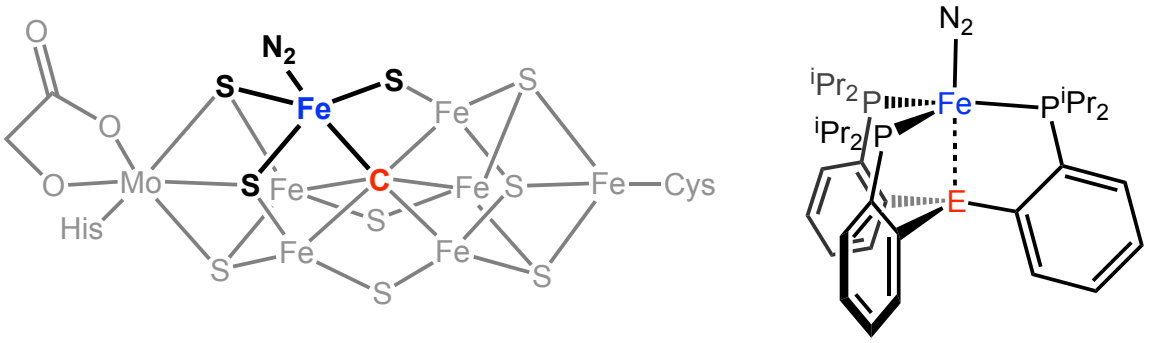

Figure 1.9 One representation of a partial structural model of the FeMoco core. One potential iron binding site (left) is shown in blue. For the corresponding model complex (right), E = Si, C, B.

Interestingly, these studies corroborate the potential for terminal iron dinitrogen complexes to facilitate multi-electron chemistry, but they do not elucidate any special properties of carbide ligands. Indeed, the carbon-based ligands are actually outperformed by their borane counterpart. Surprisingly, the systematic effect of many elements *trans* to a metal coordination site are poorly understood. Two initially limiting cases are considered: a main group element *trans* to an open binding site versus a *trans* transition metal. These two scenarios are considered in the following two sections.

1.2 Bonds between transition metals and main group metals

The elements phosphorous, nitrogen, and oxygen are ubiquitous in ligand design for transition metals. The organometallic chemistry of metal-carbon and metal-silicon bonds has been extensively studied, and active research in this field continues today. However, metal-carbon and metal-silicon interactions are relatively "innocent" and behave similarly to typical ligands for transition metals. Other elements, such as antimony, have now been shown to interact with metal sites quite differently than its lighter congeners,[iv] and constructive applications of these interactions are rapidly developing.[39].

Synthetically, incorporation of boron, aluminum, gallium, or indium in the first coordination sphere of a transition metal is rare, and their interactions with transition metals are poorly understood.[40] Of note, this gap does not reflect the absence of these elements: $GaCl_3$ and $AlCl_3$ are standard reagents, as their halophilicity makes them useful halide-abstraction reagents. Indeed, the halophilic nature of these elements likely contributes to their absence from metal primary coordination spheres, as halide abstraction will weaken or eliminate the interactions between these elements and transition metals.[41-43]

Moreover, these elements interact quite differently in metal primary coordination spheres than do typical ligands. Most ligands for transition metals are either X- or L- type

---

[iv] Sb(III) acts analogously to P(III) as a σ donor, but Sb(V) displays Z-bonding (vide infra) and intriguing sensitivity to the nature of metal-bound halides. This "coordination non-innocence" is highly sensitive to oxidation state.

ligands, denoting that the metal-ligand interaction has either a covalent bond or a dative donation of electron density, respectively.[44] The X-type ligand is a simple covalent bond, typically of σ-type symmetry (e.g., •H, •Cl, •OR). By definition, L-type ligands are dative donors, which is typically ascribed as a ligand-to-metal donation of one or more electron pairs (e.g., linear LX or planar LX_2). Some of these ligands are also noted for metal-to-ligand π backbonding (*e.g.*, phosphines, CO), where electrons from the transition metal will partially occupy ligand antibonding or nonbonding orbitals. In contrast, Group 13 metals in the first coordination sphere of a metal site act as a Z-type ligand, which has an open p_z orbital and accepts electron density from a metal-based σ-symmetry orbital. Practically, this "inverse-dative" effect will decrease the electron density at the metal center, making it more electron poor.

Much of the work in this area has focused on metal-boranes. The highly successful trisphosphinoborane (TPB) ligand was introduced by Bourissou and coworkers, who demonstrated that a series of M(TPB) complexes could be readily prepared (M = Ni, Pd, Pt, CuCl, Cu, AgCl, AuCl).[45] The modular synthesis of these complexes is shown in Figure 1.10. Despite possessing two sets of isoelectronic and isostructural complexes, trends in this series defy trivial analysis. Crystallographically, short metal-borane distances and borane pyramidalization corroborate the presence of metal-borane interactions. However, the metal-borane distances vary substantially due to the difference between first, second, and third row metal sizes, and only a minor trend is

observed in the metal-B distance upon accounting for the different the covalent radii.[v] Additional parameters, such as solution state nuclear magnetic resonance spectroscopic behavior or analysis of the solid-state crystal structures, do not display monotonic behavior.

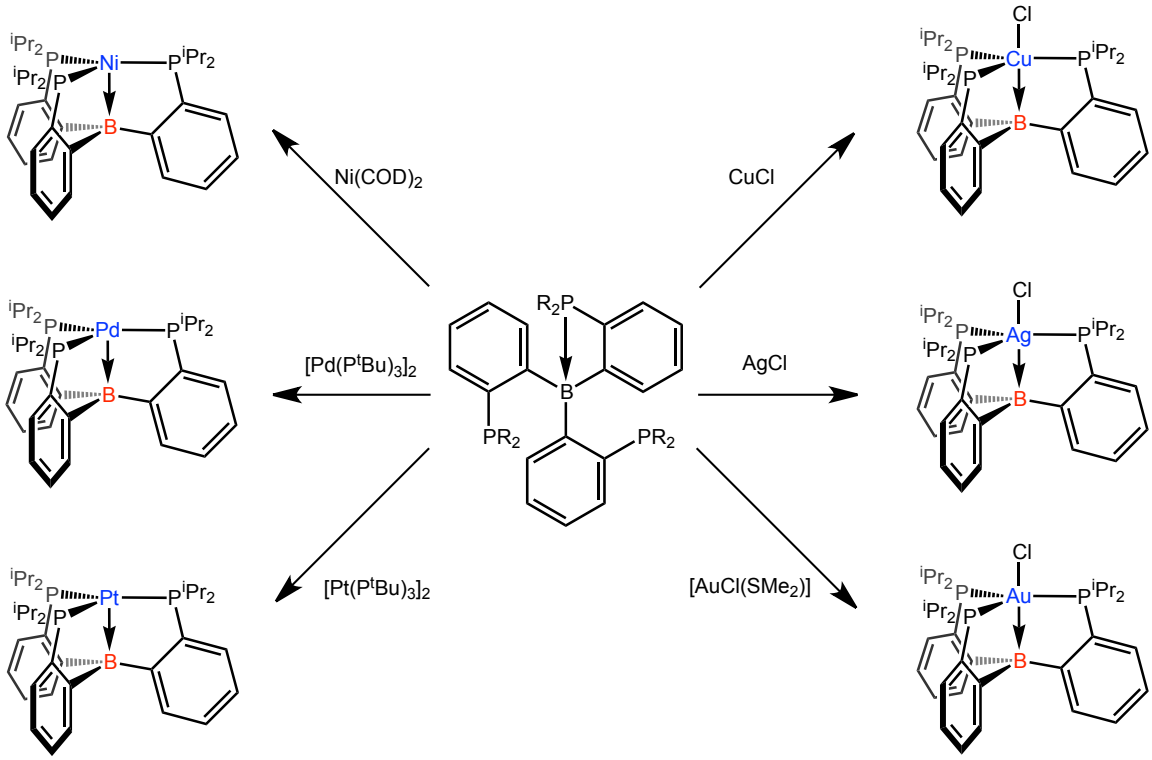

Figure 1.10 Simplified metallation strategy for M(TPB) species

It is noteworthy that these complexes C_3 symmetric complexes are isostructural within a given group: the Group 10 metals all exhibit a trigonal monopyramidal geometry, whereas the Group 11 metals exhibit a trigonal bipyramidal geometry. The trigonal bipyramidal gold chloride complex can be converted to the cationic trigonal

[v] A direct comparison of different metal-element bond lengths is misleading. The distance is often normalized against a common set of radii to provide a quatitative value, *r*, for direct comparison. Additional details are provided in the following chapters, where appropriate.

monopyramidal gold complex upon addition of $GaCl_3$, and the Peters group demonstrated that addition of the non-coordinating salt $Na[BAr^F{}_4]$[vi] yields the trigonal monopyramidal copper species (Figure 1.11).[46] Curiously, loss of the halide in both cases is shown to weaken the metal-borane interaction, which is attributed to the loss of a 3-center, 2-electron bond. Amazingly, the copper complex can then undergo two stepwise reductions, which X-ray absorption studies confirm are localized primarily at boron.[46]

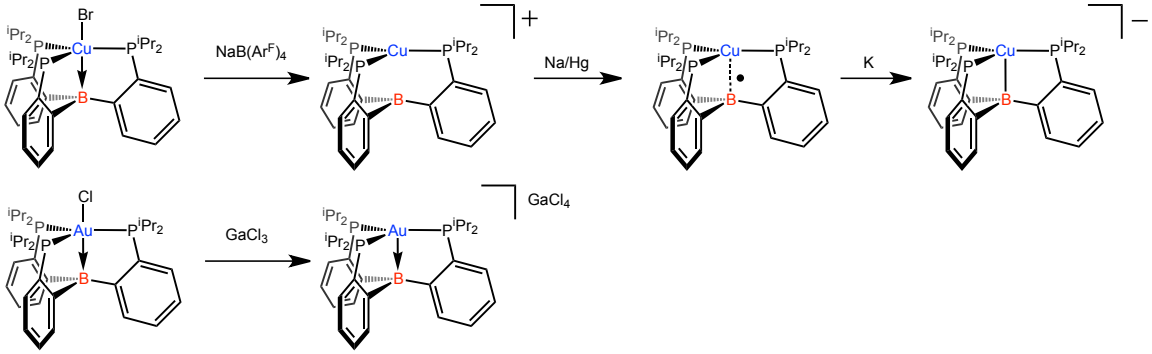

Figure 1.11 Generation of trigonal monopyramidal gold and copper complexes in (TPB)

Several of these metal-boranes display temperature-dependent ^1H NMR spectra. The dependence is thought to reflect a fluxional motion resulting from inversion between one C_3 conformer and its formal enantiomer. These barriers are observed to vary between 14.7 and approximately 17 kcal/mol, though notably they do *not* track well with any metal-borane parameters. Bourissou proposed that the strength of the metal-borane bond correlates inversely with the observed barrier, but this hypothesis has not been validated. Though the metal-borane interactions are computationally observed to strengthen from 3d to 5d metals, it is necessarily true that metal-phosphine backbonding will also vary by

[vi] $BAr^F{}_4 = B(3,5{-}(CF_3)_2C_6H_3)_4$

metal site. One can control for the metal-ligand backbonding by preparing the corresponding aluminum(III),[43] gallium(III),[41] and indium(III)[42] complexes, but unfortunately halide abstraction from the metal occurs in all cases and terminates the Z-type interaction.

As previously noted, the Peters group has extensively studied Fe-E interactions (E = C, Si, B), especially with respect to nitrogen reduction. Several ligands have been used, including $PhBP^{iPr}_3$, SiP^{iPr}_3, CP^{iPr}_3, $C^{Si}P^{Ph}_3$ and TPB.[14, 16, 17, 19, 21, 37, 47] Figure 1.12 shows several of the crystallographically confirmed iron complexes with these ligands.

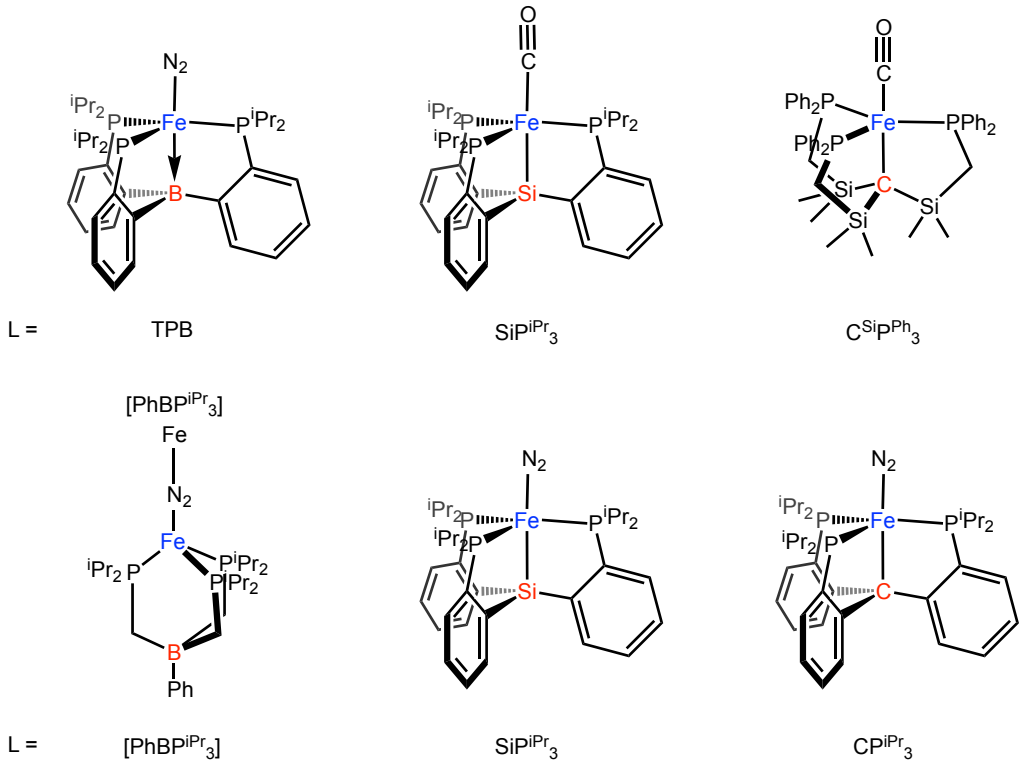

Figure 1.12 Ligand platforms for low-valent iron chemistry. The $Fe(N_2)$ and Fe(CO) complexes are shown with the corresponding ligand notation.

Because this work is concerned with formulating a functional model of dinitrogen reduction, it makes sense to refer to it with respect to the Chatt-type cycle.

Chronologically, initial work involved a borate with pendant phosphine groups, [PhBP$^{iPr}_3$].[47] No interactions were observed between iron and the borate moiety in [PhBP$^{iPr}_3$]FeCl, but reduction of the ferrous starting material under an N_2 atmosphere yields a di-iron complex in which each iron is pseudotetrahedral and bridged by N_2 (see Figure 1.12). Alternatively, if [PhBP$^{iPr}_3$]FeCl undergoes metathesis with Li(dbabh),[vii] an iron(IV) nitride intermediate is formed (Figure 1.13).[14, 15] Unfortunately, [PhBP$^{iPr}_3$]FeN undergoes reductive coupling to μ-(N_2)[Fe[PhBP$^{iPr}_3$]]$_2$ upon removal of solvent or standing in solution at room temperature. Importantly, though this system runs in the "wrong" direction, *i.e.* dinitrogen synthesis, these data demonstrated that that iron could cycle through multiple oxidation states to accommodate π-basic and π-acidic ligands in a single ligand set. This electronic flexibility is critical to a Chatt-type catalytic cycle, which must be able to bind π-acidic dinitrogen as well as stabilize the π-basic nitride intermediate.

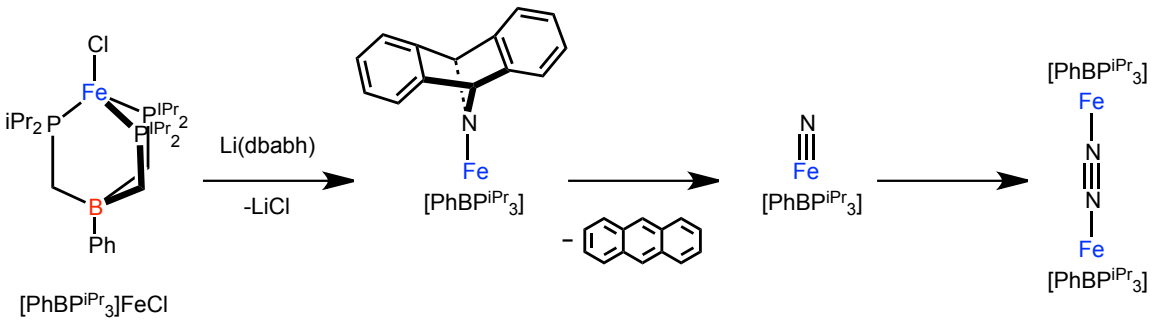

Figure 1.13 Metathesis of [PhBP$^{iPr}_3$]FeCl to generate the iron(IV) nitride [PhBP$^{iPr}_3$]FeN. The nitride then undergoes reductive coupling to yield the known species μ-(N_2)[Fe[PhBP$^{iPr}_3$]]$_2$.

[vii] dbabh = 2,3:5,6-dibenzo-7-azabicyclo[2.2.1]hepta-2,5-diene

This ligand architecture also stabilizes a terminal iron(III) imide, [PhBP$^{Ph}_3$]FeNR (R = aryl), which mimics the iron imide suggested by the Chatt cycle.[48] Upon reaction with hydrogen gas, the iron(III) imide is reduced to an iron(II) amide (Figure 1.14).[49] Upon further reaction under a hydrogen atmosphere, the primary aryl amine is released and a partially hydrogenated benzene adduct is formed. Though the reaction is slow, taking days to proceed, it nonetheless validates the ability of a terminal iron-imide to undergo hydrogenation and release of amine.

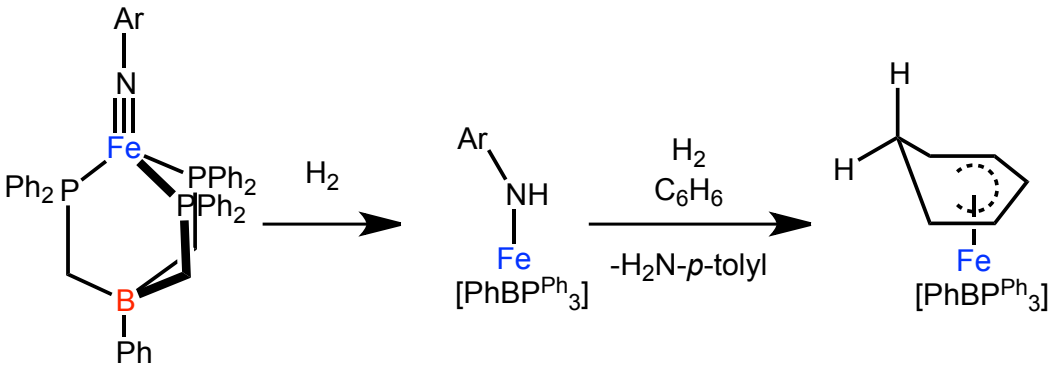

[PhBP$^{Ph}_3$]FeNAr

Figure 1.14 Stepwise hydrogenation of an iron(III) imide to a formally iron(II) cyclohexadienyl species and generation of a primary arylamine.

The preceding examples reflect the second half of the Chatt cycle, wherein the N-N bond scission has already occurred, and there are no interactions *trans* to the binding site. The breaking of the N-N bond is of fundamental importance, and transformations of bound dinitrogen at iron centers are rare. Gratifyingly, several Chatt-type intermediates relevant to N_2 reduction are observed upon installation of an element in the *trans* site. Metallation of the SiP$^{iPr}_3$ ligand with iron under an N_2 atmosphere and in the presence of a strong reductant yields the terminal dinitrogen complex [SiP$^{iPr}_3$]Fe(N_2), which can be

further reduced to a formally Fe(0) state.[16, 50] This anionic complex, Na[[SiP$^{iPr}_3$]Fe(N_2)], readily reacts with trimethylsilylchloride (TMSCl) to produce the silyldiazenido complex [SiP$^{iPr}_3$]FeNNSiMe$_3$ (Figure 1.15). This reaction represents a two-electron reduction at N_2 and is analogous to the first protonation/reduction of the distal nitrogen atom in the Chatt cycle.[16]

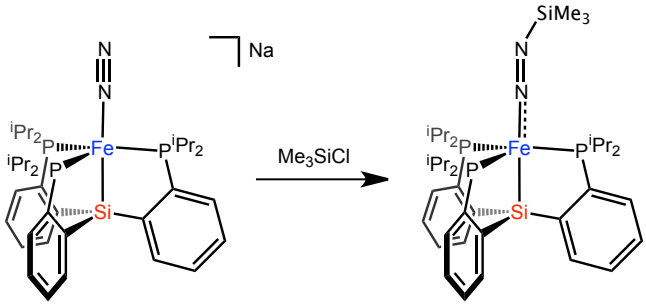

Figure 1.15 Silylation of the distal nitrogen atom in Na[[SiP$^{iPr}_3$]Fe(N_2)]

Following the formation of the silyldiazenido complex, additional functionalization of the distal nitrogen atom would yield a hydrazido derivative. This chemistry has not been reported for the [SiP$^{iPr}_3$] framework, but the two-electron and four-electron reductions of N_2 were demonstrated in (TPB)Fe(N_2) species (Figure 1.16).[17, 36]

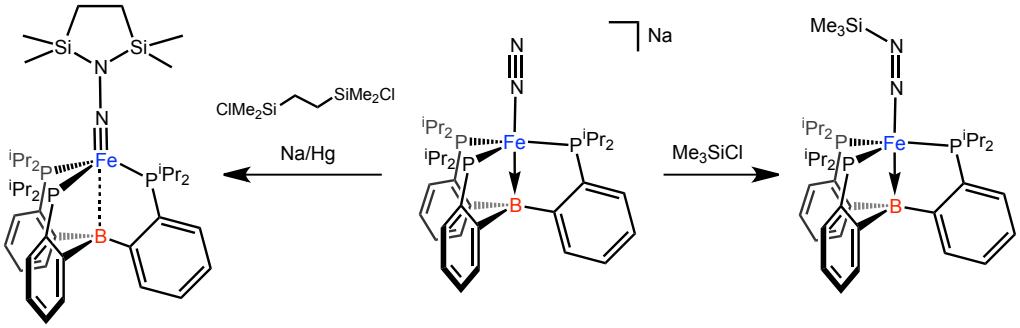

Figure 1.16 Single and double silylation of the distal nitrogen atom in Na[[SiP$^{iPr}_3$]Fe(N_2)]

Similarly to Na[[SiP$^{iPr}_3$]Fe(N_2)], the borane analog Na[(TPB)Fe(N_2)] reacts with TMSCl to furnish a silyldiazenido complex. Alternatively, addition of the disilylating reagent 1,2-bis(chlorodimethylsilyl)ethane (CDSE) and excess reductant cleanly yields the iron(II) disilylhydrazido product, reflecting a four-electron reduction at N_2.[36] The connectivity of this structure—*i.e*, functionalization at only the distal nitrogen atom—could not be verified crystallographically, but low-spin nature of the iron(II) center permitted extensive multinuclear NMR spectroscopic assignments that are fully consistent with this formulation. Further functionalization of the disilylhydrazido moiety in this framework was unsuccessful and produces only intractable mixtures.

However, use of the diphosphinoborane (DPB) framework also permits isolation of the disilylhydrazido complex, which was confirmed crystallographically.[20] In this case, the iron is pseudo-five coordinate and has stabilizing interactions with an unsubstituted arene ring instead of a third phosphine arm (Figure 1.17). Similar metal-arene interactions have been observed in (DPB)Ni complexes.[51]

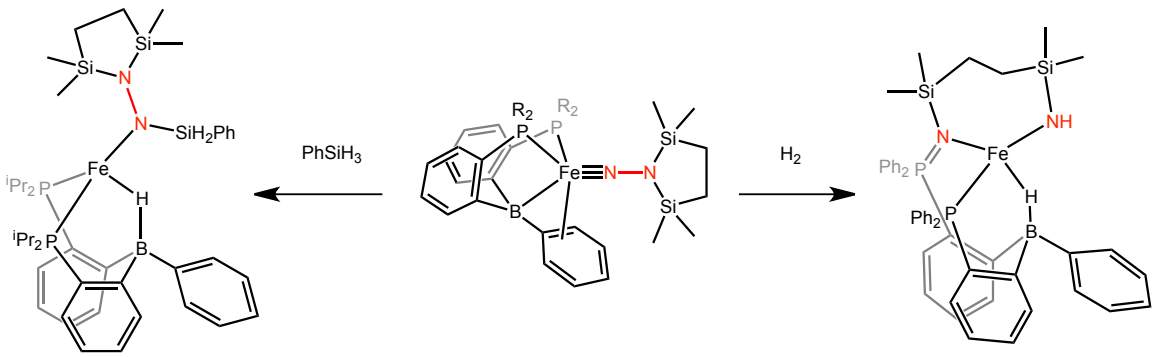

Figure 1.17 Silylation of a disilylhydrazide and cleavage of the N-N bond in (DPB)Fe complexes.

Because of the increased flexibility provided to the iron center upon removal of one phosphine ligand, additional functionalization is possible at the proximal nitrogen (Figure 1.17, top). The iron-borane bond reacts with phenyl silane to cleave the Si-H bond, generating both an Fe-μ-(H)-B interaction and a Si-N bond. Alternatively, hydrogenation of the disilylhydrazide cleaves the N-N bond; interestingly, the electrons to break the final N-N bond appear to come from one of the phosphines, which is oxidized to a phosphinimine. The reaction with dihydrogen induces homolytic cleavage of H_2, again generating the hydridic Fe-μ-(H)-B interaction, while the remaining nitrogen site is protonated to form an iron-amide bond. The formation of the Fe-μ-(H)-B appears to be highly thermodynamically favorable, as it also appears for (TPB)Fe(N_2) species in the presence of dihydrogen.[38]

Though breaking the N-N bond in these silylated complexes also inevitably yields ligand decomposition, catalytic conditions with acid substrates have been surprisingly successful in generating ammonia. Both $[(TPB)Fe(N_2)]^-$ and $[[CP^{iPr}_3]Fe(N_2)]^-$ are competent catalysts for the formation of ammonia derived from N_2, and their efficiencies are comparable to other known catalysts: the TPB ligand produces up to 7 equivalents of ammonia per iron site, and the CP^{iPr}_3 ligand produces up to 4 equivalents per iron site. These species represent the first examples of iron model complexes capable of catalytically generating ammonia directly from dinitrogen. The catalyst deactivation pathway is known in (TPB)Fe(N_2) and involves the formation of Fe-μ-(H)-B motif. Because hydrogen gas is inevitably produced as a byproduct from the addition of acid

and reductant, this product is extremely difficult to avoid, though it has been demonstrated to effect slow hydrogenation of unsaturated C=C bonds to regenerate (TPB)Fe(N_2). Additional work is clearly warranted to further explore the benefits of main group elements, especially Lewis acids, *trans* to an open binding site at a transition metal.

However, it is noteworthy that these functional models contain only a single iron site rather than the eight metal sites in FeMoco. The prospect of multimetallic cooperativity is intriguing, especially with regard to the possible delocalization of charge, and metal-metal bonds are strongly implicated in several biological systems. The prospect of a *trans* transition metal influence is therefore also worthy of study.

1.3 Multiple bonds between two transition metals

Multiple metal-metal bonds were first recognized in 1963,[viii] when $[Re_3Cl_{12}]^{3-}$ was unambiguously shown to possess formal double bonds.[52] In the following year, the first quadruple bond was demonstrated in $Re_2Cl_8^{2-}$,[53] and the first triple bond was reported in 1966 with $Re_2Cl_5(CH_3SCH_2CH_2SCH_3)_2$.[54] Nearly forty years elapsed prior to Power and coworkers' report of the quintuple bond in Cr_2Ar_2 (Ar = 2,6-(2,6-$^{iPr}C_6H_3)C_6H_3$).[55] X-ray crystallography has been a critical tool for the confirmation of metal-metal bonds, and today collection of the solid-state structures is routine. Surprisingly, the overwhelming majority of metal-metal bonds are still homobimetallic, as shown in Figure 1.18. Several factors are responsible for this result, but the main contribution is the synthetic difficulty of generating a heterobimetallic species that can be easily separated from its homobimetallic counterparts.[56, 57]

The bonding picture between metals is quite different than main group element bonds, as metals can form up to five bonding interactions wherein all *d* orbitals are involved. The bonding interactions are therefore maximally composed of one σ (d_z^2), two π (d_{xz}, d_{yz}), and two δ (d_{xy}, $d_{x^2-y^2}$) bonds. The exact ordering and occupation of these orbitals varies, depending both on the ligands, the geometry about the metal center, and the identity of the metals themselves.[56, 58] Homobimetallic species with single, double, triple, and quadruple bonds are now well known, but the chemistry of quintuple bonds is

---

[viii] Complexes with multiple metal-metal bonds have been synthesized since at least 1844, when Peligot reported on a chromium complex now recognized as having a quadruple bond. This work was not appreciated as unusual until re-examined by Garner and King over a hundred years later. See reference 74 for further details.

new and largely unknown. Moreover, the chemistry of heterobimetallic species with multiple bonds is also poorly developed outside of the Group 6 triad.[56, 57]

The supporting ligands for metal-metal bonds fall into a number of general classes, several of which are shown in Figure 1.19.[ix] Quintuple bonds are now known in four ligand classes in a variety of geometries: class I is formally monodentate, though it is currently represented only by dichromium complexes that are stabilized by a Cr-C_{ipso} interaction.[55, 59] Class II contains both dichromium[60-64, 65] and dimolybdenum[66] species; the dichromium species are planar and two-coordinate with respect to the ligand, whereas the corresponding dimolybdenum species have been shown to retain a bridging salt in addition to the conserved, coplanar ligands. Class III is represented by a sole dichromium complex and was the first trigonal example of a quintuple bond.[67] Class IV contains, maximally, quadruple bonds and is not believed to support quintuple bonds[56] due to the relative energies of the bonding orbitals.[x] Class V is similar to class III except for the installation of a tertiary amine cap,[68, 69] though examples in this class are currently limited to single bonds. The presence of the amine has actually been shown to enhance a dicobalt bond,[69] and quintuple bonds should be isolable in this framework. Class VI is the most recent contribution to the literature and represents the first example of a heterobimetallic quintuple bond.[70, 71]

[ix] This classification system is adapted and expanded from that of Tsai *et al*. from references 74 and 75.

[x] Drawn here as solely nitrogenous ligands, this class also encompasses carboxylates and mixed N,O donors, the most notable of which is 2-methyl-6-hydroxypyridine (mhp). Cotton and coworkers have also extensively studied halide and diphosphine complexes with quadruple bonds. Though not discussed here, these works actually represents the majority of metal-metal multiple bond literature. Interested readers are directed to reference 72.

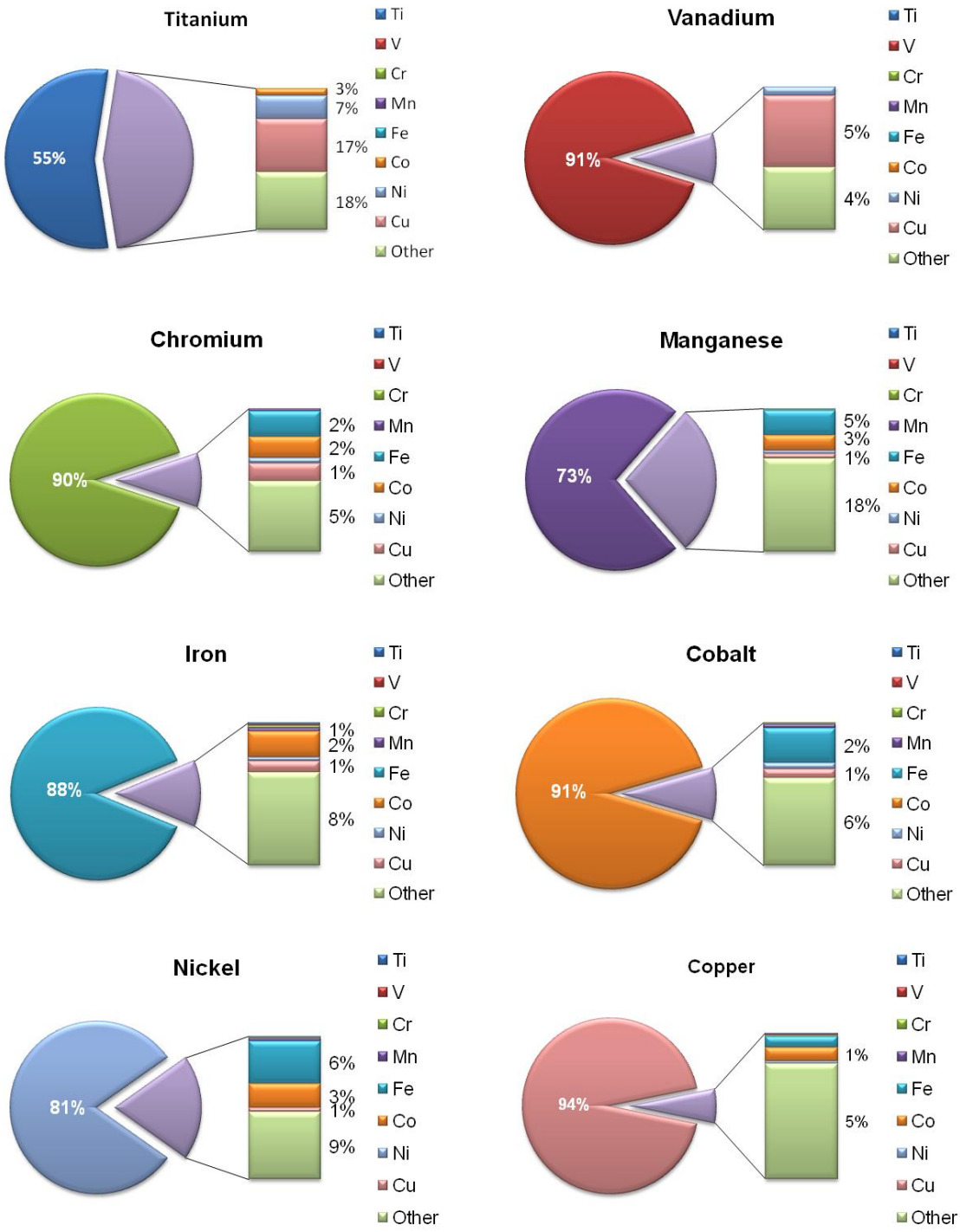

Figure 1.18 Metal-metal interactions of first-row transition metals. The inset percentage in each chart signifies homobimetallic complexes, and all heterobimetallic species are provided in the side bar. Values less than 1% are not listed. "Other" refers to 4*d* and 5*d*

metals. Data is from the Cambridge Crystallographic Database and encompasses all metal-metal interactions less than or equal to 3.0 Å.

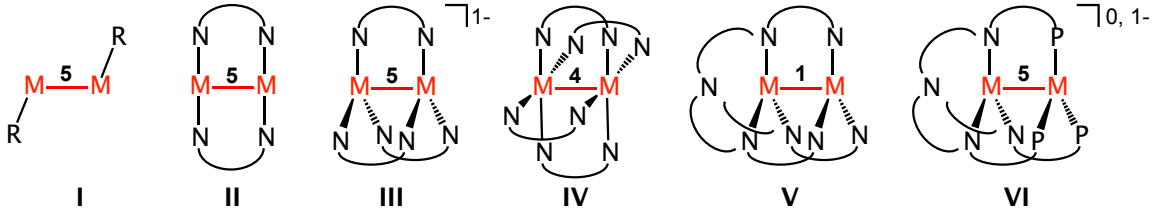

Figure 1.19 Selected classes of metal-metal bonds known in the literature. The bimetallic unit is highlighted in red for clarity, and the number above the bond represents the maximal bond order known for this motif.

Even within an identical ligand class, different metals can show remarkably different behavior. An extreme case is shown in Figure 1.20, comparing essentially isostructural Cr_2, Fe_2, and Co_2 complexes in a class III tris-formamidinate framework.[67, 72, 73]

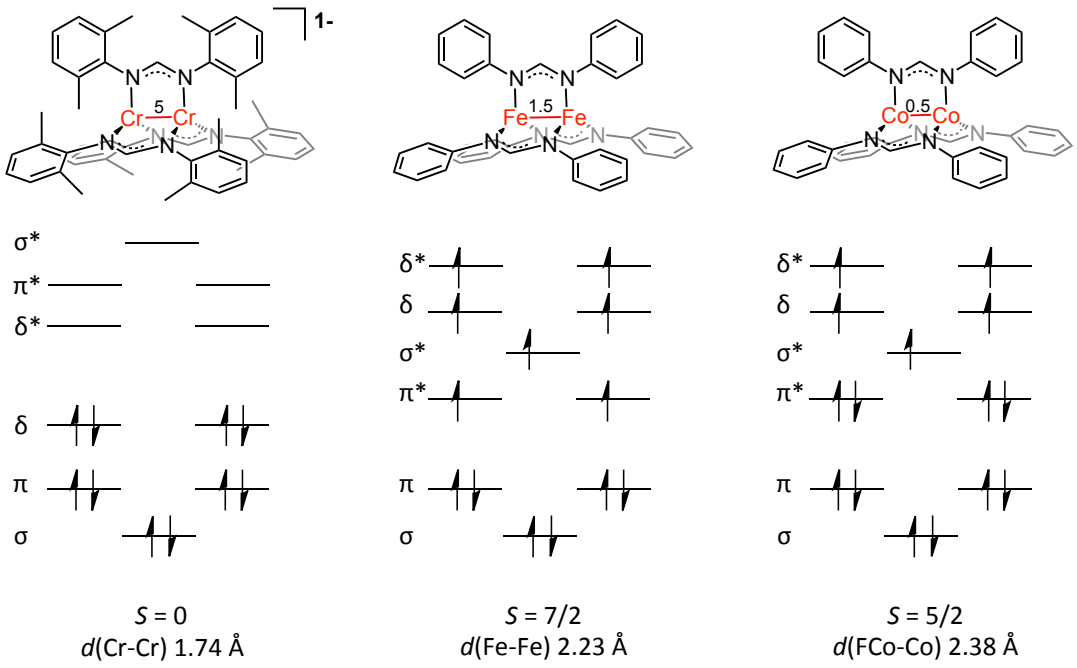

Figure 1.20 Molecular orbital diagrams of Cr_2, Fe_2, and Co_2 complexes. The spin state *S* and metal-metal distances are also provided.

All three molecules have the same three-fold symmetry, yet the electronic structures of these complexes are in stark contrast. For dichromium, all ten electrons are antiferromagnetically coupled and reside only in bonding orbitals. As a result, the electrons fully populate the σ, π, and δ orbitals, yielding a net diamagnet and a quintuple bond.[67, 74] For both dicobalt and di-iron, the electrons couple ferromagnetically, yielding the high spin $S = 5/2$ and 7/2 states, respectively.[72, 73] Too, the δ and δ* orbitals are higher in energy than the antibonding σ* and π* orbitals, which substantially mitigates the effect of the stronger σ and π bonds. As a result of high spin configuration, the antibonding orbitals are substantially populated, and the bond order (BO) is dramatically reduced from 5 in dichromium to 1.5 in di-iron and 0.5 in dicobalt. The qualitatively different bonding schemes can be inferred experimentally from differences in the metal-metal bond length, as the dichromium distance (1.74 Å) is considerably shorter than the di-iron (2.23 Å) or dicobalt (2.38 Å).

It is critical to note here that these descriptions are highly simplified formulations of the metal-metal interaction.[56, 57] Metal-metal bonds are known to have strong configuration interactions, and therefore some additional contributions to the wavefunction are always present. In quintuply bonded dichromium, for example, additional contributions include configurations in which antibonding σ*, π*, and δ* orbitals are occupied. This population of antibonding orbitals therefore lowers the "real" bond order relative to the formal bond order, sometimes substantially. One instructive example of this effect is the metal-metal bond distance: chemists intuitively associate

shorter bond distances with high bond order, but this assumption is not *necessarily* correct.[56] Dichromium species with formal quadruple bond are known to have metal-metal distances ranging between 1.798 and 2.531 Å, and the metal-metal bond can be highly sensitive to axial ligation. In one case, Cotton showed that dichromium complexes with axial π donors are capable of lengthening the bond by as much as 0.3 Å *in the same complex*, where the only difference was the inclusion of solvent in the crystal lattice that changed the orientation of the π donor.[75] The surprisingly large magnitude of this effect is obviously problematic, as the metal-metal bond length is often one of the easiest parameters to identify.

The relevancy of formal bond orders has therefore been investigated by numerous theoretical groups, and detailed collaborative work has supported the assignment of high bond orders in several of these complexes.[74, 76, 77] In the nine years since Power's initial report, approximately twenty complexes containing quintuple bonds have been established, all but one of which contain either dichromium or dimolybdenum. The heterobimetallic complex consists of a chromium-manganese bond. These structures and their distances are shown in Figure 1.21.[60, 62-64, 65, 66, 67, 78] Though dichromium alone is known to have over 150 crystallographically characterized complexes with quadruple bonds, the generality of the quadruple bond was not immediately apparent. Upon the discovery of the quadruple bond in $Re_2Cl_8^{2-}$, Cotton wrote: "It appears that the formation of extremely short, presumably quadruple, bonds between d^4-ions of the second- and third-row transition elements may be quite general." The severity of this understatement

was only recognized later,[56] and the quintuple bond may yet be shown to be quite synthetically versatile. Theoretical calculations have already been used to suggest several synthetic heterobimetallic targets, including V–Mn, V–Tc, Nb–Mn, Cr–Mo, and Nb–Tc.[79]

Interestingly, Power's quintuply bonded species, d(Cr-Cr) = 1.80 Å,[55, 59] is only modestly shorter than the shortest quadruple bonds, 1.83 Å.[80] The gas phase dichromium distance, 1.68 Å,[81] sets the lower-bound for bond length, and the modest contraction relative to quadruple bonds was initially surprising. The synthesis of more dichromium complexes has now shown that the bond distance tends to be 1.75 Å or less, which appears to be independent of the coordination number at chromium.[60, 62, 64, 65, 67] The Kempe group has enforced a shortest dichromium distance, 1.70 Å, by cleverly utilizing a bulky guanidinate group to decrease the ligand bite angle.[65] Because the ligands bridge between two metal centers, lowering the bite angle sterically pushes the metal centers slightly closer together and results in a perceptibly shorter bond. Attempt to further decrease the length of the metal-metal bond with this strategy have been unsuccessful. In all of these cases, experimental studies verify that the bimetallic unit is engaged in quintuple bonding.

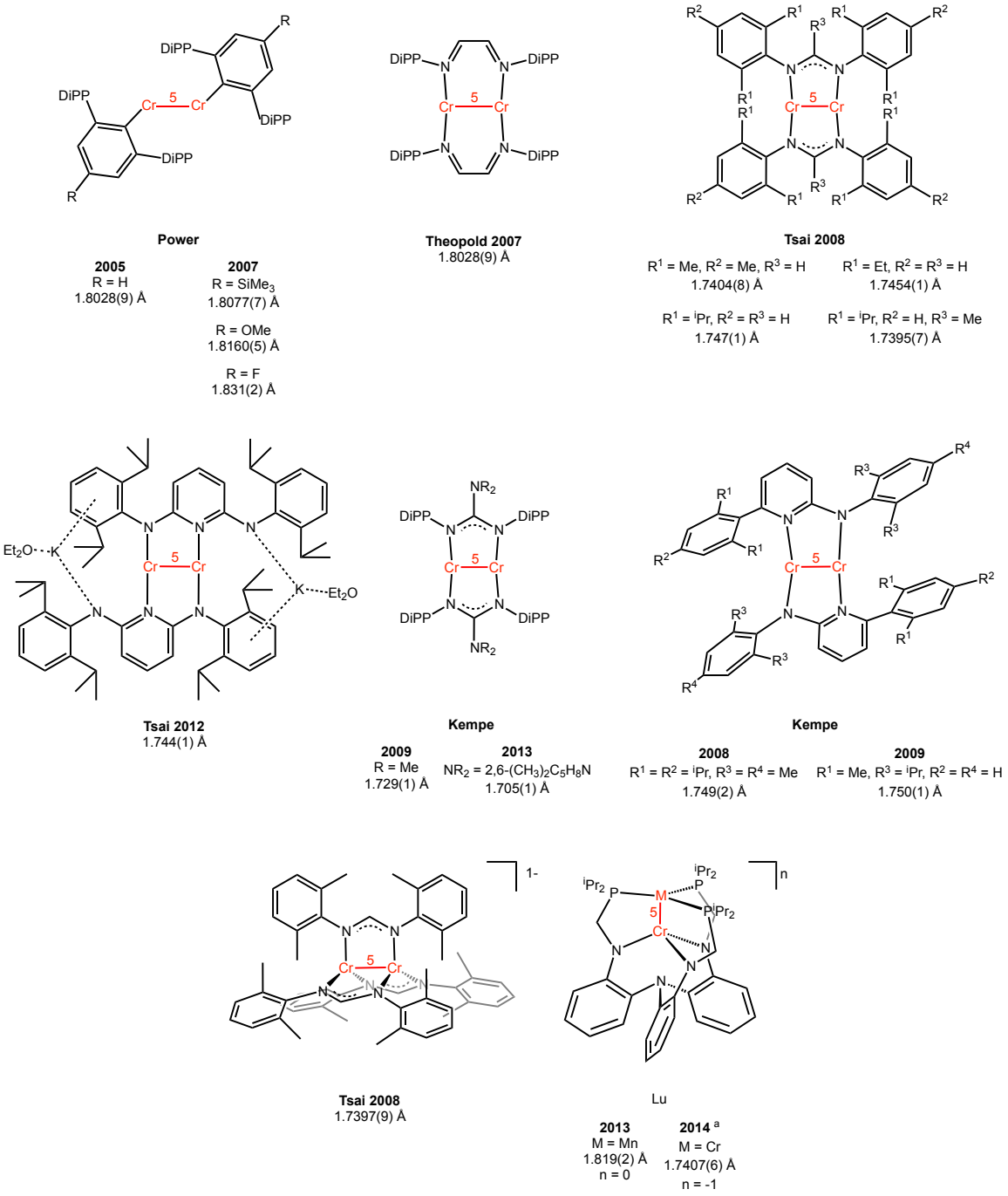

Figure 1.21 Selected complexes containing dichromium quintuple bonds. The metal-metal bond is highlighted for clarity, and the colored number indicates the bond order. The dichromium distance is listed under each respective complex or year. DiPP = diisopropylphenyl. [a] Year submitted for publication.

Our initial report of a MnCr complex containing quintuple bonds was the first example of heterobimetallic quintuple bonds, but heterobimetallic triple and quadruple bonds have also been investigated by Collman, Cotton, and others.[82, 83, 84, 85-89] These studies have primarily been conducted with either intratriad tetragonal paddlewheel complexes or intertriad phorphyrins and are summarized in Tables 1.1 and 1.2, respectively.

Table 1.1 Comparison of quadruply bonded Group 6 homo- and heterobimetallic species

Parameter	FBO	Ligands	Cr_2	CrMo	Mo_2	MoW	W_2
Bond length (Å)	4	Cl_4P_4 [a]	n/a	n/a	2.14(2)	2.21(2)	2.28(2)
	4	$(\mu\text{-mph})_4$ [b]	1.889(1)	n/a [c]	2.065(1)	2.091(1)	2.161(1)
	4	$(\mu\text{-}O_2CMe)_4$	1.96(1)	2.050(1)	2.0934(8)	n/a	n/a
	4	$(\mu\text{-}O_2CCMe_3)_4$	n/a	n/a	2.088(1)	2.080(1)	2.19(1)
^{31}P NMR shift (ppm)	4	$Cl_4(PMe_3)_4$	n/a	n/a	-8.3	−27.9 (Mo) 11.2 (W)	-7.3
Diamagnetic anisotropy [c]	4	$Cl_4(PP)_2$ [d]	n/a	n/a	-4450	-5100	-5700
Rotational barrier [d]	4	$(toep)_2$ [e]	n/a	n/a	10.8(1)	10.6(1)	12.9(1)
Vibrational Frequency	4	$(\mu\text{-mph})_4$	556	504	425	384	284

[a] P_4 = Average of six, nine, and five homologues, respectively, with monodentate and bidentate phosphines [b] mph = 2-methyl-6-hydroxypyridine [c] No crystal data is available due unresolvable Mo_2 contamination [d] in 10^{-36} m^3 [d] in kcal/mol [d] in kcal/mol [e] toep = tolyloctaethylporphyrin

In group 6, 2-methyl-6-hydroxypyridine (mph) has been shown to support all known bimetallic combinations, though the mixed-metal CrMo species could not be separated from a $Mo_2(mhp)_4$ contaminant. In the tetracarboxylate frameworks, Cr_2, CrMo, and Mo_2 bimetallics can be synthesized in the prototypical tetra-acetate framework, whereas the Mo_2, MoW, and W_2 variations are accessible upon substitution of the CH_3 for a ^{t}Bu group. As expected, the metal-metal distance increases

monotonically as each site is replaced by heavier congeners, which is in accord with the larger radii for 4*d* and 5*d* metals. The slightly shorter distance for $MoW(\mu\text{-}O_2CCMe_3)_4$ relative to $Mo_2(\mu\text{-}O_2CCMe_3)_4$ may result from several factors, none of which have been convincingly shown to dominate.[57] Disappointingly, the Mo_2, MoW, and W_2 triad does not display an obvious trend with respect to the ^{31}P chemical shift of bound phosphines, nor do the rotational barriers of Mo_2, MoW, and W_2 porphyrin complexes display a clear trend even as the stretching frequency decreases monotonically between Cr_2 and W_2 porphyrin complexes. In the latter case, the cofacial porphyrins have large surfaces areas and considerable dispersion interactions, which demonstrates that the barrier to breaking the δ bond is lower than pure ligand-ligand interactions.

Until recently, the only examples of intertriad heterobimetallic complexes were bisporphyrin complexes produced by Collman and coworkers. These complexes possess triple to quadruple bonds and have been characterized by Raman spectroscopy, ^1H NMR spectroscopy, and X-ray crystallography when available. Table 2.1 includes only those species that have been crystallographically characterized, but several other homo- and heterobimetallic species have been undoubtedly identified on the basis of ^1H NMR.[82, 83, 84, 85]

Table 1.2 Comparison of structurally characterized heterobimetallic phorphyrin complexes

MM' Core	Ground State configuration	Complex	MM' Bond length (Å)
MoRu	$\sigma^2\pi^4(\delta^{nb})^2(\delta^{nb}/\pi^*)^1$	[(oep)MoRu(tpp)] $^{+\,a}$	2.181(2)
	$\sigma^2\pi^4\delta^2(\delta^*/\pi^*)^1$	$[(tpp)MoRu(oep)]^+$	2.211(2)
MoOs	$\sigma^2\pi^4(\delta^{nb})^2(\delta^{nb}/\pi^*)^1$	[(oep)MoOs(tpp)]	2.238(3)
WRu	$\sigma^2\pi^4\delta^2(\delta^*/\pi^*)^1$	$[(oep)WRu(tpp)]^+$	2.297(2)
MoRe	$\sigma^2\pi^4\delta^2$	$[(tpp)MoRe(oep)]^+$	2.235(1)

[a] Oep = octaethylporphyrin, tpp = tetraphenylporphyrin\

This family of complexes is small but important, as the 1993 report of $[(oep)MoOs(tpp)]^+$ and $[(tpp)MoRu(oep)]^+$ was the first demonstrable example of metal-metal multiple bonds between different triads.[83] Even today, these species are quite rare. In addition to further reports from the Collman group, the Thomas group has reported FeV triple bonds[86] as well as FeCr and CoCr double bonds,[87] and the Lu group has reported on MnCr quintuple bonds, FeCr triple bonds, and CoCr double bonds.[71, 78] New ligand frameworks have overcome some of the synthetic challenges in creating new bimetallic pairs, and further work will be necessary to characterize the electronic structures and reactivity profiles of these previously unknown heterobimetallic species.

1.4 Scope of Thesis

The objective of this dissertation is to synthesize a double-decker ligand framework, N(*o*-(NHCH$_2$P(^{i}Pr)$_2$)C$_6$H$_4$)$_3$, capable of supporting various bimetallic species wherein one metal site is protected and *trans* to the open coordination site on the second. By systematically varying both metal sites, intrinsic properties of different metal-metal bonds can be elucidated and used to activate small molecule substrates. In the second chapter, this ligand is shown to support a series of metallalumatranes with inverse dative bonds between aluminum and nickel, cobalt, or iron. The cobalt- and iron-alane complexes also bind and modestly activate dinitrogen. In the third chapter, the zerovalent iron and cobalt centers are shown to be amenable to one-electron reduction, yielding subvalent iron(1-) and cobalt(1-) centers. Furthermore, the anionic iron-alane is shown to undergo a four-electron reduction at dinitrogen in the presence of the silylating reagent 1,2-bis(chlorodimethylsilyl)ethane, demonstrating multi-electron reduction of terminally ligated dinitrogen at a single iron site. In the fourth chapter, investigations of iron-chromium complexes show the first isolable example of metal-metal multiple bonding between different first row transition metals. In the fifth chapter, manganese-chromium and dichromium complexes are shown to engage in triple to quintuple bonding, generating extremely short metal-metal bonds. A series of isoelectronic complexes is prepared that contain Cr_2, MnCr, and FeCr cores. Investigation into these complexes shows that the strength of the isoelectronic chromium-metal interaction increases as the paired metals become more similar, *i.e.*, FeCr < MnCr < CrCr.

Chapter 2

Metal-Alane Adducts with Zero-Valent Nickel, Cobalt, and Iron

In part from:

Rudd, P. A.; Liu, S.; Gagliardi, L.; Young, V. G., Jr.; Lu, C. C. "Metal-Alane Adducts with Zero-Valent Nickel, Cobalt, and Iron" *J. Am. Chem. Soc.* **2011**, *133*, 20724-20727.

2.1 Overview

A heptadentate, double-decker ligand has been synthesized in order to isolate systematically varied bimetallic complexes. The ligand N(*o*-($NHCH_2P(^iPr)_2$)C_6H_4)$_3$ (**1**, H_3L^{iPr}) has been deprotonated with *n*-butyl lithium and metallated with aluminum(III), generating the monometallic species **2**, AlL^{iPr}. Complex **2** can be further metallated with a nickel(0) source to generate NiAlL, **3**, as well as cobalt(II) or iron(II) bromides and two equivalents of reductant to generate the dinitrogen complex N_2CoAlL^{iPr}, **4**, or the dinitrogen sandwich complex (μ-N_2)($FeAlL^{iPr}$)$_2$, **5**. These formally zero-valent complexes are the first reported metallalumatranes and add to the few examples of metal-alane bonds. Complexes **3** – **5** have been investigated by multinuclear NMR spectroscopy, UV-vis-NIR spectroscopy, single crystal X-ray diffraction, and theoretical calculations. The strength of the metal-alane bond increases in the order iron < cobalt < nickel.

2.2 Introduction

Metal-ligand interactions are fundamentally important in governing the scope and selectivity of chemical transformations, and the ability to rationally predict and control chemical processes is the heart of modern chemistry. Organic and inorganic chemists have developed numerous methods to accomplish a variety of chemical reactions with a high degree of selectivity in the solution state, but homogeneous catalysts are notably non-viable on an industrial scale. For instance, the ability of dirhodium systems to catalyze the activation of C-H bonds is well developed, and some of these complexes are known to exhibit over one million turnovers prior to catalyst decomposition. Nevertheless, the involvement of precious metals, catalyst deactivation pathways, and energy costs to extract organic products from an organic medium limits the effective use of these highly efficient catalysts.[3]

However, dirhodium systems are actually quite developed in comparison to most transition metal catalysts, especially those for highly difficult reduction chemistry. For instance, the most efficient catalyst designed for reduction of dinitrogen to ammonia has only twelve turnovers per metal center.[12, 19, 21, 22] The solid-state catalysts used in the industrial Haber-Bosch process are significantly more robust, and typical industrial iron-based catalysts have a typical lifetime of approximately fourteen years.[6] The solid-state process, despite being extremely energy-intensive, achieves a conversion efficiency of approximately 97%.[6] As a result of the long lifetime, relatively cheap catalyst material, and highly optimized efficiency, the industrial system is unlikely to be supplanted by any

homogeneous process.[3] However, the activity of pure iron in this system is lower than that of a material doped with potassium or aluminum, confirming that the interaction of iron with other metals might have substantial and beneficial effects.[6, 11]

Similarly, Tauster and co-workers showed that the deposition of Group 8 metal surfaces on titania supports strongly increase the rates of carbon monoxide reduction to methane, ultimately increasing these rates by an order of magnitude.[90] Moreover, this increase was found on Fe, Rh, Ni, and Pt, which suggested that some novel organization of the metal surface was promoting a highly efficient, catalytically competent production of methane. One proposal suggested that the TiO_2 support interacted with the surface to form metal-metal bonds, which was confirmed with K-edge EXAFS on a system containing Ti and Rh.[91] It is also noteworthy that EXAFS found the Ti-Rh distance in these complexes to be 2.53 Å, representing a significant contraction compared to the 2.68 Å of the intermetallic species. These properties, coined strong metal-support interactions (SMSI), were intensely studied to determine the reaction scope and utility.

Naturally, chemists were quite interested in attempting to model this type of interaction, which could lead to further rational design of both solid- and solution-state catalysts. The simplest model of these systems involves only two sites, and numerous groups made substantial contributions to understanding heterobimetallic metal-metal bonds.[57, 92-94] However, these early systems were often only viable for a handful of metal-metal combinations, and no broad trends were shown to exist in either electronic structure or reactivity. Importantly, the use of both redox inactive (Al, K) and redox active (Ti)

promoters suggests that different pathways might be operative in each case, and thus the study of the metal-metal bonding interactions are of fundamental interest.[3, 6] This chapter, in addition to chapter 3, will discuss the interactions of a transition metal with a redox-inactive metal site. Chapters 4 and 5 will discuss the interactions between two redox-active transition metals.

With respect to the redox-inactive metal sites, incorporation of boron, aluminum, gallium, or indium in the first coordination sphere of a transition metal is rare and their interactions with transition metals remain poorly understood.[40] Typically, in fact, ligands for transition metals are either X- or L- type ligands, which denotes that the metal-ligand interaction is composed of either a covalent interaction or a dative donation of electron density, respectively.[44] The X-type ligand is a simple covalent bond, typically of σ-type symmetry (e.g., •H, •Cl, •OR). L-type ligands are defined by their dative donation, which is typically ascribed as a ligand-to-metal donation of one or more electron pairs (e.g., linear LX or planar LX_2), though some of these ligands are also noted for metal-to-ligand backbonding (e.g., phosphines, CO). In metal-to-ligand backbonds, electrons from the transition metal will partially occupy π-symmetry anti-bonding orbitals. In contrast, Group 13 metals in the first coordination sphere of a metal site are expected to act as a Z-type ligand, which has an open p_z orbital and accepts electron density from a metal-based σ-symmetry orbital. Practically, this "inverse-dative" effect will decrease the electron density at the metal center, making it more electron poor. The first crystallographic evidence of a metal-alane Z-type interaction was reported in 1979 by Burlitch and

Hughes, who appear to have regarded it as a curiosity.[95] More recently, a series of Z-type ligands was reported by Bourissou and coworkers, who have extensively investigated M-B interactions (M = Ni, Pd, Pt, CuCl, Cu, AgCl, AuCl).[45] Despite a series of isoelectronic complexes, trends in this series are non-trivial to interpret due to the fact that the metal-phosphine bonds should vary according to the metal center, and the corresponding complexes with aluminum(III),[43] gallium(III),[41] and indium(III)[42] abstract chlorides from the metal center and terminate the Z-type interaction. Selected examples of Z-type interactions are shown in Figure 2.1.

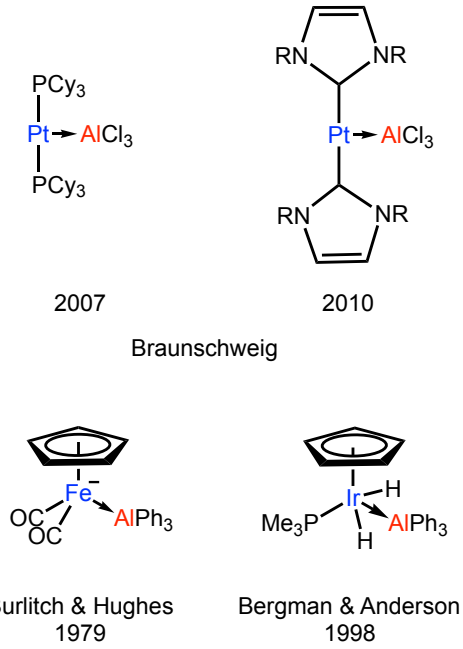

Figure 2.1 Structurally characterized Z-type interactions with aluminum prior to this work

With respect to reactivity studies, Z-type ligands are still rare. The Nagashima group has demonstrated that nickel-titanium complexes are rapid allylation catalysts, in contrast to their monometallic precursors.[96] The Thomas group has shown that a related

cobalt-zirconium species is capable of CO2 reduction,[97] Kumada coupling,[98] and hydrosilylation.[99] The Peters group has recently investigated the interactions of Fe-B and Ni-B complexes, demonstrating both dinitrogen reduction chemistry (Fe)[17, 20, 36, 38] and hydrogenation (Ni, Fe),[38, 51] though these results are currently limited solely to boratrane systems. Importantly, however, the iron-borane systems are stable for both π-basic and π-acidic ligands, which is believed to be important for the intermediates of dinitrogen reduction.[17, 19, 36] The electronic flexibility of Peters' iron-borane is shown in Figure 2.2.

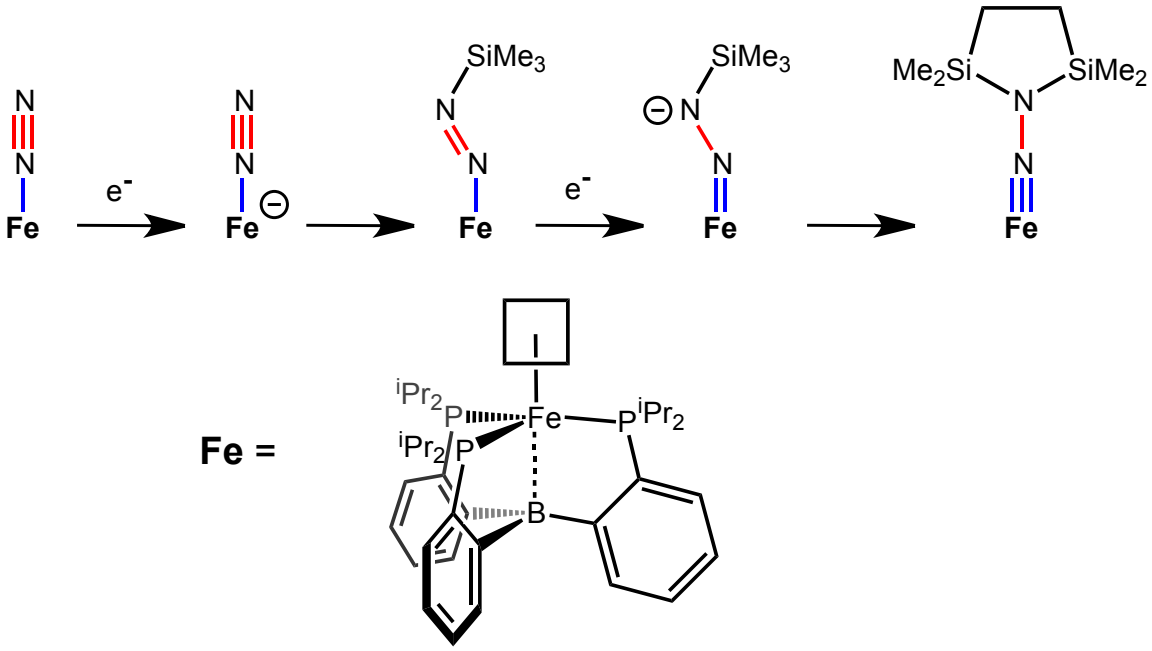

Figure 2.2 Stepwise reduction of the π-acidic N-N bond (red) and formation of π-basic silylhydrazide and disylylhydrazide species (blue).

The following sections discuss a general method to synthesize uncommon metal-alane bonds as a comparison for tuning Z-type ligands. The double-decker ligand used here is shown to be amenable to a general procedure for metallation, allowing straightforward synthesis of various derivatives.

2.3 Results and Discussion

The ligand N(*o*-(NHCH$_2$P(^{i}Pr)$_2$)C$_6$H$_4$)$_3$ (**1**, H$_3$L^{iPr}) is generated cleanly in only four steps from commercial reagents, as shown in Figure 2.3.[70] First, tris(2-nitrophenyl)amine is generated as described by Jones and MacBeth *via* nucleophilic aromatic substitution, though the purification process is substantially expedited by simply washing the crude reaction mixture with copious water and acetone to yield the bright yellow tris(2-nitrophenyl)amine.[100] The nitro- groups are then hydrogenated in conditions similar to those of Hu and coworkers, utilizing only one atmosphere of hydrogen gas and a 10 mol percent loading of Pd/C. Under one atmosphere of H_2, the reaction often takes three days to complete even under vigorous agitation.

The air-sensitive, colorless complex tris(2-aminophenyl)amine is then reacted with di-isopropylphosphinomethanol,[101] which undergoes a triple dehydration reaction to generate the air-sensitive ligand **1**, H$_3$L^{iPr}. The reaction to generate the ligand proceeds smoothly in dimethylsulfoxide (DMSO) at temperatures between 60 – 100 °C and may be complete within only four hours. Nevertheless, the reaction is typically run for overnight before solvent is removed *in vacuo*. The remaining off-white solid is reconstituted in diethyl ether and filtered, which removes any incompletely reacted amine containing either the mono- or bis-substituted phosphine products. The crude reaction mixture also typically contains one equivalent of DMSO per ligand, suggesting hydrogen bonding with the ligand, but the residual solvent can be removed either by prolonged heating at 100 °C under vacuum or rinsing the solids with copious acetonitrile. The typical scale

for this reaction utilizes approximately four grams of amine and five grams of phosphine, generating over eight grams of **1**. The metallation procedure was inspired by Gade[102] and can be accomplished by deprotonation with *n*-butyl lithium at – 45 °C in diethyl ether, though addition of $AlCl_3$ at temperatures above −100 °C yields a mixture of products. Alternatively, addition of the thawing Li_3L^{iPr} to a frozen solution of $AlCl_3$ in diethyl ether yields AlL^{iPr} (**2**) in nearly quantitative yield and excellent purity.

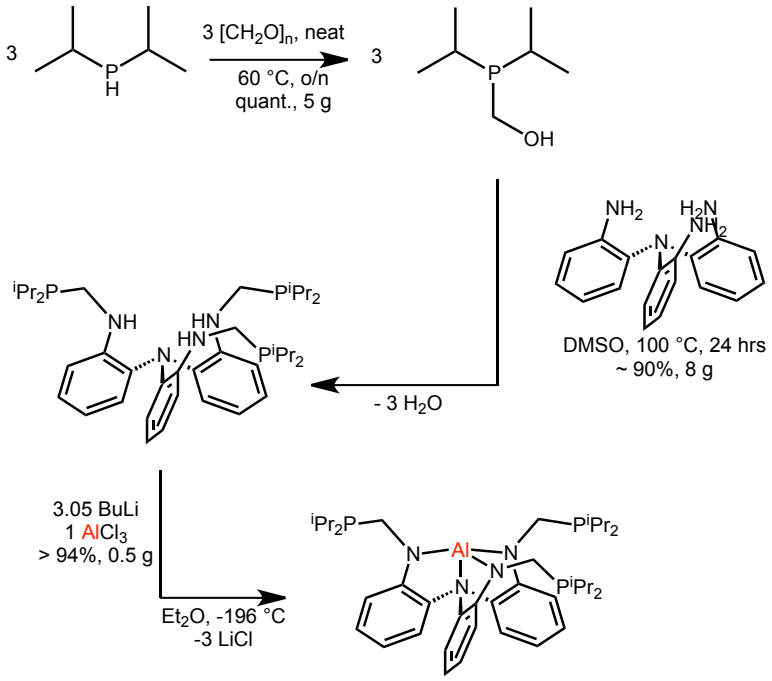

Figure 2.3 General scheme for ligand synthesis and metallation

These metallation conditions have been shown to work well with a variety of metals, though in some cases the metallations proceed more cleanly in THF than in diethyl ether. In addition to Al^{3+}, the following monometallic complexes have proven tractable: Ga^{3+}, In^{3+}, Sc^{3+}, Cr^{3+}, Mn^{2+}, and V^{3+}. The gallium, indium, and scandium complexes will be discussed in Chapter 3. The chromium complexes will be discussed in

chapters 4 and 5. The manganese species appears unsuitable due to the intrinsic lability of Mn^{2+}, which strongly predisposes the complex towards transmetallation. The vanadium species are under active investigation and will be discussed elsewhere.[103]

Several other bases are sufficiently strong as to deprotonate H_3**1**, such as benzyl potassium, potassium hydride, and potassium hexamethylsilylamide. However, the potassium complex K_3**1** was not found to react with $AlCl_3$ at room temperature in THF, the reasons for which are currently unclear. A recent report by Arnold and coworkers utilizes K_3L^{iPr} as a ligand for uranium(III) chemistry and utilizes pyridine as a metallation solvent,[104] suggesting that THF may simply be insufficiently polar to metallate K_3L^{iPr}.

Initial metallation of **2** was accomplished by adapting the procedure of Bourissou and coworkers, and $Ni(COD)_2$ (COD = 1,5-cyclooctadiene) was added to a stirred solution of **2** in THF. Unlike the tris(phosphino)borane (TPB) of that system, **2** reacts nearly instantly and cleanly generates **3** and two equivalents of free COD. Encouraged by the facility of this reaction, **2** was mixed with either cobalt(II) bromide or iron(II) bromide and two equivalents of the reductant potassium graphite (KC_8)[105] to generate the zero-valent metallalumatrane species. The synthetic scheme for **3** – **5** is shown in Figure 2.4. Characterization data of **1** – **5** is discussed in the following subsections. The use of other iron(II) or cobalt(II) sources (*e.g.*, acetate, chloride, iodide) or non-polar solvents was unsuccessful.

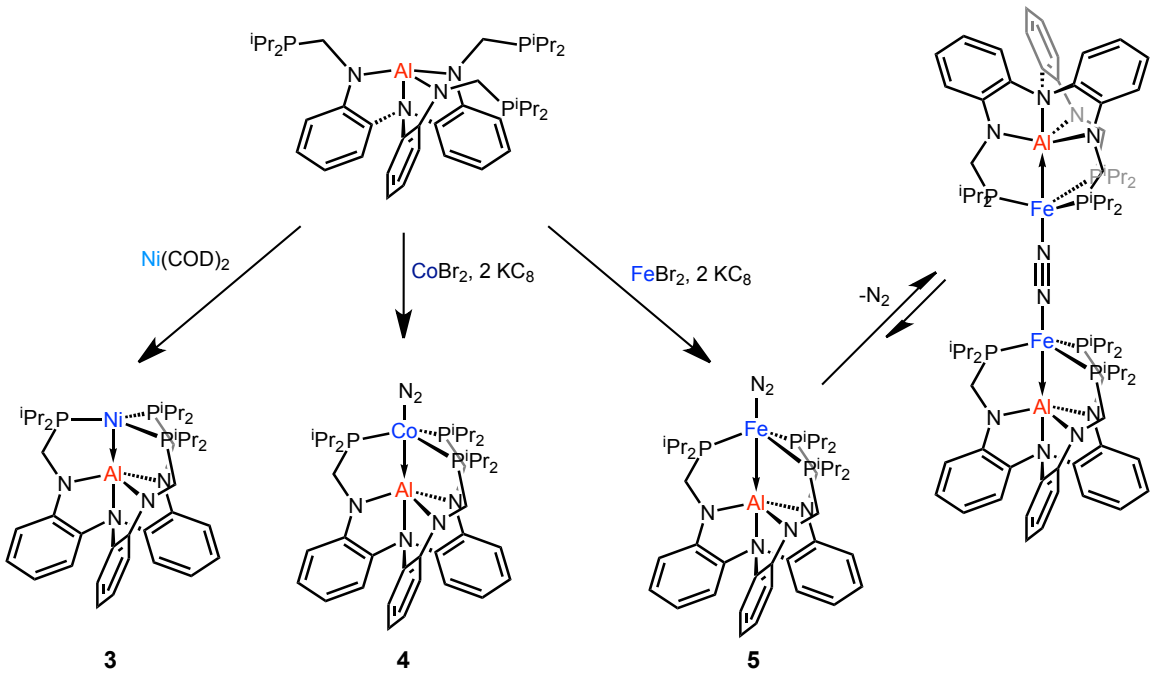

Figure 2.4 Generation of bimetallic complexes **3** – **5** from monometallic AlL^{iPr} **2**

2.3.1 Nuclear Magnetic Resonance Studies

Proton nuclear magnetic resonance (NMR) is a valuable tool to quickly determine the suitability of a particular reaction or reaction conditions, and the inclusion of pendant phosphine donors also allows for interrogation of the ^{31}P nucleus in addition to the ^{1}H nucleus. Phosphorous has only one naturally occurring isotope with an I = ½ nuclear spin, and the ^{31}P nucleus has comparable sensitivity to ^{1}H, so each diamagnetic complex possesses a diagnostic ^{31}P shift. Similarly, ^{27}Al is the sole naturally occurring isotope, but the I = 5/2 nuclear spin is known to generate broad signals under certain conditions. The ^{27}Al information is also presented, but the extreme linewidths and unusual insensitivity have thus far precluded useful interpretation. Unless noted otherwise, all

NMR interpretations have been assisted by crystallographic characterization (Section 2.3.2) to definitively identify the structure.

The ligand H_3L^{iPr} has a diagnostic ^{31}P shift at 3.05 ppm, which shifts downfield to 8.5 ppm upon metallation with $AlCl_3$. The ^{1}H NMR spectrum of **2** exhibits seven sharp peaks, indicating free rotation of P-C bonds. Figure 2.5 shows an annotated ^{1}H NMR spectrum of **2** with peak assignments. The ^{31}P spectrum possesses a single resonance and is consistent with free rotation of the phosphine arms. In contrast, the trisphosphino -borane (TPB) and -alane (TPA) ligands studied by Bourissou and coworkers exhibit ambiphilicity, wherein one phosphine coordinates to the internal Lewis acidic site.[43, 106] The ^{27}Al spectrum of **2** possesses one extremely broad signal at 82.2 ppm.

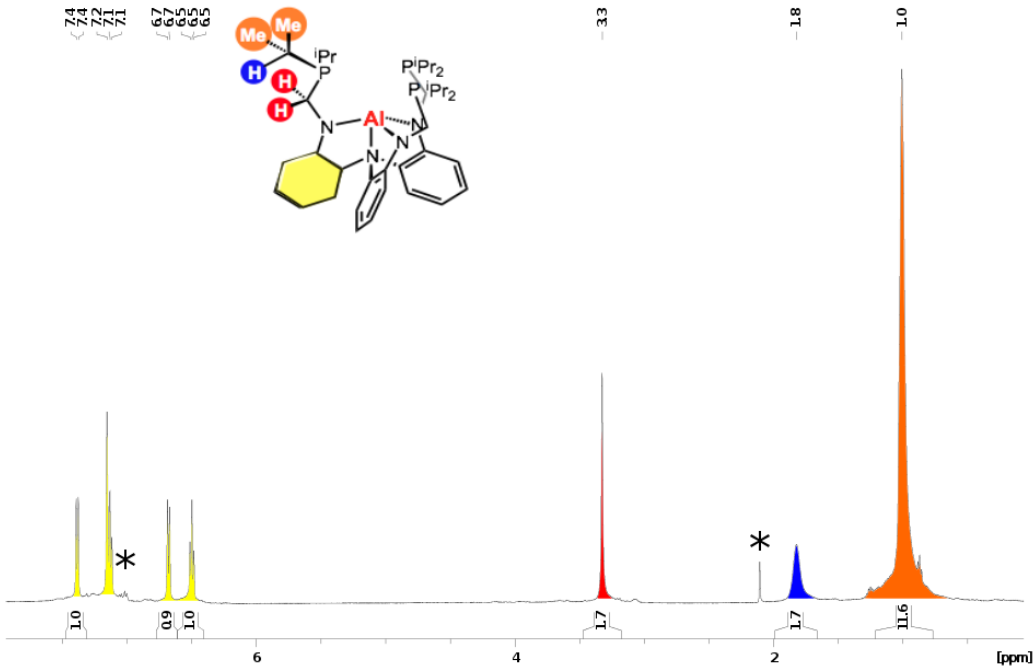

Figure 2.5 Assignment of NMR peaks in **2** (C_6D_6, ^{1}H 300 MHz)

Upon addition of $Ni(COD)_2$ to a solution of **2** in THF or toluene, the solution immediately develops a deep brown color. The ^1H NMR shows exclusively diamagnetic signals, in accord with the expected d^{10} configuration on nickel. The ^{31}P spectrum of **3** shows only one signal, which has shifted downfield from 8.5 ppm to 49.4 ppm. Unlike **2**, the ^1H NMR demonstrates a locked geometry on the NMR timescale: the methylene backbone splits into two resonances ($^1J_{HH}$ = 12 Hz), which is consistent with a geminal coupling. The methine resonances also separate by approximately 0.5 ppm and exhibit coupling to the methyl groups, but the magnitude is comparable to instrument resolution. The methyl resonances split in an approximate 1:2:1 ratio, and each resonance is coupled to both the methine proton and the phosphorous nucleus, yielding a quartet signal. The ^1H NMR for **3** is shown in Figure 2.6, including assignments. Upon metallation with nickel, the ^{27}Al resonance shifts slightly upfield to 78.6 ppm. Due to the linewidth of the spectrum, this change is not considered to be significant.

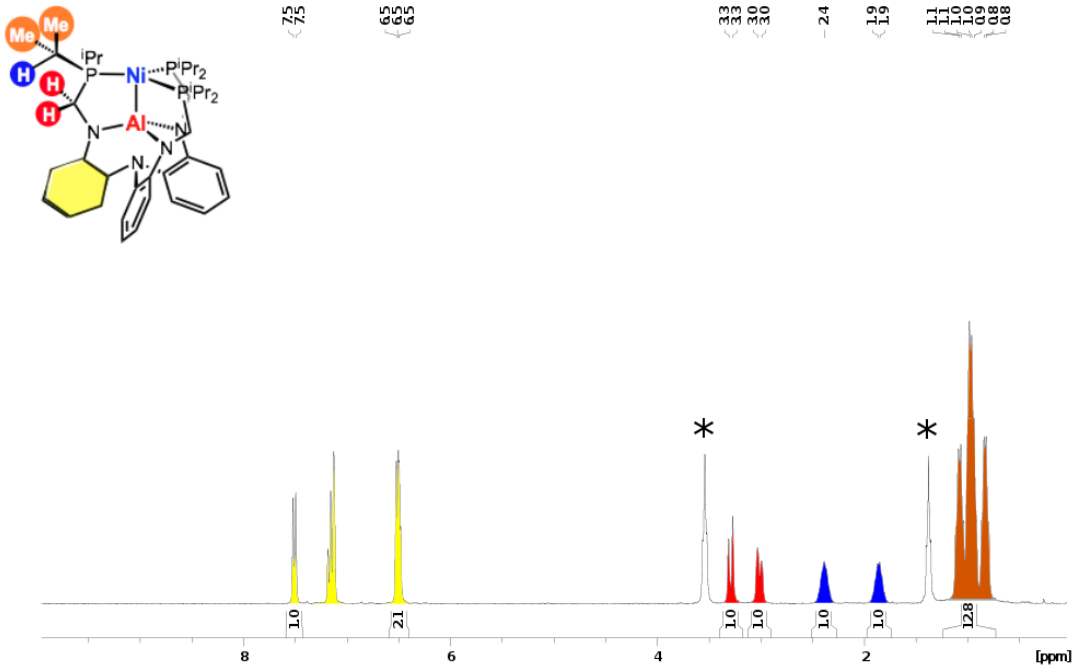

Figure 2.6 ^{1}H NMR spectrum of NiAlL^{iPr} **3** (C_6D_6, ^{1}H 300 MHz, * denotes residual THF solvent).

Initial metallation of **2** with cobalt(II) bromide in THF yields a dark blue solution; in a related phosphinoamide system, the Thomas group has noted a spontaneous reduction from Co(II) to Co(I) in the presence of a monometallic precursor,[107, 108] though there is no evidence for a spontaneous reduction event to generate the a monovalent cobalt species en route to **4**. Addition of only one equivalent of KC_8 to the reaction of **2** and $CoBr_2$ yields a paramagnetic species with observed C_3 symmetry that is proposed to be the monohalide Co(I) species BrCoAlL^{iPr}, **4-Br**, as a second equivalent of KC_8 yields **4**. Additional characterization of this complex was hindered by the high solubility of the complex, and no crystalline material was obtained. In light of these difficulties, further

studies were not undertaken, but the use of hexamethyldisiloxane to crystallize CrL^{iPr} and $[FeCrL^{iPr}][BAr^{F}_{4}]$ in Chapters 4 and 5, respectively, suggests one potential avenue to crystallize highly soluble complexes of L^{iPr}.

Complex **4** is isolated in good yield as a brown powder. The ^{1}H NMR of **4** displays 12 paramagnetically shifted resonances between -3.9 and 78.6 ppm (Figure 2.7). The number of peaks is consistent with a completely locked geometry on the NMR timescale, which requires that all four methyl groups, both methine protons, and both methylene protons are magnetically inequivalent. No peaks can be assigned due to the paramagnetism of **4**, which also precluded the collection of ^{31}P or ^{27}Al spectra.

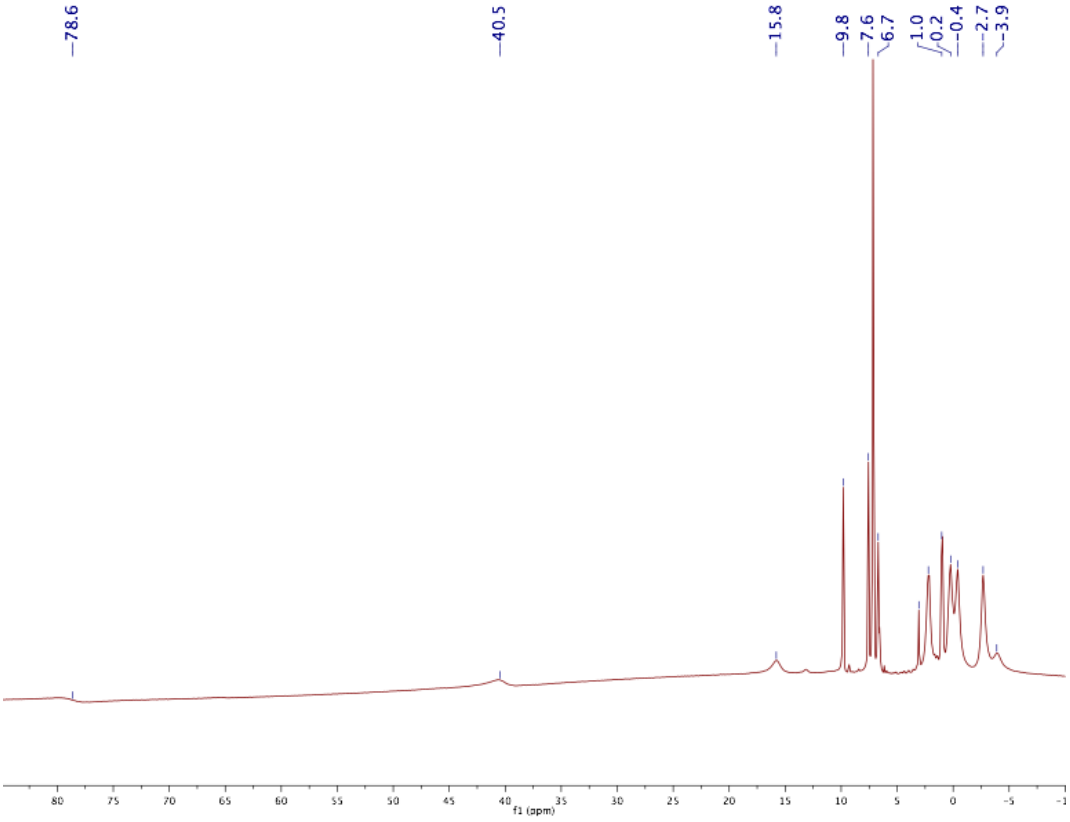

Figure 2.7 ^{1}H NMR spectrum of N_2CoAlL^{iPr} **4** (C_6D_6, 300 MHz)

Analogously to **4**, addition of iron(II) bromide to a THF solution of **2** yields a dark red solution with a complicated NMR pattern. Addition of 1 equivalent of KC_8 yields a complex that is assigned as **5-Br** due to generation of **5** upon addition of a second equivalent of reductant. Similar to **4-Br**, the high solubility of **5-Br** hampered the ability to unambiguously identify **5-Br** crystallographically. Additionally, the paramagnetism precludes a solution-state structure assignment.

Complex **5**, isolated as a brown powder, also exhibits strong paramagnetic broadening effects in solution, and NMR resonances range between -15.8 ppm and 84.7 ppm. At least twelve resonances are observed, which is again consistent with the structure being locked into C_3 geometry on the NMR timescale. The ^{1}H NMR of **5** is shown in Figure 2.8, though again the paramagnetism does not allow for identification of individual resonances. Whether the solution state behavior of **5** is reflected in the solid-state structure is unclear, as the infrared spectrum displays a strong resonance at 2011 cm^{-1}, which is identical to that of the related N_2FeTPB complex published by Peters and coworkers.[17] However, it should be noted that the solid-state structure of N_2FeTPB has not yet been reported in the literature, and the assignment of that complex was based on IR spectroscopy and DOSY NMR spectroscopy. The dinitrogen ligand is evidently labile in N_2FeTPB and was reported to have inconsistent combustion analyses. The spectrum of **5** can plausibly be assigned as either the dinitrogen sandwich, μ-$N_2(FeAlL^{iPr})_2$, identified by single crystal X-ray diffraction or the terminal dinitrogen complex N_2FeAlL^{iPr} indicated by infrared spectroscopy. Due to the number of peaks being approximately

consistent with one molecule in solution, it seems likely that any solution state equilibrium strongly favors either the terminal or bridging species, but the possibility of both species in solution cannot be definitely discounted

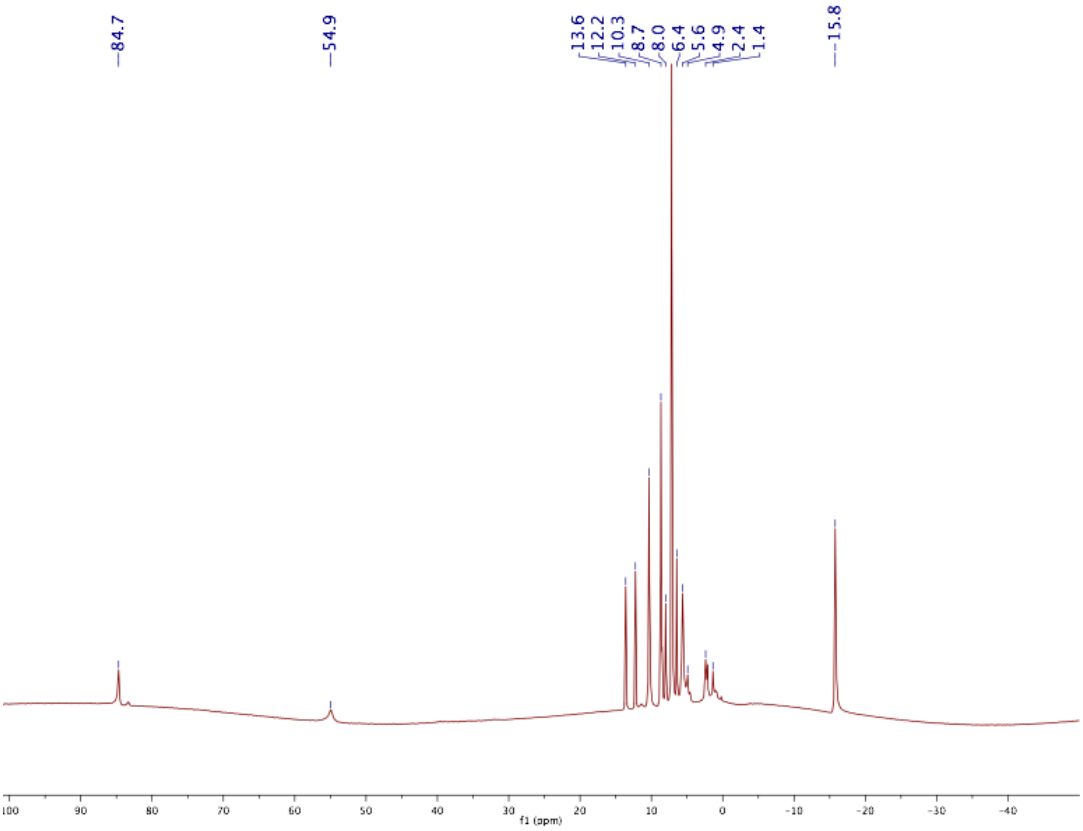

Figure 2.8 ^{1}H NMR spectrum of **5** (C_6D_6, 300 MHz).

2.3.2 Single Crystal X-ray Diffraction and Infrared Spectroscopy Studies

Single crystal X-ray studies were performed on complexes **2** – **5**. Each complex crystallizes in a different space group: **2** crystallizes in the trigonal space group R-3, **3** in the triclinic group P-1, **4** in the monoclinic group $C_{2/c}$, and **5** in the hexagonal group $P6(3)_{22}$. The structure of complex **2** is shown in Figure 2.9 as an acetonitrile adduct, evidencing a trigonal bipyramidal environment around the aluminum center. Unlike in

the TPB platform, there is no evidence for a phosphine-alane interaction, and the phosphine arms splay outwards in a C_3 symmetry dictated by the space group. In addition to establishing the ligand connectivity, the structure of **2** also yields Al-$E_{quatorial}$ and Al-N_{axial} distances for comparison with the bimetallic species, which are important to verify that no redox events occur at the aluminum center even in the presence of a highly-reduced transition metal center.

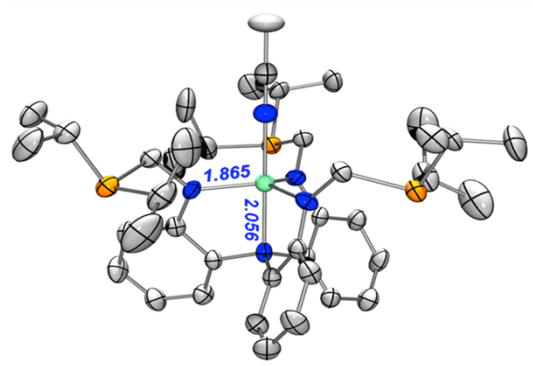

Figure 2.9 Solid-state structure of **2**, shown at the 50% probability level. H atoms and noncoordinating solvent molecules have been omitted for clarity. The values in blue represent the Al-N distances (Å).

Complexes **2** – **4** each possess a solvent molecule in the crystal lattice, but complex **5** crystallizes in a hexagonal space group and possesses large solvent accessible channels running along the crystallographic *c* axis. As a result of the large volume and non-polar channel walls, refinement of solvent molecules was not possible, and the entire void space was treated with the SQUEEZE function of the PLATON software package. The extended unit cell is shown in Figure 2.10 with all Q density omitted. Additional details regarding data collection and analysis can be found in Section 2.5, and further

discussion will focus on metrical analysis and any interesting crystallographic features of the structure.

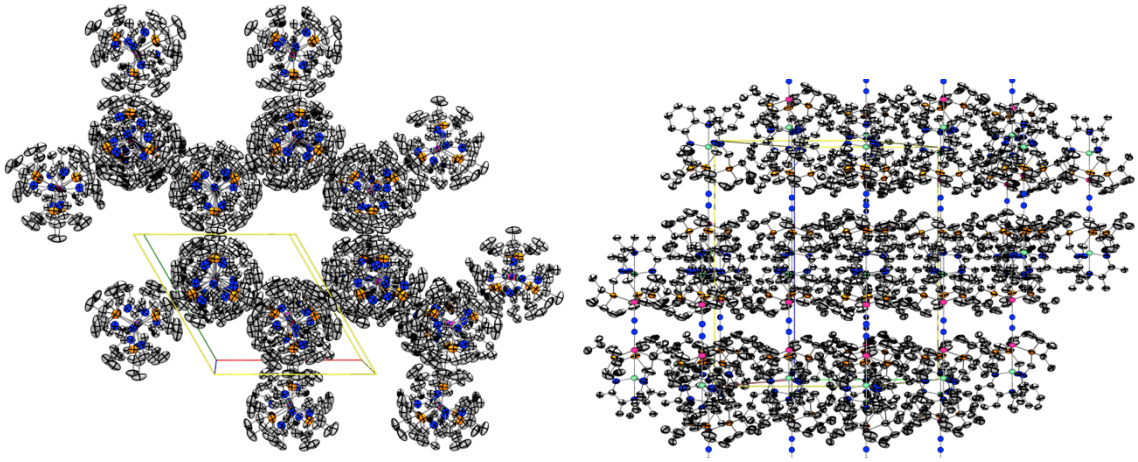

Figure 2.10 Views down the crystallographic *c* axis (left) and *a* axis (right) of **5**. Hydrogen atoms omitted for clarity.

For structures **3** – **5**, the main parameter of interest is the metal-aluminum bond, which gives a first order indicator of the strength of the metal-alane interaction. However, each metal center will have a distinct radius, which prevents a direct comparison between bond lengths. Cotton and coworkers presented the idea of the formal shortness ratio, *r*, as a means of normalizing disparate metallic radii to permit fair comparisons, where values above unity are less strongly interacting and values below unity indicate multiple bond character. The ratio *r* is defined as the distance between the two metals divided by the distance between the intermetallic radii, as calculated by Pauling.[109] Pauling's values are taken from the atomic radii in a bulk sample of a given element, though, and this definition does poorly when applied to interactions with main

group elements. Hence, interactions between transition metals and non-transition metals often substitute the covalent radii in the place of intermetallic radii, though the values diverge sharply as a result and cannot be directly compared to one another. In this chapter, as well as Chapter 3, the covalent radii will be utilized to compare metal-alane bonds, whereas Chapters 4 and 5 will utilize the metallic radii.

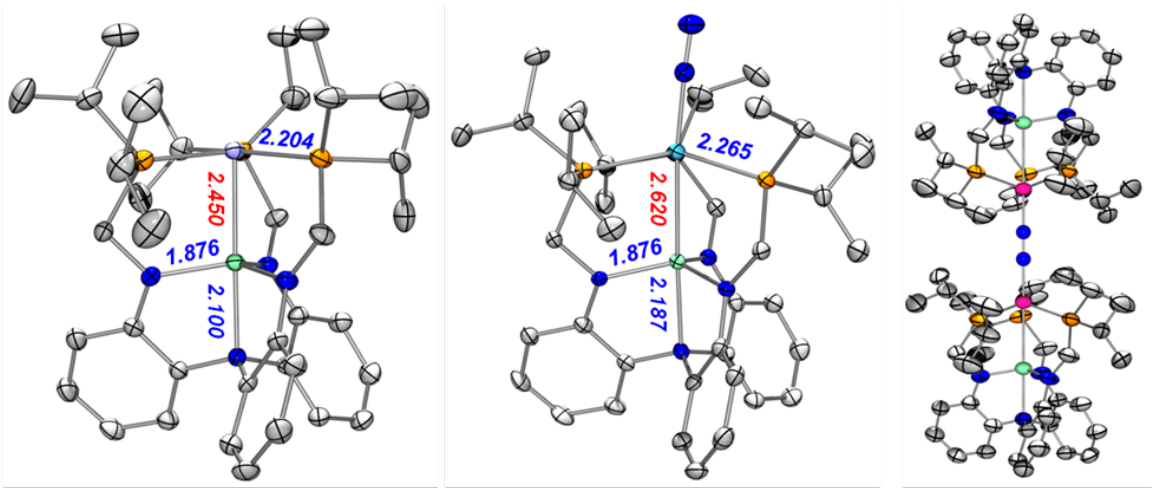

Figure 2.11 Solid-state structures of **3** – **5**, at the 50% probability level. H atoms and solvent molecules have been omitted. The values in blue represent the Al-N distances or M-P distances (Å), and the values in red represent the M-Al distance (Å). The values for **5** have been omitted for clarity; see Table 2.1.

The solid-state structures of **3** – **5** are shown in Figure 2.11. The zero-valent Ni complex **3** is shown to be trigonal pyramidal at nickel, which is notable insofar as it yields an unsaturated 16 electron species with an open binding site. However, this geometry is consistent with the solid-state structure of NiTPB, which also shows a trigonal pyramidal geometry at a formally nickel(0) center. The zerovalent Co and Fe species, by contrast, each bind a dinitrogen molecule and possess a trigonal bipyramidal

geometry at the metal center. The cobalt complex **3** binds dinitrogen in a terminal fashion and is a 17 electron species. The zero-valent iron species **5**, in contrast, binds dinitrogen in a bridging fashion and is a formally 16 electron species. The difference in dinitrogen binding modes between **4** and **5** is noteworthy, especially in the context of dinitrogen activation chemistry. Terminal coordination of dinitrogen often produces only modest activation of N_2, but the addition of a second metal site capable of backbonding into π^* orbitals has been known to induce a spontaneous two-electron reduction of dinitrogen in some ligand frameworks.[10] The differences between the zero-valent complexes **3** – **5** are therefore of substantial interest in assessing the activation of dinitrogen, and the metrical bond parameters are presented in Table 2.1.

Table 2.1 Geometrical parameters, including bond lengths (Å) and angles (°) for complexes **2** – **5**[a]

	2·CH_3CN	**3**	**4**	**5**
M – Al (Å)	n/a	2.4501(10)	2.6205(11)	2.809(2)
r[b]	n/a	1.00	1.06	1.11
N-N (Å)	n/a	n/a	1.107(4)	1.146(7)
M – P (Å)	n/a	2.204(1)	2.265(1)	2.343(2)
Al –N_{eq} (Å)	1.865(5)	1.876(2)	1.876(3)	1.904(3)
Al–N_{apical} (Å)	2.056(10)	2.100(2)	2.187(3)	2.176(4)
M to P_3-plane (Å)	n/a	+ 0.127	+ 0.421	+ 0.692
Al to N_3-plane(Å)	+ 0.193	+ 0.257	+ 0.324	+ 0.315
Σ (P-M-P) (°)	n/a	359.00	349.46	335.03
Σ (N-Al-N) (°)	356.84	354.46	351.26	351.56
M-Al-N_{apical} (°)	n/a	179.14	177.81	180

With respect to the metal-alane bond, Table 2.1 shows that the r value for **3** is 1.00, whereas it increases slightly to 1.06 for **4** and 1.11 for **5**. Due to the chelate nature of the ligand, the presence of metal-aluminum interactions is not immediately obvious,

but the fact that all values are near unity argues that a metal-alane interaction is present in all three complexes. In the literature, values as high as 1.3 have been used to support the presence of metal-borane interactions,[17] though the interactions are substantially weakened as the *r* value increases. One indication that such an interaction exists is seen in the Al-N_{apical} distance, which is located *trans* to the metal site and should be expected to compete for dative donation into the Al p_z orbital. The lengthening of this distance from 2.056 Å in **2** to 2.100(2), 2.187(3), and 2.176(4) Å in **3**, **4**, and **5**, respectively, supports the assignment of metal-alane interactions. This interaction is additionally corroborated on the basis of UV-vis-NIR spectroscopy, which is discussed in Section 2.3.4. On the basis of the *r* values, the strength of the interaction is proposed to increase as Fe-Al < Co-Al < Ni-Al.

The presence of the dinitrogen ligand admittedly complicates a rigorous, quantitative comparison of the metal-alane interaction, as backbonding with dinitrogen should compete with the Z-bond from iron to aluminum. It is apparent that the iron-alane interaction is appreciably weaker than the nickel-alane interaction, which may reflect the increasing strength of the metal-N_2 interaction. One indicator of the disparate metal-alane interaction strengths is the displacement of the metal center from the center of the P_3 plane, which is only 0.127 Å above the P_3 plane for the coordinatively unsaturated Ni center. The Co and Fe centers, by contrast, lie 0.421 Å and 0.692 Å above the P_3 plane, respectively, indicating that the metal centers are substantially more removed from the Al^{3+} center. Aluminum also rises relative to the N_3 plane, but the displacement only

increases by 0.067 Å, whereas the metal center moves upward by 0.565 Å as nickel is swapped for iron.

The dinitrogen ligand is only modestly activated in **4** and **5**. Crystallographically, the distances of 1.107(4) Å and 1.146(7) Å are similar to the N-N distance in free dinitrogen (1.09 Å) and broadly indicative of neutral ligands.[10] Examples of reduced dinitrogen ligands in the literature typically have N-N distances of at least 1.18 Å and do not typically exhibit N_2 lability, but reduction of the N_2 ligand cannot be confidently assigned without corroboration by IR spectroscopy. Solid-state KBr pellets of **4** and **5** show one strong N_2 stretch each, at 2084 cm^{-1} and 2011 cm^{-1} respectively (Figure 2.12). These values are consistent with a neutral N_2 ligand, and the value for **5** is nearly identical to N_2FeTPB, which is formulated as a terminal dinitrogen complex.[36] However, the crystal structure of **5** shows the sandwich complex μ-N_2(FeAlL^{iPr})$_2$, which crystallizes in a centrosymmetric fashion and would not be expected to have an IR stretch for N_2. The selection rules for Raman (rR) suggested that **5** may exhibit a resonant Raman stretch upon excitation at the appropriate wavelength, and data was collected on a frozen solution-state (THF) sample at multiple wavelengths, though no stretches were observed in the N_2 region of the spectrum.

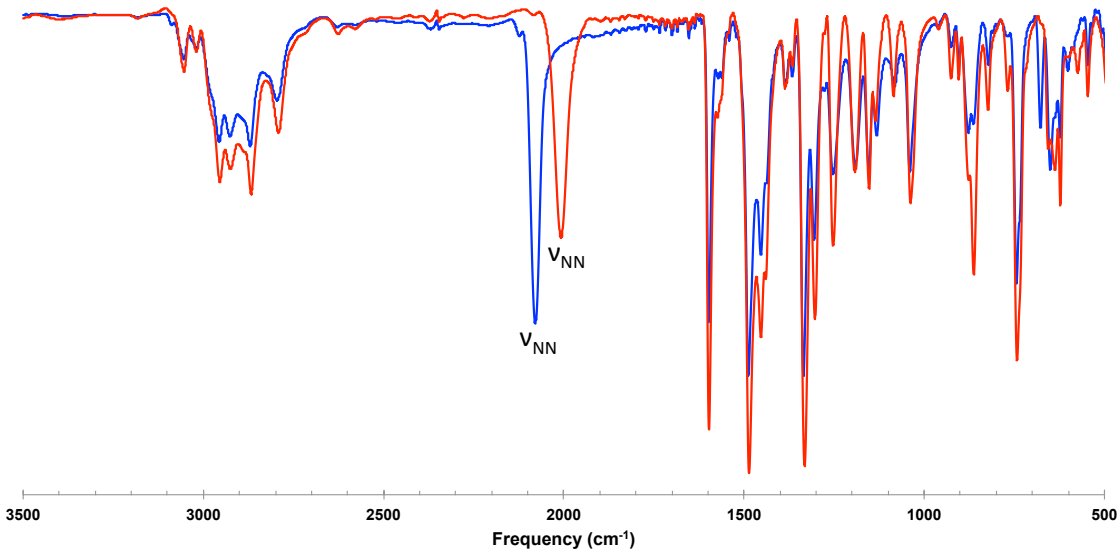

Figure 2.12 Solid-state infrared spectroscopy of **4** (blue) and **5** (red) (KBr pellet).

2.3.3 Cyclic Voltammetry Studies

Solution-state electrochemistry, particularly cyclic voltammetry (CV), is a useful tool to quickly determine the electrochemical potential of any accessible redox events in a system. Due to the systematic nature of the present study, electrochemistry offers valuable insights regarding the stability and reduction potentials of **3** – **5**.

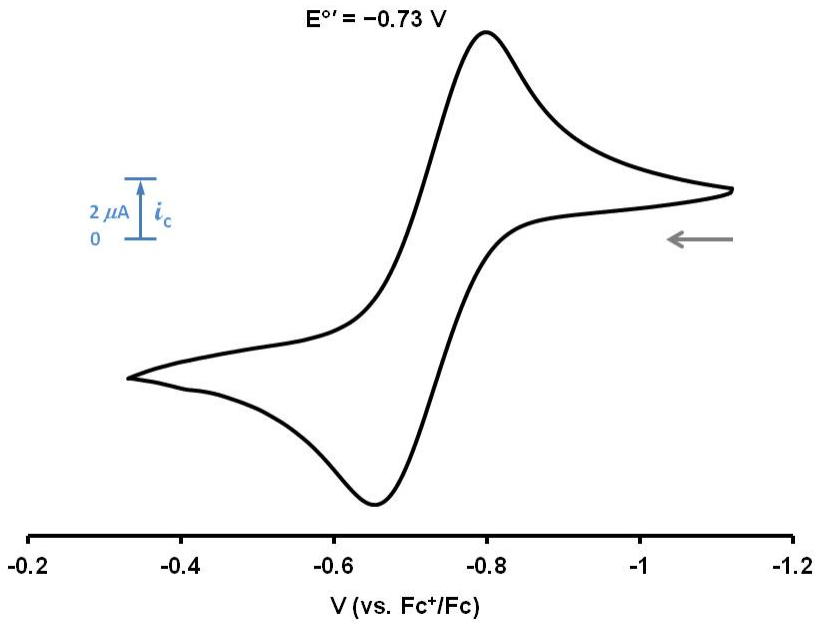

Figure 2.13 Cyclic voltammogram of NiAlL^{iPr} **3** in 0.1 M [^{n}NBu$_4$]PF$_6$ in THF (scan rate = 50 mV/s).

Figure 2.13 shows the voltammogram of **3**, which displays a single reversible oxidation event at –0.73 V versus the Fc/Fc$^+$ couple that is assigned as the Ni^0/Ni^{1+} redox couple. The reduction potential of this complex is relatively mild, and the reversibility of this complex suggested that isolation of the cationic species **3^{ox}** might be possible. Chemical oxidation with ferrocenium hexafluorophosphate in THF does yield the loss of brown color and generation of a new, yellow paramagnetic product, but this product does not appear to be indefinitely stable in solution and decomposed sufficiently quickly as to preclude growth of single crystals for X-ray analysis. The potential disparity between electrochemical reversibility and chemical stability is well known, as the electrochemical timescale is seconds, and complexes may be electrochemically accessible but chemically

inaccessible. No additional reductive events were seen, indicating that the Al^{III}/Al^{II} couple is inaccessible within the electrochemical window, and oxidations at potentials more positive than –0.73 V were irreversible and likely indicate demetallation, ligand oxidation, or some combination of the two.

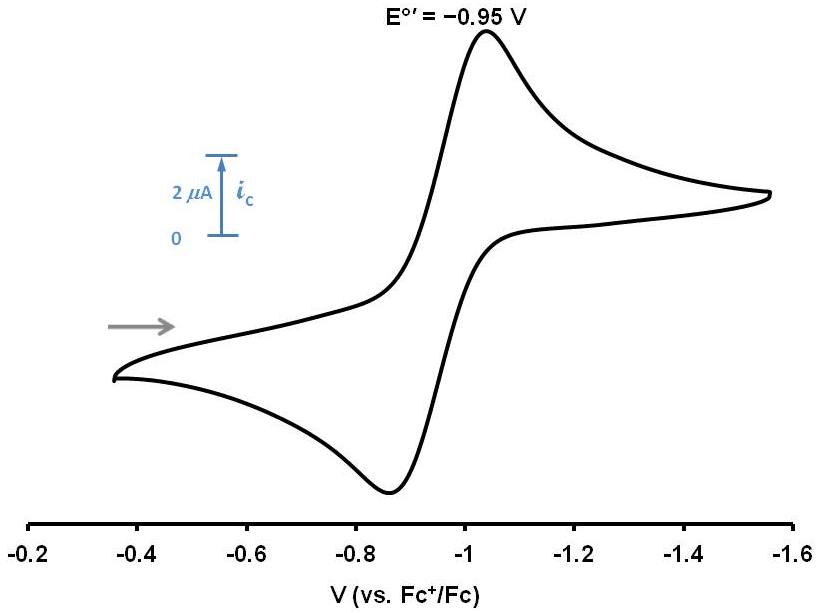

Figure 2.14 Cyclic voltammogram of N_2CoAlL^{iPr} **4** in 0.1 M $[^nNBu_4]PF_6$ in THF (scan rate = 50 mV/s)

Figure 2.14 shows the voltammogram for **4**, which shows a fully reversible reduction event at –0.95 V assigned as the formal Co^0/Co^{1-} couple. The reductive event is assigned as occurring at cobalt, rather than aluminum, on the basis of several factors: (1) the $Al^{III/II}$ couple is not observed in the voltammogram for **3**, (2) the reversible couple in **4** is substantially milder than expected for a $Al^{III/II}$ couple, (3) reduction at Co yields an electronically saturated, 18-electron metal center, and (4) the isoelectronic d^{10}

configurations of Co^{1-} and Ni^{0} may exhibit similar reduction potentials. The formally reduced cobaltate has indeed been synthesized,[110] and it is shown in Chapter 3 that this electronic assignment is correct.

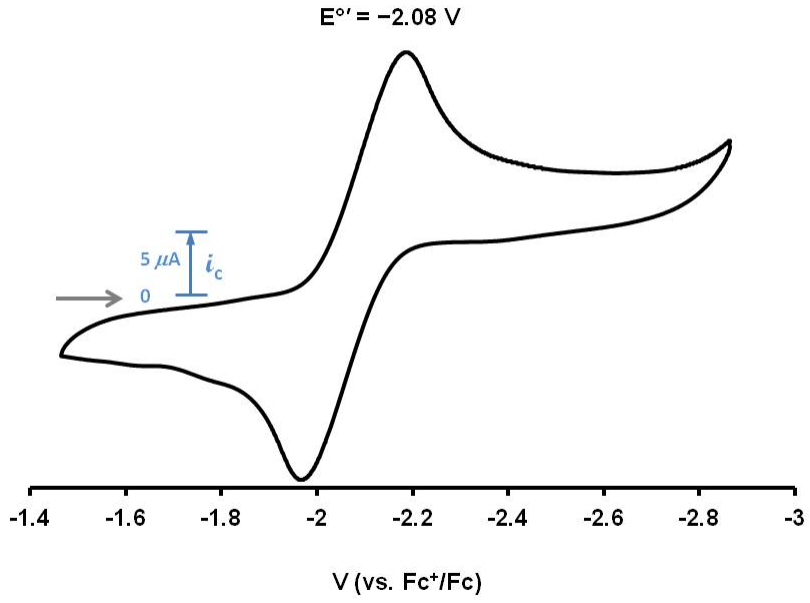

Figure 2.15 Cyclic voltammogram of **5** in 0.1 M $[^{n}NBu_4]PF_6$ in THF (scan rate = 50 mV/s).

Figure 2.15 shows the voltammogram for **5**, which shows a fully reversible reduction event at −2.08 V assigned as the formal $Fe^{0/1-}$ couple. The reductive event is assigned as occurring at iron by analogy to **3** and **4**, but the reduction potential is necessarily expected to be higher due to the lack of stabilization in a formally 17-electron configuration. The magnitude of the shift between the potentials for **4** and **5** (c. 1.12 V) is dramatic, but the potential for **5** is actually slightly less reducing than the related N_2FeTPB complex, which has a reversible reduction couple at – 2.19 V.[17] The shift to a

milder potential is qualitatively expected, although the magnitude of the shift is smaller than one might predict for swapping the Lewis acidic center.

2.3.4 UV-vis-NIR Spectroscopy and Density Functional Theory Calculations

The M−Al interaction in this series was also interrogated with UV−vis−NIR spectroscopy. Common to all of the complexes is a band with $\lambda_{max} \approx 340$ nm, which is assigned to the $\pi \rightarrow \pi^*$ transition of the ligand backbone. While AlL^{iPr} has no signal beyond 380 nm, the rest of the complexes have absorptions in the visible and/or NIR regions. Complex **3** has three visible peaks with $\lambda_{max} = 430$, 490, and 600 nm. Complexes **4** and **5** have NIR bands at 1400 and 890 nm, respectively, though the former is weak ($\varepsilon <$ 100 L mol^{-1} cm^{-1}). In the visible region, **4** has a few relatively weak bands, whereas **5** has an intense absorption with $\lambda_{max} = 411$ nm. The nature of these transitions was elucidated with time-dependent density functional theory (TD-DFT) calculations (see below).

We conducted DFT studies to obtain a better understanding of the M−Al electronic structures beyond the general $(M-Al)^n$ descriptor. The DFT-optimized geometries of **3**, **4**, and **5** corresponded to the experimental structures well when the Al and M atoms were treated with SDD and SDD+2f pseudopotential basis sets, respectively [6-311+G(2df,p) for P and N and 6-31G(d) for C and H atoms; M06-L;17 Gaussian 09].

In all cases, open-shell calculations were employed, and no spin density (i.e., radical character) was found on any ligand atoms, including Al or N_2. The qualitative correlation diagram based on the calculations is shown in Figure 2.16. As expected, the

$d_{xy}/d_{x^2-y^2}$ and d_{xz}/d_{yz} pairs are degenerate for (Ni−Al)[10] and (Fe−Al)[8], whereas the d_{xy} and $d_{x^2-y^2}$ orbitals are nondegenerate for (Co−Al)[9]. For **3**, the lowest unoccupied molecular orbital (LUMO) is primarily a Ni $4p_z$ orbital.

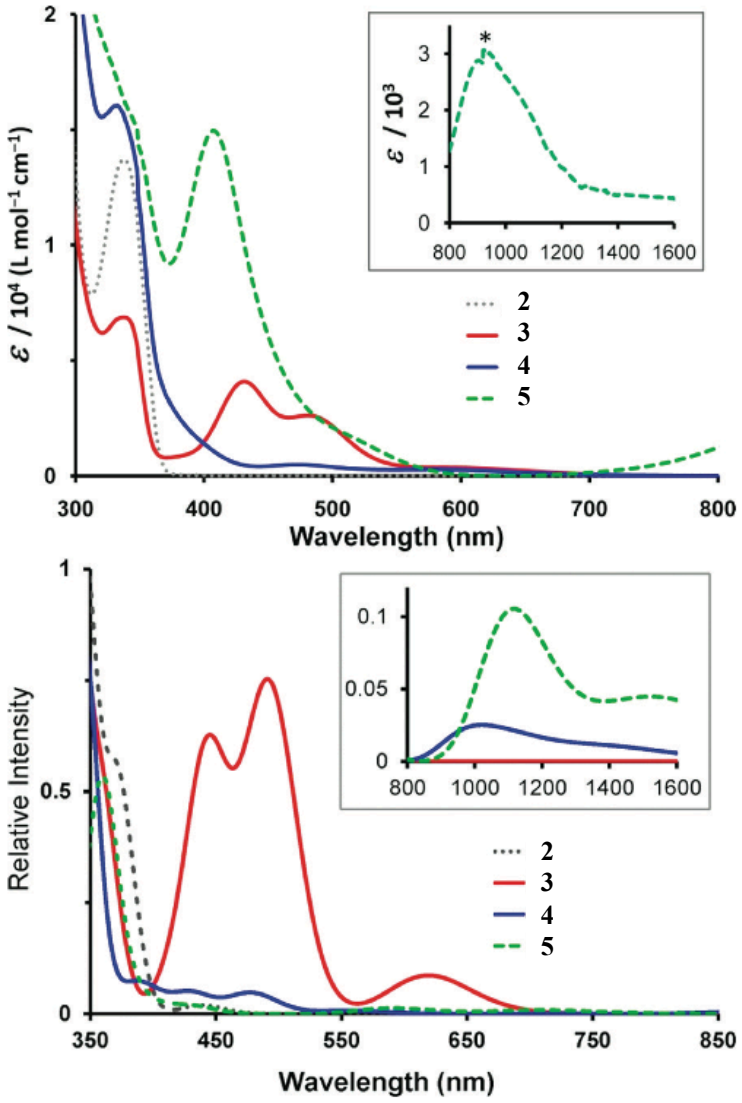

Figure 2.16 (top) UV−vis spectra of **2**, **3**, **4**, and **5** in THF at room temperature. Inset: NIR spectrum of 5 (* denotes the swapping of light sources). (bottom) TD-DFT-predicted UV−vis− NIR spectra of **2**(CH_3CN), **3**, **4**, and **5**. The inset shows the NIR region.

TD-DFT calculations (B3LYP, ORCA 2.7.0b) with solvent considerations (COSMO) were also performed to predict the electronic absorption spectra (Figure 2.16, bottom). The general agreement between the calculated and experimental spectra is good. Ligand-to-ligand charge-transfer (LLCT) transitions occur in the UV range, and in all three metal complexes, intense π-based LLCT bands are seen between 325 and 360 nm (experimental ~340). For **3**, three distinct bands are predicted in the visible range at λ_{max} = 440, 490, and 620 nm, in excellent agreement with the experimental spectrum of **3**. These transitions are assigned as follows: 440 nm, d_{xz}/d_{yz} to $4p_z$ (LUMO); 490nm, (d_{z^2} +Lπ) to $4p_z$; 620nm, $d_{xy}/d_{x^2-y^2}$ to $4p_z$. The more pure d_{z^2} to $4p_z$ transition is predicted at 360 nm, appearing as a shoulder on the LLCT band in Figure 2.17. Because several transitions involve the LUMO, the ligand-field energies can be extracted: $\Delta(d_{z^2}, d_{xz}/d_{yz})$ = 0.66 eV; $\Delta(d_{xz}/d_{yz}, d_{xy}/ d_{x^2-y^2})$ = 0.79 eV; $\Delta(d_{xy}/d_{x^2-y^2}, 4p_z)$ = 2.0 eV.

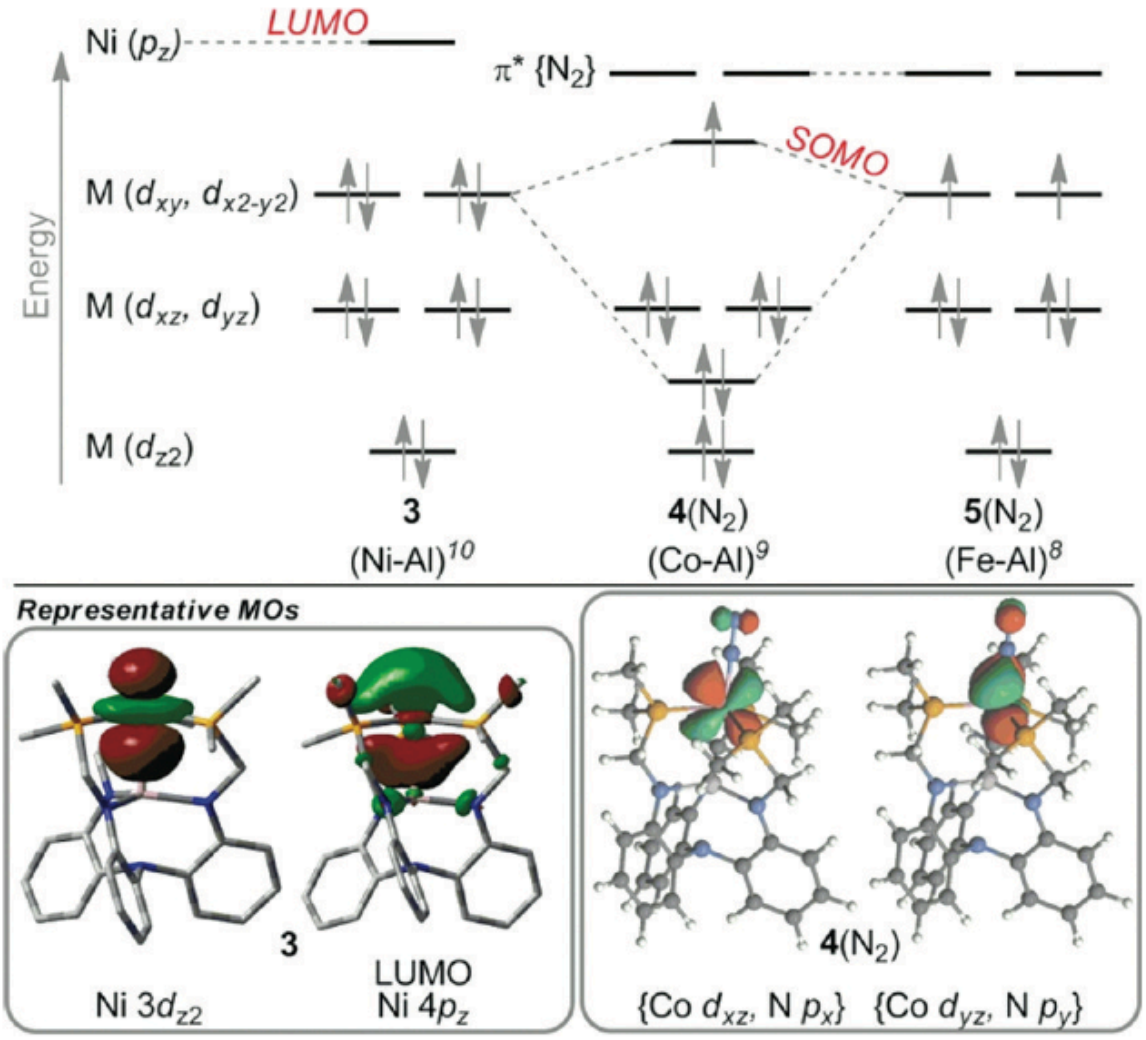

Figure 2.17 Qualitative correlation diagram for the d-orbital manifold and the LUMOs for **3**, **4**, and **5**. MO energies are not drawn to scale.

Some important information can be gleaned even though the TD-DFT results for Co complex **4** and Fe complex **5** are complicated by MO mixing in the ground and excited states. Excitations to the metal p_z orbital occur near 300 nm. Far-visible bands arising from metal d → π*(N_2) transitions occur at 400 and 431 nm for **4** and 362 nm for **5**. Additional d_{z2} (Fe) → π*(N_2) peaks are red-shifted to 432 and 434 nm. Metal *d*–*d* transitions into the singly occupied MO (SOMO) account for the remaining bands at 557,

990, and 1133 nm for **4** and at 592 and 1113 nm for **5**. There are two noteworthy discrepancies between the calculated and experimental spectra. The NIR bands for Co are predicted to have similar intensities as the visible bands, yet experimentally only a very weak signal is observed at 1400 nm ($\varepsilon < 100$ L mol^{-1} cm^{-1}). Problematically, the far-visible bands for **5** are predicted to have relatively low intensity, but experimentally, the 411 nm band is remarkably intense ($\varepsilon = 1.5 \times 104$ L mol^{-1} cm^{-1}). In the case of the Fe complex, we have made the simplifying assumption that the N_2-bridged species is a minor species in solution relative to terminal N_2-coordination. If this is not the case, then additional transitions are expected for **5** and could possibly account for the intense band at 411 nm.

2.4 Conclusions

A binucleating double-decker ligand N(*o*-(NHCH$_2$P(^{i}Pr)$_2$)C$_6$H$_4$)$_3$ (H_3L^{iPr}) was synthesized in good yield and metallated with Al(III). These metallalumatranes were shown to stabilize interactions of zero-valent metals with aluminum(III), and both the cobalt- and iron-alanes show dinitrogen binding and activation as well as an electrochemically accessible reduction event. The presence of a reductive event is promising with respect to further activation and potential functionalization of the N_2 unit. The synthesis and reactivity of these reduced complexes is described in the next chapter.

Surprisingly, the iron-alumatrane complex was found to be nearly spectroscopically identical to the iron-boratrane reported by Peters and coworkers, suggesting that the alane moiety exhibits only a minor perturbation the iron site relative to a borane. Proposing that the alane was insufficiently Lewis acidic to exhibit strongly different characterization, we undertook the synthesis of gallane, indane, and scandium(III) complexes that are also described in the next chapter.

2.5 Experimental

General Considerations

Unless otherwise stated, all manipulations were performed under a dinitrogen atmosphere in an Mbraun Atmosphere glovebox or using standard Schlenk techniques. Standard solvents were deoxygenated by sparging with dinitrogen and dried by passing through activated alumina columns of a SG Water solvent purification system. Deuterated solvents were purchased from Cambridge Isotope Laboratories, Inc., degassed via freeze-pump-thaw cycles, and stored over activated 4 Å molecular sieves. ^{1}H and ^{31}P NMR spectra were recorded on Varian 300, 400, and 500 MHz spectrometers at ambient temperature unless otherwise stated. Proton chemical shifts were referenced to residual solvent, and ^{31}P NMR was referenced to 85% H_3PO_4 at 0 ppm. Because of the solution-state proton equivalence within these systems, the reported integrations should be tripled to match the expected absolute values. Elemental analyses were performed by Atlantic Microlab, Inc. (Norcross, GA) or Complete Analysis Laboratories, Inc. (Parsippany, NJ). ESI mass spectrometry data was collected on a Bruker BioTOF II instrument. UV-visible and near infrared spectra were recorded on a Cary Bio 100 and Cary-14 spectrophotometers. Cyclic voltammetry was performed with a CH Instruments 600 electrochemical analyzer with a one-cell setup, comprising a glassy carbon working electrode, a platinum wire counter electrode, and $Ag/AgNO_3$ reference electrode in acetonitrile. Analytes were measured in 0.1 M $[^{n}NBu_4]PF_6$ THF solutions and internally referenced to the Cp_2Fe/Cp_2Fe^{+} redox couple.

Both tris(2-nitrophenyl)amine and tris(2-aminophenyl)amine were synthesized according to the preparation of Jones and MacBeth. Potassium graphite (KC_8) was prepared according to the literature.[105] The reagents $Ni(COD)_2$ and $AlCl_3$ were purchased from Aldrich and used without further purification. Diisopropylphosphine and metal dibromide were purchased from Strem and used without further purification.

Synthesis of diisopropylphosphinomethanol

Diisopropylphosphinomethanol was synthesized according to literature procedure,[101] but little characterization data was given. To paraformaldehyde (1.27 g, 42 mmol) in a vial, one equivalent of diisopropylphosphine (5.0 g, 42 mmol) was added dropwise. To this slurry, a stir bar was added, and the neat mixture was stirred at 60 °C for four hours, during which time the solution becomes transparent. The yield is quantitative. ^{1}H NMR (ppm, CD_3CN, 300 MHz): 3.29 (d, $^2J_{HP}$ = 6 Hz, 2H); 2.56 (br, 1H); 1.21 (m, 2H); 0.44 (m, ~12H). ^{31}P NMR (ppm, CD_3CN, 121 MHz): 7.36 (s).

Synthesis of 2,2',2''-tri(diisopropylphosphinomethylamino)triphenylamine

Diisopropylphosphinomethanol (1.20 g, 8.14 mmol) was added to a solution of tris(2-aminophenyl)amine (0.588 g, 2.0 mmol) in DMSO (approx.. 2 mL). The vial containing phosphine was rinsed with DMSO (approx. 4 mL) to ensure full transfer, and the solution was sealed in a Schlenk flask. The solution was stirred at 100 °C overnight, at which point a milky white opaque suspension was evident. The reaction was dried *in vacuo* overnight at 65 °C. The solid was collected on a medium porosity frit and washed with

anhydrous DMSO and then with acetonitrile (2 x 20 mL). A bright white powder was isolated (1.23g, 90%). Proton assignments are based on HMQC and HMBC NMR studies. ^{1}H NMR (C_6D_6, 300 MHz): δ 6.99 (t, *J* = 9 Hz, aryl CH, 1H); 6.92 (d, *J* = 9 Hz, aryl CH, 1H); 6.65 (d, *J* = 9 Hz, aryl CH, 1H); 6.49 (s, *J* = 9 Hz, aryl CH, 1H), 4.11 (s, N*H*, 1H); 3.10 (d, $^{2}J_{HP}$ = 15 Hz, CH_2P^{i}Pr$_2$, 2H); 1.53 (br, C*H*Me$_2$, 1H); 1.30 (br, C*H'*Me$_2$, 1H); 0.94 and 0.84 (d, *J* = 6 Hz, CH_3, 12H). ^{31}P NMR (C_6D_6, 121MHz): δ 3.05 (s). ESI-MS (m/z): 703 ([M + Na]$^{+}$); 719 ([M + K]$^{+}$).

Synthesis of Al(N(o-(NCH$_2$P(^{i}Pr)$_2$)C$_6$H$_4$)$_3$) **2**

Compound **1** (0.509g, 0.74 mmol) was dissolved in diethyl ether (approx. 4 mL) and frozen in a LN_2 coldwell bath. The frozen solid was then layered with ^{n}BuLi (0.910 mL, 2.27 mmol) and slowly thawed to room temperature overnight. The solution was then refrozen in a LN_2 coldwell bath and added while thawing to a frozen solution of $AlCl_3$ (0.101 g, 0.760 mmol) in diethyl ether (approx. 2 mL). The solution was then allowed to thaw quickly by stirring at rt. After 1 h, the light yellow solution with white precipitate was dried *in vacuo* and redissolved in toluene. The white precipitate was filtered away using a glass-fiber filter pipette, and the off-white solution was collected and dried *in vacuo*, then washed with a minimum of cold diethyl ether (approx. 2 mL, −35 °C). A white solid was isolated (0.430 g, 81.6%). Single crystals were obtained via vapor diffusion of diethyl ether into a concentrated acetonitrile solution of **2**. ^{1}H NMR (C_6D_6, 300 MHz): δ 7.39 (d, *J* = 6.0 Hz, aryl CH, 1H); 7.12 (t, obscured by solvent, aryl CH); 6.68 (d, *J* = 9.0 Hz, aryl CH, 1H); 6.51 (t, *J* = 9.0 Hz, aryl CH, 1H); 3.33 (s, CH_2, 2H);

1.83 (br, C*H*, 2H); 1.01 (br, CH_3, 12H). ^{31}P NMR (C_6D_6, 121 MHz): δ 8.5 (s). ^{27}Al NMR (C_6D_6, 75 MHz): δ 82.2 (s). UV-Vis (in THF): (nm, ε [M^{-1} cm^{-1}]) 344 (12,800). Anal. Calcd. for **2**(CH_3CN), $C_{41}H_{63}AlN_5P_3$: C, 66.02; H, 8.51; N, 9.39. Found: C, 66.55; H, 8.00; N, 9.76.

Synthesis of NiAl(N(o-($NCH_2P(^iPr)_2$)C_6H_4)$_3$) **3**

A solution of **2** (0.099 g, 0.14 mmol) was dissolved in toluene (approx. 2 mL) and added to solid Ni(COD)$_2$ (0.040 g, 0.14 mmol). The resulting solution was stirred for one hour, becoming an intense brown. The volatiles were removed *in vacuo*, giving a dark brown powder (0.122 g, quantitative). Single crystals were obtained by slow evaporation of a concentrated solution diethyl ether of **3** into toluene. ^{1}H(^{31}P) NMR (C_6D_6, 300 MHz): δ 7.51 (d, *J* = 6.0 Hz, aryl CH, 1H); 7.18 (t, *J* = 6 Hz, aryl CH, obscured by solvent); 6.50 (d, *J* = 6.0 Hz, aryl CH, 1H); 3.29 (d, *J* = 12 Hz, C*H*H'P^{i}Pr$_2$, 2H); 3.01 (d, *J* = 12 Hz, CH*H'*P^{i}Pr$_2$, 2H); 2.39 (br, C*H*, 1H); 1.87 (br, C*H*, 1H); 1.08 to 0.84 (overlapping multiplets, CH_3, 12H). ^{31}P NMR (C_6D_6, 121MHz): δ 49.39 (s). ^{27}Al NMR (C_6D_6, 75 MHz): δ 78.6 (s). UV-VIS (in THF): (nm, ε [mol^{-1} cm^{-1}]) 340 (7,300), 430 (4,300), 490 (2,700), 600 sh (300). Anal. Calcd. for **3**, $C_{39}H_{60}AlN_4NiP_3$: C, 61.35; H, 7.92; N, 7.34. Found: C, 61.42; H, 7.98; N, 7.25.

Synthesis of N_2CoAl(N(o-($NCH_2P(^iPr)_2$)C_6H_4)$_3$) **4**

A solution of **2** (0.100 g, 0.15 mmol) was dissolved in THF (approx. 4 mL) and added to a stirring THF solution (approx. 4 mL) of $CoBr_2$ (0.033 g, 0.15 mmol). The resulting dark blue solution was stirred for one hour. To this solution, a suspension of KC_8 in THF was

added in portions, and the reaction mixture was stirred for an additional hour. The resulting yellow-brown solution was filtered through Celite, and the solvent was removed *in vacuo*, giving a dark yellow-brown film. The film was washed with pentane and ether, then reconstituted in benzene and filtered. Lyophilization yielded a dark brown powder (0.071 mg, 60.0%). Single crystals were obtained by evaporation of a concentrated solution of **3** in diethyl ether into toluene. ^{1}H NMR (C_6D_6, 300 MHz): δ 13.63 (s); 9.03 (s); 7.04 (s); 6.66 (s); 6.36 (s); 2.37 (br); 1.24 (s); 0.28 (br); −1.92 (br); −2.62 (br). IR (cm^{-1}): KBr pellet, ν[N_2] = 2084; THF solution cell, ν[N_2] = 2081. UV-Vis-NIR (THF): (nm, ε [mol^{-1} cm^{-1}]) 333 (17,000), 475 (450), 580 sh (250), 1,460 (100). Anal. Calcd. for **4**(N_2), $C_{39}H_{60}AlN_6CoP_3$: C, 59.16; H, 7.64; N, 10.61. Found: C, 59.20; H, 7.69; N, 10.48.

Synthesis of $N_2FeAl(N(o\text{-}(NCH_2P(^iPr)_2)C_6H_4)_3)$ **5**

A solution of **2** (0.067 g, 0.95 mmol) was dissolved in THF (approx. 4 mL) and added to a stirring THF solution (approx. 4 mL) of $FeBr_2$ (0.021 g, 0.99 mmol). The resulting dark red solution was stirred for one hour. To this solution, a suspension of KC_8 in THF was added in portions, and the reaction mixture was stirred for an additional hour. The red-yellow solution was filtered through Celite, and solvent was removed *in vacuo*, giving a dark red-brown film. The film was washed with pentane and ether, then reconstituted in benzene and filtered. Lyophilization yielded a maroon powder (0.036 mg, 47.8%). Compound **5** can be crystallized by vapor diffusion of hexane into a toluene solution of **5**, and a single-crystal X-ray diffraction study determines the structure as (μ-N_2)($FeAlL^{iPr}$)$_2$. ^{1}H NMR (C_6D_6, 300 MHz): δ 84.5 (s); 54.6 (s); 13.54 (s); 12.18 (s); 10.26 (s); 8.60 (s);

7.95 (s); 6.41 (s); 5.57 (s); 3.21 (s); 1.07 (s); 0.83 (s); −15.78 (s). IR (KBr pellet, cm^{-1}) 2010 (ν[N_2]). UV-Vis-NIR (toluene): (nm, ε [M^{-1} cm−^{1}]), 346 sh (15,100), 409 (14,900), 890 (3,000). Anal. Calcd. for (Fe(AlL^{iPr}))$_2$(μ-N_2), $C_{78}H_{120}Al_2Fe_2N_{10}P_6$: C, 60.47; H, 7.81; N, 9.04. Found: C, 60.42; H, 7.84; N, 8.94.

X-Ray Crystallographic and Structure Refinement Details

A colorless needle of **2**, a brown plate of **3**, a brown plate of **4**, and a yellow needle of **5** were placed onto the tip of a 0.1 mm diameter glass capillary and mounted on a Bruker SMART Platform CCD diffractometer for data collection at 123(2) K for **3**-**5** and 173(2) K for **2**. The data collection was carried out using Mo Kα radiation (graphite monochromator). The data intensity was corrected for absorption and decay (SADABS). Final cell constants were obtained from least squares fits of all measured reflections. The structure was solved using SHELXS-97 and refined using SHELXL-97. A direct-methods solution was calculated which provided most non-hydrogen atoms from the E-map. Full-matrix least squares / difference Fourier cycles were performed to locate the remaining non-hydrogen atoms. All non-hydrogen atoms were refined with anisotropic displacement parameters. Hydrogen atoms were placed in ideal positions and refined as riding atoms with relative isotropic displacement parameters. Crystallographic data are summarized in Table 1. Complex **2** possesses a disordered acetonitrile molecule on a -3 position that could not be appropriately modeled and was removed using the SQUEEZE function of the PLATON program; approximately 589 $Å^3$ of void space is present,

containing 116 electrons. Complexes **3** and **4** possess a toluene and diethyl ether, respectively, that can not be satisfactorily modeled anisotropically due to the proximity of nearest neighbors; these solvent molecules therefore remain isotropic. Complex **5** contains large channels down the *c* axis with several benzene solvent molecules that could not be adequately modeled. The SQUEEZE function of the PLATON program[17] was utilized to remove peaks in this channel. Accordingly, 1770 Å^3 of void space remains in the unit cell, accounting for 695 electrons.

Table 2.2 Crystallographic Parameters for Complexes 2 – 5

	2(CH_3CN)	**3**	**4**	**5**
Chemical Formula	$C_{47}H_{72}N_8P_3Al$	$C_{85}H_{128}Al_2N_8P_6Ni_2$	$C_{82}H_{130}Al_2Co_2N_{12}OP_6$	$C_{78}H_{120}Al_2Fe_2N_{10}P_6$
Moiety Formula	($C_{41}H_{63}AlN_5P_3$) 3 (CH_3CN)	2 ($C_{39}H_{60}AlN_4NiP_3$) (C_7H_8)	2 ($C_{39}H_{60}AlN_6CoP_3$) ($C_4H_{10}O$)	(μ-N_2) ($FeAlC_{39}H_{60}N_4P_3$)$_2$
Formula weight	869.02	1619.11	1657.2	1549.32
Crystal system	Trigonal	Triclinic	Monoclinic	Hexagonal
Space group	R-3	P-1	C2/*c*	P6(3)$_{22}$
a (Å)	18.378(3)	11.228(5)	18.866(2)	15.5814(6)
b (Å)	18.378(3)	14.192(7)	20.369(2)	15.5814(6)
c (Å)	27.486(8)	14.309(6)	22.851(2)	27.275(2)
α (deg)	90	70.753(6)	90	90
β (deg)	90	80.530(6)	103.5120(10)	90
γ (deg)	120	82.984(6)	90	120
Z	6	1	4	2
D_{calcd} (g cm^{-3})	1.077	1.270	1.289	0.970
λ (Å), μ (mm^{-1})	0.71073, 0.164	0.71073, 0.627	0.71073, 0.573	0.71073, 0.417
T (K)	173(2)	123(2)	123(2)	123(2)
θ range (deg.)	1.48 to 27.51	1.52 to 27.48	2.22 to 27.19	1.51 to 24.970
Reflns collected	29246	24130	9740	24996
Unique reflns	3163	8659	6816	6083
Data/restraints/parameters	3163, 1, 186	8473, 34, 474	9734, 7, 484	3123, 0, 152
R_1, wR_2 ($I > 2\sigma(I)$)	0.0429, 0.1309	0.0424, 0.1010	0.0487, 0.1228	0.0470, 0.1420

Computational Details

Theoretical calculations were carried out on the complexes using density functional theory (DFT) and the complete active space self-consistent field method with second order perturbation theory (CASSCF/CASPT2). No symmetry constraints were used. (*DFT*) Initial starting points for geometry optimizations were taken/derived from experimentally determined X-ray structures. The geometry optimizations were performed with the M06-L functional, which has been proven to be fairly accurate for transition metal compounds, in the Gaussian09 program package. The aluminum atom was treated with SDD basis set while the transition metals were treated with SDD+2f pseudopotential. The nitrogen and phosphorus atoms were treated with the 6-311+G(2df,p) basis set, and all other atoms were treated with the 6-31G(d) basis set. Vibrational frequencies for the DFT-optimized structures were also computed at the same level of theory. All complexes computed had no negative frequency except for the Al-$NCCH_3$ which had a negative frequency corresponding to the rotation of the methyl group belonging to the acetonitrile molecule. TD-DFT calculations were performed with the B3LYP functional implemented using the ORCA program. The TZVPP and TZVP basis sets were used for the transition metals and all other atoms respectively, the RI Approximation for HF and hybrid DFT (RIJCOSX) and the COSMO solvation model were also applied for higher accuracy.

(*CASSCF/CASPT2*) The optimized geometries from the DFT calculations were taken for further multiconfigurational electronic structure analysis and orbital

visualization using the MOLCAS quantum chemistry software. To reduce the computation cost of these calculations, the Cholesky decomposition technique was applied in all calculation, the Douglas-Kroll-Hess Hamiltonian was also applied to account for relativistic effects. In all of these calculations, the ANO-RCC-VTZP basis set was used for the transition metals and aluminum, ANO-RCC-VDZP basis set was used for nitrogen and phosphorus and the ANO-RCC-MB basis set was used for carbon and hydrogen. CASSCF/CASPT2 single-point energy calculations were performed with an active space of 11 electrons in 11 orbitals for N_2CoAlL^{iPr} and an active space of 10 electrons in 11 orbitals for both $NiAlL^{iPr}$ and N_2FeAlL^{iPr} to gain insight on the frontier orbitals of these complexes. CASSCF multi-root calculations were then preformed to confirm and verify excitations predicted by TD-DFT in order to obtain a better understanding of the theoretical UV-Vis-NIR spectra.

Chapter 3

Dinitrogen Activation at Cobalt and Iron Metallalumatranes

In part from:

Rudd, P.A.; Planas, N.; Bill, E; Gagliardi, L.; Lu, C.C. "Dinitrogen Activation at Cobalt and Iron Metallalumatranes." *Eur. J. Inorg. Chem.* **2013***, 22-23,* 3898-3906.

3.1 Overview

Reductions of the N_2-bound metallalumatranes N_2CoAlL^{iPr} (**1**) and (μ-N_2)$(FeAlL^{iPr})_2$ (**2**) by one electron yield the formally subvalent species [crypt-2,2,2(K)][N_2CoAlL^{iPr}] (**1**^{red}) and [18c6(K)][N_2FeAlL^{iPr}] (**2**^{red}), respectively. The diamagnetic cobalt species **1**^{red} is assigned as a d^{10}, $S = 0$ complex with a formal cobaltate (Co^{1-}) oxidation state. The paramagnetic iron species **2**^{red} is assigned as a formally Fe^{1-} species on account of crystallographic distances, electron paramagnetic resonance spectroscopy, and density functional theory calculations. Complex **2**^{red} is a rare example of a 17-electron iron species, and reduction at the iron center is confirmed by Mössbauer spectroscopy. Complexes **1**^{red} and **2**^{red} were assessed for the multi-electron reduction of dinitrogen, specifically toward N-Si bond formation, with 1,2-bis(chlorodimethylsilyl)ethane (CDSE). Reactions with **1**^{red} regenerate **1**, but reactions with **2**^{red} at low temperature generate the iron-disilylhydrazido species **3**, which is the result of a net four-electron reduction at N_2 and an iron(II) center. Synthesis of **3** at room temperature also yields a second product, identified by NMR spectroscopy as the formally iron(III) analogue **3**^{ox}.

Several additional bimetallic species were also prepared wherein the aluminum center is swapped for Ga(III), In(III), or Sc(III). Iron and cobalt complexes were prepared analogously to the metal-alane complexes, and preliminary data supports binding and activation of N_2 by these complexes. The electronic structures are spectroscopically similar, though the iron-indium complex appears to exhibit Lewis-acidity at iron despite

the formal zerovalent oxidation state. This unexpected effect highlights the promise of studies with modular *trans* elements.

3.2 Introduction

Studies of multi-electron reductions of small molecules are fundamentally important, but perhaps none is more interesting than the reduction of dinitrogen to diazene, hydrazine, or ammonia.[1] The biological process is performed by nitrogenases, which possess multi-metallic active sites containing seven iron atoms and an eighth metal site that can be either iron, molybdenum, or vanadium.[1, 4, 111] Due to the complexity of nitrogenases, the exact mechanism for this transformation is unknown, yet the product of this reaction, ammonia, is responsible for essentially all bio-derived nitrogen atoms.[6] The advent of commercial nitrogen fixation, the Haber-Bosch process, is an unheralded success of chemistry and engineering despite the notoriously high energy demands.[7] At present, ammonia is synthesized on a massive scale of 80 x 10^9 kg every year and is unlikely to be readily displaced by another process.[3, 7, 8]

Both the solid-state Haber-Bosch and enzymatic nitrogenases are highly energy-intensive yet reasonably efficient pathways, but frustratingly few homogeneous systems are catalytically competent to reduce dinitrogen to ammonia. Shockingly, the first transition metal complex to bind dinitrogen was only discovered by Allen and Senoff fifty years after the Haber-Bosch process was established![112] Though substantial efforts were devoted to generating a homogenous catalytic system, for decades the field was dominated by stoichiometric tungsten and molybdenum chemistry—the results of this work firmly established two potential pathways for a terminally bound dinitrogen at one transition metal site.[4] The so-called symmetric and asymmetric pathways differ with

respect to the order of protonation: the symmetric pathway proposes that both nitrogen atoms are protonated prior to N-N cleavage, whereas the asymmetric pathway proposes that only the distal nitrogen atom is protonated prior to N-N bond cleavage and ammonia formation. Figure 3.1 shows an example of the asymmetric reduction pathway in the stoichiometric Chatt cycle. Reduction across bridging metal sites has also been considered, and Holland has shown that low-coordinate iron sites are capable of cleaving dinitrogen stoichiometrically under certain circumstances.[11] These systems are more synthetically difficult and somewhat less well-studied. The presence of dinitrogen bound side-on to a single metal site is only known for a sole osmium complex and is meta-stable, suggesting that a side-on monometallic pathway is unlikely.

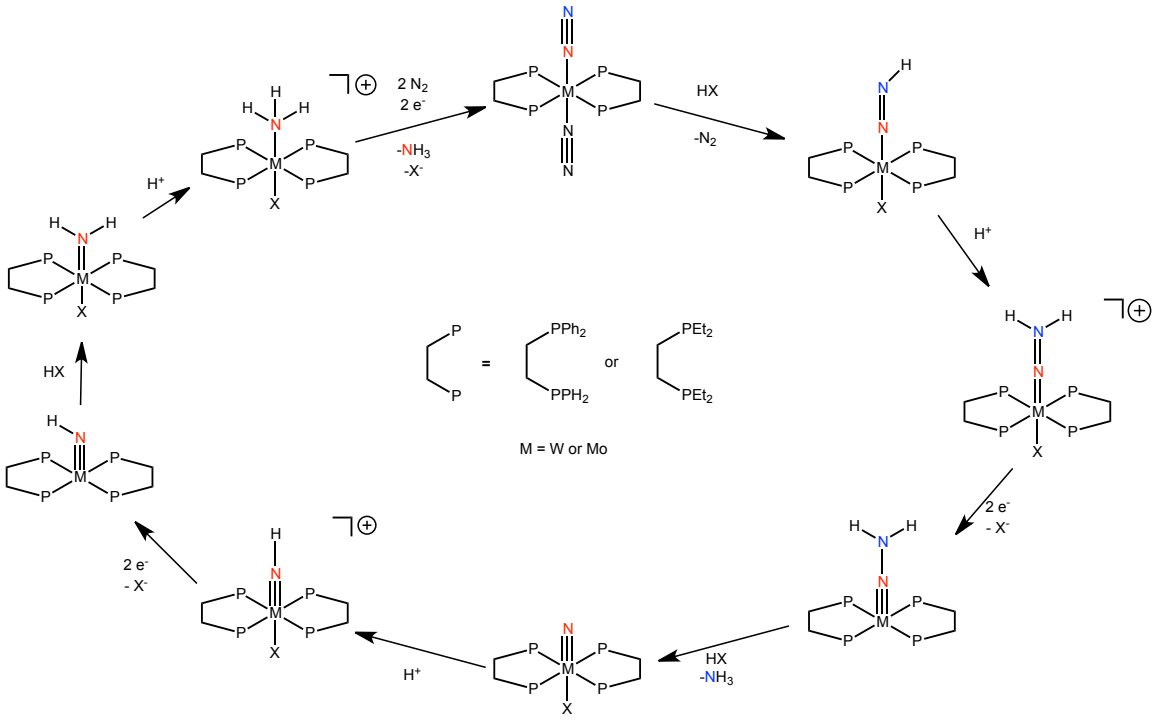

Figure 3.1 Example of the asymmetric Chatt cycle. The proximal (red) and distal (blue) nitrogen sites have been highlighted for clarity.

It is now believed that the mechanism of nitrogenases likely involves a bridging pathway across two iron sites rather than an isolated molybdenum site,[1] but synthetic functionalization chemistry has largely proceeded in systems with either a single iron or molybdenum site.[12, 13, 18, 19, 21, 22, 36] The first catalytic reduction of dinitrogen to ammonia was accomplished by Schrock and coworkers, who reported a molybdenum site protected by an extremely bulky ligand set.[12] Under highly optimized conditions, including solvent, time, the source of the acid, and reductant choice, this system is capable of only four turnovers. Mechanistic studies have suggested an asymmetric pathway, detailed in Figure 3.2, for which most of the intermediates have been identified or isolated.[13] Additional catalysts in recent years have also included a dimolybdenum pincer complex capable of twelve turnovers per molybdenum site,[22] an iron-boratrane capable of six turnovers,[21] and an iron-carbatrane capable of four turnovers.[19] Each of these systems is highly dependent on reaction conditions, and even minor experimental changes can obliterate catalytic activity.

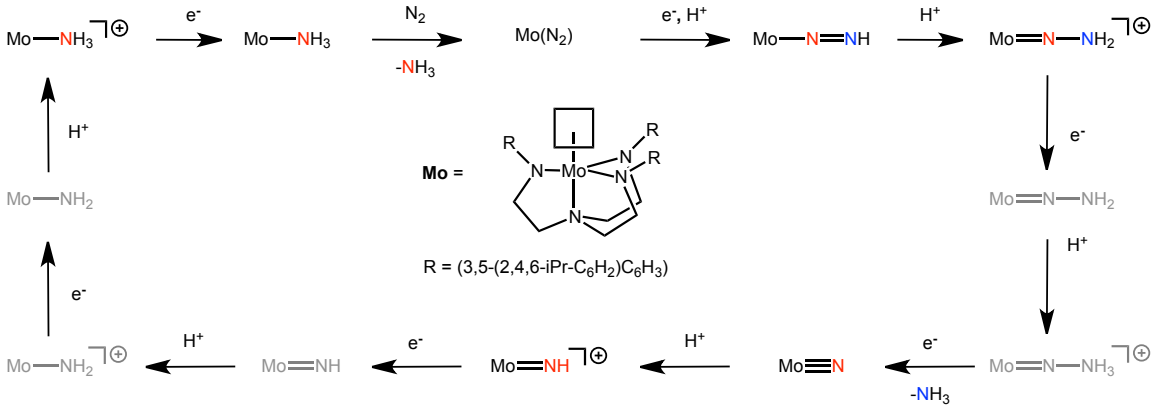

Figure 3.2 Proposed mechanistic cycle for the catalytic reduction of dinitrogen. The mechanism is asymmetric, denoted by the proximal (red) and distal (blue) nitrogen atoms. Observed intermediates are in color and proposed, but unobserved, intermediates are gray.

Though catalytic systems yielding ammonia are highly desirable, the six-electron reduction in the presence of protons is quite difficult to control selectively. Good progress has been made in recent years on the six-electron reduction of dinitrogen in the presence of silylation reagents, which have been shown to generate tris(trimethylsilyl)amine as an ammonia analog.[23, 24, 33] Interestingly, these reactions are capable of utilizing either molybdenum *or* iron, though the yields for molybdenum complexes depend on ligand and the yields for iron complexes do not. The mechanism for this reaction is poorly understood, and the reaction itself is quite slow, though ultimately these catalysts are shown to exhibit over two hundred turnovers with an optimized molybdenum system and approximately twenty-five turnovers with iron systems. Importantly, this result demonstrates that the dinitrogen reduction chemistry can be accomplished via silylation as well as protonation.

The Peters group has also exploited silylation chemistry to accomplish two- and four-electron reduction of iron-dinitrogen complexes and generation of metal-bound diazenide and hydrazide products.[20, 36] Though the diazenide complexes are not shown to be further reactive, the hydrazide products have shown a propensity to cleave the remaining N-N bond.[36] In particular, iron-boratrane systems have shown excellent promise with respect to both stoichiometric transformations and catalytic reduction of dinitrogen as a direct result of their electronic flexibility, making these types of systems a prime target for further research.

One avenue for such studies is variation of the borane for other Lewis-acidic moieties, *e.g.*, alanes, gallanes, and indanes, which is readily accomplished with the present ligand, $N(o\text{-}C_6H_4\text{-}HNCH_2P^iPr_2)_3$. This chapter discusses the synthesis and characterization of these complexes and the four-electron reduction of dinitrogen with a mononuclear iron-alane.

3.3 Results and Discussion

The zerovalent cobalt- and iron-alanes **1** and **2** from the previous chapter were shown to undergo an electrochemical reduction to the formally cobalt(1-) and iron(1-) oxidation states. Reduction of **1** and **2** with one equivalent of potassium graphite (KC_8) in THF smoothly yields the singly reduced complexes $\mathbf{1}^{red}$ and $\mathbf{2}^{red}$, which are respectively brown and yellow (Scheme 3.1). The reduced complexes can be isolated as a THF solvate of the potassium salt but are not crystalline and typically exhibit isolated yields in excess of the theory yield due to excess solvent and unprecipitated salts. These complexes become tractable upon the addition of 2,2,2-cryptand ($\mathbf{1}^{red}$) and 18-crown-6 (18c6, $\mathbf{2}^{red}$), which typically allow isolation of > 70% of either complex.

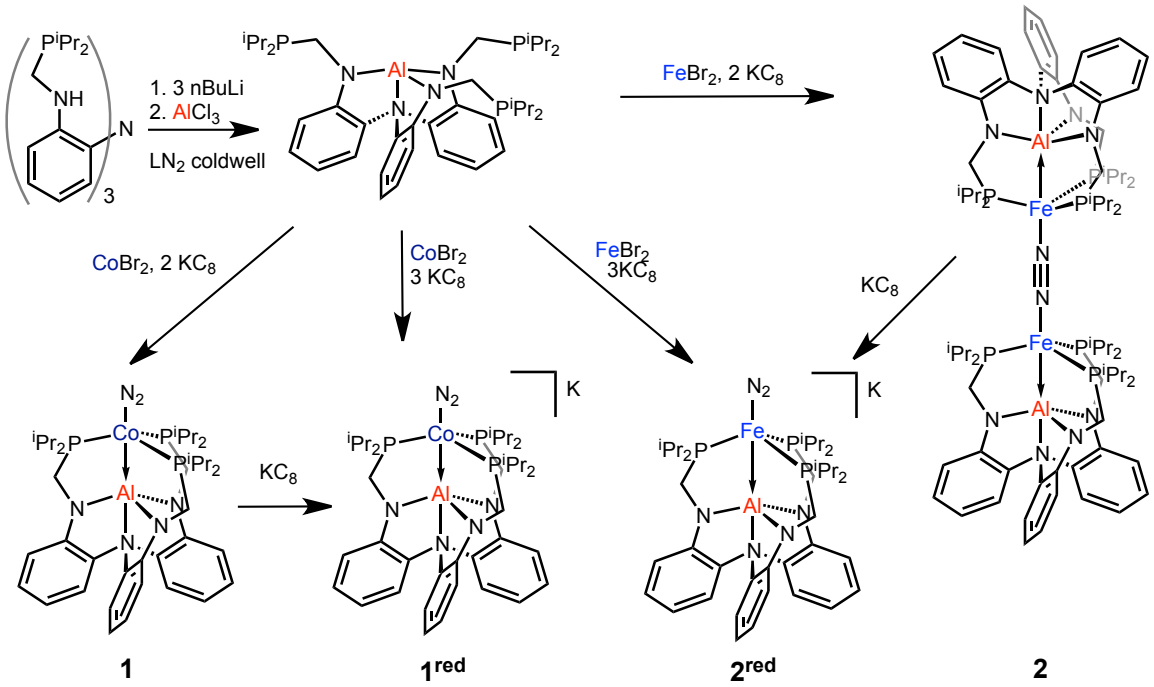

Scheme 3.1 Synthetic scheme to generate $\mathbf{1}^{red}$ and $\mathbf{2}^{red}$

Both **1**^{red} and **2**^{red} bind dinitrogen in a terminal fashion with a modest activation of the N_2 unit. These reduced complexes were investigated towards dinitrogen functionalization, and it was found that the addition of 1,2-bis(chlorodimethylsilyl)ethane (CDSE) to **2**^{red} in the presence of KC_8 generates a low-spin iron(II)silylhydrazido species **3** (Figure 3.2), whereas no analogous reactivity was found in the case of **1**^{red}.

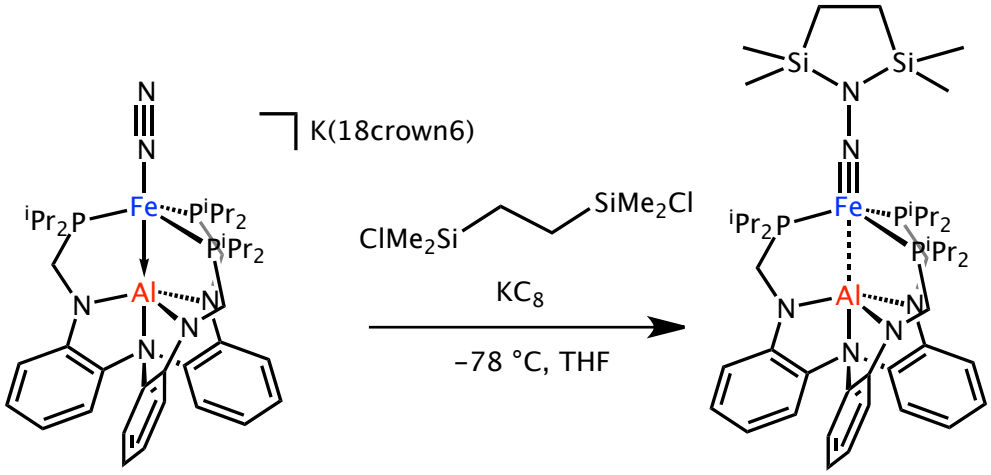

Scheme 3.2 Functionalization of N_2 to form $((SiMe_2CH_2)_2N_2)FeAlL^{iPr}$ **3**.

The following sections detail characterization data of these iron and cobalt species; Sections 3.3.5 and 3.3.6 additionally details preliminary work done on complexes incorporating gallium(III), indium(III), or scandium(III) instead of aluminum(III).

3.3.1 Nuclear Magnetic Resonance Studies

Preliminary confirmation of **1**^{red} and **2**^{red} was provided by NMR spectroscopy, which indicated a new diamagnetic product for the brown **1**^{red} and a new paramagnetic product for the yellow-brown **2**^{red}. The ^{1}H NMR spectrum for **1**^{red} displays sharp aryl resonances but broad methyl, methylene, and methine resonances (Figure 3.3). The

methylene resonances are seen to be diastereotopic in the THF-solvated complex, though the separation between the two peaks is minor (< 0.2 ppm). The intrinsic crystallinity of this complex is low, and the addition of crypt-222 obscures the methylene and methine resonances. The methylene and methine resonances were not assigned by 2-dimensional NMR due to the broad linewidths, which precluded effective observation of the coupling. Instead, the peaks were assigned based on the isoelectronic $NiAlL^{iPr}$: the more upfield resonances (2.04 ppm) were assigned as the methine protons, and the more downfield resonances (2.72 ppm) were assigned as the methylene protons. The cryptand resonances are unshifted relative to the free molecule (3.48 and 2.48 ppm). The methyl resonances for **2** are also split into two groups, indicating two different magnetic environments for the methyl groups, which is consistent with the "up, down" orientations of the isopropyl groups as seen in the solid-state X-ray crystallography structures. The diastereotopic nature of the methylene protons suggests that the molecule possesses C_3 symmetry in solution, though the barrier to the threefold inversion is low and nearly energetically accessible at room temperature. Upon raising this temperature slightly, the methylene peaks should coalesce and allow for a preliminary calculation of the C_3 inversion barrier. This behavior is further discussed in Section 3.3.6, as there are currently insufficient data in the literature against which to compare these findings.

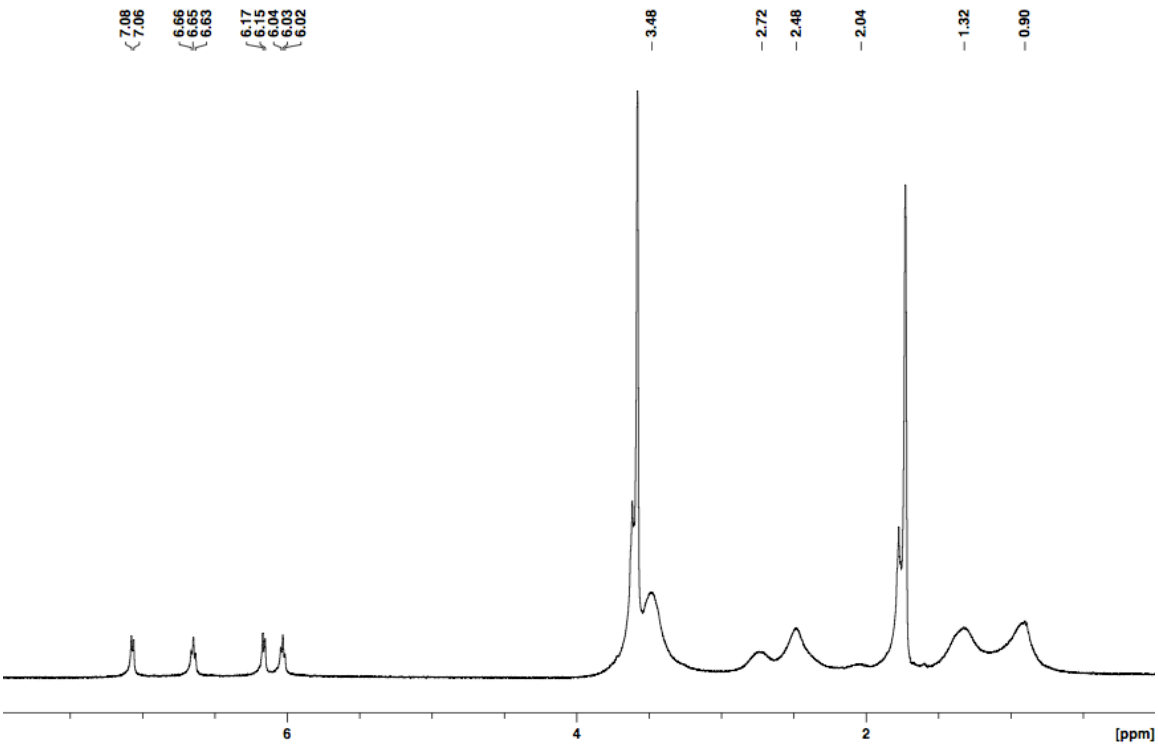

Figure 3.3 ^{1}H NMR spectrum of [K(crypt-222)][**1**^{red}] in THF-d_8.

Consistent with the diamagnetic formulation and idealized C_3 symmetry, the ^{31}P spectrum of **1**^{red} displays only one relatively broad peak at 54 ppm (Figure 3.4). This value is close to the 49 ppm resonance for the nickel-alane complex NiAlL^{iPr}.[70] Given the isoelectronic nature of NiAlL^{iPr} and **1**^{red}, similar ^{31}P NMR shifts may be expected.

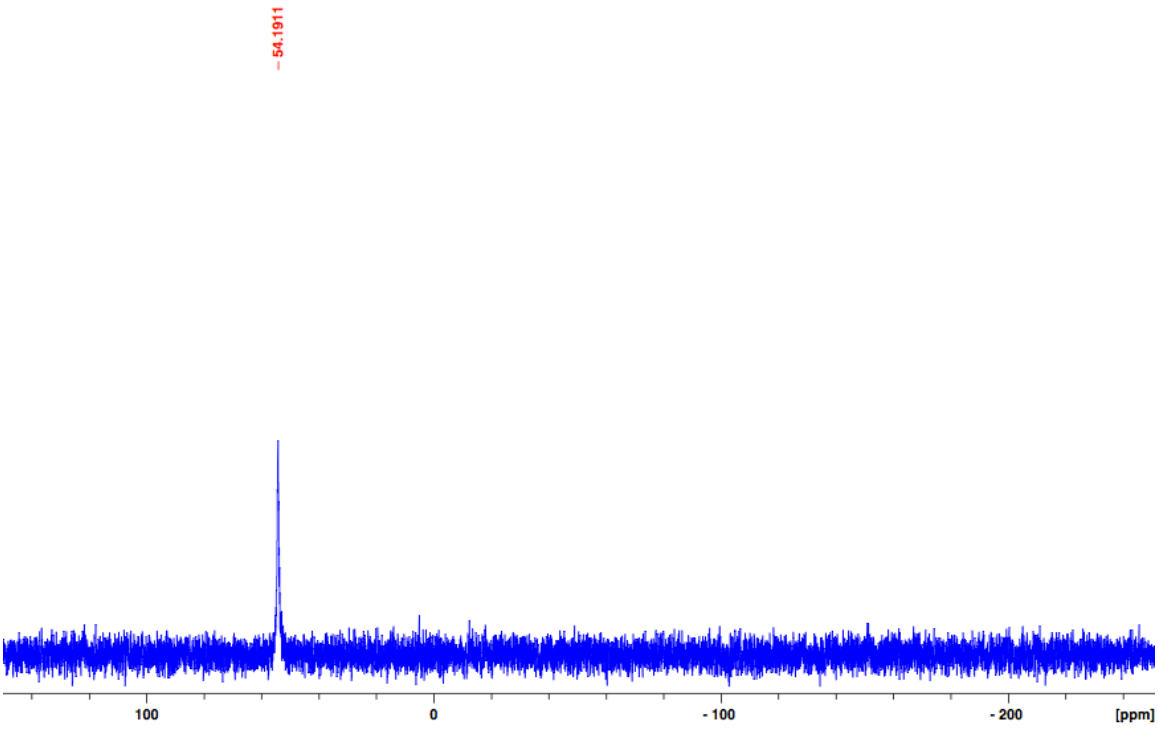

Figure 3.4 ^{31}P NMR spectrum of [K(crypt-222)][**1**^{red}] in THF-d_8.

In contrast, complex **2**^{red} is paramagnetic with an S = ½ ground state as determined by EPR (*vide infra*), which is consistent with the predicted 17-electron species. The NMR spectrum is paramagnetically broadened, and ten resonances appear between 51 and −3 ppm, suggesting that this complex is also locked in C_3 symmetry on the NMR timescale. The downfield paramagnetic resonances show temperature dependence between ambient temperature and −80 °C, at which point the spectrum becomes relatively featureless. No ^{31}P or ^{13}C signals were observed at any temperature. The room temperature spectrum of **2**^{red} is shown in Figure 3.5.

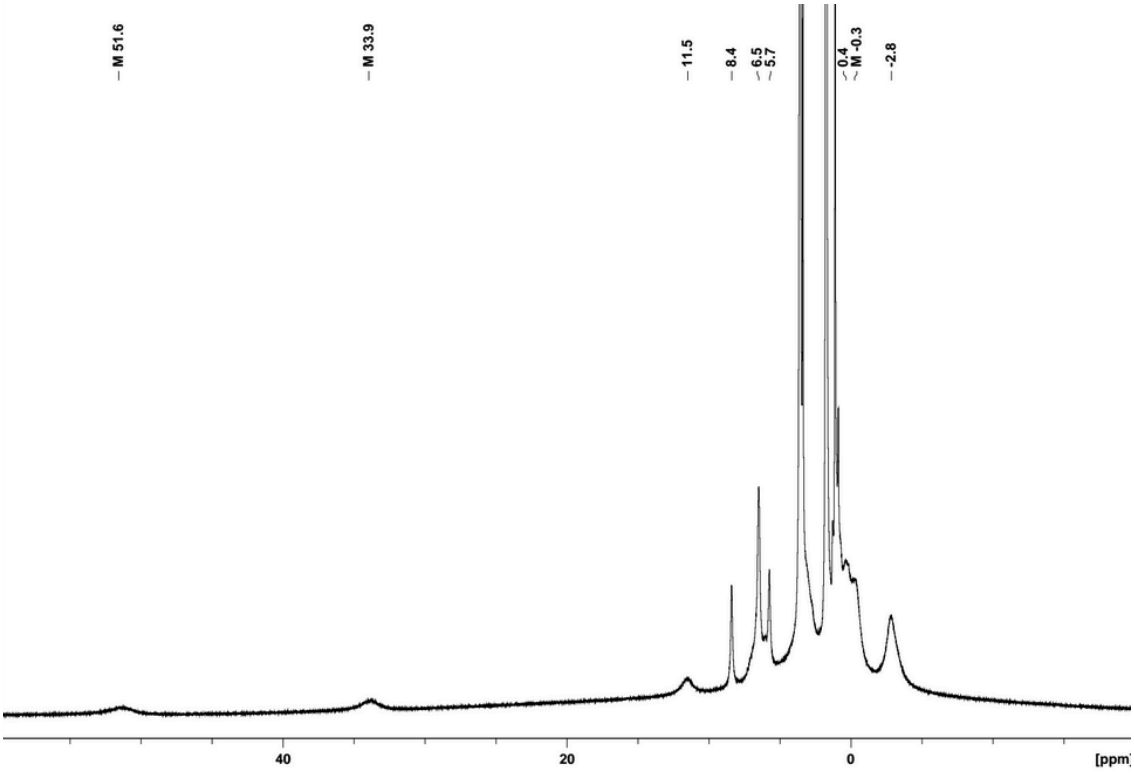

Figure 3.5 Room temperature ^{1}H NMR spectrum of [K(THF)$_6$][**2**^{red}] in THF-d$_8$.

Neither **1**^{red} or **2**^{red} appears to react productively with either trimethylsilyl chloride (TMSCl) or trityl radical; the addition of TMSCl to **1**^{red} cleanly regenerates **1** in quantitative yield by NMR, and neither **1** nor **1**^{red} appears to react with the trityl radical. These results suggest that 2-electron reduction to a diazenide is unfavorable in this system. In contrast, **1**^{red} reacts quickly upon addition of the disilylating reagent 1,2-(chlorodimethylsilyl)ethane (CDSE) to cleanly yield **1** at room temperature but a complicated mixture at −78 °C. The ^{1}H NMR for these reactions are shown in Figure 3.6. No products were identified in the low-temperature reaction, and it is unclear whether any dinitrogen functionalization has occurred.

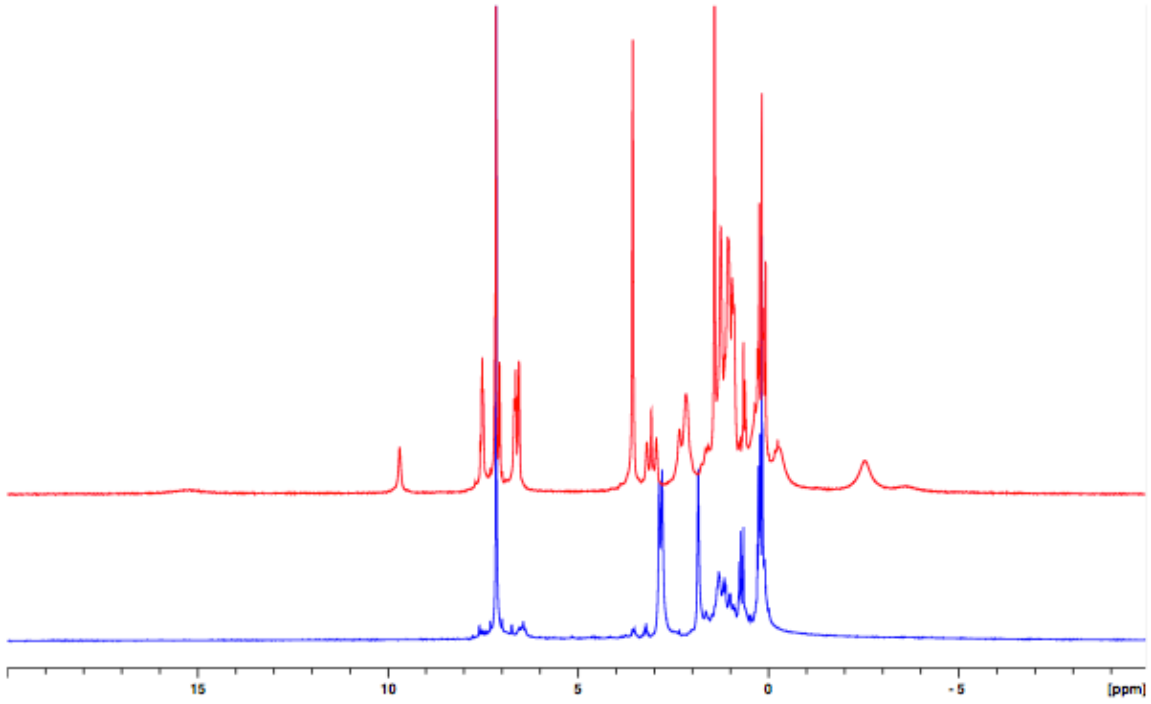

Figure 3.6 (top) ^{1}H NMR spectrum of the reaction at rt: **1**^{red} + CDSE; (bottom) ^{1}H NMR spectrum of the same reaction at −78 °C. NMR spectra were acquired in C_6D_6.

Notably, the addition of CDSE to **2**^{red} at room temperature yields two new products, the diamagnetic blue complex **3** and the blue-green paramagnetic complex **3**^{ox} (Figure 3.7). The generation of **3** was unexpected under these conditions; though CDSE has been previously reported to silylate metal-bound dinitrogen at both iron[17, 20] and tungsten,[113] the iron complex **2**^{red} does not possess enough electrons to generate **3** stoichiometrically![11] Complex **3**^{ox} has the expected iron(III) oxidation state, and the

[11] The reaction between **2**^{red} and CDSE should generate **3**^{ox}, which is a four-electron oxidation from Fe^{1-} to Fe^{III}. The counterion for the *in situ* generated **3**^{ox} is unclear, as it could not be separated from **3** nor prepared directly.

source of the extra electron to transform ferrous **3**^{ox} into ferric **3** is currently unknown but may derive from internal disproportionation reactions.

Nevertheless, the exclusive generation of **3** can be accomplished by running the reaction at approximately −50 °C in the presence of one equivalent of KC_8. The consumption of CDSE occurs rapidly at this temperature, though consumption of KC_8 does not occur until the reaction is warmed to ambient temperature. The reaction also generates an unknown brown product in minor yield, which can be removed by reconstitution in diethyl ether and filtration to yield **3** in decent yield (70%). The brown byproduct does not display any paramagnetic peaks in the ^{1}H NMR spectrum. The observed diamagnetic resonances are sufficiently broad as to preclude even a tentative number of resonances. However, no multinuclear NMR signals were observed. The identity of the byproduct is therefore wholly unknown.

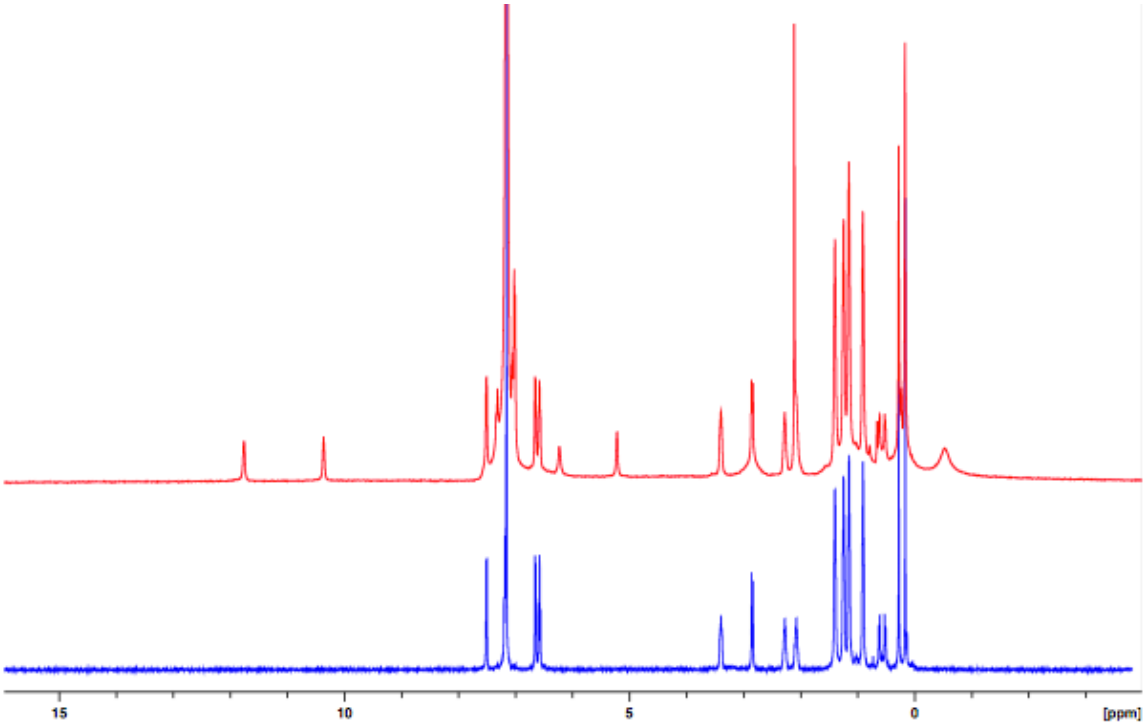

Figure 3.7 ^{1}H NMR overlay of the reaction: **2**^{red} + CDSE at rt (top) and at −78 °C with KC_8 (bottom). NMR spectra were acquired in C_6D_6.

Complex **3** contains numerous NMR-active nuclei, allowing for the identification of the proton, carbon, phosphorous, and silicon resonances. The ^{31}P, ^{29}Si, and ^{27}Al spectra show one peak each, at 79.9 and 8.5, and 70.2 ppm respectively. The significant downfield ^{31}P shift is consistent with oxidation at the metal center, though it is still 20 ppm upfield of the related iron(II) disilylhydrazido trisphosphineborane complex prepared by Peters and Moret.[17] The ^{29}Si resonance for **3** is also comparable to the (TPB)-iron(II)disilylhydrazide. The precursors **2** and **2**^{red} were both paramagnetic, precluding the collection of ^{27}Al spectra, but the resonance for **3** (70.2 ppm) is approximately 10 ppm upfield of the nickel-alane (78.6 ppm), corroborating the weaker metal-alane interaction in **3**, as also observed by solid-state crystallography.

The ^{1}H spectrum for **3** displays a locked ligand geometry around the bimetallic core, yielding the maximal twelve ligand peaks expected for a C_3 symmetry; notably, however, the N-N bond appears to be in free rotation on the NMR time scale, as only two silylmethyl resonances are observed. The silylmethyl groups are essentially invariant with respect to temperature and do not decoalesce even at −80 °C. The identities of all resonances were elucidated using 2-dimensional COSY spectroscopy and are shown in Figure 3.8.

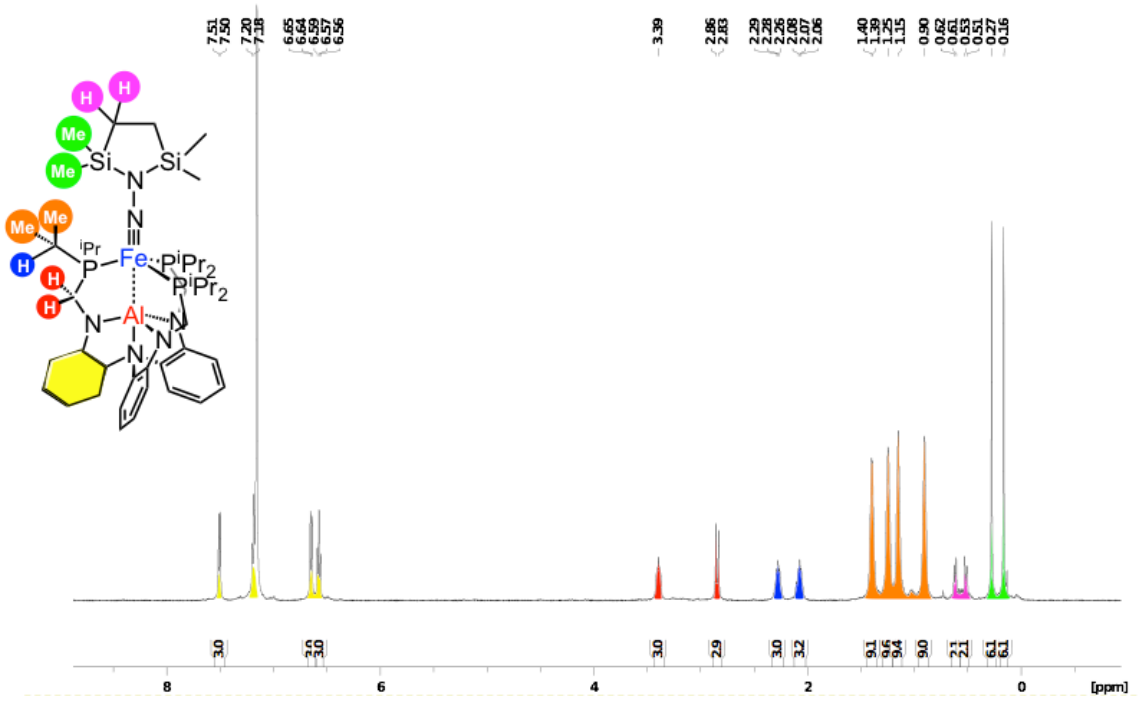

Figure 3.8 ^{1}H NMR peak assignments for **3**, assigned by COSY (500 MHz, benzene-d_6).

Surprisingly, complex **3** appears to be highly inert to further reactivity. The related iron-disilylhydrazine species prepared by Peters is shown to react further upon standing for two weeks, cleaving the N-N bond and generating a terminal iron-amide and oxidizing one phosphine arm,[17, 20] though no evidence of this internal reactivity is seen in

3 over the course of weeks. Rather, prolonged heating of **3** seems to slowly generate modest quantities of **1**. Complex **3** was not found to react with triphenyl phosphine, which allowed the use of PPh_3 as an internal ^{31}P NMR standard to monitor the loss of **3** under irradiation by a set of four mercury vapor lamps. The disappearance of the ^{31}P resonance for **3** appears to be non-linear, and the experiment was stopped after three weeks—at that point, approximately 88% had been consumed, and the only new product generated in the ^{1}H spectra is **1**. Selected times in the ^{31}P experiment are shown in Figure 3.9. Control reactions showed that this conversion occurs even in the absence of N_2, suggesting that the bridging dinitrogen of the reformed **1** is somehow related to the N_2 core of **3**.

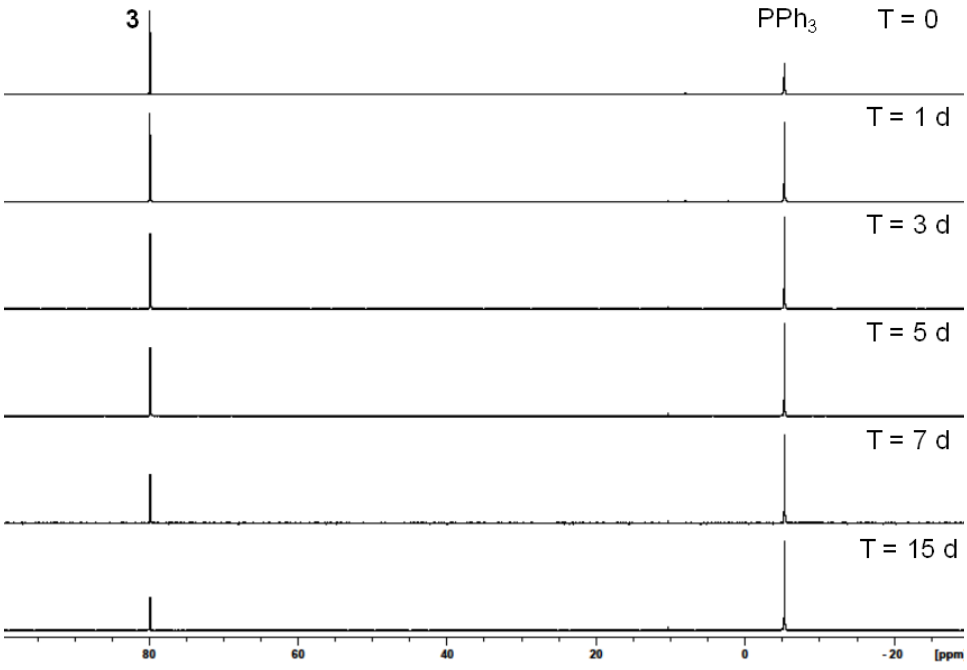

Figure 3.9 ^{31}P NMR loss of **3** relative to PPh_3 under irradiation.

The free rotation observed in the proton NMR of **3** and the apparent generation of **1** upon heating suggested that the N-N bond might be sufficiently accessible and activated to allow further reactivity, but these attempts have been unsuccessful to date. The use of strong methylating reagents (i.e., methyl triflate) yields unidentified ligand decomposition in nearly exclusive yield. No reaction is observed upon addition of donor ligands (*e.g.,* CO, ^{t}butylisocyanide, trimethylphosphine). The low-spin iron(II) center might be expected to be kinetically unreactive, and oxidation to the paramagnetic $\mathbf{3^{ox}}$ was accomplished using ferrocenium (B(*m*-$(CF_3)C_6H_3)_4$) ($FcBAr^F_4$). Other oxidants, such as ferrocenium hexafluorophosphate or ferrocenium tetraphenylborate, were found to yield only intractable mixtures. This independent generation of $\mathbf{3^{ox}}$ accounts for all paramagnetic peaks observed in the room temperature synthesis of **3**, as seen in Figure 3.10.

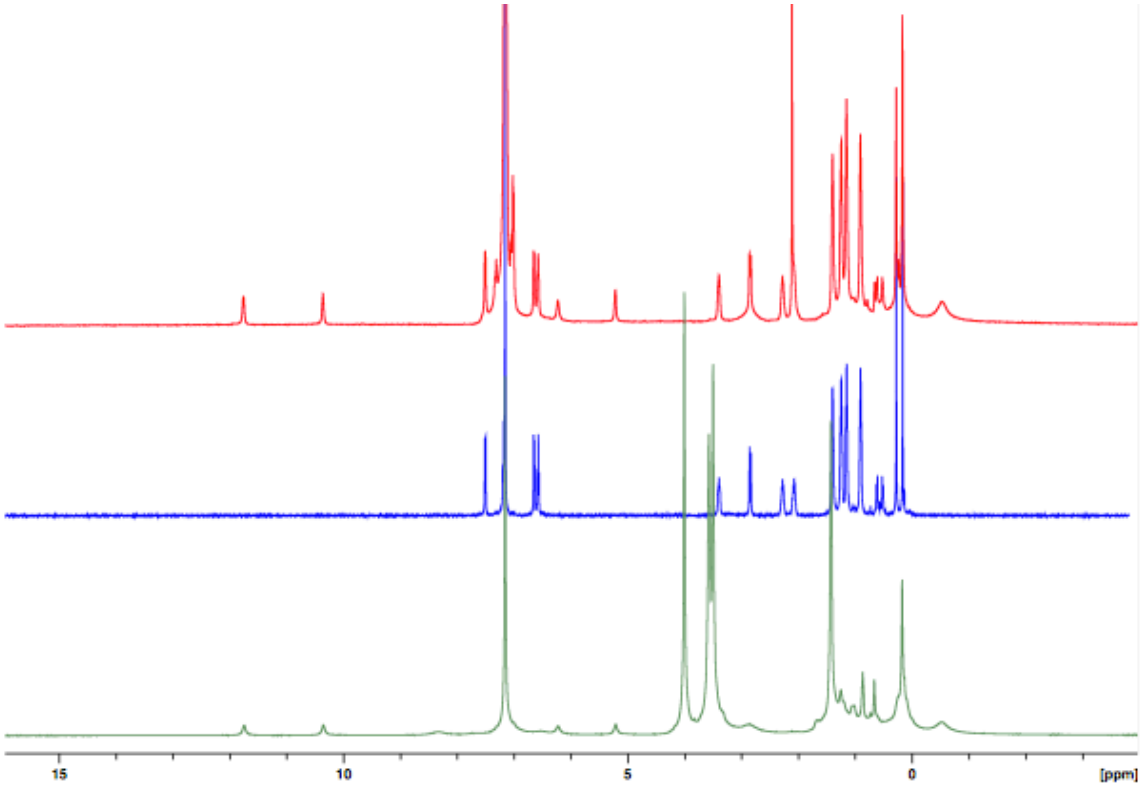

Figure 3.10 ^{1}H NMR spectrum of the reaction: $\mathbf{2}^{\mathbf{red}}$ + CDSE at rt (top); ^{1}H NMR spectrum of isolated **3** (middle); and ^{1}H NMR spectrum of the reaction: **3** + $FcBAr^{F}_{4}$ (bottom). All spectra are in C_6D_6 at rt. In the bottom reaction, free Fc can be seen at 4.0 ppm.

Upon oxidation to the paramagnetic $\mathbf{3}^{\mathbf{ox}}$, no reactions were observed with either CO or PMe_3 even upon mild heating for days. Reactivity studies of **3** were broadly complicated by two factors: first, synthesis of **3** proceeds more smoothly on larger scales because the crown ether can only be efficiently removed via crystallization. Second, however, the reformation of **1** from **3** can typically be spectroscopically detected within days, even when the solids are stored in the dark at −30 °C. These conflicting factors, compounded by the modest yields of each reaction step, have stymied further reactivity studies. One can imagine a direct route to hydrazine derivatives starting from the

commercially available reagents 1,1-dimethylhydrazine or 1,1-diphenylhydrazine. A proposed scheme to generate these hydrazine species is shown in Scheme 3.3 and is consistent with the formation of tungsten-hydrazido species.

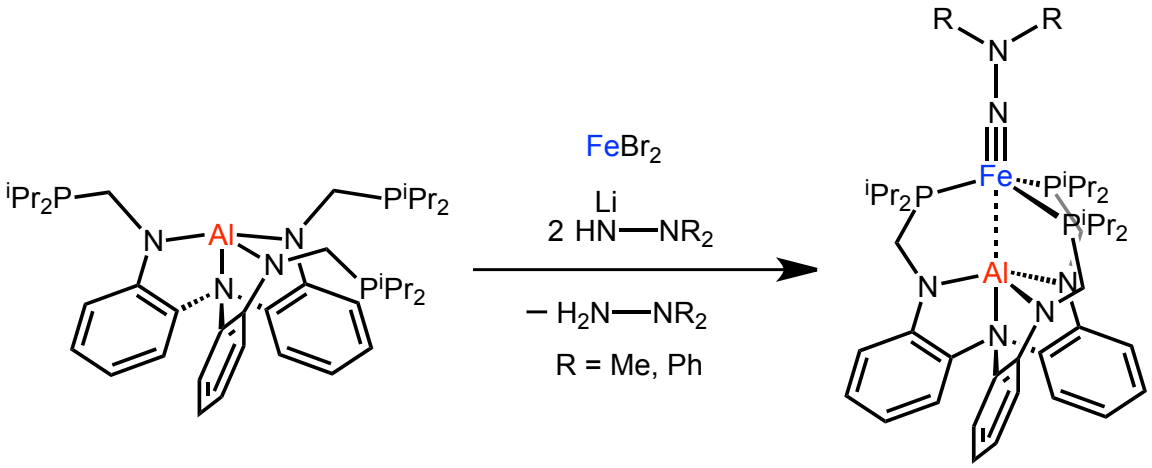

Scheme 3.3 A proposed pathway to directly generate various metal-hydrazide derivatives

3.3.2 Single Crystal X-ray Diffraction Studies

Single crystal diffraction studies were performed for [K(crypt-222)]**1**^{red}, [18c6(K)]**2**^{red}, and **3**. The general crystallographic details will be discussed first, followed by a comparison of **1**, **1**^{red}, **2**, **2**^{red}, and **3**. Additional crystallography details are also given in Section 3.5.

Complex **1**^{red} is only crystalline upon the addition of crypt-222, whereupon it neatly crystallizes in the trigonal space group *P3*. The observed solid-state structure has three arms of **1**^{red} along a three-fold axis the *c* axis in addition to one cryptand on a general position. Unexpectedly, the best crystallographic refinement requires a lithium counter-ion rather than potassium. The incorporation of lithium can be rationalized, as lithium chloride may not have been fully removed from the monometallic aluminum

complex. The cryptand molecule is geometrically unsuited to bind lithium, yielding the substantial distortions from 3-fold symmetry and requiring its placement on a general position. A survey of the Cambridge crystallographic database confirms that the lithium-oxygen distances are all in the expected range and are broadly inconsistent with potassium binding. The solid-state structure of $\mathbf{1}^{red}$ is shown in Figure 3.11.

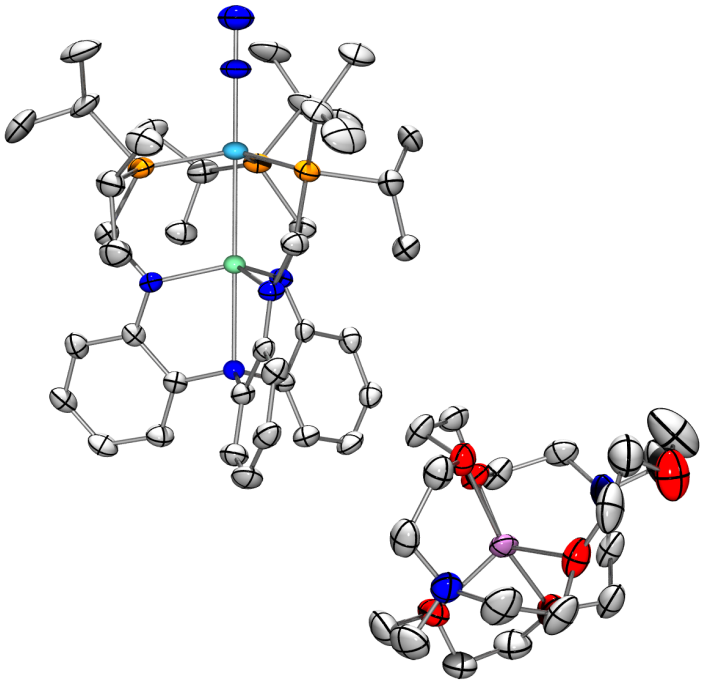

Figure 3.11 Solid-state structure of [Li(crypt-222)][$\mathbf{1}^{red}$] shown with 50% thermal ellipsoids. Hydrogen atoms have been omitted for clarity. Only one of three unique molecules is shown.

Complex $\mathbf{2}^{red}$, in contrast, does not yield single crystals either as a THF solvate or as a cryptand salt. The addition of 18c6 marginally increases the crystallinity, but all crystals diffracted relatively poorly between −100 and −150 °C. The structure was ultimately collected at −150 °C and solved in the space group *Pbca*. Three disordered

THF molecules are present in addition to the complex of interest, and the crystallographic deficiencies are primarily localized on the solvent molecules. The potassium counterion is chelated equitorially by all six oxygen donors and has an additional close-contact to both the N_2 unit and an axial THF donor. The potassium-N_2 distance is comparable to similar 18c6 complexes in the Cambridge Crystallographic Database and is consistent with a second feature in the infrared spectrum assigned as a potassium-N_2 contact-ion pair. The potassium-bound THF is likely to be labile, as combustion analysis is consistent with the solvent-free complex. The main residue is shown in Figure 3.12.

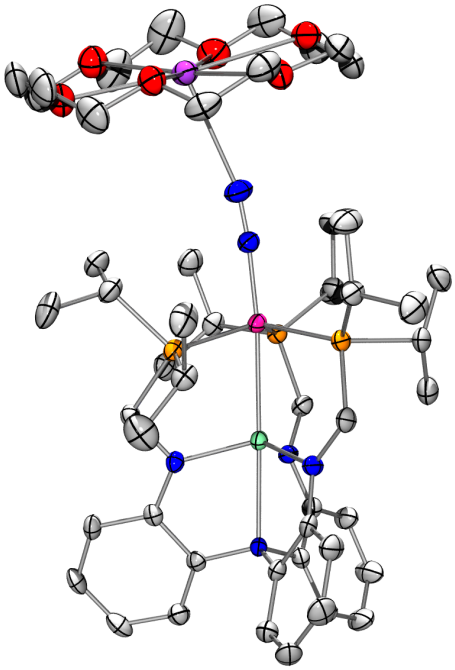

Figure 3.12 Solid-state structure of [18c6(K)][$\mathbf{2}^{\mathbf{red}}$] shown with 50% thermal ellipsoids. Hydrogen atoms and three THF molecules per asymmetric unit have been omitted for clarity. One THF molecule is bound to K^+ (*trans* to N_2), while the other two are non-coordinating.

Complex **3** is highly crystalline as a pure material, and will crystallize readily out of pentane, hexane, ether, and benzene. Problematically, crystallization from either pentane or hexane yields a crystal system, likely Cc, with three molecules in the asymmetric unit that cannot complete the refinement of the structure solution. Crystallization from either diethyl ether or benzene yields high-quality crystal structures wherein the solvent molecule is non-coordinating; crystallization from ether occurs in the space group $P2_1/c$ and was determined to be more feasible for bulk samples. The solid-state structure is shown in Figure 3.13.

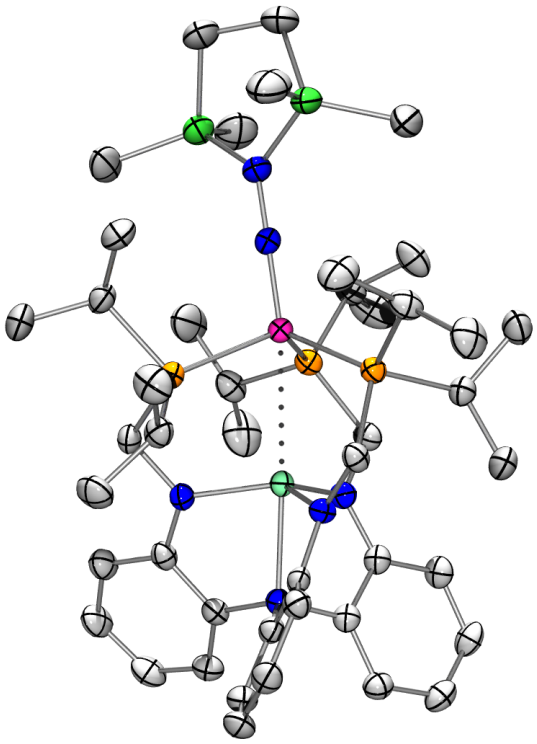

Figure 3.13 Solid-state structure of $(SiMe_2CH_2)_2N_2FeAlL^{iPr}$ **3** shown with 50% thermal ellipsoids. Hydrogen atoms have been omitted for clarity. A non-coordinating Et_2O molecule is also not shown.

A comparison of the metrical parameters for **1**, **2**, $\mathbf{1}^{red}$, $\mathbf{2}^{red}$, and **3** is shown in Table 3.1. Of note, the dinitrogen ligand changes from bridging ($M_2(\mu\text{-}N_2)$) to terminal coordination ($M\text{-}N_2$) upon reduction of **2** to $\mathbf{2}^{red}$. Crystallographically, the changes in parameters between **1**, **2**, and their reduced congeners are all consistent with a formal reduction at the transition metal site. The aluminum-nitrogen interactions would be expected to lengthen upon reduction due to electronic repulsion, whereas the metal-phosphine interactions would be expected to shorten due to increased metal-phosphine backbonding. Though the $Al\text{-}N_{eq}$ distances do elongate slightly by 0.022 and 0.052 Å for $\mathbf{1}/\mathbf{1}^{red}$ and $\mathbf{2}/\mathbf{2}^{red}$, respectively, the Co-P and Fe-P bonds shorten more significantly by 0.089 and 0.112 Å, respectively. Additionally, reduction at the transition metal site is expected to decrease the metal-N_2 distance as a consequence of greater backbonding interactions, which is observed by contractions of 0.048 and 0.050 Å for cobalt and iron, respectively. One would expect that a decrease in the metal-N_2 distance should be coupled with an increase in the N-N distance, but little can be said given that N-N bond distances are statistically indistinguishable upon reduction.

Table 3.1 Geometric parameters, including bond lengths (Å) and angles (deg), for complexes **1**, [Li(crypt-222)][**1**^{red}], **2**, [K(18c6)][**2**^{red}], and **3**.

Complexes	**1**	**1**^{red}	**2**	**2**^{red}	**3**[a]
N−N	1.107(4)	1.110(8)	1.146(7)	1.135(4)	1.351(3)
M−N_2	1.841(3)	1.793(6)	1.843(4)	1.783(3)	1.661(2)
M−Al	2.6202(9)	2.507(2)	2.809(2)	2.574(1)	2.8237(8)
r[b]	1.06	1.01	1.11	1.02	1.12
M−P	2.2408(8) 2.2712(8) 2.2859(9)	2.177(1)	2.3404(9)	2.226(1) 2.226(1) 2.234(1)	2.2461(7) 2.2538(7) 2.2779(7)
Al−N_{eq}	1.872(2) 1.878(2) 1.879(2)	1.898(3)	1.852(3)	1.902(3) 1.904(3) 1.908(3)	1.861(2) 1.861(2) 1.875(2)
Al−N_{ap}	2.187(2)	2.324(6)	2.176(4)	2.340(3)	2.178(2)
∑(P-M-P)	349.47(5)	351.29(2)	335.03(3)	350.08(4)	331.53(3)
∑(N-Al-N)$_{eq}$	351.5(2)	345.34(7)	351.56(9)	344.4(1)	351.65(9)

[a] Average of three unique molecules. [b] Ratio of the M−Al bond length to the sum of the M (low-spin) and Al covalent radii.

One additional consequence of reduction is the contraction of the metal-alane bond. As previously noted, the empirical *r* value is used to quantify the extent of interaction between two sites. The *r* values decrease for both the CoAl and FeAl systems upon reduction, where the CoAl bond contracts from 1.06 to 1.01 and the iron-aluminum bond contracts from 1.11 to 1.02. Both of these contractions are significant, representing changes of at least 0.1 Å in the absolute metal-aluminum distance. It is qualitatively clear that increasing the electron count increases the strength of the Z-type interaction, though not necessarily in a linear manner. For clarity, the increased bond polarity is diagrammed

against the electron count in Figure 3.14. The contraction in the *r* value between **2**/**2**$^{\mathbf{red}}$ is most substantial and may indicate that the formation of a much stronger iron-alane interaction is necessary to stabilize the low-valent iron site.

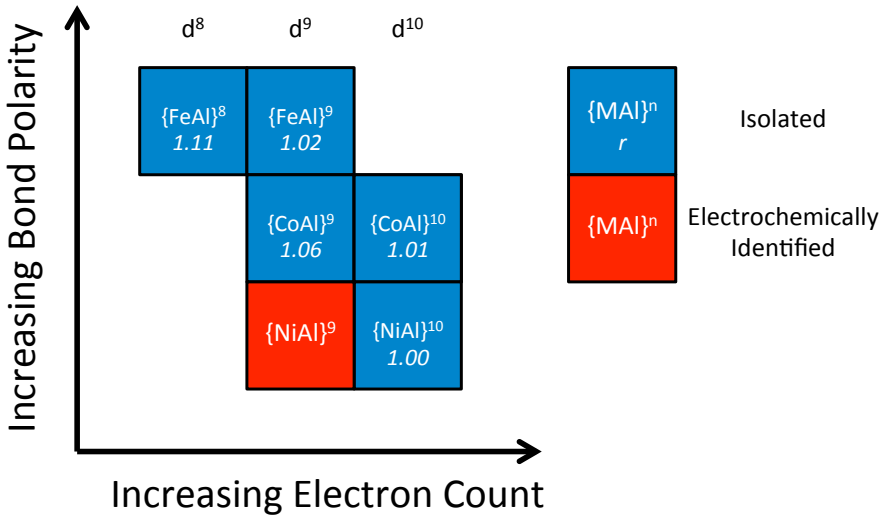

Figure 3.14 Bond polarity versus electron count for the metal-alane complexes

The Lewis-acidic role of the alane moiety appears to be important in stabilizing low-valent iron in particular. Additional work in the laboratory has shown that zerovalent nickel can be selectively installed into the P_3 coordination site without the need for a second metal,[78] and preliminary work suggests that a zerovalent cobalt can also be installed in the P_3 plane. However, attempts to install the corresponding zerovalent iron in the P_3 plane yielded only free ligand and Fe_2L^{iPr},[114] which were observed by ^{1}H NMR and X-ray crystallography, respectively.

Additionally, the structure of **3** shows unambiguously that a four-electron reduction of dinitrogen has occurred. The N-N bond elongates dramatically (0.216 Å), which is consistent with a four-electron reduction to hydrazine.[10] In support of this

assignment, no N=N or N≡N stretches were observed in the IR spectrum of **3**. The iron-phosphine distances expand slightly, consistent with a higher oxidation state at iron, and the contraction in the Fe-N(disilylhydrazido) distance by 0.122 Å is indicative of a much stronger iron-nitrogen bond. Lastly, the observed distances and geometries are in excellent agreement with those of Peters' iron-boratrane disilylhydrazido species as computed with density functional theory.[36]

3.3.3 Mössbauer and Electron Paramagnetic Resonance Spectroscopy Studies

Due to the unusual nature of the iron complexes **2** and $\mathbf{2}^{\mathbf{red}}$, we undertook additional spectroscopic studies to further elucidate the electronic properties of these complexes: two complementary techniques to study the electronic properties of iron are electron paramagnetic resonance (EPR) and ^{57}Fe Mössbauer spectroscopy.

Efforts were made to collect the X-band EPR spectra for both **2** and $\mathbf{2}^{\mathbf{red}}$, but the S = 1 integer spin state will often be EPR silent. The absence of an EPR signal results from the even-electron, non-Kramers systems that can possess zero-field splitting values larger than the microwave quanta used by the instrument, and this phenomenon is exacerbated in trigonal symmetry.[115] Indeed, complex **2** displays no EPR features between 2 – 30 K in either the parallel or perpendicular modes. The reduced complex $\mathbf{2}^{\mathbf{red}}$, though, has a non-integer spin and is EPR active in the perpendicular mode. The observed spectrum, shown in Figure 3.15, confirms the S = ½ ground state and shows axial symmetry with g_z = 2.195 and $g_x = g_y$ = 2.04.

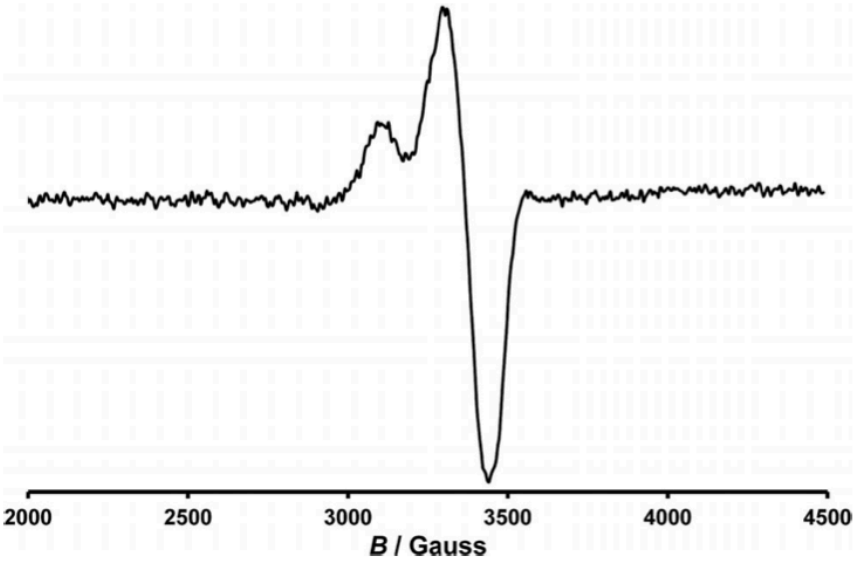

Figure 3.15 X-band EPR spectrum (dX″/dB) of K(crypt-222)[$\mathbf{2}^{\mathbf{red}}$] in frozen THF (1 mM, 20.0 K, frequency = 9.65 GHz, modulation to 10 G, power = 0.2 mW).

The EPR spectrum for $\mathbf{2}^{\mathbf{red}}$ is consistent with a d^9 metal center, as there is no observed coupling to the ^{27}Al nucleus (I = 5/2), which is the sole naturally occurring aluminum isotope. Additionally, the axial spectrum is highly reminiscent of copper(II) systems in which the unpaired electron resides in the xy-plane, such as in $d_{x^2-y^2}$.[116] These observations strongly support the assignment of an iron(1-) (ferrate) oxidation state. It is noted that the 17-electron ferrate states are highly unusual: formal examples are $[Fe_2(CO)_8]^{2-}$ and $[Fe(\eta_4\text{-anthracene})_2]^-$,[117] though Wolf and coworkers have utilized Mössbauer spectroscopy to suggest that low-valent polycyclic aromatic hydrocarbons may actually represent iron(II) species with anionic ligand radicals.[118]

Zero-field Mössbauer spectroscopy also supports the change on oxidation state between **2** and $\mathbf{2}^{\mathbf{red}}$, though a definitive assignment of oxidation state is not currently possible. Without an applied magnetic field, Mössbauer spectra have two diagnostic

features: the isomer shift and the quadrupole splitting. The isomer shift is defined as the midpoint between the quadrupole doublets and reflects the *s* electron density of the iron nucleus. As a result, the isomer shift (IS) is often taken as a proxy for the iron oxidation state, though it can be strongly affected by the spin state and the covalency of the metal-ligand bonds. The results of these differing effects are more well known for iron(II) through iron(V), and relatively little is known about the Mössbauer spectra for low-valent iron. In particular, metal-ligand backbonding can substantially affect the isomer shift—indeed, iron(0) and iron(I) complexes may exhibit similar isomer shifts to the analogous iron(II) complexes.[15] The Mössbauer spectra for **2** and $\mathbf{2}^{\mathbf{red}}$ are shown in Figures 3.16 and 3.17, respectively, and it is apparent that the isomer shift does in fact decrease from 0.54 to 0.38 mm s^{-1}.

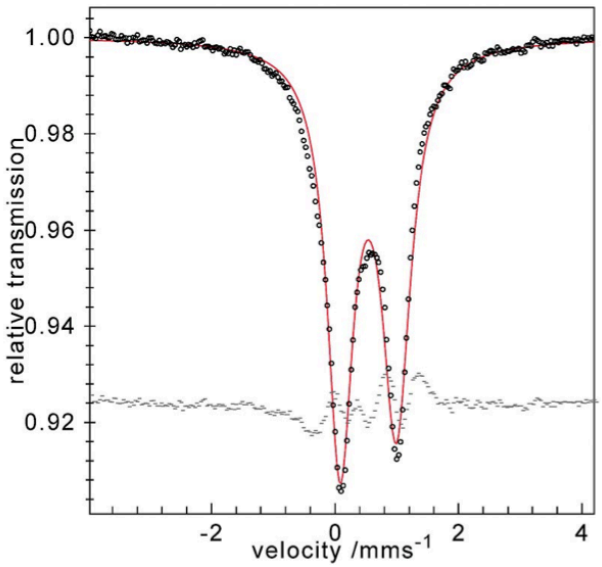

Figure 3.16 Zero-field ^{57}Fe Mössbauer spectra of **2** at 80 K.

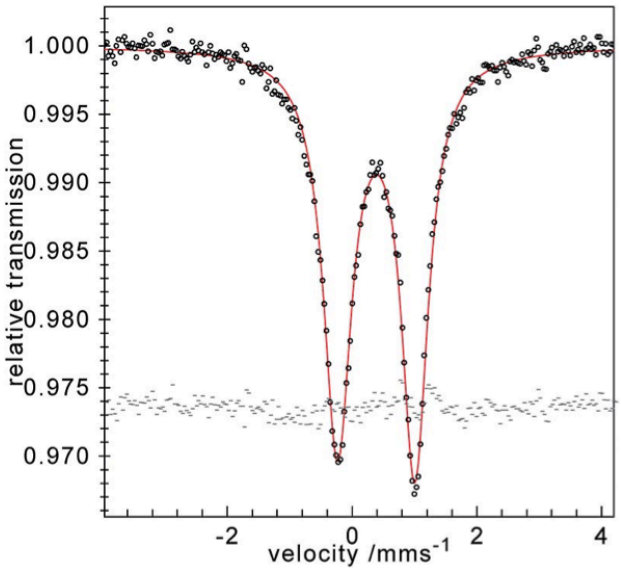

Figure 3.17 Zero-field ^{57}Fe Mössbauer spectra of $\mathbf{2}^{-}$ at 80 K.

Interestingly, the isomer shift change is towards a lower value upon reduction, though lower values are actually expected upon oxidation. The isomer shifts themselves are consistent with iron(II) species, whereas it is readily apparent that the iron site must have a lower "real" oxidation state than ferrous. Definitive assignment of the oxidation states may only be assignable upon synthesis of several different complexes and examination of the iron K-edge energy with X-ray absorption spectroscopy, though it is apparent here that the most reasonable oxidation states are in fact the zerovalent and subvalent formulations.

The quadrupole splitting term in Mössbauer refers to the distance between the quadrupole doublets, which reflects the electronic field gradient (EFG) at the iron nucleus. A higher distortion of the EFG, such as from a highly asymmetric ligand environment, will yield a higher quadrupole splitting value. The quadrupole splitting increases slightly from **2** to $\mathbf{2}^{\mathbf{red}}$, which is consistent with a stronger interaction along the

iron-aluminum vector, but the absolute values of 0.91 and 1.24 mm s^{-1} are unexceptional in the context of typical iron Mössbauer spectra.

3.3.4 Density Functional Theory Calculations

Additional confirmation of the iron(1-) (ferrate) oxidation state for $\mathbf{2}^{\mathbf{red}}$ was provided in the form of density functional theory calculations. Starting with the crystal structure, the ligand isopropyl groups were truncated to methyl groups, and the M06L functional was used to optimize the geometry. The resulting structure of $\mathbf{2Me}^{\mathbf{red}}$ agrees very well with experiment. For instance, the computed N–N bond length of 1.135 Å matches exactly to that in the experimental structure. The *d* orbital splitting pattern is shown in Figure 3.18 and consists roughly of two high-lying orbitals (d_{xy}, $d_{x2–y2}$) over three low-lying orbitals (d_{xz}, d_{yz}, d_{z2}), which is typical of trigonal symmetry. The d_{z2} orbital, which is the lowest lying of the *d* set, is presumably stabilized by mixing with an empty p_z orbital at aluminum. The $d_{x2–y2}$ orbital is the singly occupied molecular orbital (SOMO). The π^* N_2 molecular orbitals are found at higher energies (SOMO+4, SOMO+5), and consequently, they are unoccupied, which is consistent with dinitrogen binding as a neutral ligand.

The spin density at iron is 1.10, which corresponds to approximately one unpaired electron residing at iron. The spin density plot, shown in Figure 3.19, demonstrates that the lone electron is localized in the xy plane. By considering spin–orbit coupling from the mixing of *d* orbitals, the electronic configuration $(d_{xz})^2(d_{yz})^2(d_{z2})^2(d_{xy})^2(d_{x2–y2})^1$ is expected to give rise to a relatively large g_z (from greater mixing of the SOMO with d_{xy})

and two smaller g_x and g_y values (from lesser mixing of the SOMO with d_{xz} and d_{yz}). As discussed above, the observed axial EPR signal of **2**^{red} is fully consistent with this electronic configuration.

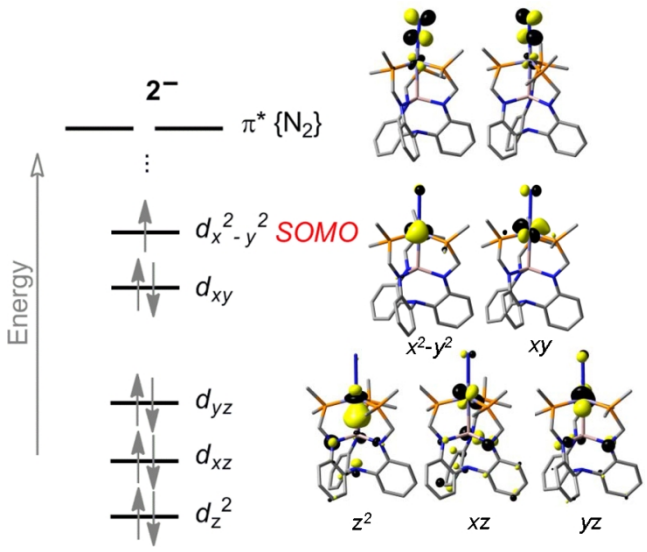

Figure 3.18 Qualitative MO diagram for **2Me**^{red}. Hydrogen atoms have been omitted for clarity. Atom color coding: C, grey; N, blue; P, orange; Al, pink; Fe, purple.

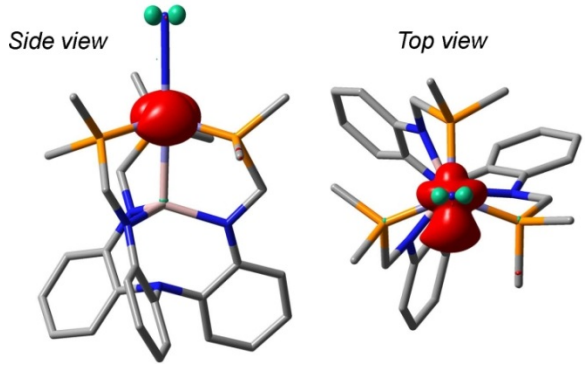

Figure 3.19. Spin density plot for **2Me**^{red} with positive (red) and negative (green) spin densities. The only significant spin densities (absolute value > 0.1) are: Fe, +1.10 and N_β of N_2, −0.13. Hydrogen atoms have been omitted for clarity. Atom color coding: C, grey; N, blue; P, orange; Al, pink; Fe, purple.

3.3.5 Preliminary Results with Iron Bimetallics of Ga^{3+}, In^{3+}, and Sc^{3+}

Due to the promising results seen with Al^{3+} as a supporting metal site, the Group 13 metals were obvious initial targets, as was Sc^{3+}. Metallations in Et_2O (In) or THF (Sc, Ga) cleanly afforded the monometallic precursors GaL^{iPr}, InL^{iPr}, and ScL^{iPr}. The highly modular synthetic scheme suggested that the cobalt and iron bimetallics of these species might be readily available. Crystal structures of the monometallic species were obtained by either diffusion of pentane into THF (GaL^{iPr}) or evaporation of Et_2O solutions (InL^{iPr}, ScL^{iPr}) and are shown in Figure 3.20.

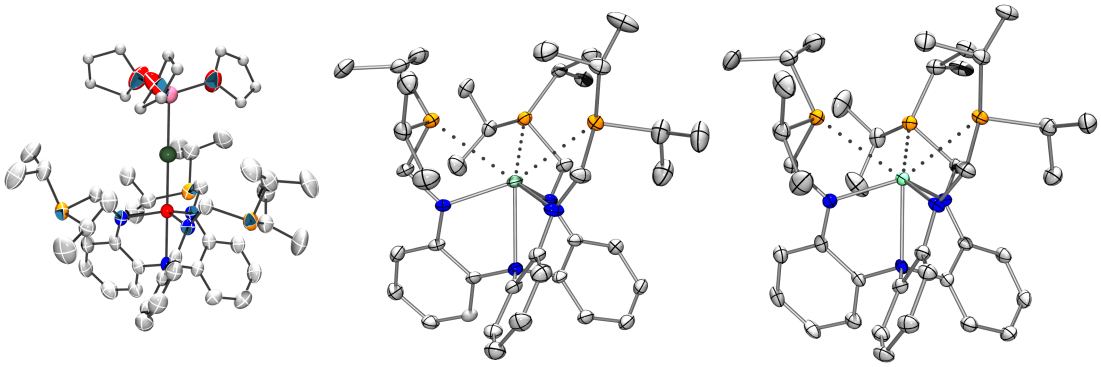

Figure 3.20 Solid-state structures of ML^{iPr} (M = Ga (left), In (middle), Sc(right)) shown with 50% thermal ellipsoids. Hydrogen atoms have been omitted for clarity.

As expected, the single-crystal structures confirm the proposed connectivity for each complex. The structure of colorless GaL^{iPr} was, unexpectedly, the lithium chloride THF solvate, which emphasizes the necessity of a rigorously non-polar purification scheme. Unlike AlL^{iPr}, which was crystallized as an acetonitrile adduct, yellow-orange InL^{iPr} and colorless GaL^{iPr} show close contacts between all three phosphines to the metal center, which is sitting appreciably above the N_3 plane. The metric parameters of these

structures are shown in Table 3.3 and are unremarkable compared to literature tris-amides of scandium, indium, or gallium. The ^{1}H NMR spectra for the monometallic species exhibit fluxional behavior, which is consistent with the long metal-phosphine distances. The ^{31}P NMR spectra, though, show a substantial metal dependence: AlL^{iPr}, 8 ppm; GaL^{iPr}, 20 ppm; InL^{iPr}, 39 ppm; ScL^{iPr}, −11 ppm.[12]

Table 3.2 Metrical Parameters for ML^{iPr} (M = Al, Ga, In, Sc).

	AlL^{iPr}	GaL^{iPr}	InL^{iPr}	ScL^{iPr} [a]
M –N_{eq} (Å)	1.865(5) [b]	1.919(4) [b]	2.119(3)	2.089, 2.095(3)
			2.126(3)	2.094, 2.100(3)
			2.137(3)	2.107, 2.109(3)
M–N_{apical} (Å)	2.057(10)	2.236(7)	2.474(3)	2.397, 2.398(2)
M to N_3-plane (Å)	+ 0.193	+ 0.346	+ 0.670	+ 0.632, 0.646
Σ (N-M-N) (°)	356.84(7)	350.46(6)	331.66(13)	333.95(10)

[a] Two molecules are present in the asymmetric unit. [b] Three-fold crystal symmetry results in one M-N distance

The general metallation procedure is shown below in Scheme 3.4. Initial attempts focused on iron complexes because of the previously observed nitrogen reduction with the iron-alane $\mathbf{2}^{\mathbf{red}}$. Initial metallation with $FeBr_2$ and GaL^{iPr} (**4**) or InL^{iPr} (**5**) and two equivalents of reductant gives disparate ^{1}H NMR spectrum relative to both each other and the related iron-alane complex (Scheme 3.4). The color of **5** is additionally noted to be a vibrant green, in contrast to the brown color of both the iron-alane and the putative iron-gallane **4**. No product was observed with ScL^{iPr} and iron(II) bromide: according to NMR, the sole isolated product after the reaction is ScL^{iPr}.

[12] Few Sc-P interactions are known, but the ^{31}P NMR shifts for these complexes cluster roughly around 0 ppm.

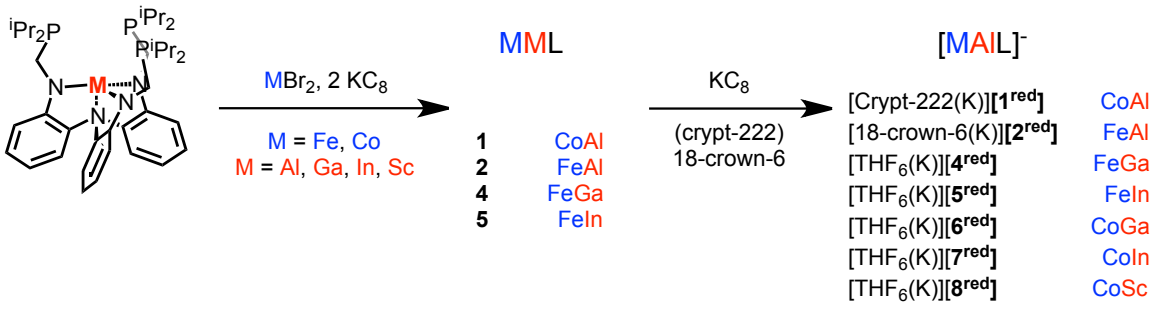

Scheme 3.4 General route for Lewis acid-bimetallic complexes

A crystal structure of complex **5** was obtained from a diffusion of pentane into a THF solution, yielding the structure of **5** as seen in Figure 3.21. Surprisingly, the structure has the expected iron-indane motif but also shows a bromide anion with a Fe-Br distance of 2.4100(8) Å. Due to the short nature of this contact and potential redox activity at indium, the possibility of iron(I), indium(II) oxidation states was considered. Due to the negligible change in In-$N_{equatorial}$ distances between InL^{iPr} and **5** (Δ = +0.012 Å), the assignment of In(II) is unlikely. The cause of the bromide ion binding is currently uncertain, but we note that it is consistent with an iron center in which the d_{z2} orbital has been dramatically lowered in energy due to the dative donation into indium. This interaction should be expected to make iron a stronger σ-acceptor, which, in accord with the total absence of N_2 binding (IR), may actually prevent initial loss of bromide prior to dinitrogen binding. We additionally note that the related $NiInL^{iPr}$ complex has been prepared, which will spontaneously bind both N_2 and H_2 at room temperature and pressure.[119] This behavior is dissimilar to $NiAlL^{iPr}$, which corroborates the effect of a *trans*-indium center inducing ligand binding. As judged by solubility and NMR spectroscopy, the iron-gallane **4** does not appear to have the same halide-binding

properties as **5**. The bromide ligand in **5** appears tightly bound, and does not dissociate upon extended stirring in non-polar solvents (toluene, benzene) in which **1**, **2**, and **4** are soluble. Despite the halide binding, the iron-indium distance is a relatively short 2.5637(6) Å (r = 0.96), which is actually shorter than the iron-aluminum contacts in either **2** or $\mathbf{2}^{red}$ despite the larger size of indium.

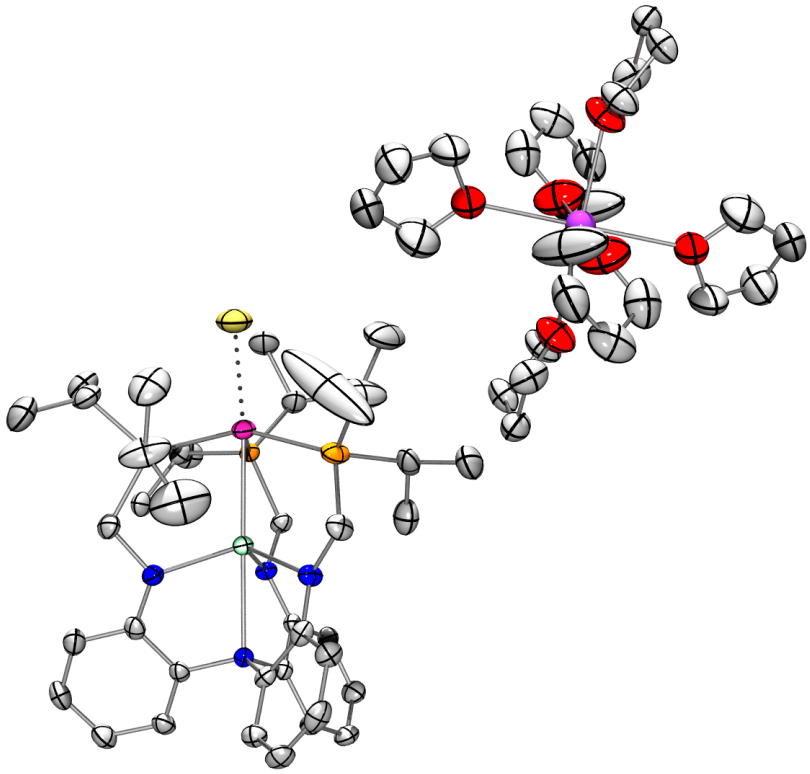

Figure 3.21 Solid state crystal structure of $[K(THF)_6][BrFeInL]$ (**5**)

The reduced, formally iron(1-) complex is expected to expel bromide due to electronic repulsion of two anionic centers, allowing for isolation of dinitrogen complexes. Indeed, reduction of **5** with KC_8 yields a new product, $\mathbf{5}^{red}$, in the ^1H NMR spectrum as well as a new stretch appears in the IR spectrum at 2020 cm^{-1}. This complex,

assigned as the salt $[K(THF)_6][N_2FeInL]$, was not found to be crystalline under a variety of conditions, including chelation with 18c6 or 2,2,2-cryptand. Addition of the metathesis reagent PPNCl (PPN = (bistriphenylphosphino)iminium) yields large, dichroic green-brown single crystals upon sitting overnight. Analysis of these crystals by single-crystal diffraction demonstrates that, contrary to expectations, a chloride adduct of zero-valent iron has instead formed. Due to the nearly quantitative yield of this reaction, the ultimate fate of the lost electron is currently unknown. Indeed, the iron-indane $\mathbf{5}^{\mathbf{red}}$ appears to be remarkably halophilic, as addition of CDSE and one equivalent of potassium graphite at room temperature generated numerous products by ^{1}H NMR spectroscopy—only one of these products was sufficiently crystalline to determine the solid-state connectivity, and it possessed an apical halide ligand.

The reduced complex $\mathbf{4}^{\mathbf{red}}$ can be prepared by analogous means to $\mathbf{2}^{\mathbf{red}}$ and $\mathbf{5}^{\mathbf{red}}$, but it is similarly non-crystalline. Despite the difficulties in determination of the solid-state structure for the iron-gallium and iron-indium complexes, preliminary Mössbauer and EPR experiments suggest that the isolated anionic species $\mathbf{4}^{\mathbf{red}}$ and $\mathbf{5}^{\mathbf{red}}$ maintain nearly identical electronic environments. The Mössbauer spectrum of the iron-indane species, shown in Figure 3.22, has an isomer shift of 0.38 mm s^{-1}, which is nearly identical to that of $\mathbf{2}^{\mathbf{red}}$ (0.37 mm s^{-1}). The EPR spectrum of the iron-gallane (Figure 3.23), meanwhile, possesses an EPR spectrum with $g_y \approx 2.29$, $g_x = g_z \approx 2.09$. The high g

values again represent a d^9 species with an unpaired electron in the xy-plane, confirming the identity as a ferrate complex.[13]

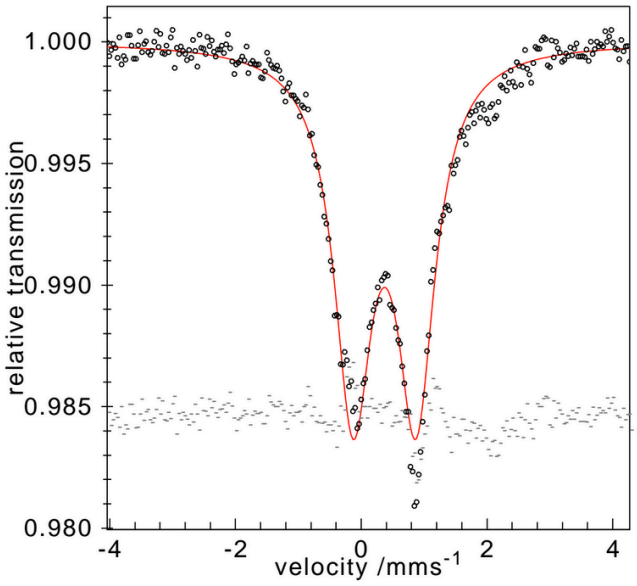

Figure 3.22 Zero-field ^{57}Fe Mössbauer spectra of **5**^{red} at 80 K

[13] Unlike **2**^{red}, the EPR of **4**^{red} shows some hyperfine coupling that is presumed to originate from the three ^{31}P (I= ½) nuclei in the xy plane. It should be noted, however, that both ^{69}Ga (60% natural abundance) and ^{71}Ga (30% natural abundance) have I = 3/2 nuclei and would yield similar splitting patterns. This interpretation is rejected on account of the high *g* values and unambiguous ferrate assignment of **5**^{red}, but it does complicate efforts to simulate the spectrum.

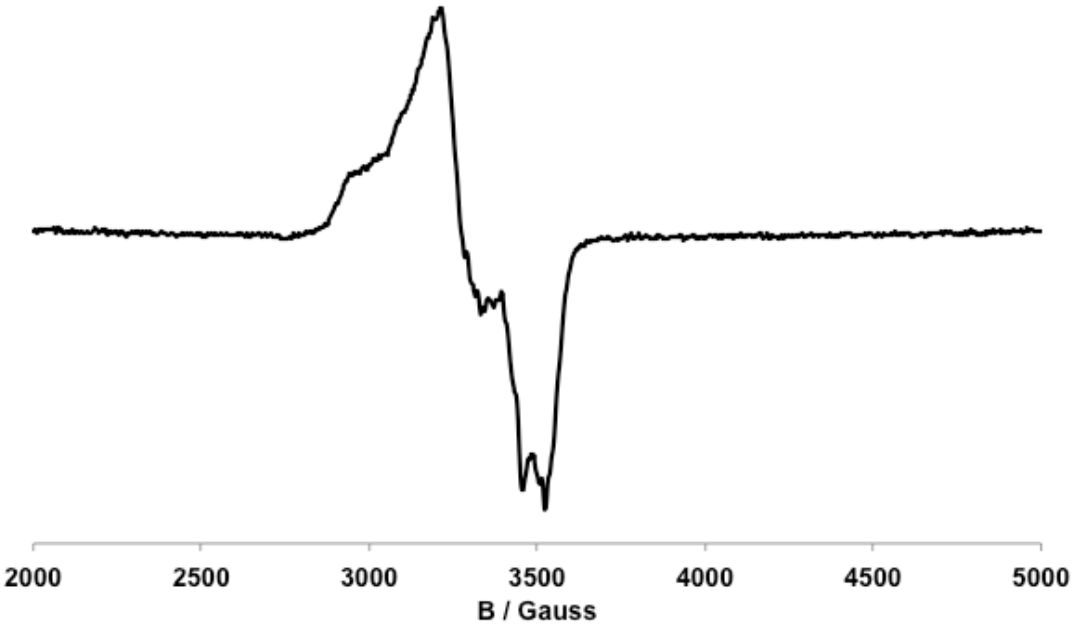

Figure 3.23 X-band EPR spectrum (dX″/dB) of $\mathbf{4}^{red}$ in frozen THF (1 mM, 57 K, frequency = 9.65 GHz, modulation to 10 G, power = 0.2 mW). The spectrum is invariant between 17 and 57 K.

Given the similar electronic structure observed by Mössbauer and EPR, one might expect that the overall electronic features of the iron sites are unperturbed. However, analysis via cyclic voltammetry finds that the reduction potentials shift dramatically between **2**, **4**, and **5**. The reduction potential of **2** is −2.08 V, which similar to that of the N_2FeTPB complex (−2.18 V), but the reduction potentials of **4** and **5** are substantially milder, as $E_{1/2}$ = −1.57 and −1.54 V, respectively. It is not immediately clear why **4** and **5** would have such similar reduction potentials, nor why the reduction potential has dropped by nearly one half volt—the extra electron should reside on an orbital on the d_{xy} plane, which should be minimally altered upon variation of the Lewis acid. The voltammograms of $\mathbf{4}^{red}$ and $\mathbf{5}^{red}$ are shown in Figure 3.24.

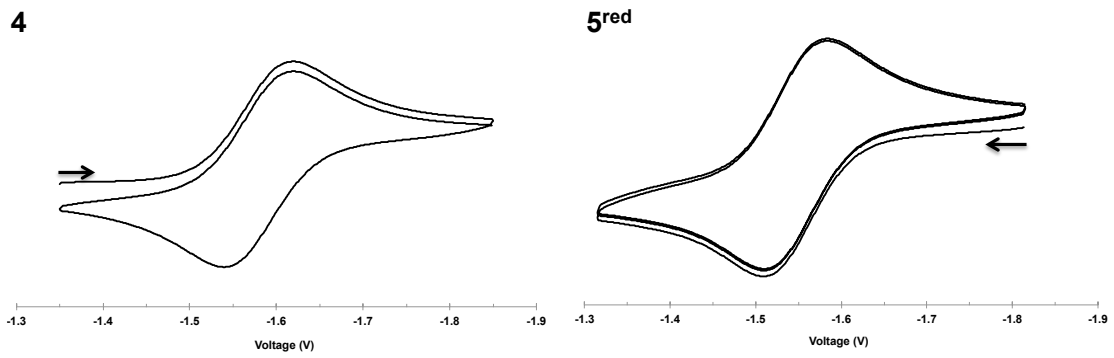

Figure 3.24 Cyclic voltammograms of **4** (reduction) and $\mathbf{5}^{red}$ (oxidation) in THF (0.4 M $TBAPF_6$, **4**, 100 mV/s; $\mathbf{5}^{red}$, 50 mV/s)

The cyclic voltammogram for $\mathbf{5}^{Br}$ was also collected and is shown in Figure 3.25. The $E_{1/2}$ value, −1.55 V, is nearly identical to that of $\mathbf{5}^{red}$, −1.54 V, but $\mathbf{5}^{Br}$ displays a strong dependence on scan speed. At scan speeds of 100 – 250 mV/s, the reduction is essentially irreversible, whereas it becomes mostly reversible at 5 mV/s (Δ = 135 mV). This behavior is not well understood, though it does corroborate the milder reduction potential seen in $\mathbf{5}^{red}$.

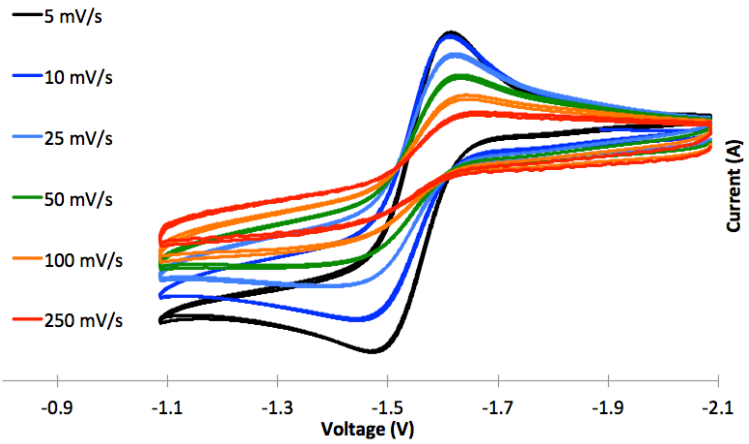

Figure 3.25 Cyclic voltammotram of $\mathbf{5}^{Br}$ in THF (0.4 M $TBAPF_6$, 5 – 250 mV/s)

3.3.6 Preliminary Results with Cobalt Bimetallics of Ga^{3+}, In^{3+}, and Sc^{3+}

Because $\mathbf{4}^{red}$ and $\mathbf{5}^{red}$ are clearly viable synthetic targets, the cobaltate analogs were prepared in an analogous manner to the aluminum species (see Scheme 3.4). Gratifyingly, the ^{1}H NMR spectra (Figure 3.26) for these derivatives all appear to be diamagnetic, as was the cobalt-aluminum species $\mathbf{1}^{red}$**.** Notably, the resonances for the CoGa ($\mathbf{6}^{red}$) and CoIn ($\mathbf{7}^{red}$) are centered at the same chemical shifts as $\mathbf{2}^{red}$, though they appear to become more fluxional. For $\mathbf{7}^{red}$, all methyl groups are magnetically equivalent, indicating rapid rotation around the P-C bonds as well as a low-energy barrier between the formally enantiomeric C_3 rotamers. The CoSc ($\mathbf{8}^{red}$) spectrum is substantially sharper than the Group 13 analogs and exhibits apparent C_{3V} symmetry, as both methyl groups are observed.

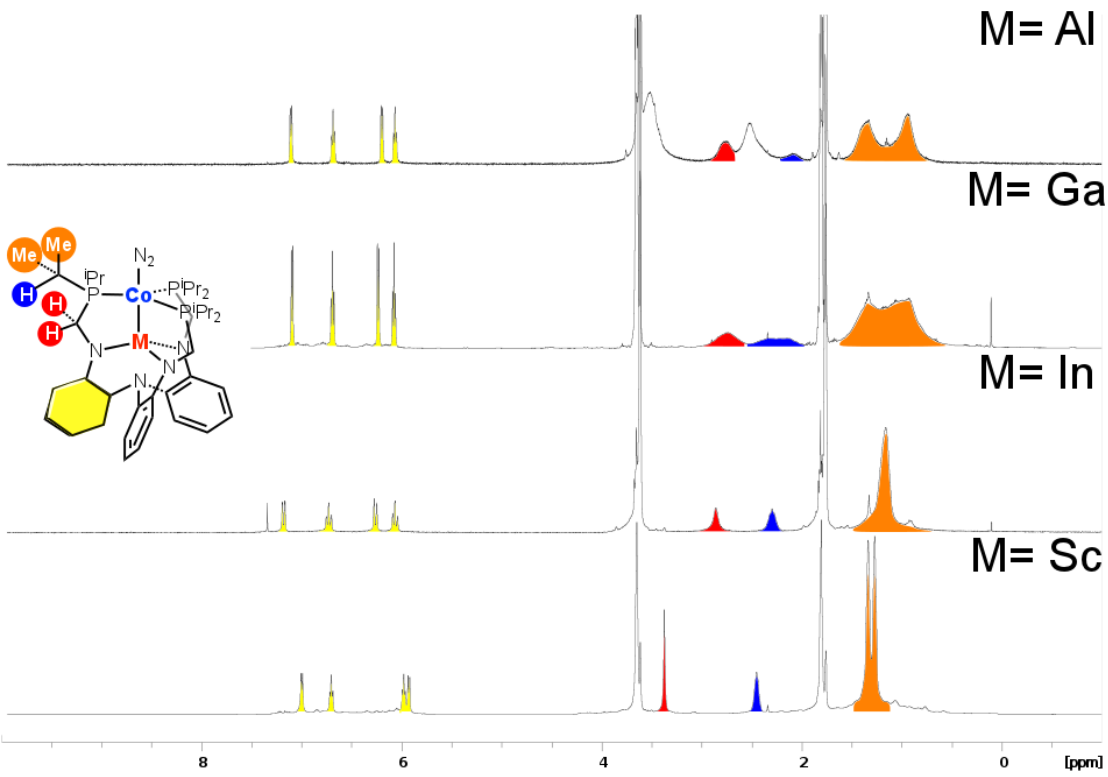

Figure 3.26 ^{1}H NMR assignments for bimetallic cobalt species (500 MHz, THF-d_8). For M = Al, the unmarked resonances correspond to crypt-222.

Though the ^{1}H NMR show little change upon variation of the supporting Lewis acid, the ^{31}P NMR show a progressive downfield shift from **2**^{red} (54 ppm) to **6**^{red} (63 ppm) to **7**^{red} (75 ppm), which is shown in Figure 3.27. Interestingly, the ^{31}P signal shifts even though the phosphine moiety, presumably, does not directly interact with the substituted element. Additionally, these shifts suggest that the cobalt center is becoming progressively more electron-poor, consistent with the expected effects of the stronger expected Z-bonds with gallium and indium. At present, the anomalously low shift for the cobalt-scandium **8**^{red} is not understood; more bafflingly, the ^{31}P is extremely broad,

whereas the ^{1}H NMR spectrum is sharper than the corresponding alane, gallane, and indane moieties.

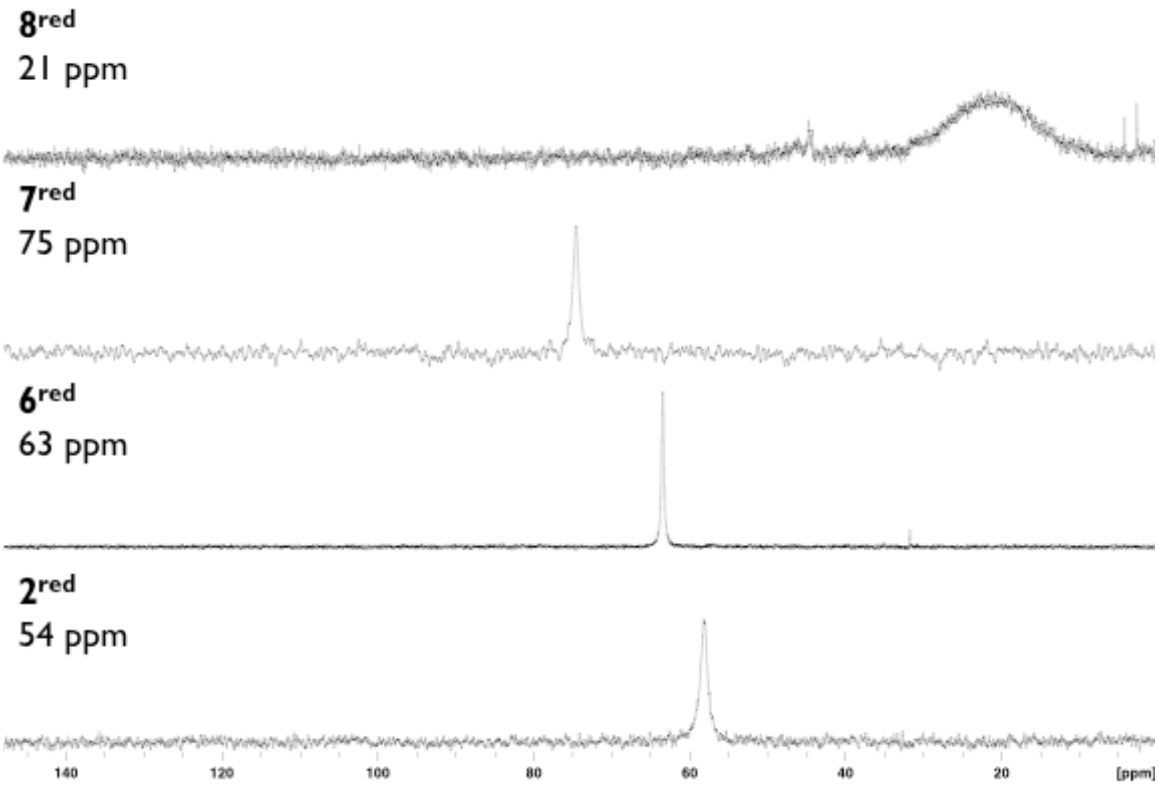

Figure 3.27 ^{31}P NMR spectra for **2**^{red}, **6**^{red}, **7**^{red}, and **8**^{red} (THF-d_8, 121 MHz). The diagnostic resonance for each species is indicated.

In accordance with the obvious changes in the ^{1}H and ^{31}P NMR spectra, it was expected that the cyclic voltammetry of **6**^{red}, **7**^{red}, and **8**^{red} would exhibit one oxidative wave at a milder potential than that seen in 2red. The voltammograms for **6**^{red} and **7**^{red} are shown in Figure 3.28 and each display one oxidative feature. Two independent measurements of the scandium complex **8**^{red} found no reversible electrochemical events.

For $\mathbf{6}^{red}$ and $\mathbf{7}^{red}$, the oxidative features are centered at - 0.937 and - 0.967 V, respectively, which are nearly identical to the -0.95 V seen in $\mathbf{2}^{red}$.

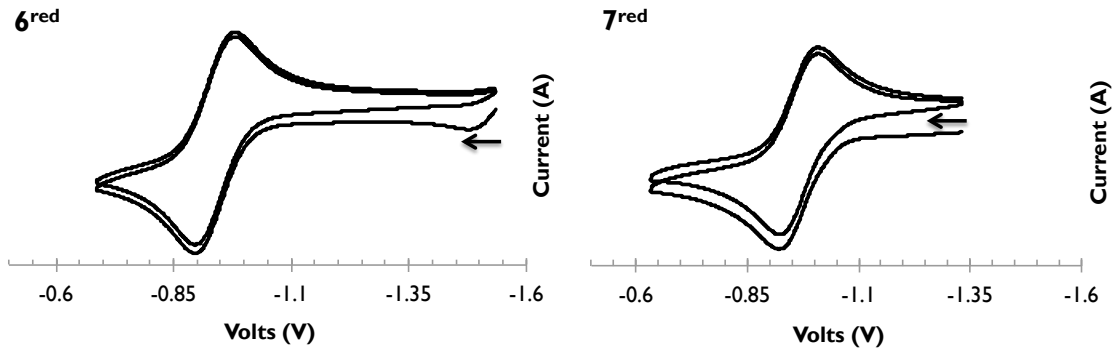

Figure 3.28 Cyclic voltammograms of $\mathbf{6}^{red}$ and $\mathbf{7}^{red}$ in THF (0.4 M $TBAPF_6$, 100 mV/s)

This insensitivity is highly surprising, especially as it contrasts sharply with the iron-indane and iron-gallane species, which shift anodically by approximately 0.5 V relative to the aluminum species. The ultimate cause of these perturbations is currently unclear, and it is likely that solid-state structures and theoretical calculations could elucidate the origin of this behavior.

3.4 Conclusions

Reduction of the cobalt- and iron-alane complexes **1** and **2** was shown to generate complexes with cobaltate (Co^{1-}) and ferrate (Fe^{1-}) oxidation states. These complexes bind and modestly activate dinitrogen, and addition of a silylating reagent to the ferrate complex induces a controlled four-electron reduction at dinitrogen. The dinitrogen-derived product is formally a deprotonated disilylhydrazine derivative and could not be further functionalized to cleave the remaining N-N bond or the Fe=N bond. Upon prolonged heating or photolysis, the iron-disilylhydrazide appears to slowly decay to the binuclear iron(0) complex **2**, containing a bridging dinitrogen.

Preliminary work has been done to systematically vary the ancillary metal site from aluminum to gallium, indium, and scandium. Initial results suggest that bimetallic complexes of Ga, In, and Sc retain the ferrate or cobaltate oxidation states. The electrochemistry of the cobalt complexes shows little variation, whereas the iron complexes exhibit dramatically milder reduction potentials than their borane and alane counterparts. Additionally, bimetallic iron-indium complexes are shown to possess Lewis acidity at a formally zero-valent iron site. Variation of the supporting Lewis-acid therefore shows an unexpected difference between cobalt and iron complexes, providing a new avenue for tuning future reactivity studies.

3.5 Experimental

General Considerations

Unless otherwise stated, all manipulations were performed under a dinitrogen atmosphere in an MBraun Atmosphere glovebox or using standard Schlenk techniques. Standard solvents were deoxygenated by sparging with dinitrogen and dried by passing through activated alumina columns of a SG Water solvent purification system. Deuterated solvents were purchased from Cambridge Isotope Laboratories, Inc., degassed via freeze-pump-thaw cycles, and stored over activated 4 Å molecular sieves. 1,2-bis(chlorodimethylsilyl)ethane was purchased from Aldrich and used without further purification. ^{1}H NMR spectra were recorded on a Bruker 500 MHz spectrometer at ambient temperature unless otherwise stated. All ^{1}H and ^{13}C NMR spectra are referenced to internal residual solvent. Room temperature UV-Visible/Near-IR spectra were collected on a Cary-14. Infrared spectroscopy was collected on a Bruker Tensor-37 FTIR using the OPUS 6.5 software. Complexes N_2CoAlL^{iPr} (where AlL^{iPr} = Al[N(*o*-C_6H_4-$NCH_2P^iPr_2)_3$]) and N_2FeAlL^{iPr} were synthesized according to literature procedures. [70] [70] [70] [70] [70] [70] [70] [37a] [23] [23] [23] [23] [23] Perpendicular-mode X-band EPR spectra were recorded at 20 K on a Bruker EPP 300 spectrometer equipped with an Oxford ESR 910 liquid helium cryostat and an Oxford temperature controller. X-band EPR spectra were simulated using EPR program (version W95) written by Professor Frank Neese (University of Bonn, Germany).

Synthesis of [K(crypt-222)][N_2CoAlL^{iPr}] ((K(crypt-222))[**1**^{red}]).

A solution of AlL^{iPr} (0.117 g, 0.16 mmol) was dissolved in THF (~4 mL) and mixed with a stirred slurry of cobalt(II) chloride (0.038 g, 0.28 mmol) in THF (4 mL) for twelve hours. During this time a homogenous, bright blue solution formed. After one hour, a slurry of KC_8 (0.077 g, 0.57 mmol) in THF (2 mL) was added dropwise over several minutes. Within minutes, a dark brown solution formed with precipitation of KBr and C(*s*). The sample was filtered through Celite in a glass-fiber filter pipette and washed with minimal THF until the washings ran clear. A solution of 2,2,2-cryptand (0.065 g, 017 mmol) was added in THF (1 mL) to the stirred solution. The brown solution is dried *in vacuo*, washed with copious diethyl ether, and further dried, yielding a brown powder (0.148 g, 75%). Single crystals of Li(crypt-222)[**1**^{red}] were grown by diffusion of n-pentane into a concentrated solution of **1**^{red} in THF. A lithium chloride contaminant from the ligand deprotonation step is thought to account for the presence of the lithium counter-cation in the X-ray structure. ^{1}H NMR (THF-d_8, 500 MHz): δ 7.06 (d, 1H); 6.65 (t, 1H); 6.16 (d, 1H); 6.03 (t, 1H); 3.47 (br, 8H); 2.73 (broad s, 2H); 2.47 (broad s, 6.0H); 2.04 (broad s, 1H); 1.32 (broad s, 6H); 0.90 (broad s, 6H). ^{31}P NMR (C_6D_6, 121MHz): δ 54.2. ^{27}Al NMR (C_6D_6, 75 MHz): δ 69.0. ^{13}C NMR (THF-d_8, 125 MHz): δ 138.4; 126.5; 125.8; 110.1; 108.3; 71.1; 68.3; 67.7; 54.6; 25.6; 20.2. IR (cm^{-1}): KBr pellet, ν[N_2] = 1993. No discernible UV-VIS transitions are observed between 400-2100 nm. From 400 nm, the electronic absorption spectrum tails off into the NIR region. Anal. Calcd for

K(crypt-222)[**1**^{red}] $C_{57}H_{96}N_6P_3O_6CoAlK$: C 56.70, H 8.01, N 9.28. Found: C 56.67, H 8.13, N 9.10.

Synthesis of [18c6(K)][N$_2$FeAlL^{iPr})] ([18c6(K)][**2**]).

A solution of N_2FeAlL^{iPr} (0.123 g, 0.15 mmol) was dissolved in THF (c. 4 mL), and a slurry of potassium graphite (0.017 g, 0.15 mmol) in THF (c. 4 mL) is added dropwise over several minutes. During this time a bright red solution formed. The dark solution formed concomitant with precipitation of KBr and C(*s*). The sample was filtered through Celite in a glass-fiber filter pipette and washed with minimal THF until washings run clear. A solution of 18c6 (0.041 g, 015 mmol) was added in THF (c. 1 mL) to the stirred solution. The brown-red solution is dried *in vacuo*, washed with diethyl ether (3x2 mL), and further dried, yielding a brown powder (0.118 g, 75%). Single crystals of **1** were grown by diffusion of n-pentane into a concentrated solution of **1** in THF. ^{1}H NMR (ppm, THF-d_8, 500 MHz): 51.4; 33.9; 11.6; 8.4; 6.4; 5.7; 0.8; 0.3; -0.3; -2.8. IR (cm^{-1}): KBr pellet, $\nu[N_2]$ = 1925. UV-VIS (in THF): (nm, ε [M^{-1} cm^{-1}]), 520 (sh, 890); 820 (sh, 245); 1515 (285). Anal. Calcd for K(18c6)[**2**] $C_{51}H_{84}N_6P_3O_6FeAlK$: 56.09 C, 7.75 H, 7.70 N. Found: 55.97 C, 7.85 H, 7.56 N.

Alternative synthesis of ([18c6(K)][**2**]):

A solution of N_2FeAlL^{iPr} (0.271 g, 0.38 mmol) is dissolved in THF (c. 4 mL) and added to a stirring solution of iron(II) bromide (0.084 g, 0.39 mmol) in THF (c. 2 mL). After one hour, a slurry of potassium graphite (0.130 g, 1.17 mmol) in THF (c. 8 mL) is added dropwise over minutes. The solution is allowed to stir one hour, during which time a

dark red solution forms. The solution is directly filtered through Celite in a glass-fiber filter pipette, and a solution of 18c6 (0.102 g, 0.38 mmol) in THF (c. 1 mL) is added to the filtrate and briefly stirred. The solvent is removed *in vacuo*, and the dark brown solid is thoroughly washed with diethyl ether (10 x 0.5 mL), removing a red-orange solution. The brown oil **2** is then dried in vacuo to yield a brown powder (0.350 g, 83%).

Synthesis of $((SiMe_2CH_2)_2)N_2FeAlL$ (**3**).

A solution of K(18c6)[**2**] (0.098 g, 0.09 mmol) was dissolved in THF (c. 6 mL) and mixed with a stirred slurry of potassium graphite (0.016 g, 0.21 mmol) in THF (c. 4 mL) at -78°C for thirty minutes. A separate solution of 1,2-bis(chlorodimethylsilyl)ethane (0.019 g, 0.09 mmol) was dissolved in THF (c. 6 mL) and cooled to -78°C for thirty minutes, then added drop-wise over several minutes. The solution is allowed to stir in the cold well for one hour, developing a red-brown color within minutes. After one hour, the solution is removed from the cold well and stirred an additional one hour at room temperature, during which time the potassium graphite is consumed concomitant with precipitation of KBr and C(*s*). The solution is then removed *in vacuo*, reconstituted in toluene, and filtered through Celite in a glass-fiber filter pipette to yield a light blue solution that gives a bright blue solid upon removal of solvent (0.070 g, 70%). 18c6 can be further removed by crystallizing a solution of **3** in n-hexane at −25°C overnight. Single crystals of **3** were grown by concentrating a solution of **3** in diethyl ether and allowing it to sit at room temperature for days. ^{1}H NMR (ppm, C_6D_6, 500 MHz): 7.50 (d, 3H, $^2J_{HH}$=6Hz, Ar CH); 7.19 (coincident with benzene-d_6; assigned by COSY, Ar

C*H*); 6.64 (d, 3H, $^{2}J_{HH}$=5.7Hz, Ar C*H*); 6.57 (t, 3H, $^{2}J_{HH}$=7.6Hz, Ar C*H*); 3.39 (broad s, 3H, PC*H*$_2$N) 2.84 (d, 3H, $^{2}J_{HH}$=11.2 Hz, PCH$_2$N); 2.27 (broad s, 3H, PC*H*); 2.08 (broad s, 3H, PC*H*); 1.39 (broad s, 9.0H, PCHC*H*$_3$); 1.24 (broad s, 10H, PCHC*H*$_3$); 1.14 (broad s, 10H, PCHC*H*$_3$); 0.90 (broad s, 9H, PCHC*H*$_3$); 0.60 (broad s, 2H, SiC*H*$_2$); 0.52 (broad s, 2H, SiC*H*$_2$); 0.27 (broad s, 6H, SiC*H*$_3$); 0.16 (broad s, 6H, SiC*H*$_3$). ^{31}P NMR (C_6D_6, 121MHz): δ 79.91 (s). ^{27}Al NMR (C_6D_6, 100 MHz): δ 70.2 (s). ^{29}Si NMR (THF-d_8, 99 MHz): δ 8.05. ^{13}C NMR (C_6D_6, 125MHz): δ 137.4; 129.6; 126.5; 126.0; 114.7; 23.4; 21.1; 20.5; 19.6; 9.1; −0.1. UV-VIS (in THF): (nm, ε [M^{-1} cm^{-1}]), 610 (400); 800 (115); 1145 (100). Anal. Calcd for Fe(N_2($SiMe_2CH_2$)$_2$)(AltraPhos) **3** $C_{45}H_{76}AlFeN_6P_3Si_2$: 57.93 C, 8.21 H, 9.01 N. Found: 57.86 C, 8.26 H, 8.97 N.

Preliminary synthesis of M[N(*o*-C_6H_4- $NCH_2P^iPr_2)_3$]) (M = Ga, In, Sc)

The monometallic Ga, In, and Sc complexes were synthesized analogously to the monometallic aluminum complex Al[N(*o*-C_6H_4- $NCH_2P^iPr_2)_3$] except that metallation occurs in THF rather than Et_2O. The isolated Sc species is white, and the Ga and In species are yellow powders. These complexes have been confirmed by single crystal diffraction experiments but not combustion analysis, so yields and UV-vis-NIR data are omitted. The ^{1}H and ^{31}P NMR data are provided:

M = Ga: ^{1}H NMR (ppm, C_6D_6, 500 MHz): 7.4 (d, 1H); 7.1 (t, 1H); 6.6 (d, 1H); 6.5 (t, 1H); 3.4 (s, 2H); 1.8 (s, 2H); 1.0 (d, 12H). ^{31}P NMR (C_6D_6, 121MHz): δ 20 (s).

M = In: ^{1}H NMR (ppm, C_6D_6, 500 MHz): 7.48 (d, 1H); 7.21 (t, 1H); 6.61-6.56 (overlapping d, t, 2H); 3.21 (s, 2H); 1.85, 1.70 (br overlapping s, 2H); 1.03, 0.99, 0.87, 0.75 (br overlapping s, 16H). ^{31}P NMR (C_6D_6, 121MHz): δ 39 (s).

M = Sc: ^{1}H NMR (ppm, C_6D_6, 500 MHz): 7.40 (d, 1H); 7.21 (t, 1H); 6.54 (t, 1H); 6.28 (d, 1h); 3.48 (d, 1H); 3.03 (d, 1H); 1.73, 1.68 (overlapping sept, 2H); 1.10, 1.04, 0.88, 0.76 (overlapping quartets, 16H). ^{31}P NMR (C_6D_6, 121MHz): δ −11 (s).

Preliminary synthesis of ($FeGa[N(o\text{-}C_6H_4\text{-}NCH_2P^iPr_2)_3]$) (**4**)

Complex **4** is synthesized analogously to the bimetallic complex **2**. The isolated species is a brown powder. Connectivity has *not* been confirmed by single crystal diffraction experiments nor not combustion analysis, so yields and UV-vis-NIR data are omitted. No IR stretches were observed in the N_2 region (KBr pellet). ^{1}H NMR (ppm, C_6D_6, 500 MHz): 35.5; 30.7; 12.4; 10.4; 8.36; 5.5; 3.6; 2.0; 1.4; 0.96; 0.88; −7.7

Preliminary synthesis of ($(K(THF)_n)(N_2FeGa[N(o\text{-}C_6H_4\text{-}NCH_2P^iPr_2)_3])$) (**4^{red}**)

Complex **4^{red}** is synthesized analogously to the bimetallic complex **2^{red}**. The isolated species is a brown powder. Connectivity has *not* been confirmed by single crystal diffraction experiments nor not combustion analysis, so yields and UV-vis-NIR data are omitted. ^{1}H NMR (ppm, C_6D_6, 500 MHz): 39.6; 32.0; 9.1; 8.5; 7.0; 6.0; 0.3; −0.4; −3.4

Preliminary synthesis of $[(K(THF)_6)][BrFeIn[N(o\text{-}C_6H_4\text{-}NCH_2P^iPr_2)_3]$ (**5**)

Complex **5** is synthesized analogously to the bimetallic complex **2**. The isolated species is a green powder. Crystals can be grown from diffusion of pentane into a concentrated solution of **5**, yielding dichroic green-brown crystals. Bulk purity has *not* been

established by combustion analysis, so yields and UV-vis-NIR data are omitted. ^{1}H NMR (ppm, C_6D_6, 500 MHz): 32.8; 12.1; 10.7; -4.6; -7.5.

Preliminary synthesis of $(K(THF)_n)(N_2FeIn[N(o\text{-}C_6H_4\text{-}NCH_2P^iPr_2)_3])$ (**5**^{red})

Complex **5**^{red} is synthesized analogously to the bimetallic complex **2**^{red}. The isolated species is a brown powder. Connectivity has *not* been confirmed by single crystal diffraction experiments nor not combustion analysis, so yields and UV-vis-NIR data are omitted. ^{1}H NMR (ppm, C_6D_6, 500 MHz):

Preliminary synthesis of $(K(THF)_n)(N_2CoM[N(o\text{-}C_6H_4\text{-}NCH_2P^iPr_2)_3])$

(M = Ga, **6**^{red}; M = In, **7**^{red}; M = Sc, **8**^{red})

Complex **6**^{red}, **7**^{red}, and **8**^{red} are synthesized analogously to the bimetallic complex **2**^{red}. The isolated species are brown powders. Connectivity has *not* been confirmed by single crystal diffraction experiments nor not combustion analysis, so yields and UV-vis-NIR data are omitted. ^{1}H NMR (ppm, C_6D_6, 500 MHz):

M = Ga, **6**^{red}: ^{1}H NMR (ppm, C_6D_6, 500 MHz): 7.0 (d); 6.6 (t); 6.2 (t); 2.7 (br s); 3.2, 2.1 (br overlapping s); 1.3, 0.9 (br overlapping d). ^{31}P NMR (C_6D_6, 121MHz): δ 63 (s).

M = In, **7**^{red}: ^{1}H NMR (ppm, C_6D_6, 500 MHz): 7.13 (d, 1H); 6.68 (d, 1H); 6.22 (d, 1H); 6.02 (t, 1H); 2.82 (s, 1H); 2.25 (s, 1H); 1.12 (s, 12H). ^{31}P NMR (C_6D_6, 121MHz): δ 75 (s)

M = Sc, **8**^{red}: ^{1}H NMR (ppm, C_6D_6, 500 MHz): 6.9 (d); 6.7 (t); 6.6 (t); 5.9 (d); 3.3 (s); 2.4 (s); 1.3, 1.2 (overlapping s). ^{31}P NMR (C_6D_6, 121MHz): δ 21 (s).

X-Ray Crystallographic Data Collection and Refinement of the Structures

Single crystals of Li(crypt-222)[**1**^{red}] and K(18c6)[**2**] were grown by vapor diffusion of *n*-pentane into a concentrated THF solution at room temperature. Single crystals of **3** were grown in a concentrated solution of diethyl ether at room temperature. A yellow block of Li(crypt-222)[**1**^{red}] (0.20 x 0.20 x 0.10 mm^3), red-orange block of K(18c6)[**2**] (0.10 x 0.1 x 0.05 mm^3), a violet plate of **3** (0.5 x 0.4 x 0.1 mm^3), and a colorless hexagon of $(THF)_3LiCl[GaN(o\text{-}C_6H_4\text{-}NCH_2P^iPr_2)_3]$ (0.2 x 0.2 x 0.1 mm^3) were placed on the tip of a glass capillary and mounted on a Bruker APEX II CCD diffractometer for data collection at 173(2) K. The data collection was carried out using Mo-Kα radiation (graphite monochromator). Single crystals of $M[N(o\text{-}C_6H_4\text{-}NCH_2P^iPr_2)_3]$ (M = Sc, In) were grown by evaporation of concentrated Et_2O solutions. A colorless block of $Sc[N(o\text{-}C_6H_4\text{-}NCH_2P^iPr_2)_3]$ (0.43 x 0.48 x 0.05 mm^3) and a yellow block of $In[N(o\text{-}C_6H_4\text{-}NCH_2P^iPr_2)_3]$ (0.43 x 0.49 x 0.27 mm^3) were placed on the tip of a glass capillary and mounted on the tip of a glass capillary and mounted on a Bruker D8 Photon 100 CMOS diffractometer for data collection at 123(1) K. The data collection was carried out using Cu-Kα radiation (normal parabolic mirror monochromator). The data intensity was corrected for absorption and decay (SADABS). Final cell constants were obtained from least squares fits of all measured reflections. The structure was solved using SHELXS-97 and refined using SHELXL-97. A direct-methods solution was calculated which provided most non-hydrogen atoms from the E-map. Full-matrix least squares / difference Fourier cycles were performed to locate the remaining non-hydrogen atoms. All non-hydrogen

atoms were refined with anisotropic displacement parameters. Hydrogen atoms were placed in ideally and refined as riding atoms with relative isotropic displacement parameters. While K(18c6)[**2**] is crystallographically well ordered, three THF molecules (including one coordinated to potassium) show substantial disorder. The structure factor values (R_1 6.0%; wR_2 16.0%) primarily reflect the disorder of these solvent molecules. Lastly, we note that alerts in the IUCR checkCIF application relate almost exclusively to solvent, and the nature of these alerts (*e.g.*, high/low Ueq, short C(sp3)-C(sp3) bonds, H—H contacts) relates to the inability of these solvent molecules to settle in a satisfactory manner. Crystallographic data are summarized in Table 3.3. The monometallic species M[N(*o*-C_6H_4- $NCH_2P^iPr_2)_3$]) (M = Ga, In, Sc) are tabulated separately in Table 3.4.

Table 3.3 Crystallographic Data for Li(crypt-222)[1^{red}], K(18c6)[2], and 3

	Li(crypt-222)[**1**^{red}]	K(18c6)[**2**]	**3**
chemical formula	$C_{57}H_{94}N_8O_6P_3AlCoLi$	$C_{63}H_{108}N_6O_9P_3FeAlK$	$C_{49}H_{86}N_6OP_3Si_2FeAl$
formula weight	1173.16	1308.4	1007.16
crystal system	Trigonal	Orthorhombic	Monoclinic
space group	R3	Pbca	P21/c
a (Å)	19.047(1)	19.565(1)	12.3688(12)
b (Å)	19.047(1)	20.577(1)	19.3615(19)
c (Å)	43.403(3)	34.679(2)	23.290(2)
α (deg)	90	90	90
β (deg)	90	90	103.461(1)
γ (deg)	120	90	90
V (Å3)	13637(3)	13983(1)	5424.2(9)
Z	9	8	4
Dcalcd (g cm−3)	1.286	1.243	1.233
✦(Å), μ (mm−1)	0.71073, 0.431	0.71073, 0.412	0.71073, 0.467
T (K)	173(1)	173(1)	173(1)
θ range (deg)	2.14 – 27.48	2.27 – 23.95	2.288 – 26.968
reflns collected	12934	14351	12356
unique reflns	9970	7997	8892
data/restraint/ parameters	12934/1/694	14351/0/758	12356/0/568
R1, wR2 (I > 2σ(I))	0.0526, 0.1369	0.0614, 0.1677	0.0447, 0.1187

Table 3.4 Crystallographic Data for ML^{iPr} (M = Ga, In, Sc)

	GaL^{iPr}	InL^{iPr}	ScL^{iPr}
chemical formula	$C_{39}H_{60}N_4P_3Ga$ * $C_{12}H_{24}O_3LiCl$	$C_{39}H_{60}N_4P_3In$	$C_{39}H_{60}N_4P_3Sc$
formula weight	1005.78	792.64	722.78
crystal system	Hexagonal	Monoclinic	Triclinic
space group	*P6(3)*	*C2/c*	*P-1*
a (Å)	13.1878(11)	19.9403(5)	10.4354(4)
b (Å)	13.1878(11)	10.3406(3)	20.3324(7)
c (Å)	20.0918(16)	38.4138(10)	20.6392(7)
α (deg)	90	90	63.764(2)
β (deg)	90	100.8960(10)	85.013(2)
γ (deg)	120	90	85.916(2)
V (Å^3)	3026.2(4)	7777.9(4)	3920.7(2)
Z	3	8	4
D_{calcd} (g cm^{-3})	1.104	1.354	1.224
λ (Å), μ (mm^{-1})	0.71073, 0.616	1.54178, 6.262	1.54178, 2.997
T (K)	173(1)	123(1)	123(1)
θ range (deg)	1.78 – 27.51	2.339 – 68.2155	2.38 – 68.1665
reflns collected	35077	7058	14124
unique reflns	4668	6399	10909
data/restraint/ parameters	4668/1/192	7058/0/424	10909/0/871
R_1, wR_2 ($I > 2\sigma(I)$)	0.0682, 0.2051	0.0447, 0.1136	0.0555, 0.1524

Computational Details

Geometry gas phase optimizations of **2red^{Me}** were performed employing the M06L functional[120] using the Gaussian09 suite.[121] For C and H atoms, the 6-31G(d) basis set was used,[122] whereas 6-311+G(2df,p) was employed for N, O, P and Cl and the Stuttgart SDD and SDD+2f contracted pseudopotential basis sets on for Al and Fe, respectively.[123] Initial starting points for geometry optimizations was taken/derived from the experimentally determined X-ray structure without imposing any symmetry constraints. The DFT calculations were performed with the broken symmetry option (unrestricted

calculations). The nature of all stationary points was verified by analytical computation of vibrational frequencies at the same level of theory. No negative frequencies were found.

Chapter 4

Multiple Metal-Metal Bonds in Iron-Chromium Complexes

In part from:

Rudd, P. A.; Liu, S.; Planas, N.; Bill, E.; Gagliardi, L.; Lu, C. C. "Multiple Metal-Metal Bonds in Iron-Chromium Complexes" *Angew. Chem. Int. Ed. Eng.* **2013**, *52*, 4449-4452.

4.1 Overview

The ligand N(*o*-(NHCH$_2$P(^{i}Pr)$_2$)C$_6$H$_4$)$_3$ (H_3L^{iPr}) is metallated with chromium(III) to yield the monometallic species CrL^{iPr} (**1**). This complex is additionally metallated with iron(II) in the presence of two equivalents of reductant to yield the bimetallic species $FeCrL^{iPr}$ (**2**). This complex has rich electrochemical properties, including one reversible reduction and two reversible oxidations. Chemical reduction of **2** with potassium graphite yields $[FeCrL^{iPr}]^-$ (**3**). Unlike the metal-alanes, neither **2** nor **3** binds dinitrogen. The solid-state structures for **2** and **3** demonstrate unusually short iron-chromium distances of 1.944 and 1.975 Å, which correspond to formal shortness ratios (*r*) of 0.82 and 0.83. The Mössbauer spectra of **2** and **3** exhibit extremely large quadrupole doublets of 5.92 and 5.20 mm s^{-1}, respectively, which are comparable in magnitude only to high-valent iron nitrides species with a formal triple bond. Complete active space (CAS) calculations show the presence of formal triple bonds in the dominant electronic configurations of **2** and **3**. Consideration of all contributing configurations of the wavefunction yields effective bond orders of 2.21 and 2.30, respectively. These complexes represent the first examples of isolated multiple bonds between two different first row metals.

4.2 Introduction

Multiple, covalent bonding interactions between two isolated metals were unknown just one hundred years ago, and much of the progress in understanding this phenomenon has occurred only in the last fifty years.[56] The first unambiguous identification of quadruple metal-metal bonds was by Cotton and coworkers in 1963, who concluded that the eclipsed chloride ligands in $Re_2Cl_8^{2-}$ were due to a metal-metal δ-symmetry bonding orbital.[53] Surprisingly, the first quadruple bond was synthesized substantially earlier: in 1844, Peligot prepared a chromium(II,II) tetracarboxylate complex that was misunderstood for over one hundred years and was correctly reformulated only in 1970.[56] This initial synthesis was performed under carbon dioxide, which was the only available inert atmosphere at the time, and was an early indicator as to the sensitivity metal-metal multiple bonds toward decomposition. After the initial report of δ bonding, additional publications regarding ditechnicium and dimolybdenum demonstrated the general nature of multiple metal-metal bonding.[124, 125] The systematic study of metal-metal bonds has blossomed in the last five decades, in part due to the now-routine nature of single-crystal diffraction studies in assessing solid-state structures. According to the Cambridge Crystallographic Database, every transition metal in Groups 5 through 10 has at least one species with crystallographically identified metal-metal multiple bonds. It is notable, however, that most of these examples contain two of the same metal, and generalized metal-metal interactions are overwhelmingly dominated by

homobimetallic species. Figure 4.1 shows the known bimetallic interactions for each of the first-row metals.

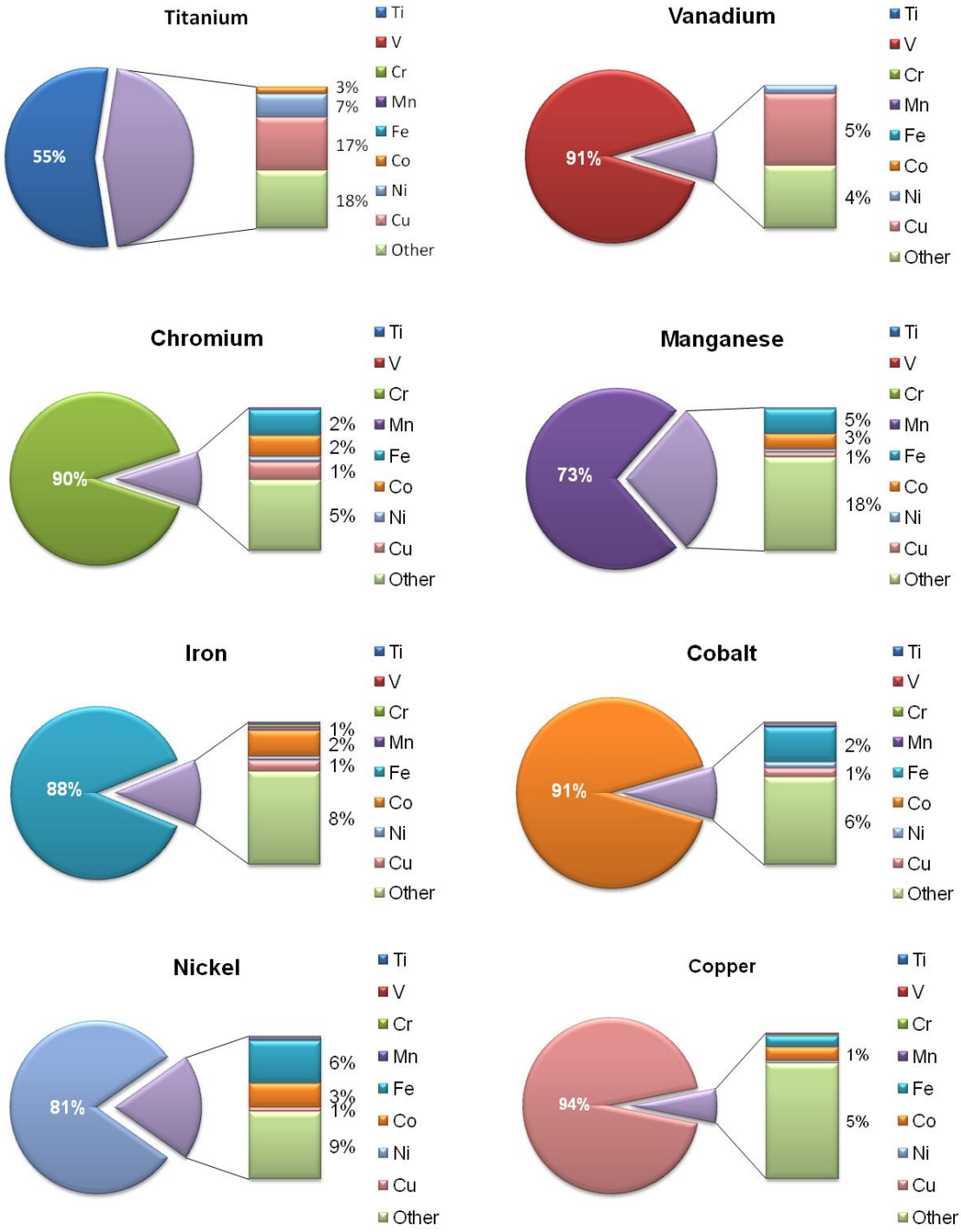

Figure 4.1 Metal-metal interactions of first-row transition metals. The inset percentage in each chart signifies homobimetallic complexes, and all heterobimetallic species are provided in the side bar. Values less than 1% are not listed. "Other" refers to 4*d* and 5*d*

metals. Data is from the Cambridge Crystallographic Database and encompasses all metal-metal interactions less than or equal to 3.0 Å.

In large part, the disparity of studies between homo- and heterobimetallic species stems from the synthetic difficulty associated with the synthesis and separation of the heterometallic complex from the homometallic species. For somewhat historical reasons, the study of metal-metal bonds often uses symmetric ligand sets such as halides, formamidinates, or diphosphines,[56, 57, 60, 66, 67, 82, 124, 126, 127-129] and these ligands are typically unable to form exclusively heterometallic complexes. In the synthesis of the MoW bisporphyrin complexes, for instance, a statistical product distribution is obtained, yielding a ratio of 1:1:2 for the Mo_2 : W_2 : MoW products.[82] Separation is obviously challenging in these circumstances, as the identical ligand environments do not provide any trivial means of separation, such as column chromatography or crystallography. The Collman group developed an elegant solution to this problem by exploiting the variation in redox potential as Mo is substituted for W, which allows separation after successive cycles of reduction and oxidation referred to as "redox titration."[82, 83, 84, 85] The successful separation of the heterobimetallic complexes is generalizable, which lead to the first example of multiple bonds between transition metals of different groups, MoRu.[85] However, this approach is only viable for 4d and 5d metal centers, and Collman notes that 3d metal porphyrins are not stable under the relevant reaction conditions.[57] Other mixed-metal syntheses, such as to yield CrMo or MoW within traditional carboxylate frameworks have had some success but have not been generalized to include bimetallic complexes of different groups.[130]

The best examples of metal-metal bonds between two different groups are arguably the so-called "early-late" heterobimetallic complexes.[94] These complexes were inspired by the strong metal-support interactions introduced in Chapter 2, and several of these complexes are worth noting.[93, 94, 131] First, Gade and coworkers prepared a variety of early-late complexes via metathesis reactions between titanium, zirconium, or hafnium halides and anionic iron, ruthenium, or cobalt salts.[102, 132, 133] Upon metathesis, unbridged and thermally stable metal-metal bonds are observed. Though the metal-metal bond is highly susceptible to homolytic cleavage in all circumstances,[94] density functional theory (DFT) calculations suggest that the bond contains both ionic and covalent character.[133] The Wolczanski lab eschewed the unbridged nature of these metal-metal bonds and used bidentate alkoxyphosphine ligands to pre-arrange the orientation of the bimetallic unit prior to reduction.[134] This approach cleanly generates a complex with a short titanium-rhodium interaction of 2.21 Å, which stood as the shortest heterobimetallic distance in the literature for over a decade. In 2009, Thomas and coworkers published a complex with strong zirconium-cobalt interactions and metal-metal distance of 2.14 Å when prepared in the absence of dinitrogen.[107, 108] These "early-late" sets have recently been complemented by a series of "mid-mid" heterobimetallic species from both our laboratory and the Thomas laboratory that possess iron-chromium and iron-vanadium bonds. As previously discussed in Chapter 2, the disparate sizes of the metal ions can be misleading when discussing absolute distances. The *r* value, defined as the observed bond distance over the sum of the metallic radii, is used to normalize the bimetallic distances

here as well as Chapter 5.[109] The structures, distances, and *r* values are provided in Figure 4.2 for several early-late and mid-mid complexes.[96, 107, 134]

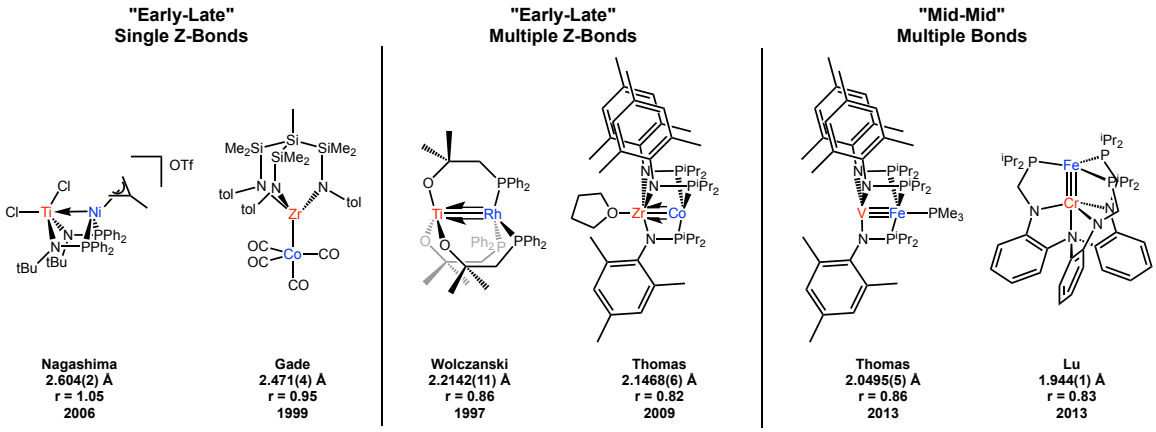

Figure 4.2 Selected examples of early-late and mid-mid heterobimetallic species

Critically, it is the inclusion of *mixed donor ligands* that allows the relatively facile synthesis of these complexes. The introduction of asymmetry into the ligand environment differentiates the two coordination environments and permits a stepwise installation of individual metal sites. It is interesting to note that even these asymmetric ligands are only κ_2 or η_2 and can easily undergo ligand rearrangement. In Thomas' chemistry, for example, typically two or three phosphinoamide ligands will bind per bimetallic unit, but it is common for the orientation of one ligand to invert the P,N coordination or for the bimetallic complex to scavenge additional phosphinoamide ligands that bind to exclusively one metal center (Figure 4.3).[135] By tethering each ligand arm to a central atom, it should be possible to eliminate this reorganization pathway and generate broad families of bimetallic complexes.

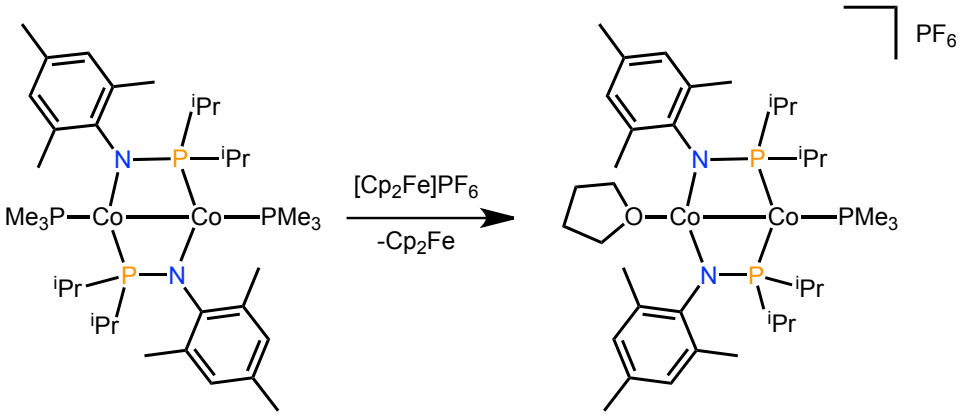

Figure 4.3 A selected example of ligand rearrangement with a η_2 phosphinoamide ligand

Generating a κ_7 ligand, as we have done here, is helpful but not requisite for the synthesis of heterobimetallic species. After publication of the work presented in this Chapter, the Thomas group showed that superficially similar iron-chromium complexes could be prepared in a tris-η_2 framework.[86, 87] However, the geometric constraints between the two ligands are quite distinct, resulting in extremely different bond manifolds.[136] The κ_7 framework here has proven ideal for generating new and unique metal-metal bonds, though, and these are the subject of the following two chapters.

4.3 Results and Discussion

The synthesis of a monometallic chromium species proceeds cleanly under similar conditions to those outlined in previous Chapters, yielding the species CrL^{iPr} (**1**) in nearly quantitative yield as a brown powder. A similar metallation procedure is utilized, wherein iron(II) bromide is added directly to CrL^{iPr} and reduced with two or three equivalents of potassium graphite (KC_8) to yield $FeCrL^{iPr}$ (**2**) or $[FeCrL^{iPr}]^-$ (**3**). The synthetic scheme to generate **1** - **3** is shown in Figure 4.4. The following sections describe the characterization data for **1** - **3**.

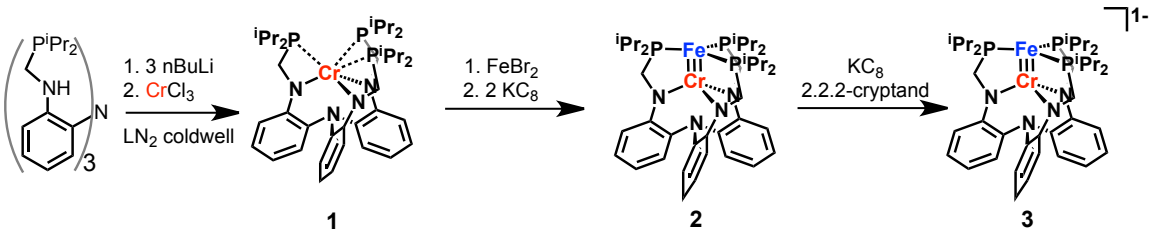

Figure 4.4 Synthesis of **2** and **3** from the monometallic chromium precursor **1**

4.3.1 Nuclear Magnetic Resonance Studies

Complexes **1** - **3** are all paramagnetic and therefore exhibit broadened NMR chemical shifts relative to diamagnetic species. Complex **1** exhibits broad resonances in the 0-6 ppm region of the spectrum in addition two flanking resonances at -19.9 and +19.2 ppm. No assignments of this spectrum are currently possible, but the most upfield and downfield resonances act as diagnostic peaks for this species. The ^{1}H NMR for **1** is shown in Figure 4.5.

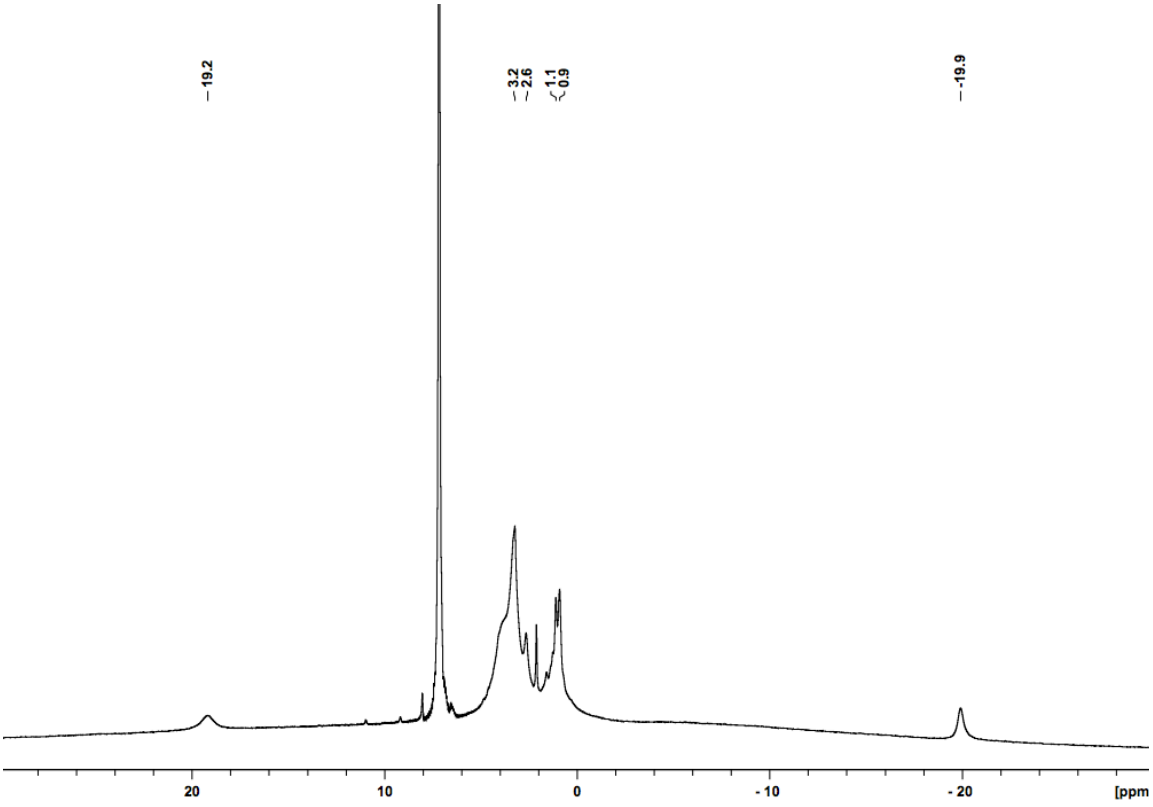

Figure 4.5 ^{1}H NMR spectrum of CrL^{iPr} (**1**) (300 MHz, C_6D_6)

Upon addition of iron(II) bromide to **1** in THF, the color changes to a dark red-brown, and the color further changes to dark green upon the addition of two equivalents of KC_8. The bimetallic species $FeCrL^{iPr}$ (**2)** is reconstituted in benzene, filtered to remove salts, and lyophilized to yield a brown powder in good yield. It is broadly soluble in standard organic solvents such as benzene, toluene, ether, and THF. No substantial changes are observed by ^{1}H NMR spectroscopy when the solvent is switched from C_6D_6 to THF-d_8. A ^{1}H NMR of **2** is shown in Figure 4.6.

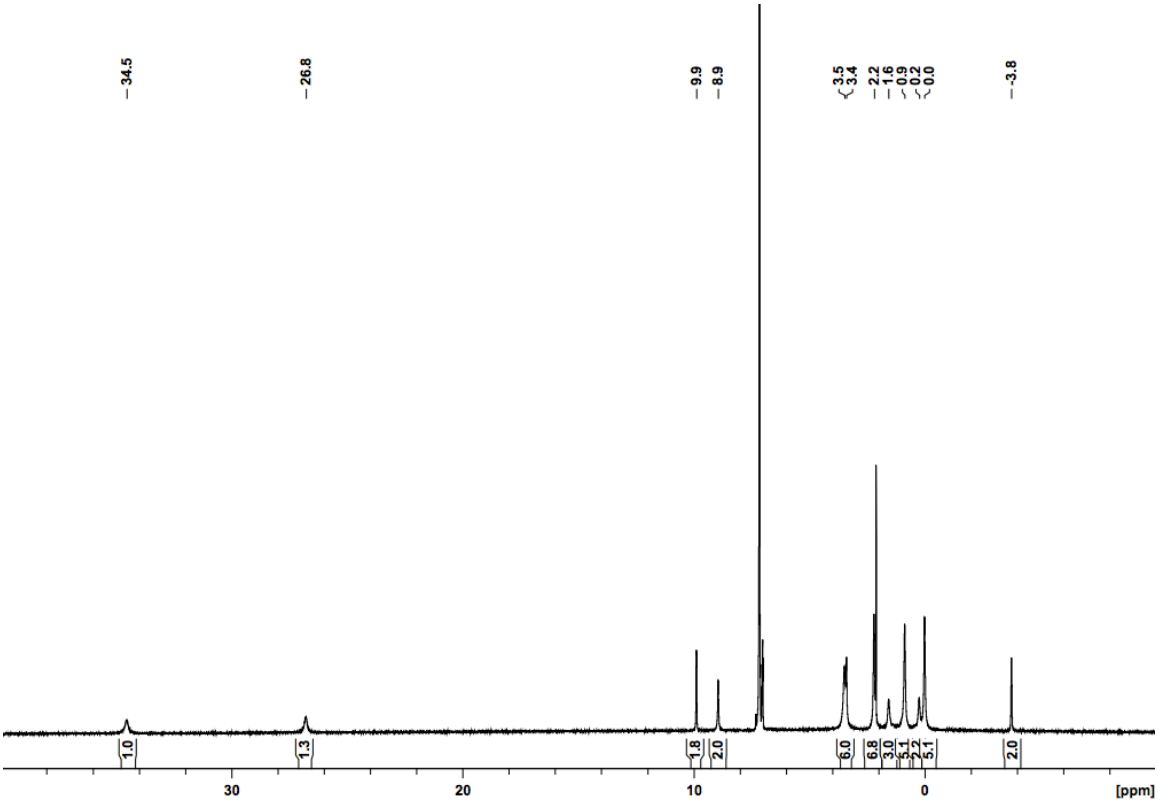

Figure 4.6 ^{1}H NMR spectrum of FeCrL^{iPr} (**2**) (500 MHz, C_6D_6)

The spectrum of **2** is only moderately paramagnetically broadened, wherein nine of the twelve peaks exist as sharp resonances between 0-10 ppm. The remaining peaks are at - 4 ppm, +27.4, and +35.2 ppm. The presence of twelve sharp peaks indicates that the molecule is conformationally locked into a C_3 geometry on the NMR timescale. The presence of 12 peaks results from the magnetic inequivalence of all four methyl groups, both methine protons, both methylene protons, and the four aryl backbone protons. On the basis of the anisotropy studies in the following chapter, the resonances at +27 and +35 ppm are believed to be the diastereotopic methylene resonances, although this assignment is tentative.

Upon addition of another equivalent of KC_8 to **2**, the green color changes to a dark red-brown, and the resulting complex $[FeCrL^{iPr}]^-$ (**3**) is isolated as a brown powder as the THF-solvated potassium salt. This complex exhibits modest solubility in Et_2O and good solubility in THF but does not yield single crystals. Attempts to metathesize **3** with PPNCl (PPN = bis(triphenylphosphine)iminium) were unsuccessful, and the presence of free triphenylphosphine in the ^{31}P NMR indicated that common metathesis reagents may react directly with **3**.

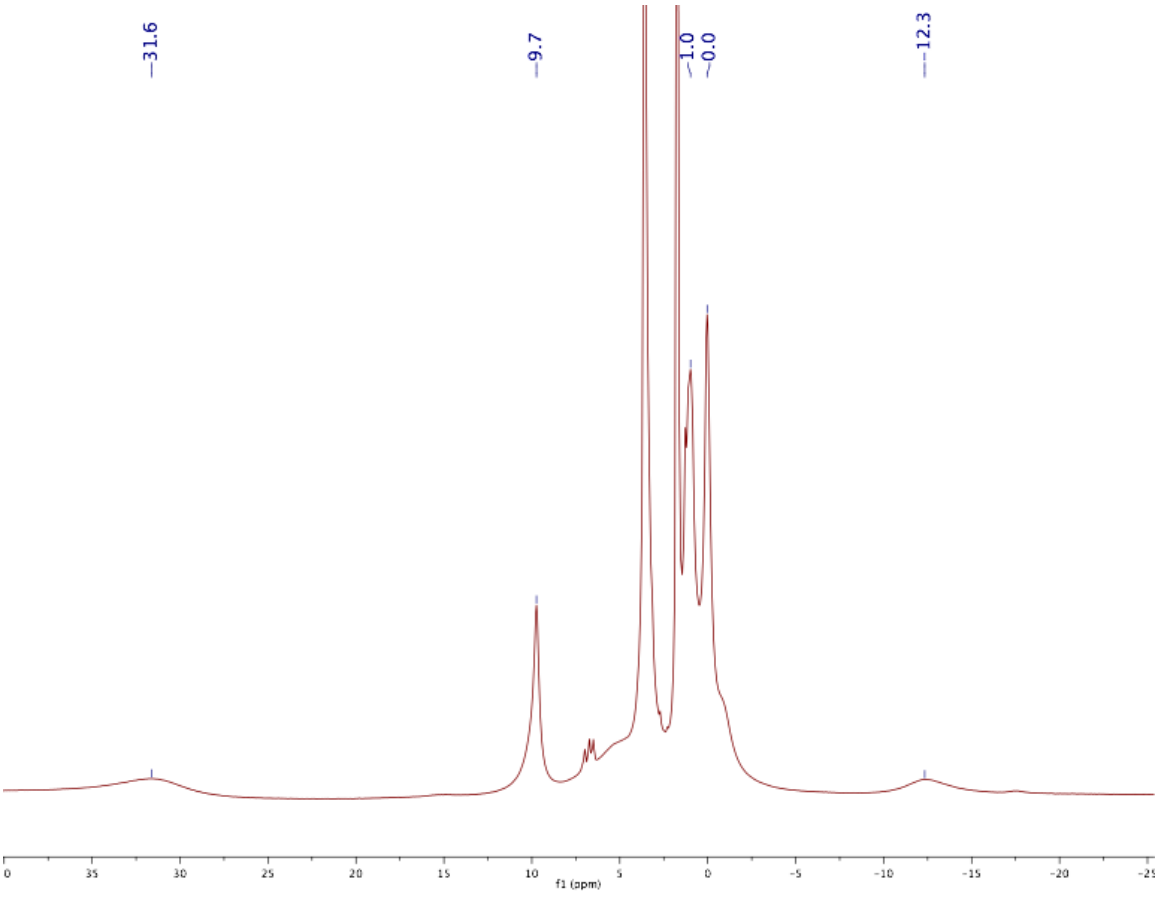

Figure 4.7 ^1H NMR spectrum of **3b** (300 MHz, THF-d_8)

The use of crown ethers was explored as one avenue to yield crystalline **3**. The 18-crown-6 (18c6) species is denoted **3a**, whereas the 2,2,2-crypt species is denoted **3b**. The encapsulated salt **3a** is tractable with respect to the generation of crystalline material, but single crystals of sufficiently high quality could not be obtained. Complex **3b** has similar solubility to **3a** but crystallizes readily from diffusion of pentane into THF. Figure 4.7 shows the ^{1}H NMR spectrum of **3b** in THF-d_8. Differences in the 1H NMR spectra between **3**, **3a**, and **3b** are essentially insignificant because the crown ether resonances are buried under broad peaks. Similar to **1**, a few broad peaks exist within the 0 - 10 ppm region, and two flanking resonances occur at -12.3 and + 31.6 ppm. Only six resonances are visible at room temperature, which is fewer than the seven expected for a solution C_{3V} symmetry.[14] Though this broadness may result from fluxional behavior, no definitive conclusions can be drawn without rigorous variable temperature NMR experiments, which were not conducted.

4.3.2 Cyclic Voltammetry Studies

The cyclic voltammetry of bimetallic complexes is not often reported, and the voltammograms for prior complexes in the literature, such as Thomas' ZrCo species,[107, 108] do not typically exhibit reversible electrochemistry. The related FeV complex, V(^{iPr}NPPh$_2$)$_3$Fe(PMe$_3$), does show a reversible oxidations at −1.26 and −0.28 V (versus

[14] Seven, eight, or twelve peaks are expected for each complex, assuming that the molecule maintains some form of C3 symmetry in solution. If the molecule maintains C3V symmetry and the P-C^{iPr} rotation is fast, seven peaks are expected as all methyl groups are averaged on the NMR timescale and the following resonances are observed: 1 CH_3, 1 CH_2, 1 CH, 4 C_{Ar}-H. If the P-C^{iPr} rotation is slow relative to the NMR timescale, eight peaks are expected due to the inequivalence of the 2 isopropyl CH_3 groups. If the molecule is locked in a C_3 conformation, then twelve resonances are expected: 4 CH_3, 1 CH_2, 1 CH, 4 C_{Ar}-H

$FeCp^{0/+}$), though these species were not prepared in an isostructural manner.[15] Similarly, the voltammogram for **2** is quite rich (Figure 4.8), and it includes both a reversible reduction and two reversible oxidations.

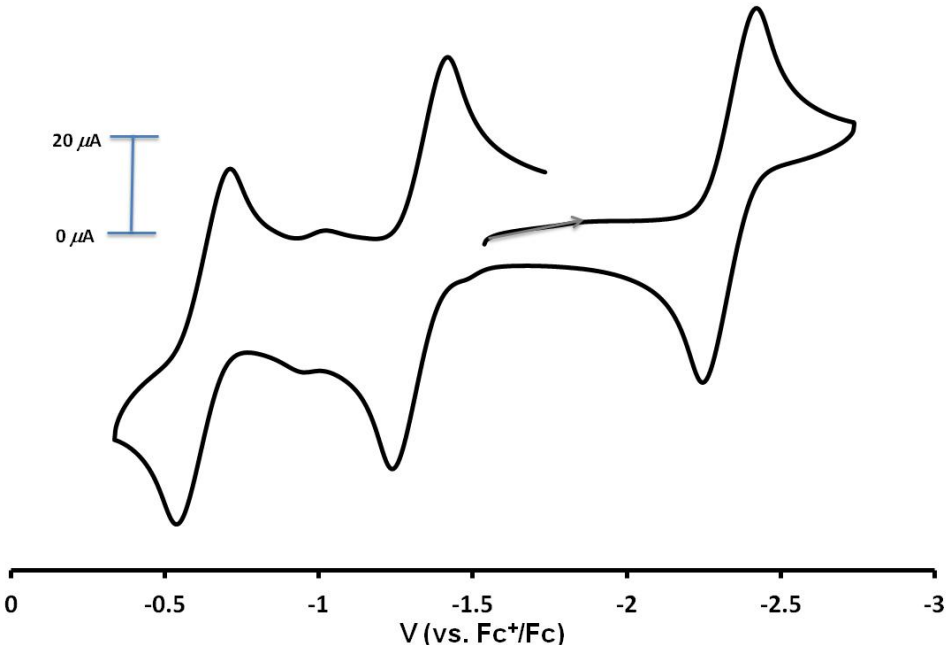

Figure 4.8 Voltammogram for **3** in THF (0.4 M $TBAPF_6$, 10 mV s^{-1})

Reduction of **2** occurs at -2.33 V versus the $Fc^{0/+}$ couple, whereas the oxidations occur at -1.32 V and -0.62 V. It is difficult to unambiguously assign the sites of redox activity, but the first reduction is tentatively assigned as a $Cr^{III/II}$ couple on the basis of Mössbauer spectroscopy, X-ray crystallography, and theoretical calculations (*vide infra*). The oxidative event at -1.32 V is established in Chapter 5 to occur at least partially at iron, and the oxidative product at -0.62 V is not stable upon chemical oxidation.

---

[15] The related $V(^{iPr}NPPh_2)_3FeBr$ was oxidized by $[FeCp_2][PF_6]$ but undergoes fluoride abstraction, yielding the dihalide complex $FV(^{iPr}NPPh_2)_3FeBr$ and preventing direct comparison.

4.3.3 Electron Paramagnetic Resonance Spectroscopy, Mössbauer Spectroscopy, and SQUID Magnetometry Studies

The spin states for **2** and **3** are of substantial interest to understanding the iron-chromium interaction. Electron paramagnetic resonance (EPR) studies can provide valuable information on half-integer spin systems. The axial EPR spectrum of **2** is identical in THF and toluene between 7 and 40 K. Below 7 K, the inverse derivative signals exhibit saturation behavior and have a significant loss in intensity. At all temperatures, the spin state is shown to be S = ½, which is consistent with a low-spin system. The g values for **2** are 1.944, 1.935, and 1.759 (g_{avg} = 1.88), which is consistent with an electron localized on chromium.[116] The EPR spectrum is broad, and no hyperfine coupling is seen to ^{52}Cr (I = 3/2, 9.5% abundance), which is the only spin-active chromium nucleus. Similarly, coupling to ^{57}Fe (I = ½, 2% abundance) is not expected nor observed. The EPR spectrum of **2** is shown in Figure 4.9.

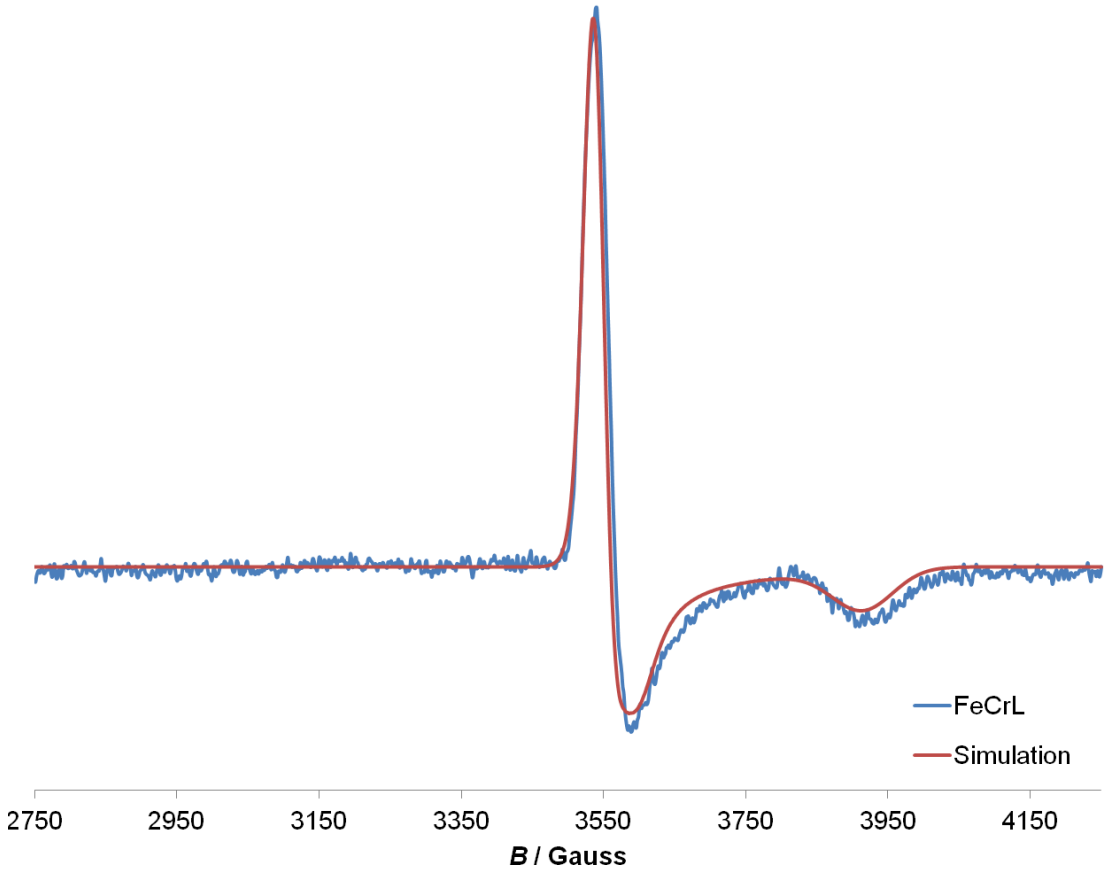

Figure 4.9 EPR spectrum of **2** in frozen toluene (9.65 GHz, 7 K). The experimental spectrum (blue) has been fitted (red) with the following values: S = ½, *g* = (1.944, 1.935, 1.759), g_{ave} = 1.88; line-widths, W = (17.50, 30.00, 50.00) Gauss. The fitting of the EPR spectrum was performed using the EPR program written by Prof. Frank Neese (version 1, 1993/1994).

SQUID magnetometry was also collected for **2**, but the observed values were consistently higher than expected (~ 2.7 μ_B), indicating an unknown impurity. Double integration of the EPR spectrum versus copper(II) nitrate found that the S = ½ signal accounts for 80% of the expected spin. The Mössbauer spectrum of **2** also displays two impurities, accounting for approximately 25% of the overall ^{57}Fe signal, suggesting that the unknown impurity involves a paramagnetic, EPR-silent iron center. Repeated efforts

to identify this impurity by NMR or UV-vis-NIR spectroscopy were unsuccessful, as no substantial variation could be identified in any spectroscopic features.

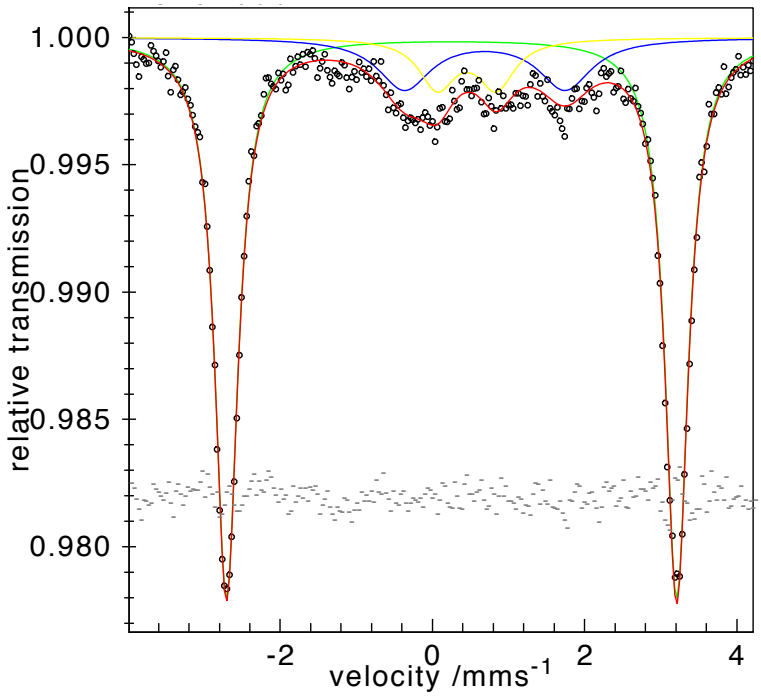

Figure 4.10 Zero-field Mössbauer spectrum of **2** at 80 K. Total data simulation (red line) of the experimental data (°) shows a major species **2** (green, see text). Two minor components were also simulated: (15.3%, blue) δ = 0.69 and ΔE_Q = 2.11 mm/s; and (10.4%, yellow)) δ = 0.45 and ΔE_Q = 0.78 mm/s.

The Mössbauer spectrum of **2** is shown in Figure 4.10, and the major component has an isomer shift (IS) of 0.25 mm s^{-1} and a quadrupole splitting (QS) of 5.92 mm s^{-1}. In Mössbauer spectroscopy, the isomer shift is defined as the midpoint between the quadrupole doublets and can allow assignment of the metal oxidation state. This assignment is possible because the isomer shift reflects the core *s* orbital electron density, which is modestly perturbed by changes in oxidation state. However, oxidation state assignments are predicated on knowing the correct range of isomer shift values, which in

turn requires a sufficient number of complexes in that oxidation state with a reasonably similar ligand environment. The isomer shift ranges for iron(II), iron(III), and iron(IV) with four to six nitrogenous ligands is well-established, but low-valent iron complexes are relatively uncommon, and the scarcity of Mössbauer spectroscopy on such species does not allow an unambiguous determination of the iron oxidation state in **2**. However, the isomer shifts are consistent with low-valent iron species published by Peters, which are also formulated as iron(0) complexes.[137]

More notably, the quadrupole splitting of 5.92 mm s^{-1} in **2** is highly anomalous. The quadrupole splitting, which is measured as the distance between the two doublets, is an indirect measurement of the asymmetry in the electronic field gradient (EFG). Relatively isotropic ligand environments will have low QS, whereas highly anisotropic environments will have substantially higher QS. Iron complexes with nitrogenous ligands typically exhibit QS values of less than 3 mm s^{-1}, and substantial variation is possible within this range. The QS is additionally affected by ligand covalency, which can assist in establishing subtle changes in the ligand environment. In the literature, values above 4 mm s^{-1} are typically exhibited by iron(IV) nitrides, which are known to exhibit quadrupole splittings of up to 6.23 mm s^{-1}.[15] These high valent iron species are found in pseudo-tetrahedral environments and are known to exist with carbene and phosphine donor sets.[14, 15, 138] Two complementary explanations for the high QS of these complexes have been proposed: Peters and coworkers have suggested that the substantial covalency of the iron-nitride triple bond polarizes the electron density along the Z axis, whereas

Smith and coworkers have emphasized the fact that these systems are low spin, and the iron non-bonding electrons are all located in d_{xy} and d_{x2-y2} orbitals.

Given that **2** is multiconfigurational and has largely filled iron-orbitals, it is tempting to attribute the large QS to a covalent FeCr interaction that is analogous to the FeN interaction. At present, the data is insufficient to determine which explanation, if either, is more appropriate. The Mössbauer spectra of **3a** and **3b** (Figures 4.11 and 4.12) are qualitatively similar to **2**, showing effectively identical IS (**2**, 0.25 mm s^{-1}; **3a**, 0.26 mm s^{-1}; **3b**, 0.29 mm s^{-1}) and similar QS (**2**, 5.92 mm s^{-1}; **3a**, 5.04 mm s^{-1}; **3b**, 5.20 mm s^{-1}). These values are overall higher than a similar FeV system recently published by Thomas and coworkers, who found relatively low quadrupole splitting.[86] In that case, the iron-vanadium bond is also longer as a result of ligand-imposed geometry constraints that prevent a shorter metal-metal bond and, presumably, higher quadrupole splitting.[136] This interpretation is corroborated by the synthesis of the iron-vanadium complex $FeVL^{iPr}$, which also possesses exceptionally large quadrupole splitting.[103]

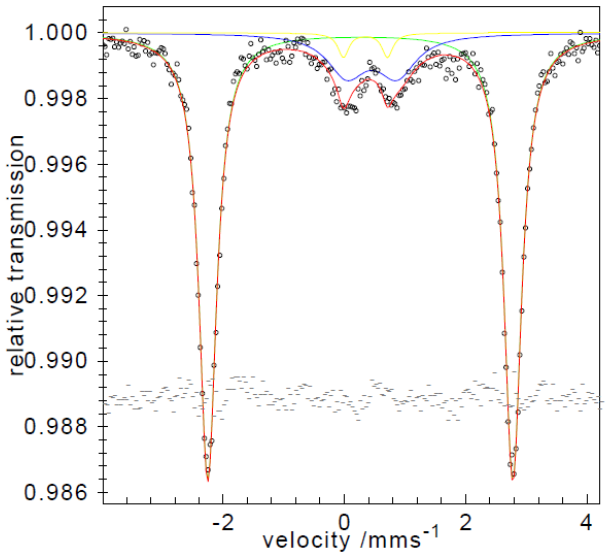

Figure 4.11 Zero-field Mössbauer spectrum of **3a** at 80 K. Total data simulation (red line) of the experimental data (°) shows a major species **3a** (81.4%, green) with $\delta = 0.26$ and $\Delta E_Q = 5.04$ mm/s. Two minor components were also simulated: (15.8%, blue) $\delta = 0.45$ and $\Delta E_Q = 0.83$ mm/s, and (2.8%, yellow) $\delta = 0.35$ and $\Delta E_Q = 0.73$ mm/s.

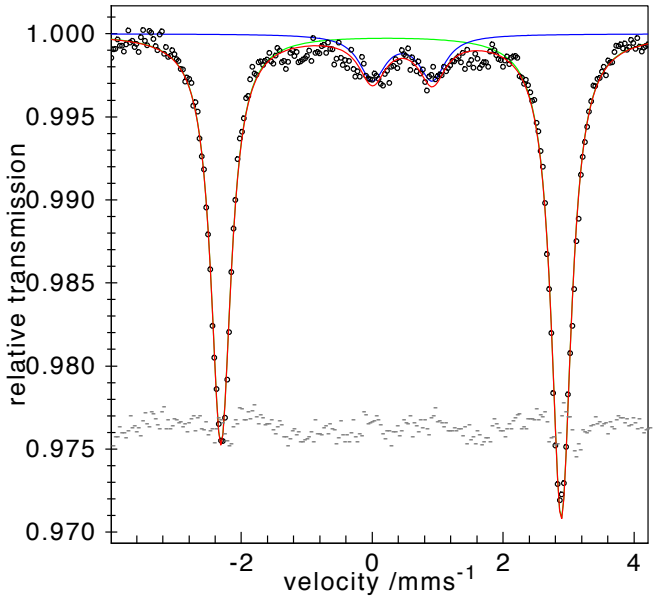

Figure 4.12 Zero-field Mössbauer spectrum of **3b** at 80 K. Total data simulation (red line) of the experimental data (°) shows a major species **3b** (88.3%, green) with $\delta = 0.29$ and $\Delta E_Q = 5.20$ mm/s. One minor component was also simulated: (11.7%, blue) $\delta = 0.46$ and $\Delta E_Q = 0.92$ mm/s.

Unlike **2**, the magnetic behavior is well-behaved and shows an energetically well-isolated triplet ground state between 20 and 290 K (Figure 4.13). The simulated *g* value, 1.91, is also consistent with a chromium-based spin. The triplet spin state is expected and in accord with the presence of paramagnetically shifted NMR and EPR-silent behavior.

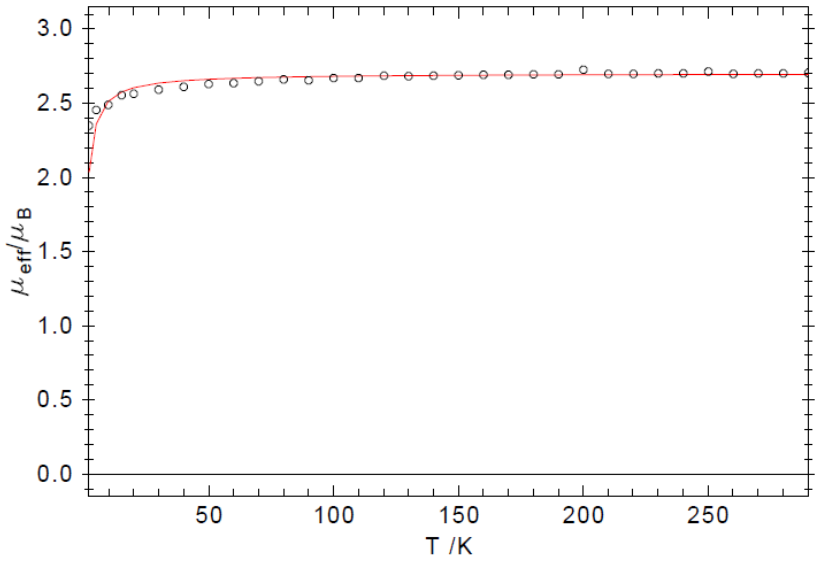

Figure 4.13 Temperature dependence of the magnetic moment, μ_{eff}, of **3a** (1 Tesla, 2.0 to 290 K). The solid lines represent the spin-Hamiltonian simulation. The parameters used for the fitting are: $S_{tot} = 1$, $g = 1.91$, theta-weiss = −1.5 K with a correction for underlying diamagnetism (calculated using tabulated Pascal's constants) of −544 x 10^{-6} cm^3/mol.

4.3.5 Single Crystal X-ray Diffraction Studies

Single crystal X-ray diffraction experiments were conducted on **2** and **3b**, though the high solubility of **1** in hydrocarbons was a substantial impediment to generating X-ray quality single crystals. Crystallographic information on **1** is provided in Chapter 5. Single crystals of both **2** and **3b** were amenable for single crystal X-ray diffraction studies. Complex **2** solves in the space group $P2_1/n$ and shows two independent molecules of **2** in the asymmetric unit. Complex **3b** solves in the space group P-3 and finds both the

cationic and anionic components on threefold symmetry axes. The metrical parameters are summarized in Table 4.2.

Most interestingly, the metal-metal bonds are quite short for both **2** and **3b**. Both metal-metal bonds are shorter than 2 Å and shorter than any crystallographically identified heterobimetallic complexes previously known. The previous record was set by the Thomas group in 2009,[107] who reported a cobalt-zirconium complex with a distance of 2.14 Å. The shorter distances in **2** and **3b** are doubtless a result of the fact that they utilize two first row metals, which are intrinsically smaller than their second and third counterparts. The ratio *r* accounts for the varying sizes of different metals and is defined as the metal-metal distance divided by the sum of the intermetallic radii of the metals. Values below unity represent a strongly bonding interaction often attributed to multiple bonding character. The *r* values of **2** and **3b** are 0.83 and 0.84, which are consistent with multiple-bonding and actually slightly larger than the 0.82 seen in Thomas' CoZr complex.

Table 4.2 Geometric parameters, including bond lengths [Å] and angles [°] for **2** and **3b**

	2 [a]	**3b**
Fe-Cr [Å]	1.943(1)	1.974(1)
	1.944(1)	
r	0.83	0.84
Fe-P [Å]	2.256(2), 2.265(1), 2.265(1)	2.244(8)
	2.266(2), 2.266(1), 2.270(2)	
Cr-$N_{equitorial}$ [Å]	1.925(3), 1.964(3), 1.990(3)	2.027(2)
	1.948(3), 1.962(3), 1.969(3)	
Cr-N_{axial} [Å]	2.275(3)	2.348(3)
	2.292(3)	
P-Fe-P [°]	118.06, 118.78, 121.37(6)	119.838(4)
	118.08, 118.34, 121.05(6)	
$N_{eq.}$-Cr-$N_{eq.}$ [°]	112.2, 116.4, 118.6(1)	113.68(5)
	113.5, 114.2, 119.3(1)	
Fe-Cr-N_{axial} [°]	176.36(7)	180
	178.71(7)	

[a] Two sets of values are given for the two unique molecules in the asymmetric unit

In section 4.3.3, the reduction of **2** to **3a** and **3b** is attributed to a chromium-based orbital on the basis of the essentially identical Mössbauer isomer shifts and low g values in both EPR and SQUID magnetometry. These findings are broadly consistent with the crystallographic results, which find a small contraction in the Fe-P distances (0.020 Å) as compared to a much larger expansion in the Cr-$N_{equatorial}$ distances (0.068 Å). The Cr-N_{axial} distance also expands (0.065 Å). The Cr therefore moves up slightly within the bimetallic pocket, and the overall metal-metal bond becomes slightly longer rather than shorter due to a concurrent movement of the iron site closer to the P_3 plane.

4.3.6 Computational Studies

To gain more insights into the electronic structure of compounds **2** and **3**, we turned to theoretical calculations using both density functional theory (DFT) and multi-

configurational quantum chemical methods (CASSCF/CASPT2). Geometry optimizations were performed at the DFT level for several possible spin states of each complex. The DFT and CASPT2 energies confirm the doublet and triplet ground states of **2** and **3**, respectively; the optimized structures of the ground states are reasonably close to the experimental structures. A qualitative MO diagram of the d-orbital manifold is shown in Figure 4.14 with the dominating electronic configurations of **2** (58 %) and **3** (60%) (CASSCF). The d-orbital manifold is comprised of delocalized σ/σ* and π/π* MOs as well as localized d_{x2-y2}/d_{xy} orbitals. No δ-bonding is evident. Though **2** and **3** each have a formal Fe-Cr bond order of 3.0 (from occupation of 1 σ + 2 π MOs), the effective bond order, which takes into account the partial occupation of the σ* and π* orbitals, is lower at 2.21 for **2** and 2.30 for **3**.

The calculated spin densities corroborate that the reduction is chromium-based in that the spin density at Cr increases by exactly one electron from **2** to **3**. For **2** and **3**, the spin-density values affirm the proposed oxidation states of Fe^0/Cr^{III} and Fe^0/Cr^{II}, respectively, with the overall spin density residing at Cr. The calculations also show that the MOs are asymmetrically delocalized over the Fe-Cr unit, as might be expected given the disparity in d-electron count between these two metals. A decomposition analysis of the MOs reveals that the d-electron count in **3** is Fe d^8 and Cr d^4, which supports the proposed oxidation states of iron(0) and chromium(II), respectively. The situation for **2** is more complicated, with the resulting electron count favoring non-integer oxidation states, namely Fe(0.5)-Cr(2.5), which may be a more accurate electronic picture for **2**.

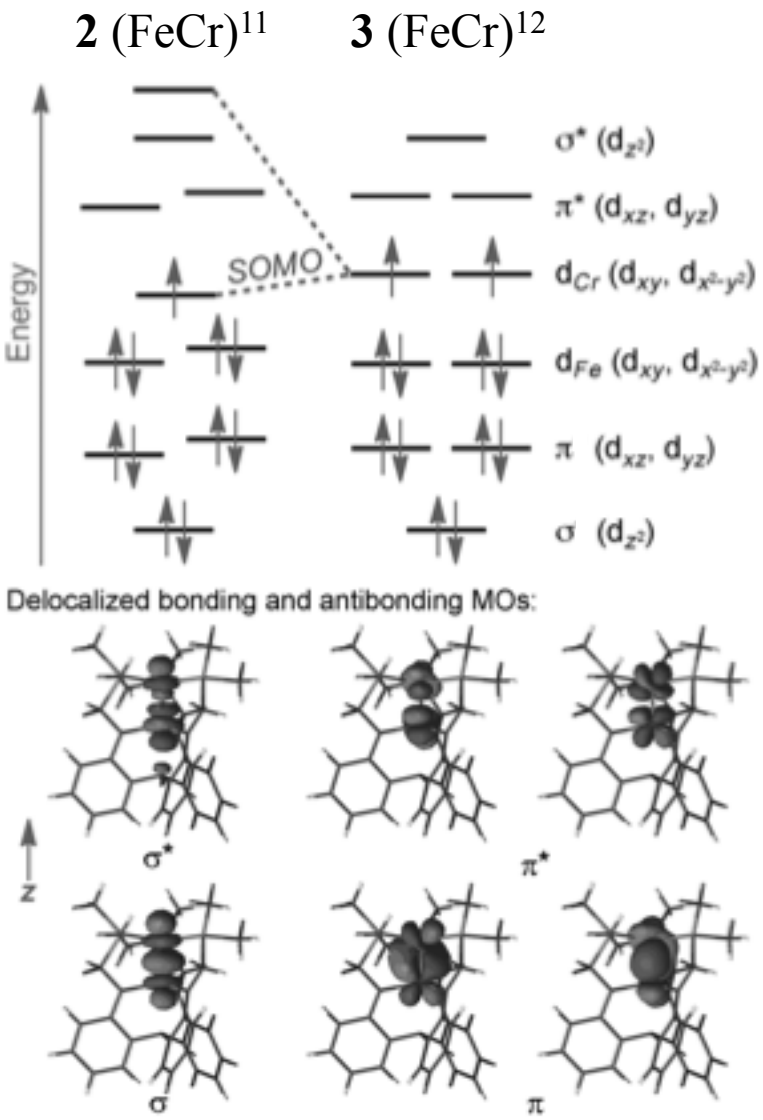

Figure 4.14 Qualitative MO diagram of the d-orbital manifold for **2** and **3**, shown with the dominant electronic configurations.

4.4 Conclusions

The heterobimetallic iron-chromium complexes **2** and **3** were prepared and represent the first isolable examples of multiple metal-metal bonds between two different first row metals. Consistent with this assignment, the iron-chromium distance is an exceptionally short 1.94 Å and the ^{57}Fe Mossbauer spectroscopy displays a large quadrupole splitting most similar to iron-nitride triple bonds. The assignment as a formal triple bond is also supported by CASSCF/PT2 calculations, which find effective bond orders of 2.21 and 2.30 for **2** and **3**, respectively.

Given the facile insertion iron, cobalt, and nickel in the metallalumatranes, we sought to generate a broad family of bimetallic complexes to better study periodic trends in heterobimetallic transition metal bonds, especially with respect to the electronic structure and rich electrochemistry of these species. The results of these studies are reported in the following chapter.

4.5 Experimental

General Considerations

Unless otherwise stated, all manipulations were performed under a dinitrogen atmosphere in an MBraun Atmosphere glovebox or using standard Schlenk techniques. Standard solvents were deoxygenated by sparging with dinitrogen and dried by passing through activated alumina columns of a SG Water solvent purification system. Deuterated solvents were purchased from Cambridge Isotope Laboratories, Inc., degassed via freeze-pump-thaw cycles, and stored over activated 4 Å molecular sieves. ^{1}H spectra were recorded on Varian 300 MHz or a Bruker 500 MHz spectrometer at ambient temperature unless otherwise stated. Elemental analyses were performed by Complete Analysis Laboratories, Inc. (Parsippany, NJ). UV-Visible spectra were collected on a Cary Bio 100; Near-IR spectra were collected on a Cary-14. Cyclic voltammetry was conducted using a CH Instruments 600 electrochemical analyzer. The one-cell setup utilized a glassy carbon working electrode, platinum wire counter electrode, and $Ag/AgNO_3$ reference electrode in acetonitrile. Analyte solutions were prepared in a THF solution of tetra-n-butylammonium hexafluorophosphate (0.1 M) and referenced internally to the $FeCp_2/FeCp_2^+$ redox couple. Infrared spectroscopy was collected on a Bruker Tensor-37 FTIR using the OPUS 6.5 software. Magnetic susceptibility data were measured from powder samples of solid material in the temperature range 2 to 300 K by using a SQUID susceptometer with a field of 1.0 T (MPMS-7, Quantum Design, calibrated with standard palladium reference sample, error <2%). The experimental data were corrected for

underlying diamagnetism by use of tabulated Pascal's constants as well as for temperature independent paramagnetism. The susceptibility and magnetization data were simulated with the program julX. X-band electron paramagnetic resonance (EPR) spectra were recorded on a Bruker E-500 spectrometer with an Oxford Instruments EPR-10 liquid-helium cryostat. Mössbauer data were recorded on an alternating constant acceleration spectrometer. The minimum experimental line width was 0.24 mm s^{-1} (full width at half-height). The sample temperature was maintained constant in an Oxford Instruments Variox or an Oxford Instruments Mössbauer-Spectromag 2000 cryostat, which is a split-pair superconducting magnet system for applied fields (up to 8 T). The field at the sample is oriented perpendicular to the γ-beam. The ^{57}Co/Rh source (1.8 GBq) was positioned at room temperature inside the gap of the magnet system at a zero-field position. Isomer shifts are quoted relative to iron metal at 300 K. Ligand N(o-C_6H_4-$NCH_2P^iPr_2)_3$] was synthesized according to literature procedures.

Synthesis of Cr[N(o-C_6H_4-$NCH_2P^iPr_2)_3$] (**1**)

Ligand N(*o*-C_6H_4-$NCH_2P^iPr_2)_3$ (0.473 g, 0.69 mmol) was dissolved in diethyl ether (c. 4 mL) and frozen in a LN_2 cold well. This solid was layered with ^{n}BuLi (0.845 mL, 2.11 mmol) and thawed to room temperature overnight. The light yellow solution was refrozen with liquid nitrogen and added while thawing to a frozen slurry of $CrCl_3$ (0.111 g, 0.70 mmol) in a 50:50 diethyl ether/THF solution (c. 4 mL total). This solution was allowed to thaw immediately and stirred for one hour. A dark brown solution with white precipitate was dried *in vacuo* and reconstituted in toluene. The solution was filtered

through a glass-fiber filter pipette, and the brown supernatant is dried *in vacuo*. A dark brown solid was isolated (0.489 g, 96%). ^{1}H NMR (ppm, C_6D_6, 300 MHz): 19.2, 3.8, 3.3, 2.7, 1.0, -20.0. Anal. Calcd for Cr[N(o-($NCH_2P(^{i}Pr)_2$)Ph)$_3$] $C_{39}H_{60}N_4P_3Cr$: 64.18 C, 8.29 H, 7.68 N. Found: 64.16 C, 8.30 H, 7.74 N.

Synthesis of FeCr[N(o-C_6H_4-$NCH_2P^{i}Pr_2)_3$] (**2**)

A solution of *Cr[N(o-($NCH_2P(^{i}Pr)_2$)Ph)$_3$]* (0.288 g, 0.36 mmol) was dissolved in THF (c. 3 mL) and mixed with a stirred slurry of iron(II) bromide (0.078 g, 0.36 mmol) in THF (c. 2 mL) for one hour. During this time a homogenous, inky brown solution formed. After one hour, a slurry of KC_8 (0.099 g, 0.73 mmol) was added in THF (c. 5 mL). Within minutes, a dark green solution formed concomitant with precipitation of KBr and C(*s*). The solution was filtered through celite in a glass-fiber filter pipette and washed with minimal THF until washings run clear. The green solution is dried *in vacuo*, yielding a black powder that is washed with minimal n-hexane until washes run clear (0.228 g, 81%). Single crystals of **3** were grown by slow evaporation from concentrated ether or benzene solutions. ^{1}H NMR (ppm, C_6D_6, 300 MHz): 35.2, 27.4, 10.0, 9.0, 3.6, 3.3, 2.2, 0.8, 0.0, -4.0. UV-VIS (in THF): (nm, ε [M^{-1} cm^{-1}]), 448 (3640); 645 (1440); 1340 (~200-240). Anal. Calcd for **1** $C_{39}H_{60}N_4P_3CrFe$: 59.62 C, 7.70 H, 7.13 N. Found: 59.53 C, 7.76 H, 7.04 N.

Synthesis of [K(18-crown-6)][FeCr(N(o-C_6H_4-$NCH_2P^{i}Pr_2)_3$)] (**2a)**

A solution of *Cr[N(o-C_6H_4-$NCH_2P^{i}Pr_2)_3$]* (0.111 g, 0.14 mmol) was dissolved in THF (c. 3 mL) and mixed with a stirred slurry of iron(II) bromide (0.030 g, 0.14 mmol) in THF

(c. 2 mL) for one hour. During this time a homogenous, inky brown solution formed. After one hour, a slurry of KC_8 (0.057 g, 0.42 mmol) was added in THF (c. 5 mL). Within minutes, a dark brown solution forms concomitant with precipitation of KBr and C(*s*). The solution was filtered through celite in a glass-fiber filter pipette and washed with minimal THF until washings run clear. A solution of 18-crown-6 (0.036 g, 0.14 mmol) is added in minimal THF, and the brown solution is dried *in vacuo*, yielding a black powder. This powder was washed with diethyl ether until washes are colorless, and the product is dried *in vacuo* to yield a dark brown powder (0.114 g, 72%). ^{1}H NMR (ppm, d_8-THF, 300 MHz): 31.6 (br), 9.7, 1.0, 0.0, -12.3. UV-VIS (THF): (nm, ε [M^{-1} cm^{-1}]): 310 (31,300); 680 (1200); 1110 (740). Anal. Calcd. for $C_{51}H_{84}CrFeKN_4O_6P_3$: 56.24 C, 7.77 H, 5.14 N. Found: 56.14 C, 7.77 H, 4.98 N.

Synthesis of 2b, [K(crypt-222)][FeCr(N(o-C_6H_4-$NCH_2P^iPr_2)_3$] (**2b**)

A solution of *Cr[N(o-C_6H_4-$NCH_2P^iPr_2)_3$]* (0.099 g, 0.12 mmol) was dissolved in THF (c. 3 mL) and mixed with a stirred slurry of iron(II) bromide (0.027 g, 0.12 mmol) in THF (c. 2 mL) for one hour. During this time a homogenous, inky brown solution formed. After one hour, a slurry of KC_8 (0.057 g, 0.42 mmol) was added in THF (c. 5 mL). Within minutes, a dark brown solution forms concomitant with precipitation of KBr and C(*s*). The solution was filtered through celite in a glass-fiber filter pipette and washed with minimal THF until washings run clear. A solution of crypt-222 (0.049 g, 0.12 mmol) is added in minimal THF, and the brown solution is dried *in vacuo*, yielding a

black powder. Single crystals were grown by layering diethyl ether on a concentrated solution and storing in a -35 °C freezer for two days.

X-Ray Crystallographic and Structure Refinement Details

A brown plate of **1** and a brown hexagonal plate of **2** were placed onto the tip of a 0.1 mm diameter glass capillary and mounted on a Bruker SMART Platform CCD diffractometer for data collection at 123(2) K for **1** and 173(2) K for **2**. The data collection was carried out using Mo Kα radiation (graphite monochromator). The data intensity was corrected for absorption and decay (SADABS). Final cell constants were obtained from least squares fits of all measured reflections. The structure was solved using SHELXS-97 and refined using SHELXL-97. A direct-methods solution was calculated which provided most non-hydrogen atoms from the E-map. Full-matrix least squares / difference Fourier cycles were performed to locate the remaining non-hydrogen atoms. All non-hydrogen atoms were refined with anisotropic displacement parameters. Hydrogen atoms were placed in ideal positions and refined as riding atoms with relative isotropic displacement parameters. Crystallographic data are summarized in Table 4.3.

Table 4.3 Crystallographic Parameters for Complexes **1** and **2b**

	2	**3b**
Chemical Formula	$C_{39}H_{60}CrFeN_4P_3$	$C_{57}H_{96}CrFeKN_6O_6P_3$
Moiety Formula	$C_{39}H_{60}CrFeN_4P_3$	$C_{39}H_{60}CrFeN_4P_3$ • $C_{18}H_{36}KN_2O_6$
Formula weight	785.67	1201.26
Crystal system	Monoclinic	Hexagonal
Space group	$P2_1/n$	P-3
a (Å)	20.009(14)	11.2611(12)
b (Å)	19.208(14)	11.2611(12)
c (Å)	22.635(16)	28.543(3)
α (deg)	90.00	90.00
β (deg)	112.916(8)	90.00
γ (deg)	90.00	120.00
Z	8	2
D_{calcd} (g cm^{-3})	1.303	1.269
λ (Å), μ (mm^{-1})	0.71073, 0.785	0.71073, 0.598
T (K)	123(2)	173(2)
θ range (deg.)	2.313 to 26.8755	1.52 to 27.47
Reflns collected	91044	12527
Unique reflns	18321	4795
Data/restraints/parameters	18321, 0, 889	4795, 0, 246
R_1, wR_2 ($I > 2\sigma(I)$)	0.0465, 0.0872	0.0405, 0.0809

Computational Details:

Theoretical calculations were carried out on the complexes using density functional theory (DFT) and the complete active space self-consistent field (CASSCF) method, followed by a multiconfigurational second-order perturbation theory (CASPT2) method. It has been demonstrated that this strategy is successful in predicting accurate results for ground and electronically excited states of bimetallic systems. No symmetry constraints were used. (*DFT*) Initial starting points for geometry optimizations were taken/derived from experimentally determined X-ray structures. Gas phase geometry optimizations were performed for the various possible spin states with the Perdew−Burke−Ernzerhof

(PBE) exchange-correlation functional. For C and H atoms, the double-ζ quality basis sets def-SV(P) was used, whereas the triple-ζ quality basis set def-TZVP was employed for N, O, and P. Additional polarized functions were introduced by using def-TZVPP for Fe and Cr. The DFT calculations were performed with the broken symmetry option (unrestricted calculations) and the resolution-of-the-identity (RI) approximation. Vibrational frequencies for the DFT-optimized structures were also computed at the same level of theory. All complexes computed had no negative frequency. Additionally, single-point calculations of the energy in solution were done with no symmetry constraints using the conductor-like screening solvation model, COSMO, as implemented in the Turbomole code, with a dielectric constant, ε = 7.58, corresponding to THF. Hyperfine parameters were calculated using the ORCA program package using the B2BLYP functional with the optimized coordinates from the DFT optimization calculations in Turbomole. For Fe atoms, the CP(PPP) basis set designed by Neese and co-workers for accurate calculations of hyperfine coupling in transition metal compounds was used. The TZVPP and TZVP basis set was applied to Cr and N while the SV(P) basis set was applied to all C and H.

CASSCF/CASPT2 Calculations. All CASSCF/CASPT2 calculations were performed with the MOLCAS-7.4 package using the DFT- optimized structures with no imposed symmetry for all possible spin states. The relativistic all-electron ANO-RCC basis sets were used for all elements. In all of these calculations, the ANO-RCC-VTZP basis set was used for the Fe and Cr, ANO-RCC-VDZP basis set was used for N and the ANO-

RCC-MB basis set was used for C and H. Scalar relativistic effects were included by using the Douglas−Kroll−Hess Hamiltonian. The two-electron integral evaluation was simplified by employing the Cholesky decomposition technique. The natural orbital occupation numbers were used for the evaluation of the effective bond order (EBO), which is calculated as the difference between the total occupancies of the bonding and antibonding molecular orbitals of the M−M bond divided by two.

CAS Choice. A complete active space was used consisting 17 electrons in 13 orbitals (17,13) for the neutral complex **1**, a similar active space of (18,13) was used for the anionic **3**. Compared to the full valence electron active space with all 3d orbitals from the metals, namely 11 electrons in 10 orbitals, we have found that the introduction of three more doubly occupied orbitals inside the active space gave rise to a better-optimized wave-function. The bigger active space gave a clear picture of the bonding and anti-bonding pairs between the two metals and corresponded to the experimental observation.

Chapter 5.

A Comparison of Isoelectronic Multiple Bonds in Chromium-M (M = Cr, Mn, Fe) Complexes

In part from:

Rudd, P.A.; Planas, N.; Carlson, R.K.; Bill, E.; Gagliardi, L.; Lu, C.C. "A Comparison of Covalent Multiple Bonds in Chromium-M (M = Cr, Mn, Fe) Complexes" *In Preparation*

and

L.J. Clouston and R.B. Siedschlag; Rudd, P.A.; Planas, N.; Hu, S.; Miller, A.D.; Gagliardi, L; Lu, C.C. "Systematic Variation of Metal-Metal Bond Order in Metal-Chromium Complexes" *J. Am. Chem. Soc.,* **2013**, *135*, 13142–13148.

5.1 Overview

The monometallic species Cr[N(*o*-($NCH_2P(^iPr)_2$)C_6H_4)$_3$] (**1**, CrL) is metallated with chromium (**2**), manganese (**3**), and iron (**4**) to generate a family of bimetallic complexes $[MCrL]^{1+,0,1-}$, that can each be isolated in at least two redox states. The solid-state structures were collected for all species and display essentially isostructural environments with extremely short metal-metal bonds between 1.74 – 1.97 Å. The formal shortness ratios (*r*) of these complexes are between 0.84 and 0.74 and are interpreted as triple to quintuple metal-metal bonds. On the basis of MCr distances and theoretical calculations, the strength of the bimetallic bond increases Fe < Mn < Cr.

The isoelectronic $(d\text{-}d)^{10}$ species contain ten *d* electrons and are $S = 0$ diamagnets, allowing thorough ^{1}H NMR spectroscopic investigations. Variable temperature ^{1}H NMR spectra indicate that the interconversions between C_3 symmetries are facile and have barriers between 12.8 and 13.4 kcal mol^{-1}. The room temperature ^{1}H NMR spectra also have methylene resonances that are shifted 2-3 ppm downfield relative to free ligand. This shift is due to the diamagnetic anisotropy of the metal-metal bond, which is calculated as −3630, −4310, and −5620 10^{-36} m^3 molecule^{-1} for Cr, Mn, and Fe respectively. The strength of the diamagnetic anisotropy is therefore related to the bond polarity, not bond order. Resonance Raman studies were undertaken to quantitatively analyze the bond strengths as a function of the bimetallic vibrational frequency; only the $(d\text{-}d)^{10}$ dichromium exhibited resonance enhancement, and the bimetallic stretch is assigned as occurring at 502 cm^{-1}.

5.2 Introduction

Multiple metal-metal bonds between different first-row metals were first reported in 2013.[71] Our report of two iron-chromium complexes with formal triple bonds was followed by the analogous synthesis of the cobalt-chromium and manganese-chromium complexes, which contain double and quintuple bonds, respectively.[78] Only two months after our report on iron-chromium complexes, the Thomas group reported on iron-vanadium phosphinoamide complexes with formal triple bonds.[86] By early 2014, the Thomas group also reported double bonds for iron-chromium complexes in the same ligand framework.[87] Including the different redox states of the bimetallic units, seven new species with multiple bonds between different first row metals were reported in the last year. Five of these contained iron and are shown in Figure 5.1. Critically, these complexes are synthetically viable because they can be metallated in a stepwise fashion, allowing for a site-specific installation of each metal center.

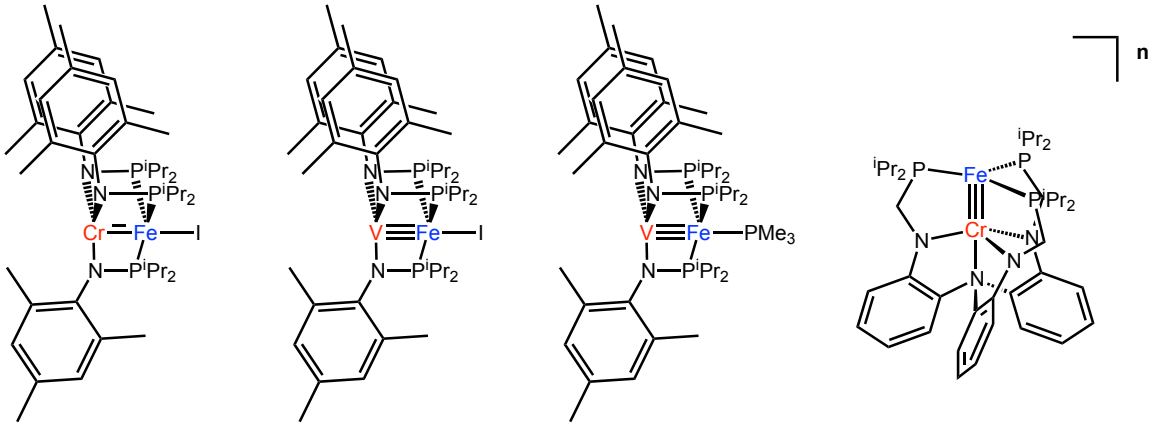

Figure 5.1 First-row heterobimetallic complexes with multiple bonds prior to this work

Both our lab and the Thomas laboratory have been successful in preparing heterobimetallic multiple bonds only with mixed amide-phosphine ligand sets.[xvi] The chief benefit of these frameworks is the ability to control the position of each metal by virtue of the metallation order, and work from our laboratory has demonstrated that the metal purity at each site is excellent.[69, 139] With respect to the preparation of multiple bonds, the metal choice is highly relevant. Mid-first row metals are excellent choices for several reasons: their intermediate *d*-electron count is valuable, as they have a sufficient number of electrons to populate multiple bonding orbitals but not so many as to necessarily begin populating anti-bonding orbitals. Additionally, the ionic charges on each metal center can minimized, which reduces electrostatic repulsion between the two metal ions as well as preventing contraction of the *d* orbitals.[58] Because δ bonds are intrinsically weak, the effects of charge and *d*-orbital overlap can be important and have been shown to exert influence comparable to that of a δ bond.[56]

Interestingly, the reduction chemistry of metal-metal bonds multiple bonds is poorly understood in the literature. The most thoroughly studied examples of metal-metal bonds are in the tetragonal framework, and these complexes have well established $(M_2)^{n+}$ cores (n = 4, 5, 6) that can be readily prepared in multiple oxidation states.[56] Instances of $(M_2)^{n+}$ cores where n = 3 or less are rare and were first prepared in trigonal systems with Fe_2 and Co_2 complexes.[73] Additional examples are now available for Cr_2,[67, 140] V_2,[141]

[xvi] Though different ligands are viable in principle, related work in our laboratory with amidinate and amide-pyridine donor sets has been shown to primarily stabilize ferromagnetic coupling and high spin states.

Mo_2,[66] FeV,[86, 103] MnCr,[78] FeCr,[71] and CoCr,[78] but the redox chemistry of these complexes is largely unexplored. The rich electrochemistry of our iron-chromium complex, $FeCr(N(o\text{-}C_6H_4\text{-}NCH_2P^iPr_2)_3)$, was demonstrated in the preceding chapter and suggested that both oxidative and reductive chemistry was possible in this ligand framework. As such, we endeavored to synthesize several first-row MCr species (M = Cr, Mn, Fe, Co, Ni) and their accessible redox states in order to quantitate the differences between isoelectronic bimetallic species, especially with respect to the electronic configuration. The results for Cr_2, MnCr, and FeCr are discussed in the following sections. The cobalt and nickel species (and their corresponding redox members) were prepared by other students and will not be discussed further.

5.3 Results and Discussion

5.3.1 Synthesis and Cyclic Voltammetry

Addition of chromium(III) chloride to the monometallic chromium complex (**1**, CrL) and three equiv. of KC_8 generated the red-brown, dichromium complex (**2**, Cr_2L) (Scheme 5.1, left). The cyclic voltammograms (CV) of dichromium **2**, manganese−chromium (**3**, MnCrL), and iron−chromium (**4**, FeCrL) are shown in Figure 5.2, and the redox potentials are given in Table 5.1. Complex **2** exhibits two reversible, one-electron transfer processes: an oxidation at −1.60 V and a reduction at −2.27 V (vs. $FeCp_2/FeCp_2^+$). Presumably, reduction of **2** generates a $(Cr_2)^{10}$ species that is isoelectronic to diamagnetic **3**. Notably, the **2**/**2**$^{\mathbf{red}}$ redox couple is close to the reduction potential of **4** (−2.33 V), which was assigned as a Cr(III)/Cr(II) redox-couple based on the similar Mössbauer isomer shifts of **4** and its one-electron reduced counterpart, **4**$^{\mathbf{red}}$.[71] The CV of **3** exhibits two reductions, the second of which is reversible only at fast scan speeds (≥250 mV/s). As noted in Chapter 4, the voltammogram of **4** has a reductive couple as well as two oxidative couples. Collectively, the CVs intimate the possibility of characterizing several redox members (see Key), including an isoelectronic $(d\text{-}d)^{10}$ subseries that comprises $[Cr_2L]^-$, MnCrL, and $[FeCrL]^+$. The $(d\text{-}d)^n$ notation refers to the total *d* electron count across both metal sites.

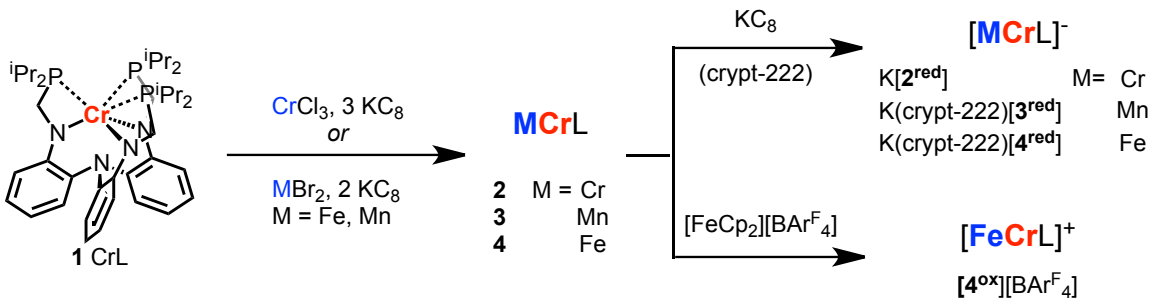

Scheme 5.1 From complex **1** (left), the syntheses of: neutral metal-chromium complexes **2** – **4** (center) and their reduced and/or oxidized counterparts (right).

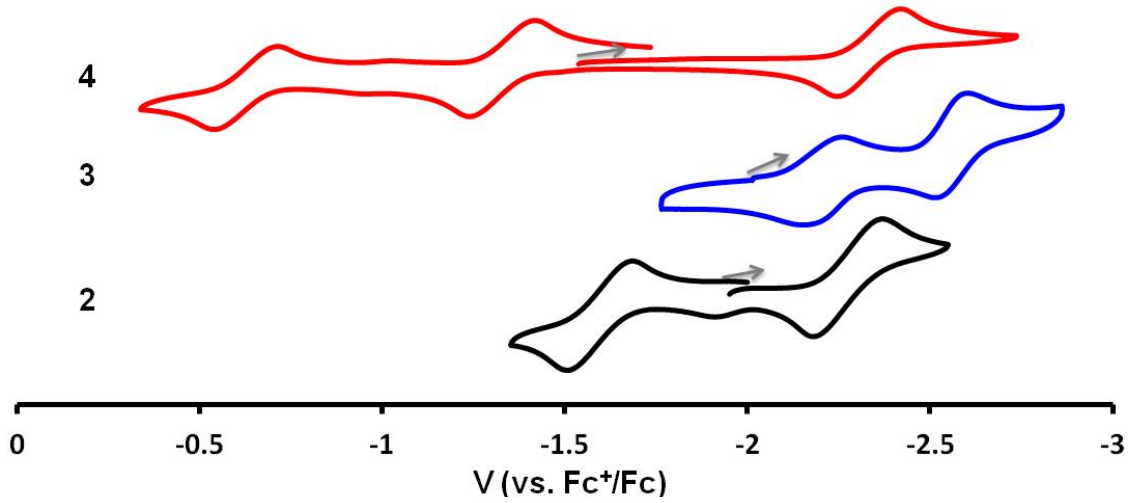

Figure 5.2 Cyclic voltammograms of **2** – **4** in [*n*Bu$_4$N]PF$_6$ THF (vs. FeCp$_2^{0/+}$). Scan rates and electrolyte concentrations for: **2**, 100 mV/s, 0.4 M; **3,** 250 mV/s, 0.4 M; and **4**, 10 mV/s, 0.1 M.

Table 5.1. Redox Potentials (V)[a] of **2** − **4**

Complex	Reduction ($E°'$)	Oxidation ($E°'$)
2	−2.27	−1.60
3	−2.21, −2.55[b]	−1.18[c]
4	−2.33	−1.32, −0.62

[a]vs. FeCp$_2^{0/+}$ [b] quasi-reversible [c] irreversible, E_{pa} reported

The reduction of **4** was previously achieved using one equiv. KC$_8$ in THF,[71] and this simple procedure proved general for reducing **2** and **3** to their reduced analogues, **2**^{red}

and $\mathbf{3}^{red}$, respectively (Scheme 5.1). In THF, the color of $\mathbf{2}^{red}$ is forest-green, whereas $\mathbf{3}^{red}$ and $\mathbf{4}^{red}$ are red-brown. One equivalent of 2.2.2-cryptand (crypt-222) was added to solutions of $\mathbf{3}^{red}$ or $\mathbf{4}^{red}$ to improve the crystallinity of the salt product, which was unnecessary for $\mathbf{2}^{red}$ (*vide infra*). Oxidation of **4** was effected smoothly using $[FeCp_2][BAr^F{}_4]$. The presence of the $BAr^F{}_4$ counter-ion renders $\mathbf{4}^{ox}$ highly soluble even in hydrocarbon solvents such as benzene. So far, efforts to isolate the dicationic species $(FeCr)^9$ have been unsuccessful.

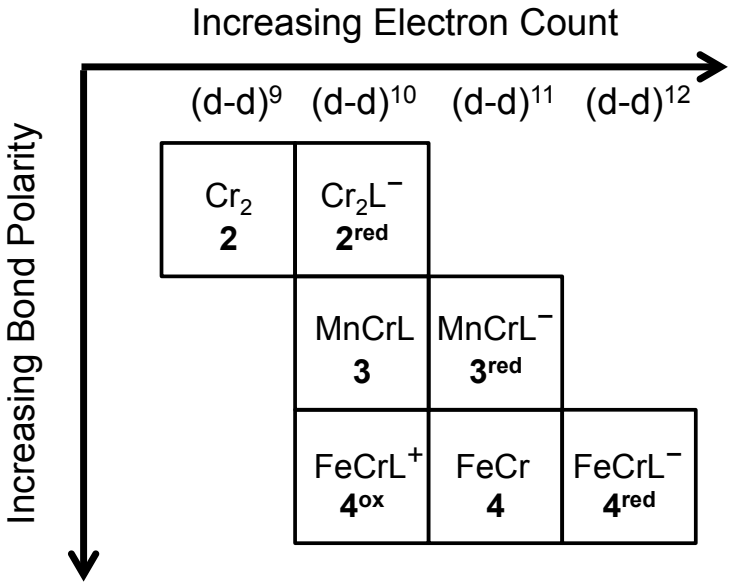

Key. Metal-chromium complexes and their $(d\text{-}d)^n$ counts. White boxes represent new compounds. Previously reported complexes are shown in light gray boxes.

5.3.2 Nuclear Magnetic Resonance and Electron Paramagnetic Resonance Studies

On the NMR timescale, the solution-state symmetry of M_2L complexes can correspond to C_3 or C_{3v}. The C_3 symmetric structure corresponds to a "locked" conformation where the methylene protons are diastereotopic, and the isopropyl groups

are distinct, giving rise to two unique methine protons and four methyl groups. Hence, the observation of 12 resonances is consistent with C_3 solution symmetry. Fast conversion between "locked" conformations would yield a time-averaged C_{3v} structure with 8 resonances, where methyl groups orient "up" or "down". If rotation of the P-C(isopropyl) bonds is also fast relative to the NMR timescale, then only 7 unique peaks are expected.

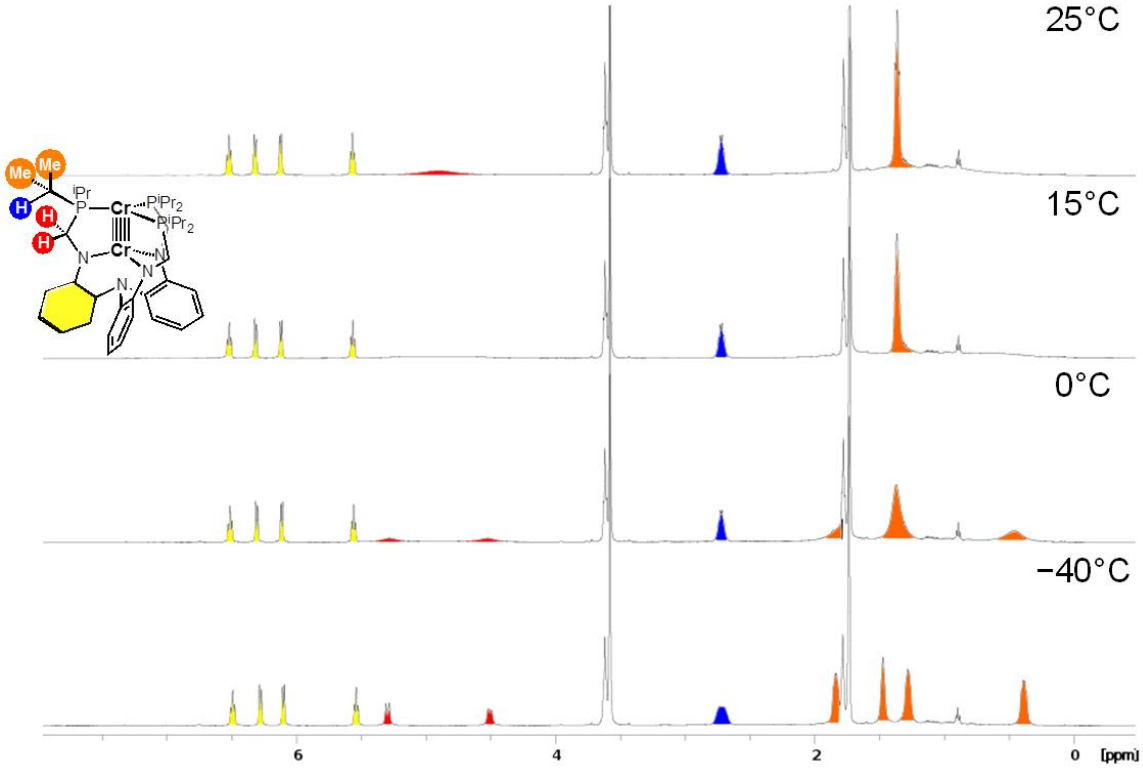

Figure 5.3 Stacked plot of variable temperature ^{1}H NMR spectra for K[**2**$^{\mathbf{red}}$] (THF−d_8, 500 MHz). Assignments are indicated by the inset color figure. For clarity, only one ligand arm is labeled.

The ^{1}H NMR spectra of the three $(d\text{-}d)^{10}$ species, $\mathbf{2}^{\mathbf{red}}$, **3**, and $\mathbf{4}^{\mathbf{ox}}$ are diamagnetic, allowing for additional comparisons. At rt, each complex exhibits C_{3V} symmetry with one sharp methyl resonance, although the methylene peak is substantially broadened. These complexes all display fluxional behavior as evidenced by the strongly temperature dependent ^{1}H NMR spectra between rt and –80°C. While the ^{31}P spectra contain only one resonance, as expected, they are largely temperature *independent* (vide infra). The coalescence of the methylene resonances of $\mathbf{2}^{\mathbf{red}}$ is observed at 15°C, as shown in Figure 5.3. At –40°C, the locked C_3 geometry is evident by the four magnetically inequivalent methyl groups and the diastereotopic methylene resonances (which are slightly overlapping). Analysis of the methylene coalescence allows for calculating the barrier of the fluxional process, and similar barrier energies are determined for $\mathbf{2}^{\mathbf{red}}$, **3**, and $\mathbf{4}^{\mathbf{ox}}$. The barrier, $\Delta G^{\ddagger}$, is calculated to be 12.9, 12.8, and 13.4 kcal mol^{-1} for $\mathbf{2}^{\mathbf{red}}$, **3**, and $\mathbf{4}^{\mathbf{ox}}$, respectively. There are two potential mechanisms for the observed fluxionality: (1) phosphine dissociation followed by rotation and re-association, or (2) a simple twisting of the methylene backbone while the phosphine arms remain associated. A series of metallaboratrane complexes have been isolated using the tri(diisopropylphosphino)borane ligand (TPB) and various metals, such as Ni, Pd, Pt, CuCl, AgCl, AuCl, and Au. The diisopropyl groups in the metallaboratrane complexes exhibit a similar fluxional behavior with energy barriers as low as 14.7 and as high as ~17.4 kcal mol^{-1}.[142] The interconversion between the "locked" C_3 geometries was proposed to involve dissociation of one phosphine arm. The twisting mechanism was

discounted on the basis that a C_{3v} intermediate structure did not converge in DFT calculations. Since the lower energy barriers appeared to correlate with stronger metal−borane interactions, the latter were suggested to directly affect phosphine lability, *i.e.*, stronger M-B interactions weaken M-P bonds and thereby increase phosphine lability. However, as the metals are all different in this study, this interpretation is complicated by the fact that phosphine lability should also change as a function of the metal.

The metal-chromium complexes here show lower energy barriers than do the metallaboratranes. This finding may be consistent with the proposal that stronger metal-chromium bonds lead to more labile phosphines. However, the barriers measured for $\mathbf{2^{red}}$, **3**, and $\mathbf{4^{ox}}$ are surprisingly similar ($\Delta \leq 0.6$ kcal/mol) considering their differences in M-Cr bonding (*vide infra*). More tellingly, the ^{31}P peaks remain essentially unchanged with variable temperature. For example, from rt to −60 °C, the ^{31}P peak for $\mathbf{2^{red}}$ only shifts from 40.8 to 42.1 ppm, and its full-width at half height varies from 6 to 8 Hz (Figure 5.4). For these reasons, we favor the twist mechanism in our metal-chromium complexes, where M-P bonds remain intact during the interconversion process.[xvii]

[xvii] To determine whether the ligand played a substantial role, the barrier of the previously reported inverse−dative Ni→Al complexwas determined to be >16.4 kcal mol^{-1}, which is sufficiently similar to NiTPB (>17.3 kcal mol^{-1}) that intrinsic ligand effects are unlikely to account for the disparity.

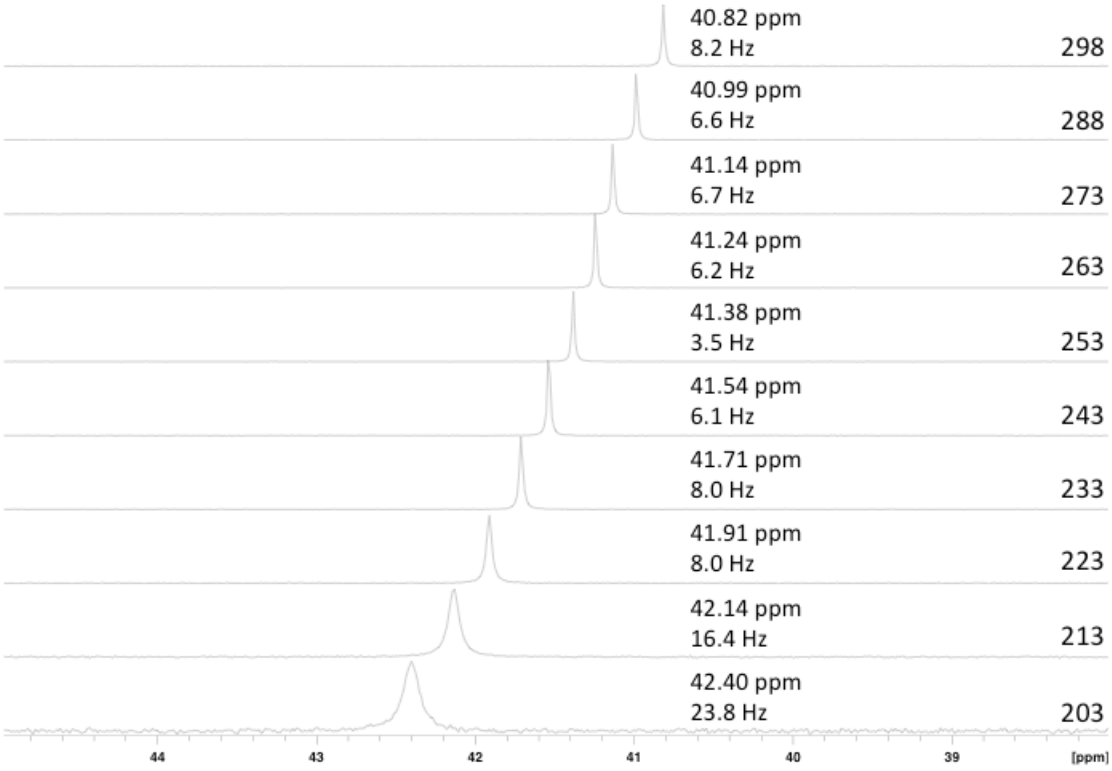

Figure 5.4 Full variable temperature ^{31}P profile of **2**^{red} (THF-d_8, 500 MHz). The peak position and peak width at half height are provided at each temperature (K).

The ^{1}H NMR spectrum of **2** is paramagnetic and displays 12 resonances, suggesting that it is locked in a C_3 environment on the NMR timescale. The S = ½ spin state was confirmed by EPR spectroscopy (Figure 5.6). The red-brown **3**^{red} is also a paramagnetic S = ½ species (Figure 5.5), though the EPR spectrum appears to contain a substantial Cr_2L contaminant that was not observed in the ^{1}H NMR spectrum. A pure EPR spectrum of **3**^{red} has not yet been obtained, but hyperfine coupling consistent with ^{55}Mn appears to be approximately 10 G. The 11 observed resonances by ^{1}H NMR spectroscopy for **3**^{red} are also consistent with C_3 symmetry. Of note, the paramagnetic ^{1}H NMR spectrum of **3**^{red} is highly similar to that of the isoelectronic iron-chromium **4**

(Figure 5.5). The most deshielded resonances in **4** can reasonably be ascribed to the methylene position, consistent with the higher diamagnetic anisotropy of iron relative to manganese (*vide infra*).

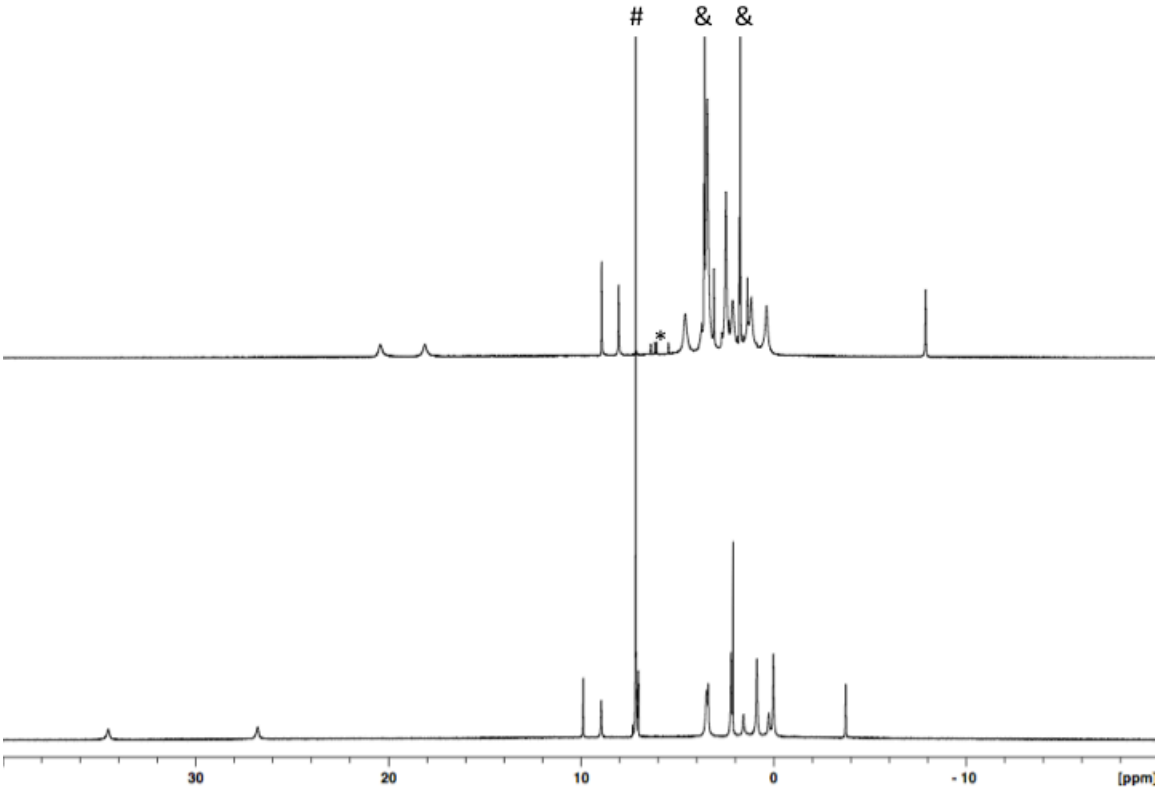

Figure 5.5 Comparison of ^{1}H NMR spectra for $\mathbf{3}^{\mathbf{red}}$ (top, 500 MHz, THF-d_8) and **4** (bottom, 500 MHz, C_6D_6). A minor diamagnetic impurity of **3** is present in $\mathbf{3}^{\mathbf{red}}$ and is denoted with *. The NMR solvent residuals are marked with # (C_6D_6) and & (THF-d_8). The spectrum for **4** is unchanged in THF-d_8 versus C_6D_6.

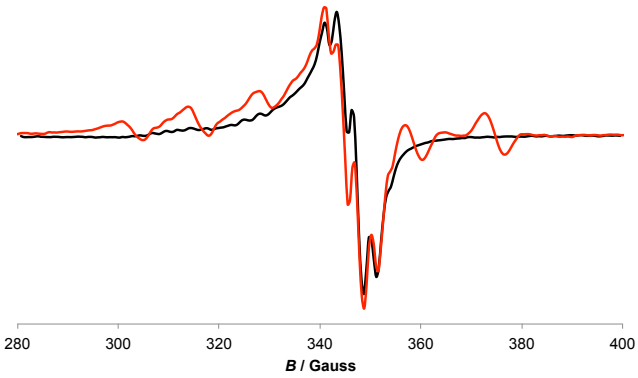

Figure 5.6 Overlaid EPR spectra of **2** (black) and **3**^{red} (red) in THF (1 mM, 20K, 9.65 GHz, power 0.2 mW).

5.3.3 Single Crystal X-ray Diffraction Studies

Single crystal X−ray diffraction studies of complexes **1**, **2**, **2**^{red}, **3**^{red}, and **4**^{ox} provided the solid−state structures shown in Figure 5.7, with their relevant geometric parameters in Table 4. For comparison, the previously reported compounds **3** and **4** are also included in Table 5.2. All the complexes are essentially three−fold symmetric and have a highly conserved coordination geometry. As anticipated based on our previous work, **1**, **2**, **2**^{red}, **3**, **3**^{red}, and **4**^{ox} all have ultra-short metal-metal bonds (<2.0 Å), suggesting multiply bonded metal atoms. The dichromium complex **2**^{red} has the shortest metal−metal bond distance in the series of 1.7407(6) Å and possesses one of the shortest dichromium distances in the literature (Table 5.3).[59, 62, 65, 67, 74, 140, 143, 144, 145] Complex **2**^{red} is isoelectronic with MnCrL **3**, which was previously determined to have a quintuple bond. The Cr-Cr bond distance in **2** is longer at 1.913(1) Å, which is consistent with a wide range of dichromium complexes with formal quadruple bonds. The metal-metal bond contracts substantially between $\{Cr_2\}^9$ **2** and $\{Cr_2\}^{10}$ **2**^{red} (Δ = −0.173 Å), which is

over twice the difference between an analogous redox pair, $[Cr_2(ArNC(H)NAr)_3]^{0/1-}$ (Δ = −0.077 Å, Ar = 2,6-$(CH_3)_2C_6H_3$). One potential reason for the relatively long Cr-Cr interaction in **2** versus $\mathbf{2}^{red}$ is the variable strength of the Cr-N_{apical} interaction, which lengthens appreciably upon reduction (Δ = 0.15 Å). The presence of axial donors is well known to elongate Cr-Cr multiple bonds, and σ donors can account for changes of 0.12 Å.[75, 146] Reduction of **2** to $\mathbf{2}^{red}$ induces contraction of Cr−P and elongation of Cr−N_{eq} bond distances by 0.036 and 0.097 Å, respectively. The greater change in the Cr−N_{eq} bond distances may suggest a more localized reduction at the Cr site in the amide-binding pocket.

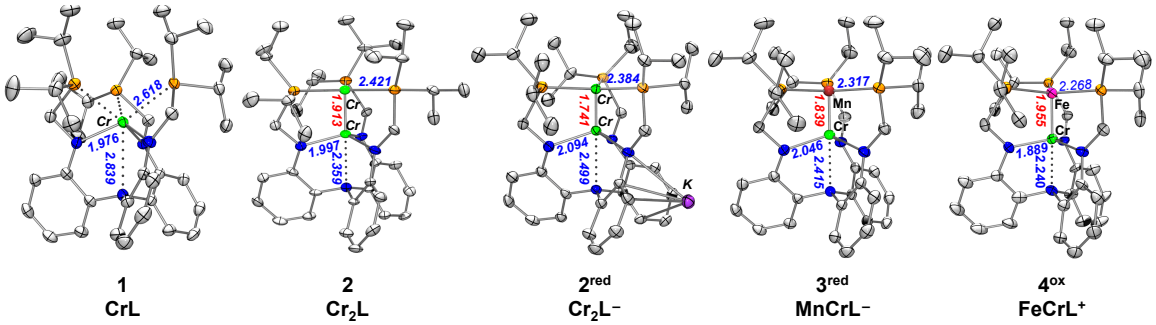

Figure 5.7 Solid−state structures of **1**, **2**, $\mathbf{2}^{red}$, $\mathbf{3}^{red}$, and $\mathbf{4}^{ox}$ by X−ray crystallography at 173 K. Thermal ellipsoids are shown at 50% probability. Hydrogen atoms and lattice solvent molecules have been omitted for clarity. Green, chromium; red, manganese; pink, iron; blue, nitrogen; yellow, phosphorous. M−Cr bond distances are given in red, and average M−P and Cr−N bond distances are given in blue.

Table 5.2 Geometrical parameters, including bond lengths (Å) and angles (°) for **2** – **4**.[a]

	2	**2^{red}**	**3**	**3^{red}**	**4**	**4^{ox}**
M−Cr (Å)	1.913(1)	1.7407(6)	1.819(2)	1.8392(7)	1.944(1)	1.955(7)
r^b	0.82	0.74	0.77	0.81	0.83	0.84
M–P (Å)	2.421(2)	2.3844(9) ± 0.004	2.379(1)	2.3170(6)	2.265(2) ± 0.004	2.268(8) ± 0.014
Cr −N_{eq} (Å)	1.997(5)	2.094(2) ± 0.014	2.021(3)	2.0467(17)	1.960(3) ± 0.019	1.889(8) ± 0.011
Cr−N_{ap} (Å)	2.359(5)	2.499	2.366(6)	2.415(3)	2.284(3)	2.240(9)
M to P_3−plane (Å)	−0.132	−0.203	−0.188	−0.174	−0.192	−0.270
Cr to N_3−plane(Å)	+0.447	+0.654	+0.498	+0.558	+ 0.412	+0.329
Σ (P−M−P) (°)	359.07	357.84	358.14	358.38	359.89(6)	355.79
Σ (N−Cr−N) (°)	345.33	331.58	342.42	338.61	349.1(2)	351.11
M−Cr−N_{ap} (°)	179.96	179.85	180	180	177.53(7)	178.08

[a] With the exception of **2^{red}**, **4**, and **4^{ox}**, the solid−state structures have approximate three−fold symmetry, so several parameters (e.g. M−P bond lengths) represent the average of three (**2^{red}**) or six (**4**) distinct values. Estimated standard deviations (esd) are provided in parentheses, and standard deviations of averages are shown with ± after the average value. [b] *r* = ratio of M−Cr bond distance to the sum of M and Cr single−bond metallic radii.[109]

Upon reduction of the {MnCr}^{10} **3** to {MnCr}^{11} **3^{red}**, the metal-metal bond lengthens slightly from 1.819(2) to 1.8392(7) Å, as expected. The latter distance is still ultrashort, reflecting a formal bond order (FBO) of 4.5. Among heterometallic complexes, the shortest metal-metal bonds are currently held by **3** and **3^{red}**, followed by the (*d*-*d*)$^{10\text{-}12}$ FeCr complexes **4^{ox}**, **4**, and **4^{red}**,[71] and the (*d*-*d*)^{9,10} FeV complexes, V(^{i}PrNPPh$_2$)FeI and V(^{i}PrNPPh$_2$)FePMe$_3$.[86] Upon reduction, the Mn−P bond distances decrease (Δ = −0.062 Å) while the Cr-N distances increase (Δ(Cr-N_{eq}) = 0.025 Å, Δ(Cr-N_{ap}) =0.049 Å), which is consistent with stronger Mn-phosphine backbonding resulting from a primarily localized reduction at Mn. Also, these bond changes are quantitatively similar to those seen in the reduction of **4** to **4^{red}**, which was assigned as Fe-based

reduction. In contrast, the oxidation of **4** did not produce any statistically significant changes in the Fe-Cr and Fe-P bond metrics. However, the esds in $\mathbf{4^{ox}}$ (up to 0.009 Å) are relatively large, which can mask even moderate changes. Alterations in the Cr-N_{eq} bond are statistically significant (Δ = 0.07(2) Å), suggesting possible oxidation at Cr. The attributions of changes in metal-ligand bond distances to changes at the local metal's oxidation states, as revealed by X-ray crystallography, are likely oversimplifications because the *d*-electrons are delocalized across the two metals, and because structural changes from reductive/oxidative perturbations can be complicated in origin. Thus, complementary spectroscopic and theoretical studies are invaluable in providing critical insights into electronic structures.

An additional important metric of the metal-metal bonding is the *r* value, which is defined as the ratio of the metal-metal bond distance to the sum of their single-bond metallic radii. The *r* value accounts for the differing sizes of various metal atoms and allows direct comparisons between homo- and heterobimetallic bonds. Values close to unity represent single bonds, and values significantly below unity indicate multiple bonds. The *r* values for all complexes here are below unity (0.74 to 0.84). The quintuply bonded species, $\{Cr_2\}^{10}$ $\mathbf{2^{red}}$ and $\{MnCr\}^{10}$ **3**, have the lowest *r* values of 0.74 and 0.77, respectively. Previously, we showed that the δ-symmetry *d*-orbitals at iron and chromium in $\{FeCr\}^9$ **4** do not interact because of their poor energy overlap, and hence, the formal bond order decreases to 3.0 ($\sigma + 2\ \pi$). Since its *r* value is close to that of **4**, $\mathbf{4^{ox}}$ is also interpreted as triply bonded. The *r* value for $\{FeCr\}^{10}$ $\mathbf{4^{ox}}$ is the highest in this series,

which is consistent with its lower bond order. The *r* values for $\{Cr_2\}^9$ **2** and $\{MnCr\}^9$ $\mathbf{3^{red}}$ are in the middle of this series, suggestive of an intermediate bond order between 3 and 5. For these $(d\text{-}d)^9$ systems, the predicted electronic configuration of $(\sigma)^2(\pi)^4(\delta)^3$ predicts an FBO of 4.5. However, the *r* values for **2** and $\mathbf{3^{red}}$ are only slightly greater than those for the Fe-Cr triply bonded complexes, **4** and $\mathbf{4^{ox}}$. A possible explanation is that the two δ-bonds are not fully formed in the cases of **2** and $\mathbf{3^{red}}$, resulting in a bond order between 3 and 4.5 (*vide infra*). In the field of metal-metal bonding, it is often demonstrated that that the expected inverse relationship between bond lengths and bond order does not always hold. Also, since δ-bonds are by nature weak, the effect of δ-bonds on bond lengths (and *r*) can be subtle.

Table 5.3 Cr-Cr bond distances for selected Cr_2 systems.

Ligand	d(Cr-Cr) (Å)	r	ref
Cr_2(2,6-(2,6-^{i}Pr$_2$C$_6$H$_3$)C$_6$H$_3$)$_2$	1.8351(4)	0.78	147, 148
Cr_2(C$_6$H$_3$-2,6-(Ph-2,6-^{i}Pr$_2$)$_2$-4-SiMe$_3$)$_2$	1.8077(7)	0.76	59
Cr_2(*N*,*N*'-bis(2,6-diisopropylphenyl)-1,4-diazadiene)$_2$	1.8028(9)	0.76	145
Cr_2L (2)	1.7407(6)	0.74	this work
Cr_2(MesNC(H)NMes)$_2$	1.7404(8)	0.74	140
Cr_2(2,6-(CH$_3$)C$_6$H$_3$)NC(H)N(2,6-(CH$_3$)C$_6$H$_3$)$_3$	1.7397(9)	0.74	67, 74
Cr_2(Me$_2$NC((2,6(^{i}Pr)Ph))$_2$)$_2$	1.7293(12)	0.74	144
Cr_2((2,6-CH$_3$C$_5$H$_8$)NC((2,6(^{i}Pr)Ph))$_2$)$_2$	1.7056(12)	0.73	65
Cr_2^{-} [a]	1.705(10) [b]	0.73	149
Cr_2	1.6788	0.72	77, 81

[a] gas phase [b] based on a Morse fit of the vibrational frequency

5.3.4 Evaluation of the Diamagnetic Anisotropy of Metal-Metal Bonds

In analogy to unsaturated organic molecules with π-bonds, complexes with multiple metal-metal bonds can have large diamagnetic anisotropies, Δχ, that impact NMR chemical shifts.[150, 151] In axially symmetric molecules, the circulating electrons in

the multiple bond can either shield (+) or deshield (-) nearby protons, depending on the proton's position within the spatial zones demarcated by the double cone, as shown in Figure 5.8 and Table 5.4. Protons in the equatorial region, e.g. methylene resonances, are expected to shift downfield if multiple bonds are present. Indeed, the methylene protons in all three (*d*-*d*)[10] complexes (**3**, $\mathbf{2^{red}}$, and $\mathbf{4^{ox}}$) are notably deshielded, appearing 2 to 3 ppm downfield relative to the methylene protons in the free ligand. The diamagnetic anisotropy ($\chi_{\parallel}-\chi_{\perp}$or $\Delta\chi$) can be calculated using the McConnell equation:[152] $\Delta\delta = \left(\frac{1}{3r^3}\right)\frac{(\chi_{\parallel}-\chi_{\perp})(1-3cos^2(\theta))}{4\pi}$, where $\Delta\delta$ is the difference in ^{1}H NMR chemical shifts of the methylene protons in the multiply bonded bimetallic versus that of a reference complex without any multiple metal-metal bonds. For the reference complex, we chose the isostructural Ni-Al bimetallic featuring a Ni→Al dative bond.[70] The other variables were extracted from the corresponding solid-state structures: r is the distance and θ is the angle of the methylene protons relative to the center and axis of the metal-metal bond, respectively.[153] By assimilating data from NMR and X-ray crystallographic studies, we make the assumption that the solution and solid-state structures are similar.

While diamagnetic anisotropies are known for several homobimetallic species, such data is limited for heterobimetallic pairings (Table 5.4).[127, 128, 151, 154] Cotton and co-workers have systematically studied a series of quadruply bonded complexes, $M_2X_4(\mu\text{-}PP)_2$, where M_2 = Mo_2, MoW, and W_2. The average $\Delta\chi$ values increase across the pairings, Mo_2 < MoW < W_2, where each substitution of a Mo center for W results in an increase of $\Delta\chi$ by approximately -640×10^{-36} m^3 molecule^{-1} (or 13%). The calculated $\Delta\chi$

values for $\{Cr_2\}^{10}$ **2**^{red}, $\{MnCr\}^{10}$ **3**, and $\{FeCr\}^{10}$ **4**^{ox} are −3630, −4310, and −5620 (x 10^{-36} m^3 $molecule^{-1}$). The diamagnetic susceptibility does not increase with respect to bond order, but rather, $\Delta\chi$ increases with the polarization of the metal-metal bond. Substituting Mn for Cr results in a 20% gain in $\Delta\chi$, while swapping Fe for Cr produces a dramatic 55% increase. This trend is well known in organic molecules, whereby heteronuclear π-bonds, e.g. C=O (+420) and N=O (+1300), exhibit larger diamagnetic anisotropies than their homonuclear analogues, e.g. C=C (+150) and C≡C (−340).[155] Finally, we note that the diamagnetic anisotropy for **2**^{red} is near in value to another trigonal dichromium complex, $[Cr_2(ArNC(H)NAr)_3]^-$, where Ar = 2,6-$Me_2(C_6H_3)$.[xviii]

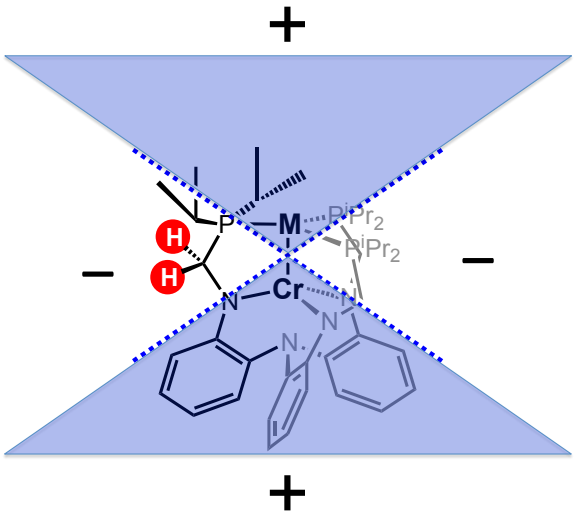

Figure 5.8 Areas of shielding and deshielding induced by the metal-metal multiple bond. The methylene protons are highlighted for clarity.

[xviii] The methyl groups also display substantial magnetic anisotropy and split into four unique resonances at – 40°C. The methyl resonances in NiAlL span across a 0.26 ppm range (1.08 to 0.84 ppm), whereas the methyl groups span 1.58 ppm in **2**^{red} (1.85 to 0.27 ppm), 1.31 ppm in **3**, and 1.06 ppm in **4**^{ox}. This broader range suggests that one isopropyl group is directed "up" and the other "down."

Table 5.4 Selected diamagnetic anisotropy as calculated in the literature

Complex[a]	$\Delta\chi$ (10^{-36} m^3 $molecule^{-1}$)	Ref.
2^{red}	−3630	this work
3	−4310	this work
4^{ox}	−5620	this work
$Cr_2(ArNC(H)NAr)_3$	−3030	67
$Cr_2(DPhF)_4$	−5230	128
$Mo_2(DPhF)_4$	−5020	128
$W_2(DPhF)_4$	−5480	128
$Re_2(DPhF)_4$	−4430	128
$Ru_2(DPhF)_4$	−3780	128
$Mo_2X_4(PP)_2$	−4450[b]	156
$MoWCl_4(PP)_2$	−5082[b]	127
$W_2X_4(PP)_2$	−5728[b]	154

[a] DPhF = diphenylformamidinate; PP = dppe, dppm, dmpm, dmpe [b] Average value

5.3.5 Theoretical Calculations

Quantum chemical studies have been conducted on the bimetallic models, **2′,** **2^{red}′**, **3^{red}′**, and **4^{ox}′**, where the isopropyl groups are truncated to methyls. Similar studies for **3′** and **4′** have been reported elsewhere.[78, 157] Geometry optimizations were performed using density functional theory (DFT) for several possible spin states and confirmed the experimentally determined ground spin states. The metal−metal bonds previously studied in this family exhibited strong electronic correlation, and we have performed complete active space self−consistent field (CASSCF) followed by second−order perturbation theory (CASPT2) calculations. These studies have accurately described similar bimetallic systems characterized by a heavy multireference character, large dynamic correlation

energy, and significant relativistic effects.[148, 158] Figure 5.9 depicts the RAS1 active space orbitals for the isoelectronic $(d\text{-}d)^{10}$ species $\mathbf{2^{red}}$ and $\mathbf{4^{ox}}$.

For trigonal coordination geometries with weak ligand fields, all five d−orbitals have the potential to participate in metal−metal bonding. The d−orbitals can combine to form one σ (d_z^2), two π (d_{xz}, d_{yz}), and two δ (d_{xy}, $d_{x^2-y^2}$) bonds. All five of these interactions are observed in the dichromium **2′** and retained upon reduction to $\mathbf{2^{red\prime}}$. The manganese-chromium **3′**, like $\mathbf{2^{red\prime}}$, possesses a $(d\text{-}d)^{10}$ configuration and five-fold bonding, as does the $(\text{d-d})^{10}$ iron-chromium **4ox′.** The appearance of δ bonds in $\mathbf{4^{ox}}$ is unexpected, as the metal-metal distance in the solid-state structure is statistically indistinguishable from **4**, which has a formal triple bond.[71] Therefore, the $(d\text{-}d)^{10}$ species all possess *formal* bonding interactions with a dominant $\sigma^2\pi^4\delta^4$ configuration. The $(d\text{-}d)^{11}$ manganese-chromium **3red′** retains one δ bond, for which the dominant configuration is $\sigma^2\pi^4\delta^2Cr^1Mn^2$; the isoelectronic **4′** has no δ bonding interactions and has a dominant configuration of $\sigma^2\pi^4\delta^2Cr^2Fe^4$. It must be noted that the presence of bonding interactions *does not* imply that the interactions are strong nor that they have a substantial contribution to the overall strength of the metal-metal bond.

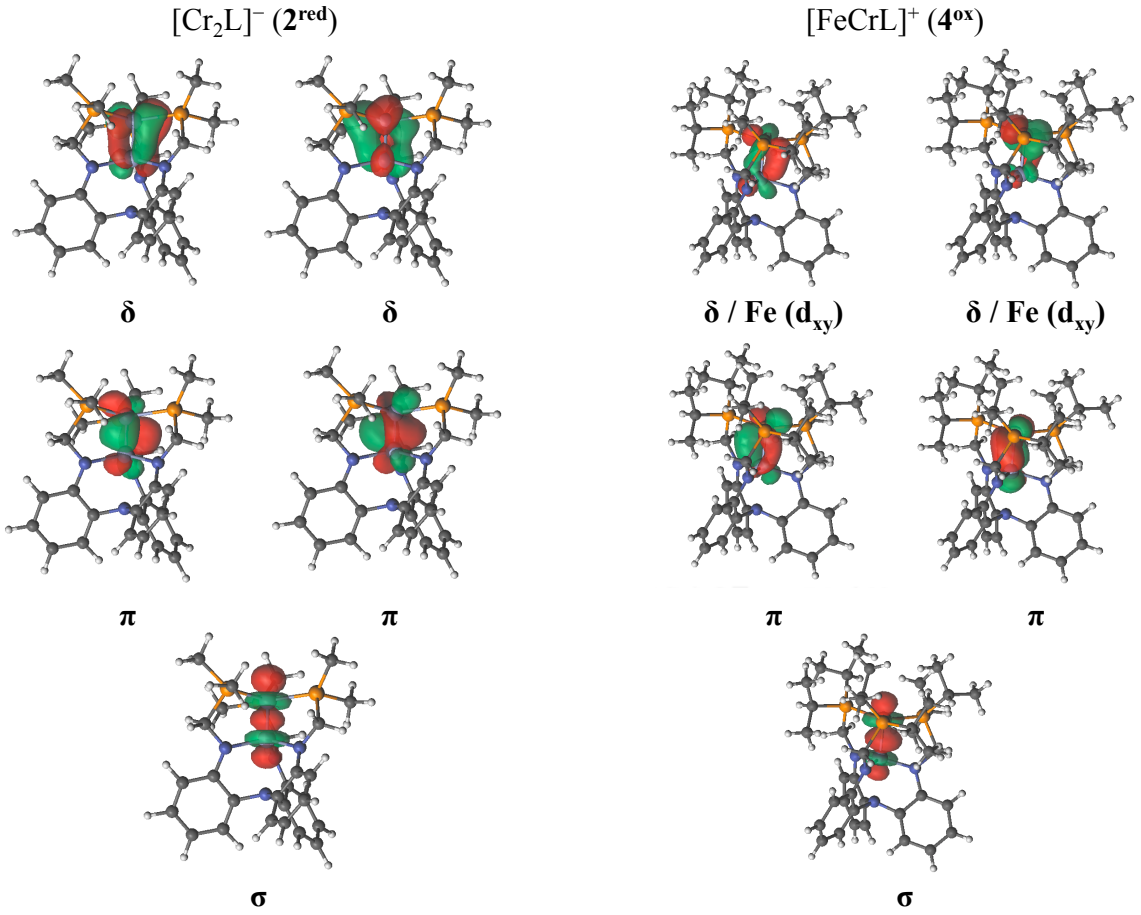

Figure 5.9 Natural bonding orbitals of σ (d_z^2), π (d_{xz}, d_{yz}), and δ (d_{xy}, $d_{x^2-y^2}$) symmetry for **2red′** and **4ox′**.

It is obvious upon visualization of the CASSCF orbitals that the heterobimetallic bonds are increasingly polarized in the isoelectronic $(d\text{-}d)^{10}$ series, as expected. The following data are also shown in Table 5.5 The dichromium species **2′** and **2red′** are anticipated to have the least polar bond on account of having the most similar orbital energies, and the σ, π, and δ contributions are roughly even across both metal sites. As anticipated, the MnCr species are modestly more polarized: **3′** has 5-10% higher polarization for all bonds relative to the isoelectronic **2red′**. The FeCr **4ox′** is slightly

more polar than **3′** with respect to σ bonding and slightly less polar with respect to π bonding, but the δ bonding contribution is nearly exclusively iron-based. Due to the similarity between **2red′** and **3′**, the assignment of quintuple bonding is justified, and the assignment of triple bonding for **4ox′** is most appropriate. As **3′** undergoes reduction, the σ and π bonds become 5-10% less polarized and the δ bond becomes 18% more polarized. The stronger σ and π contributions appear to mostly offset the near-total loss of the δ bond, accounting for the very mild elongation observed in the solid-state crystal structure. As **4ox′** undergoes reduction to **4′** and **4red′**, the σ component is nearly invariant. The π bond changes negligibly between **4ox′** and **4′** but shows an 18% polarization toward Fe upon reduction to **4red′**, which is consistent with the slightly longer distance observed by crystallography. The δ component is extremely polarized for **4ox′** and is non-bonding for **4′** and **4red′**.

Table 5.5 CASSCF orbital analysis of metal-chromium bonding orbitals

	MM' =	σ		π		δ	
		%Cr	%M	%Cr	%M	%Cr	%M
$(d\text{-}d)^9$	Cr (**2′**)	46	54	52	48	50	50
$(d\text{-}d)^{10}$	Cr (**2red′**)	46	54	48	52	39	61
	Mn (**3′**)	40	60	38	62	33	67
	Fe (**4ox′**)	33	67	45	55	13	87
$(d\text{-}d)^{11}$	Mn (**3red′**)	44	56	47[a]	53[a]	15	85
	Fe (**4′**)	31	69	45	55	8[b]	92[b]
$(d\text{-}d)^{12}$	Fe (**4red′**)	36	64	27	73	0[b]	100[b]

[a] Second π has inverted weight [b] No δ interactions, doubly occupied orbitals are localized on F

Eq. 5.1 $$EBO = \frac{bonding\ electrons - antibonding\ electrons}{2}$$

We and others have previously utilized the effective bond order (EBO, Eq. 5.1) to account for the heavy multi-reference character in metal-metal bonds and to compare the bonding in heterobimetallic species. EBO analysis of heterobimetallic species was possible in these earlier cases because the more polarized metal-metal bonds became clearly localized for π or δ interactions as a result of poor metal orbital energetic overlap. The highly polarized orbitals here complicate straightforward evaluation of the EBO because localization of the electrons onto one metal indicates that this orbital is largely non-bonding, whereas the orbitals here are delocalized but reside dominantly on one metal center. As such, ignoring the polarization in $\mathbf{4^{ox}}$ would yield the electronic configuration $\sigma^2\pi^4\delta^4$ whereas treating them as nonbonding yields a $\sigma^2\pi^4(\text{Fe } d_{xy})^4$ configuration. The best description likely lies between these two limiting scenarios, though closer to the latter configuration. The potential bonding configurations are shown in Table 5.6 along with the calculated weight percent of the dominant configuration, the *r* value, and the corresponding formal bond orders for each configuration.

Table 5.6 Potential electronic configurations for each $(d\text{-}d)^n$ species

	MM' =	Main configuration	Dominant configuration (%)	r	FBO
$(d\text{-}d)^9$	CrCr	$\sigma^2\pi^4\delta^2(\text{Cr } d_{xy})^1$	42	0.82	4
$(d\text{-}d)^{10}$	CrCr	$\sigma^2\pi^4\delta^4$	60	0.74	5
	MnCr	$\sigma^2\pi^4\delta^4$	55	0.77	5
	FeCr	$\sigma^2\pi^4(\text{Fe } d_{xy})^4$	55	0.84	3
$(d\text{-}d)^{11}$	MnCr	$\ldots \sigma^2\pi^4(\text{Mn } d_{xy})^4(\text{Cr } d_{xy})^1$	64	0.81	3
	FeCr	$\sigma^2\pi^4(\text{Fe } d_{xy})^4(\text{Cr } d_{xy})^1$	58	0.83	3
$(d\text{-}d)^{12}$	FeCr	$\sigma^2\pi^4(\text{Fe } d_{xy})^4(\text{Cr } d_{xy})^2$	60	0.84	3

Analysis of the CASSCF active space orbitals can also show the d-electron count on each metal site, assisting assignment of oxidation state. These results are consistent with the following oxidation states: **2′**, $Cr_{(P)}(1.0)Cr_{(N)}(2.0)$; **2red′**, $Cr_{(P)}(0.5)Cr_{(N)}(1.5)$; **3′**, Mn(0.9)Cr(2.1); **3red′**, Mn(0.3)Cr(1.7); **4ox′**, Fe(1.2)Cr(2.8); **4′**, Fe(0.6)Cr(2.4); **4red′**, Fe(0)Cr(2.0). Broadly speaking, these results suggest that the crystallographically-derived oxidation states may be misleading. Assignment of oxidation states based upon the solid-state structure suggests that the reduction is localized on $Cr_{(N)}$ in **2**/**2**$^{\mathbf{red}}$, Mn in **3**/**3**$^{\mathbf{red}}$, and Cr in **4**$^{\mathbf{ox}}$/**4**/**4**$^{\mathbf{red}}$, whereas the calculations suggest strong delocalization in all cases. Mössbauer spectroscopy for **4**$^{\mathbf{ox}}$/**4**/**4**$^{\mathbf{red}}$ suggests that iron changes undergoes some oxidation state change between **4**$^{\mathbf{ox}}$/**4** (vide infra), but spectroscopic changes in the oxidation states of **2**/**2**$^{\mathbf{red}}$ and **3**/**3**$^{\mathbf{red}}$ are most likely to be observed by investigating the Cr, Mn, and Fe *k*-edge X-ray absorption spectra (XAS). Some preliminary XAS data were collected for **2**, **3**, and **4** at both the chromium *k*-edge as well as the manganese and iron *k*-edges, but the corresponding charged species have not yet been collected. Future

measurements of these species are hoped to shed additional light on the spectroscopic oxidation state changes across the redox members in this series.

5.3.6 UV-vis-NIR and resonance Raman (rR) Spectroscopy

The absorbance spectra for tetragonal homobimetallic units with quadruple bonds have been extensively studied and are well understood, but trigonal bimetallics and heterobimetallic species in particular are not well understood. In the present complexes, all spectra contain a strong ligand-derived transition in the UV, but the vis-NIR regions are all sufficiently different that all transitions can reasonably be ascribed to either metal-metal or metal-ligand interactions. Despite the strong similarities in the calculated electronic configurations of these complexes, the UV-vis-NIR spectra for the isoelectronic sets are surprisingly different with respect to both the number of transitions and their λ_{max}. These data are summarized in Table 5.7 and shown in Figures 5.10 and 5.11.

Table 5.7 Visible-NIR electronic absorbance data for **2**, **2**^{red}, **3**, **3**^{red}, **4**, and **4**^{ox}

Complex	λ_{max}[a] (ε)[b]
2	495 (2300) 600 (1480) 880 (930) 1460 (140)
2^{red}	675 (1880)
3	400 (4400) 550 (1850) 1025 (2160)
3^{red}	745 (1230) 1350 (760)
4	645 (1440) 1344 (220)
4^{ox}	463 (4860) 730 (3890) 1495 (490)

[a]in nm [b]in M^{-1} cm^{-1}

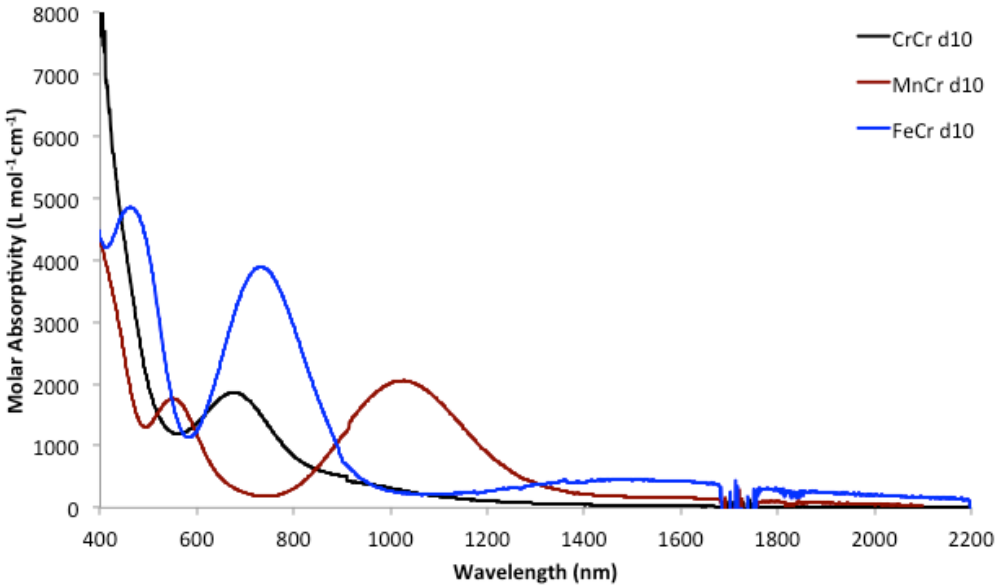

Figure 5.10 UV-vis-NIR spectra for **2**^{red} (black), **3** (maroon), and **4**^{ox} (blue) in THF. Imperfect solvent subtraction is responsible for the region between 1650 and 1750 nm.

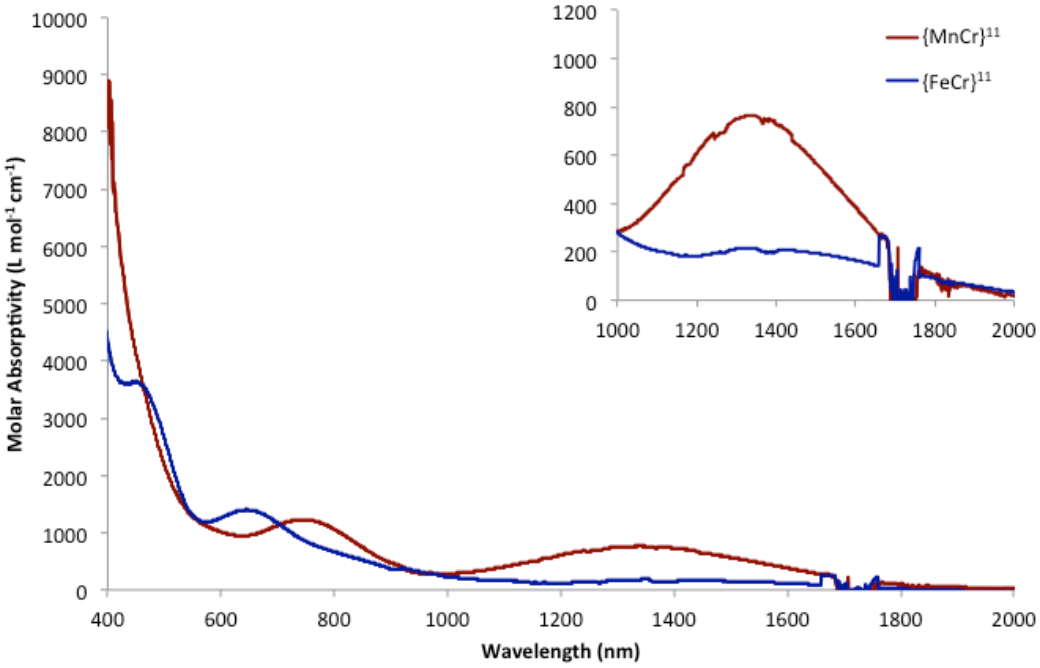

Figure 5.11 UV-vis-NIR spectra for $\mathbf{3}^{red}$ (maroon) and **4** (blue) in THF. Inset shows an expansion of the NIR region. Imperfect solvent subtraction is responsible for the region between 1650 and 1750 nm.

The most interesting assignment would certainly be the δ to δ* transition for $\mathbf{2}^{red}$ versus **3** as a quantitative evaluation of the difference between homo- and heterobimetallic quintuple bonds. Optical spectra have been collected on relatively few dichromium species with quintuple bonds, and little has been said regarding their assignment.[55, 59, 60, 63, 67] In the simplest possible case, the molecular orbital diagram for each would predict that the lowest energy transition is derived from the $\delta^4 \rightarrow \delta^3\delta^*$ excitation.[55, 58, 59, 60, 63, 67] The vis-NIR spectrum of $\mathbf{2}^{red}$ has only one feature at λ_{max} = 675 nm, which is lower energy than all but one other dichromium species and consistent a more polarized (and therefore weaker) bond. To corroborate the assignment of the 675 nm band as a $\delta^4 \rightarrow \delta^3\delta^*$ transition for $\mathbf{2}^{red}$, a resonance Raman (rR) study was performed

(λ_{ex} = 647.1 nm, 77 K). To our knowledge, only a handful of Raman studies have been reported for dichromium species,[88, 159-161] though numerous studies exist for molybdenum and tungsten systems.[162] A series of peaks were identified in the rR spectrum of 2^{red} between 350-550 cm^{-1} (Figure 5.12), including features at 363, 412, 434, and 495 cm^{-1}. Additional studies verify that none of these vibrations are related to ligand modes (vide supra). A selected portion of this spectrum is shown in Figure 5.10.

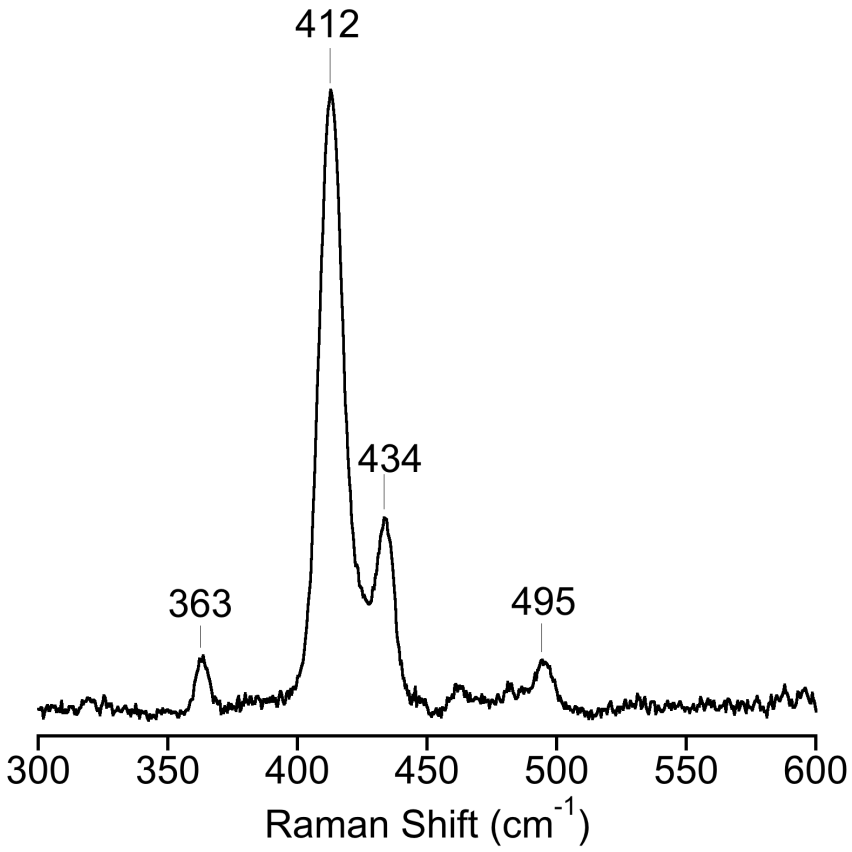

Figure 5.12 Resonance Raman spectrum of **2**^{red} (λ_{ex}: 647.1 nm, 77 K)

Ideally, excitation into the $\delta^4 \rightarrow \delta^3\delta^*$ transition should selectively enhance the bimetallic ν_{CrCr} vibration, but the observation of multiple vibrations with bimetallic

character is well-known to result from coupling to various ligand modes.[126, 161, 163] This effect is dependent on M-M-L angles and is enhanced upon significant deviation from 90˚, such as in M_2L_3 species.[126] Close inspection of the DFT-calculated vibrational spectrum of $\mathbf{2}^{\mathbf{red}}$ reveals four vibrations involving the Cr-Cr bond (341, 391, 472, and 502 cm^{-1}) that correlate well in position and intensity with the observed vibrations in the rR spectrum of $\mathbf{2}^{\mathbf{red}}$. Indeed, the three lower-energy vibrations are predicted to couple to ligand vibrations, while the fourth and highest energy feature is assigned as a relatively pure Cr-Cr vibration. As additional support for this assignment, we note that the calculated oscillator strengths for the ligand-coupled vibrations are qualitatively correct, suggesting a tentative assignment of the dichromium stretching mode ν_{CrCr} at 495 cm^{-1}. To the best of our knowledge, no rR studies exist for dichromium species with quintuple bonds. Previously reported ν_{CrCr} for dichromium complexes featuring formal quadruple bonds are reported to occur at 556 and 570 cm^{-1},[88, 159] representing modestly stronger bonds than $\mathbf{2}^{\mathbf{red}}$ on the basis of vibrational spectroscopy, even though the latter certainly has a higher bond order. The Cr-Cr bond in $\mathbf{2}^{\mathbf{red}}$ appears to be the first example of a mixed-valent dichromium species with a quintuple bond, and this polarization may account in part for the lower observed ν_{CrCr} frequency. However, the effect of axial ligands has been shown to lower the frequency of Mo-Mo bonds by 30-40 cm^{-1},[162] and it is not currently possible to deconvolute the various contributions to the metal-metal stretching mode. Despite repeated attempts, none of the other species currently under

study exhibited significantly enhanced features upon rR analysis with a variety of excitation wavelengths, precluding direct comparison of experimentally observed ν_{MM}.

It seems reasonable to suggest that the lowest energy transition in **3** is similarly $\delta^4 \rightarrow \delta^3\delta^*$, but we were unable to confirm this with rR techniques and instead turned to calculated transitions in order to help assign these spectra. Because of the strong multi-reference character in these complexes, each transition contains some contribution from multiple orbitals and none can be assigned as a "pure" $\delta^4 \rightarrow \delta^3\delta^*$ transition. SA-CASSCF/PT2 and CASSI calculations of the dominant configuration of **2red′** demonstrate significant $\delta^4 \rightarrow \delta^3\delta^*$ character and corroborate the proposed assignment for the 675 nm feature. Analysis of **3**' confirms that the lowest-energy transition (observed at 1025 nm) also shows dominant $\delta^4 \rightarrow \delta^3\delta^*$ character. The exchange of Cr for Mn can therefore be crudely attributed as destabilizing the δ bond by approximately 5,000 cm^{-1}. For **4ox′**, the lowest energy transition assignment (observed at 1495 nm) corresponds to a formally $\delta^4 \rightarrow \delta^3\pi^{*1}$ transition, though the δ orbitals reflect predominantly Fe character.

5.3.7 Mössbauer spectroscopy

Complex $\mathbf{4^{ox}}$ was subjected to ^{57}Fe Mössbauer spectroscopy in order to further elucidate the oxidation state changes between $\mathbf{4^{ox}/4/4^{red}}$. The reduction of **4** to $\mathbf{4^{red}}$ has been assigned as a Cr-centered reduction on the basis a negligible shift in the isomer shift (IS), which reflects core Fe *s* electron density and sensitive to changes in iron oxidation state. The isomer shifts of **4** and $\mathbf{4^{red}}$ are 0.25 mm s^{-1} and 0.26 mm s^{-1}, respectively,[71] so it is noteworthy that the IS of $\mathbf{4^{ox}}$ shifts to a slightly lower value, 0.18 mm s^{-1} (Figure 5.13).

The lower isomer shift is consistent with lower *s* electron density, and therefore oxidation, at the iron center, though the relatively small change leaves it unclear whether this is localized at iron or delocalized across the bimetallic unit.

Unfortunately, the isomer shifts for these complexes are not diagnostic, as the IS can change upon alteration of the coordination geometry around iron or iron-ligand backbonding. Berry *et al.* have shown that the isomer shift changes linearly between Fe(II) and Fe(VI) in iron cyclam complexes,[164] and low-valent iron species with trigonal phosphine donors appear to have broadly similar isomer shift changes as the iron oxidation state is varied (Figure 5.14). Our recent iron-alane complexes in this ligand demonstrated isomer shift changes of 0.18 mm s^{-1} upon oxidation.[110] In conjunction with other data, that shift allowed unambiguous assignment as an iron-based redox event. The Peters group has also observed isomer shift changes of ≥0.1 mm s^{-1} upon stepwise oxidations between formally Fe(0) and Fe(II) sites,[16, 37, 137] though it should be noted that this is not always the case.[165] The smaller change between **4** and $\mathbf{4^{ox}}$, 0.07 mm s^{-1}, seems to argue for a delocalized oxidation, consistent with the theoretical prediction, rather than a purely iron-centered oxidation or the chromium-centered oxidation suggested by the solid-state data.

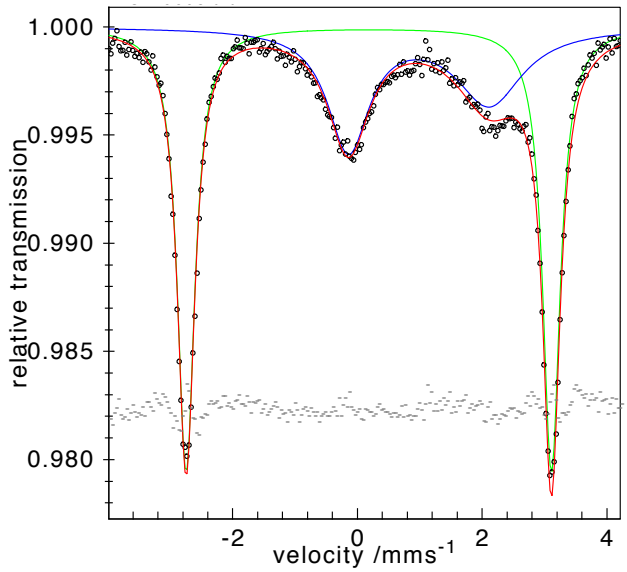

Figure 5.13 Zero-field ^{57}Fe Mössbauer spectra of **4^{ox}** at 80K. The experimental data is shown by black circles. The red line represents the best fit with δ = 0.18 mm s^{-1} and ΔE_Q = 5.86 mm s^{-1}.

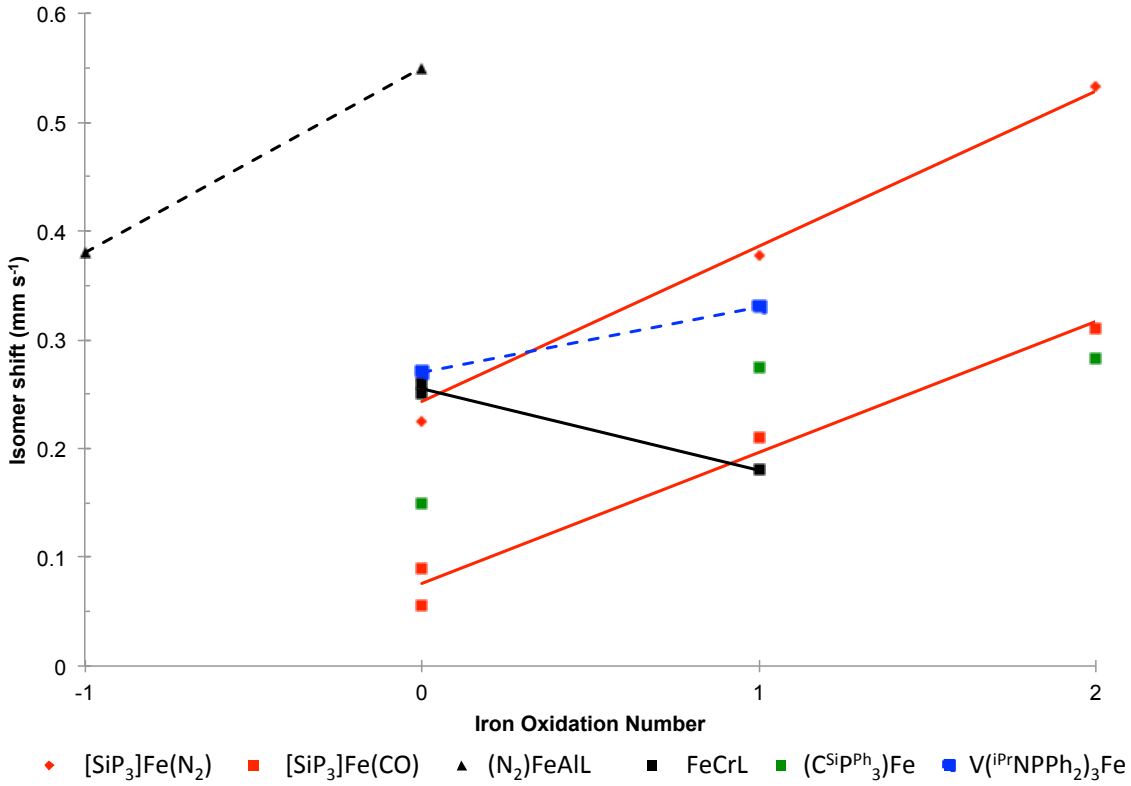

Figure 5.14 Mössbauer data for selected low-valent iron-phosphine species. Dashed lines indicate a change in the coordination sphere.

It is lastly worth noting that the Mössbauer spectra of **4** and $\mathbf{4}^{red}$ were especially unusual in that they displayed large quadrupole splitting (QS) terms, 5.92 and 5.20 mm/s respectively, that corroborate the assignment of a triple bond. Consistent with this interpretation, $\mathbf{4}^{ox}$ displays similarly large quadrupole splitting values: two independently prepared samples yielded QS values of 5.86 and 6.46 mm/s. Despite the difference in these quadrupole splittings, the IS is identical in both samples; the origin of the quadrupole splitting disparity is not currently known, but both values fully support the presence of a strong iron-chromium interaction. We additionally note that the latter of the two QS values for $\mathbf{4}^{ox}$ is higher than any complex currently known in the literature. The

current record, 6.23 mm/s, is held by an iron-nitride complex that was prepared by Peters and coworkers.[14, 15]

5.4 Conclusions

Multiple bonds between different first-row metals were first reported with the iron-chromium complexes **4** and $\mathbf{4}^{\mathbf{red}}$, and this work has now been extended to manganese-chromium and the homobimetallic dichromium. The manganese-chromium complex **3** represents the first example of a heterobimetallic quintuple bond, and the corresponding dichromium analog $\mathbf{2}^{\mathbf{red}}$ has one of the shortest Cr_2 distances in the literature. Complexes $\mathbf{2}^{\mathbf{red}}$ and **3** represent two of approximately twenty known quintuple bonds, whereas the isoelectronic iron analog $\mathbf{4}^{\mathbf{ox}}$ is assigned as a triple bond. Within two isoelectronic, isostructural sets, the M−Cr interaction increases in strength from M = Fe < Mn < Cr. In contrast, the diamagnetic anisotropy of the metal-metal bond reflects the bond polarity and decreases in strength from M = Fe > Mn > Cr.

First-row metal-metal multiple bonds have now been shown to be generalized within the double-decker framework, and it seems likely that still more previously unknown heterobimetallic cores will be accessible through this approach. The stability of heterobimetallic quintuple bonds cannot currently be predicted *a priori*, and the synthesis of additional heterobimetallic species beyond the first row may help clarify the synthetic and electronic limits at extremely high bond orders.

The chemistry of these multiply-bonded species is also largely unknown, and fundamental monometallic reactivity, such as oxidative addition, has only recently been reported in the literature. No productive reactivity was observed during initial surveys with the complexes reported here.

5.5 Experimental

General Considerations

Unless otherwise stated, all manipulations were performed inside a glovebox under an N_2 atmosphere or using standard Schlenk techniques. Standard solvents were deoxygenated by sparging with N_2 and dried by passing through activated alumina columns of a SG Water solvent purification system. Deuterated solvents were purchased from Cambridge Isotope Laboratories, Inc., degassed via freeze−pump−thaw cycles, and stored over activated 4 Å molecular sieves. ^{1}H NMR spectra were recorded on a Bruker 500 MHz spectrometer at rt unless otherwise stated. All ^{1}H and ^{13}C NMR spectra are referenced to the internal solvent residual. UV−vis−NIR spectra were collected at rt on a Cary−14 spectrometer. Cyclic voltammetry was conducted using a CH Instruments 600 electrochemical analyzer. The one−cell setup utilized a glassy carbon working electrode, Pt wire counter electrode, and $Ag/AgNO_3$ reference electrode in CH_3CN. Analyte solutions were prepared in a THF solution of 0.4 M $[^nBu_4N][PF_6]$ and referenced internally to the $FeCp_2^{0/+}$ redox couple. IR spectra were collected using a Bruker Tensor−37 FTIR instrument with the OPUS 6.5 software. The ligand $N(o\text{−}(NHCH_2P^iPr_2)C_6H_4)_3$ (abbreviated as H_3L), CrL (**1**),[157] MnCrL (**3**),[166] FeCrL (**4**),[157] and $[FeCp_2][B(3,5\text{-}(CF_3)_2C_6H_3)_4]$[167,168] were synthesized according to literature procedures.

Calculation of Diamagnetic Anisotropy and Inversion Barriers

Variable temperature NMR experiments were performed on a Bruker 500 MHz spectrometer that was calibrated with an external methanol standard. Diamagnetic anisotropy is calculated with Equation 1, where $\Delta\sigma_i$ is the difference in chemical shift (in ppm) between the resonance in a bimetallic complex versus a reference complex. The distance *r* is measured from the centroid of the metal-metal bond to the methylene proton (H), and the angle θ reflects H-($CrM_{centroid}$)-Cr. The units are 10^{-36} m^3 $molecule^{-1}$.

Eq. 1. $\Delta\sigma_i = \left(\frac{1}{3r^3}\right)\frac{(\chi_{\parallel}-\chi_{\perp})(1-3cos^2(\theta))}{4\pi}$

The barrier to inversion, $\Delta G^{\ddagger}$, is calculated with Equation 2. Temperature *T* is in K, and $k = \frac{\pi(\Delta v_0)}{\sqrt{2}}$ where Δv_0 is the difference in frequency (Hz) between the exchanging sites.

Eq. 2 $\Delta G^{\ddagger} = (1.987)(T)(23.76 + \ln\left(\frac{T}{k}\right))$

Synthesis of 2, $Cr_2(N(o\text{−}(NCH_2P^iPr_2)C_6H_4)_3)$.

A solution of **1** (0.12 g, 0.16 mmol) was dissolved in THF (c. 4 mL) and mixed with a stirred slurry of $CrCl_3$ (0.027 g, 0.17 mmol) in THF (c. 4 mL) for 15 min, forming a homogenous green solution. The solution was then added to KC_8 (0.057 g, 0.51 mmol). Within minutes, the solution turned dark brown with precipitate. After removal of solvent *in vacuo*, the sample was dissolved in toluene and filtered through a Celite plug. The brown solution was dried *in vacuo*, yielding a brown powder (0.13 g, quantitative). Single crystals of **2** were grown by diffusion of *n*−pentane into a concentrated solution of **2** in THF. ^{1}H NMR (ppm, C_6D_6, 500 MHz): 34.1, 10.8, 9.1, 5.0, 4.1, 3.4, 1.3, 1.1, 1.0, −0.5, −2.4, −15.1. UV−vis−NIR (THF) λ_{max}, nm (ε, M^{-1} cm^{-1}): 495 (sh, 2330), 600

(1480), 880 (930), 1460 (140). Anal. Calcd for **2**, $C_{39}H_{60}N_4P_3Cr_2$: 59.91 C, 7.74 H, 7.17 N. Found: 59.79 C, 7.69 H, 7.09 N.

Synthesis of K[2^{red}], K[Cr$_2$(N(o−(NCH$_2$P^{i}Pr$_2$)C$_6$H$_4$)$_3$)].

A solution of **1** (0.11 g, 0.15 mmol) was dissolved in THF (c. 4 mL) and mixed with a stirred slurry of $CrCl_3$ (0.024 g, 0.15 mmol) in THF (c. 4 mL) for 15 min, forming a homogenous green solution. The solution was then added to KC_8 (0.084 g, 0.62 mmol), forming a dark green solution with precipitate. The sample was filtered through a Celite plug and dried *in vacuo*, yielding a green powder (0.12 g, 98%). Single crystals of **2^{red}** were grown by diffusion of *n*−pentane into a concentrated THF solution of **2^{red}**. The ^{1}H NMR spectrum at rt had extremely broad peaks indicative of fluxional behavior. ^{1}H NMR (ppm, THF−d_8, 500 MHz, −80 °C): 6.39 (t, *J* = 7 Hz, 1H), 6.15 (d, *J* = 7 Hz, 1H), 6.06(d, *J* = 7 Hz, 1H), 5.45 (t, *J* = 7 Hz, 1H), 5.28 (d, *J* = 12 Hz, 1H), 4.47 (d, *J* = 12 Hz, 1H), 2.73 (br, 1H), 2.63 (br, 1H), 1.85 (br, 3H), 1.54 (br, 3H), 1.21 (br, 3H), 0.27 (br, 3H). ^{13}C NMR (ppm, THF−d_8, 126 MHz, −80 °C): 157.6, 136.5, 126.5, 124.9, 106.4, 106.1, 34.1, 29.1, 23.5, 21.2, 21.0, 19.0. ^{31}P NMR (ppm, THF−d_8, 200 MHz, −80 °C): 42.4. UV−vis−NIR (THF) λ_{max}, nm (ε, M^{-1} cm^{-1}): 315 (18300); 675 (1880). Anal. Calcd for K(**2^{red}**), $C_{39}H_{60}N_4P_3Cr_2K$: 57.06 C, 7.37 H, 6.82 N. Found: 56.97 C, 7.28 H, 6.69 N.

Synthesis of K(crypt−222)[3^{red}], [K(crypt−222)][MnCr(N(o−(NHCH$_2$P^{i}Pr$_2$)C$_6$H$_4$)$_3$)]

A solution of **1** (0.12 g, 0.16 mmol) was dissolved in THF (c. 4 mL) and mixed with a stirred slurry of $MnBr_2$ (0.027 g, 0.17 mmol) in THF (c. 4 mL) for 15 min, forming a homogenous green solution. Solid KC_8 (0.057 g, 0.51 mmol) was then added. Within minutes, the solution turned dark red−brown with precipitate. After removal of solvent *in vacuo*, the sample was washed with toluene (c. 1 mL), reconstituted in THF (c. mL) and filtered through a Celite plug onto crypt−222 (0.049 g, 0.16 mmol) in THF (c. 2 mL). The solution was dried *in vacuo* and washed with Et_2O (c. 4 mL), yielding a maroon powder (0.17 g, quantitative). Single crystals of **3** were grown by diffusion of *n*−pentane into a concentrated THF solution of **3**. ^{1}H NMR (ppm, THF−d_8, 500 MHz): 26.1, 22.9, 9.6, 7.7, 6.3, 4.8, 3.4, 2.5, 0.6, −0.1, −11.8. UV−vis−NIR (THF) λ_{max}, nm (ε, M^{-1} cm^{-1}): 745 (1230); 1350 (762). Anal. Calcd for K(crypt−222)[$\mathbf{3^{red}}$], $[K(C_{18}H_{36}N_2O_6)][C_{39}H_{60}N_4P_3CrMn]$: 57.03 C, 8.06 H, 7.00 N. Found: 57.06 C, 8.14 H, 6.97 N.

Synthesis of $\mathbf{4^{ox}}$[$\mathbf{BAr^F_4}$], [FeCr(N(o−($\mathbf{NCH_2P^iPr_2}$)$\mathbf{C_6H_4}$)$_3$)][B(3,5−($\mathbf{CF_3}$)$_2$$\mathbf{C_6H_3}$)$_4$]

To a stirring solution of **4** (0.074 g, 0.94 mmol) in THF (c. 4 mL), $FeCp_2[B(Ar_F)_4]$ (0.099 g, 0.94 mmol) in THF (c. 4 mL) was added drop−wise over 5 min, during which the color changed from green to red−brown. After removal of solvent *in vacuo*, the sample was washed with copious *n*−hexane. The remaining red−brown powder was reconstituted in THF, filtered through a Celite plug, and dried *in vacuo*, (0.144 g, 94%). Single crystals of $\mathbf{4^{ox}}$ were grown by diffusion of *n*−pentane into a concentrated THF solution of $\mathbf{4^{ox}}$. ^{1}H NMR (ppm, C_6D_6, 500 MHz, −20 °C): 7.77 (s, 8H), 7.56 (s, 4H), 7.13 (t, J = 8 Hz,

3H),7.07 (d, J = 8 Hz, 3H), 6.59 (d, J = 8 Hz, 3H), 6.45 (t, J = 8 Hz, 3H), 6.32 (s, 6H), 3.11 (br, 3H), 2.82 (br, 3H), 1.48 (m, 9H), 1.40 (m, 9H), 1.31 (m, 9H), 0.65 (m, 9H). ^{13}C NMR (ppm, THF−d_8, 126 MHz, −20 °C): 135.4 (aryl, BAr_{F4}), 128.6 (aryl); 126.6 (aryl), 120.9 (aryl), 118.1 (aryl, BAr_{F4}), 111 (aryl); 75.6 (CH_2), 32.8 (CH), 28.0 (CH), 22.4 (CH_3), 20.3 (CH_3), 19.4 (CH_3), 18.0 (CH_3). ^{31}P NMR (ppm, C_6D_6, 126 MHz, −20 °C): 26.2. UV−vis−NIR (THF) λ_{max}, nm (ε, M^{-1} cm^{-1}): 463 (4860), 730 (3890), 1495 (490). Anal. Calcd for **4**^{ox}[BAr^F_4], [$C_{39}H_{60}N_4P_3FeCr$][$C_{32}H_{12}F_{24}B$]: 51.72 C, 4.40 H, 3.40 N. Found: 51.67 C, 4.40 H, 3.26 N.

X−Ray Crystallographic and Structure Refinement Details

Single crystals of **1** were grown by adding hexamethyldisiloxane to a concentrated solution of **1** in Et_2O and storing at −30 °C. Brown plates of **1**, **2**, K(crypt-222)[**3**^{red}], and **4**^{ox}[BAr^F_4], and a green plate of K[**2**^{red}] were placed onto the tip of a 0.1 mm diameter glass capillary and mounted on a Bruker APEX II CCD diffractometer for data collection at 173(2) for **1**, **2**, K[**2**^{red}], and K(crypt-222)[**3**^{red}], and 123(2) K for **4**^{ox}[BAr^F_4]. The data collection was carried out using Mo Kα radiation (graphite monochromator). The data intensity was corrected for absorption and decay (SADABS). Final cell constants were obtained from least squares fits of all measured reflections. The structure was solved using SHELXS−97 and refined using SHELXL−97. A direct−methods solution was calculated which provided most non−hydrogen atoms from the E−map. Full−matrix least squares / difference Fourier cycles were performed to locate the remaining non−hydrogen

atoms. All non−hydrogen atoms were refined with anisotropic displacement parameters. Hydrogen atoms were placed in ideal positions and refined as riding atoms with relative isotropic displacement parameters. Complex **2** solved in the space group P321 and contained channels along the crystallographic *c* axis; although substantial electron density was observed, no solvent molecules could be located. The SQUEEZE function of the PLATON program was used to remove solvent molecules within the void space. The SQUEEZE function removed 839 electrons from a void space volume of 396 $Å^3$. These values are consistent with the presence of approximately 23 to 26 THF molecules within the channel. Independent crystals of $\mathbf{4^{ox}}[BAr^F_4]$ displayed substantial disorder at 173 and 123 K. At 123 K, the entire cationic component is disordered over two sites with a 57:43 occupancy. The anionic component exhibits rotational disorder of the CF_3 groups, which were treated as ideal rotors. One aryl ring of the counter-anion appears to exhibit a rotational disorder, precluding anisotropic refinement of the respective CF_3 group. The presumed minor component of this disorder was not located during refinement. Crystallographic data are summarized in Table 5.8.

Table 5.8 Crystallographic Details for Complexes of **1**, **2**, K[**2**^{red}], K(crypt-222)[**3**^{red}], and **4**^{ox}[BAr$^{F}_{4}$].

	1	**2**	K[**2**^{red}]•THF	K(crypt-222)[**3**^{red}]	**4**^{ox}[BAr$^{F}_{4}$]
chemical formula	$C_{39}H_{60}CrN_4P_3$	$C_{39}H_{60}N_4P_3Cr_2$	$C_{39}H_{60}N_4Cr_2P_3K \cdot C_4H_8O$	$C_{57}H_{96}N_6O_6CrMnP_3K$	$C_{39}H_{60}N_4P_3FeCr$ $C_{32}H_{12}F_{24}B$
formula weight	729.82	781.82	893.02	1200.34	1648.90
crystal system	Monoclinic	Hexagonal	Monoclinic	Trigonal	Triclinic
space group	P21/n	P321	Cc	P−3	P−1
a (Å)	11.1248(7)	16.067(3)	12.9903(19)	11.3119(7)	10.5449(8)
b (Å)	20.166(1)	16.067(3)	27.035(4)	11.3119(7)	18.5182(14)
c (Å)	17.373(1)	11.673(2)	14.055(2)	28.5164(18)	20.4402(16)
α (deg)	90	90	90	90	71.0960(10)
β (deg)	92.293(1)	90	93.906(2)	90	78.6720(10)
γ (deg)	90	120	90	120	87.5320(10)
V (Å^3)	3894.4(4)	2609.7(9)	4924.6(12)	3160.1(3)	3701.7(5)
Z	4	2	4	2	2
Dcalcd (g cm^{-3})	1.245	0.995	1.204	1.258	1.479
λ (Å), μ (mm^{-1})	0.71073, 0.449	0.71073, 0.805	0.71073, 0.853	0.71073, 0.564	0.71073, 0.512
T (K)	173(2)	173(2)	173(2)	173(2)	123(2)
θ range (deg)	1.550 to	2.260 to	2.1945 to	2.184 to	2.207 to 27.2555
reflns collected	33608	6896	26232	33862	43571
unique reflns	6647	2958	11248	4850	16967
data/restraint/par	8993/0/436	6896/0/145	9412/0/487	4397/0/226	16967/762/1030
R1, wR2 (I > 2σ(I))	0.0418, 0.0993	0.0466, 0.0972	0.0422, 0.0930	0.0327, 0.0.0851	0.1116, 0.3457

Computational Methods

A thorough quantum chemical study was performed for complexes **2**, **2**^{red}, **3**^{red} and **4**^{ox}. Analogous studies for **3, 4,** and **4**^{red} were previously reported. Gas phase geometry optimizations were performed with DFT using the Perdew−Burke−Ernzerhof (PBE) exchange-correlation functional as implemented in the TURBOMOLE 6.4 package. For C and H atoms, the double-ζ quality basis sets def-SV(P) was used. The

triple-ζ quality basis set def-TZVP was employed for N and P. Additional polarized functions were introduced for Fe, Mn, and Cr by using def-TZVPP. The DFT calculations were performed with the broken symmetry option (unrestricted calculations), and the resolution of the identity (RI) approximation was used for the Coulomb integrals. All stationary points were confirmed as minima by vibrational analysis. Initial starting points for geometry optimizations were derived from experimentally determined X-ray structures. Due to the size of the ligands, isopropyl groups were replaced with methyl groups. No symmetry constraints were used.

Subsequently, the electronic structure was further investigated using complete active space self-consistent field theory (CASSCF) with second-order perturbation theory (CASPT2) on top of the DFT/PBE optimized geometry using the Molcas 7.8 package. Relativistic effects were included through the use of the scalar Douglas−Kroll−Hess (DKH) Hamiltonian. The relativistic all-electron ANO-RCC basis sets were used for all elements. In all of these calculations, the ANO-RCC-VTZP basis set was used for the Fe, Mn, and Cr, ANO-RCC-VDZP basis set was used for N and P, and the ANO-RCC-MB basis set was used for C and H. Additionally, the Cholesky decomposition technique was used combined with local exchange screening to reduce the computational costs involved in generating the two-electron integrals significantly. Atomic charges were computed at the CASSCF level for the ground state using the LoProp procedure.

RAS Choice. Although the ground spin state for complexes **2**, $\mathbf{2}^{\mathbf{red}}$, $\mathbf{3}^{\mathbf{red}}$ and $\mathbf{4}^{\mathbf{ox}}$ could be well described with an active space of X electrons in 15 orbitals, as had been previously

done for **3, 4** and **4**^{red}, a larger active space was required for internally consistent results. Thus, restricted-active-space (RAS)SCF calculations including a large configuration interaction space were performed for all species and spin multiplicities, denoted by (X,20)/(X,10)/2, where X was 9, 10 and 11 for the $(d\text{-}d)^9$, $(d\text{-}d)^{10}$ and $(d\text{-}d)^{11}$ species respectively. In this notation, the first set of parentheses corresponds to the total number of electrons in RAS1 and RAS2 and the total number of orbitals in all of the RAS spaces. The second set of parentheses corresponds to the number of active electrons and orbitals in RAS2; the final value of 2 indicates the number of particles allowed into RAS3.

State Averaged-Complete Actve Space Self Consistent Field (SA-CASSCF) calculations were performed for the $(d\text{-}d)^{10}$ complexes. The active spaces mentioned above were reduced for the SA-CASSCF calculation in which the correlating orbitals were transferred to the virtual space. Thus a 6 root calculation with a (10,10) active space was performed the $(d\text{-}d)^{10}$ complexes. The complete active space state interaction (CASSI) method was applied to compute the transition probabilities. CASSI results served to obtain a qualitative orbital ordering based on the analysis of the energies and the nature of the orbitals involved in the electronic excitations of the various roots and to characterize the low energy vis-NIR spectroscopic transitions.

References

1. Hoffman, B. M.; Dean, D. R.; Seefeldt, L. C., *Acc. Chem. Res.* **2009**, *42* (5), 609-619; Hoffman, B. M.; Lukoyanov, D.; Dean, D. R.; Seefeldt, L. C., *Acc. Chem. Res.* **2013**, *46* (2), 587-595.
2. Lindahl, P. A., *J. Inorg. Biochem.* **2012**, *106* (1), 172-178.
3. MacLeod, K. C. H., P.L., *Nat. Chem.* **2013**, *5,* 559-565.
4. MacKay, B. A.; Fryzuk, M. D., *Chemical Reviews* **2004**, *104* (2), 385-402.
5. Hinrichsen, S.; Broda, H.; Gradert, C.; Soncksen, L.; Tuczek, F., *Annual Reports Section "A" (Inorganic Chemistry)* **2012**, *108* (0), 17-47.
6. Appl, M.: "Ammonia", *Ullmann's Encyclopedia of Industrial Chemistry,* Electronic Release, Wiley-VCH, Weinheim **2000**.
7. Schlögl, R., *Angew. Chem., Int. Ed.* **2003**, *42* (18), 2004-2008.
8. Honkala, K.; Hellman, A.; Remediakis, I. N.; Logadottir, A.; Carlsson, A.; Dahl, S.; Christensen, C. H.; Nørskov, J. K., *Science* **2005**, *307* (5709), 555-558; Ertl, G., *Angew. Chem., Int. Ed.* **2008**, *47* (19), 3524-3535.
9. Smith, J. M.; Lachicotte, R. J.; Pittard, K. A.; Cundari, T. R.; Lukat-Rodgers, G.; Rodgers, K. R.; Holland, P. L., *J. Am. Chem. Soc.* **2001**, *123* (37), 9222-9223; Holland, P. L., *Acc. Chem. Res.* **2008**, *41* (8), 905-914; Ding, K.; Pierpont, A. W.; Brennessel, W. W.; Lukat-Rodgers, G.; Rodgers, K. R.; Cundari, T. R.; Bill, E.; Holland, P. L., *J. Am. Chem. Soc.* **2009**, *131* (27), 9471-9472.
10. Holland, P. L., *Dalton Trans.* **2010**, *39* (23), 5415-5425.
11. Rodriguez, M. M.; Bill, E.; Brennessel, W. W.; Holland, P. L., *Science* **2011**, *334* (6057), 780-783.
12. Yandulov, D. V.; Schrock, R. R., *Science* **2003**, *301* (5629), 76-78.
13. Yandulov, D. V.; Schrock, R. R., *Inorg. Chem.* **2005**, *44* (4), 1103-1117.
14. Betley, T. A.; Peters, J. C., *J. Am. Chem. Soc.* **2004**, *126* (20), 6252-6254.

15. Hendrich, M. P.; Gunderson, W.; Behan, R. K.; Green, M. T.; Mehn, M. P.; Betley, T. A.; Lu, C. C.; Peters, J. C., *Proc. Natl. Acad. Sci.* **2006**, *103* (46), 17107-17112.

16. Lee, Y.; Mankad, N. P.; Peters, J. C., *Nat Chem* **2010**, *2* (7), 558-565.

17. Moret, M.-E.; Peters, J. C., *Angew. Chem., Int. Ed.* **2011**, *50* (9), 2063-2067.

18. Anderson, J. S.; Moret, M.-E.; Peters, J. C., *J. Am. Chem. Soc.* **2012**, *135* (2), 534-537.

19. Creutz, S. E.; Peters, J. C., *J. Am. Chem. Soc.* **2013**, *136* (3), 1105-1115.

20. Suess, D. L. M.; Peters, J. C., *J. Am. Chem. Soc.* **2013**, *135* (13), 4938-4941.

21. Anderson, J. S.; Rittle, J.; Peters, J. C., *Nature* **2013**, *501* (7465), 84-87.

22. Arashiba, K.; Miyake, Y.; Nishibayashi, Y., *Nat Chem* **2011**, *3* (2), 120-125.

23. Tanaka, H.; Sasada, A.; Kouno, T.; Yuki, M.; Miyake, Y.; Nakanishi, H.; Nishibayashi, Y.; Yoshizawa, K., *J. Am. Chem. Soc.* **2011**, *133* (10), 3498-3506.

24. Nishibayashi, Y., *Dalton Trans.* **2012**, *41* (25), 7447-7453.

25. Dance, I., *Chem. Commun.* **2013**, *49* (93), 10893-10907.

26. Peters, J. C.; Mehn, M. P., In *Activation of Small Molecules,* Tolman, W. B., Ed.; Wiley-VCH: Weinheim, **2006**, pp 1-41.

27. Kim, J.; Rees, D., *Science* **1992**, *257* (5077), 1677-1682; Chan, M.; Kim, J.; Rees, D., *Science* **1993**, *260* (5109), 792-794.

28. Einsle, O.; Tezcan, F. A.; Andrade, S. L. A.; Schmid, B.; Yoshida, M.; Howard, J. B.; Rees, D. C., *Science* **2002**, *297* (5587), 1696-1700.

29. Spatzal, T.; Aksoyoglu, M.; Zhang, L.; Andrade, S. L. A.; Schleicher, E.; Weber, S.; Rees, D. C.; Einsle, O., *Science* **2011**, *334* (6058), 940; Lancaster, K. M.; Roemelt, M.; Ettenhuber, P.; Hu, Y.; Ribbe, M. W.; Neese, F.; Bergmann, U.; DeBeer, S., *Science* **2011**, *334* (6058), 974-977.

30. Wiig, J. A.; Hu, Y.; Lee, C. C.; Ribbe, M. W., *Science* **2012**, *337* (6102), 1672-1675.

31. Yandulov, D. V.; Schrock, R. R., *J. Am. Chem. Soc.* **2002**, *124* (22), 6252-6253.

32. Yandulov, D. V.; Schrock, R. R.; Rheingold, A. L.; Ceccarelli, C.; Davis, W. M., *Inorg. Chem.* **2003**, *42* (3), 796-813; Schrock, R. R., *Acc. Chem. Res.* **2005**, *38* (12), 955-962.

33. Yuki, M.; Tanaka, H.; Sasaki, K.; Miyake, Y.; Yoshizawa, K.; Nishibayashi, Y., *Nat Commun* **2012**, *3*, 1254.

34. Vela, J.; Stoian, S.; Flaschenriem, C. J.; Münck, E.; Holland, P. L., *J. Am. Chem. Soc.* **2004**, *126* (14), 4522-4523.

35. Stubbert, B. D.; Vela, J.; Brennessel, W. W.; Holland, P. L., *Zeitschrift für anorganische und allgemeine Chemie* **2013**, *639* (8-9), 1351-1355.

36. Moret, M.-E.; Peters, J. C., *J. Am. Chem. Soc.* **2011**, *133* (45), 18118-18121.

37. Rittle, J.; Peters, J. C., *Proc. Natl. Acad. Sci.* **2013**, *110*(40), 15898-15903.

38. Fong, H.; Moret, M.-E.; Lee, Y.; Peters, J. C., *Organometallics* **2013**, *32* (10), 3053-3062.

39. Gualco, P.; Lin, T.-P.; Sircoglou, M.; Mercy, M.; Ladeira, S.; Bouhadir, G.; Pérez, L. M.; Amgoune, A.; Maron, L.; Gabbaï, F. P.; Bourissou, D., *Angew. Chem., Int. Ed.* **2009**, *48* (52), 9892-9895; Wade, C. R.; Gabbaï, F. P., *Angew. Chem., Int. Ed.* **2011**, *50* (32), 7369-7372; Ke, I.-S.; Myahkostupov, M.; Castellano, F. N.; Gabbaï, F. P., *J. Am. Chem. Soc.* **2012**, *134* (37), 15309-15311; Lin, T.-P.; Gabbaï, F. P., *J. Am. Chem. Soc.* **2012**, *134* (29), 12230-12238; Lin, T.-P.; Ke, I.-S.; Gabbaï, F. P., *Angew. Chem., Int. Ed.* **2012**, *51* (20), 4985-4988; Wade, C. R.; Ke, I.-S.; Gabbaï, F. P., *Angew. Chem., Int. Ed.* **2012**, *51* (2), 478-481; Ke, I.-S.; Gabbaï, F. P., *Inorg. Chem.* **2013**, *52* (12), 7145-7151; Ke, I.-S.; Jones, J. S.; Gabbaï, F. P., *Angew. Chem., Int. Ed.* **2014**, *53* (10), 2633-2637.

40. Amgoune, A.; Bourissou, D., *Chem. Commun.* **2011**, *47* (3), 859-871.

41. Sircoglou, M.; Mercy, M.; Saffon, N.; Coppel, Y.; Bouhadir, G.; Maron, L.; Bourissou, D., *Angew. Chem., Int. Ed.* **2009**, *48* (19), 3454-3457.

42. Derrah, E. J.; Sircoglou, M.; Mercy, M.; Ladeira, S.; Bouhadir, G.; Miqueu, K.; Maron, L.; Bourissou, D., *Organometallics* **2011**, *30* (4), 657-660.

43. Sircoglou, M.; Saffon, N.; Miqueu, K.; Bouhadir, G.; Bourissou, D., *Organometallics* **2013**, *32* (22), 6780-6784.

44. Green, M. L. H., *J. Organomet. Chem.* **1995**, *500* (1–2), 127-148; Parkin, G., *Organometallics* **2006**, *25* (20), 4744-4747.

45. Sircoglou, M.; Bontemps, S.; Bouhadir, G.; Saffon, N.; Miqueu, K.; Gu, W.; Mercy, M.; Chen, C.-H.; Foxman, B. M.; Maron, L.; Ozerov, O. V.; Bourissou, D., *J. Am. Chem. Soc.* **2008**, *130* (49), 16729-16738.

46. Moret, M.-E.; Zhang, L.; Peters, J. C., *J. Am. Chem. Soc.* **2013**, *135* (10), 3792-3795.

47. Betley, T. A.; Peters, J. C., *J. Am. Chem. Soc.* **2003**, *125* (36), 10782-10783.

48. Brown, S. D.; Betley, T. A.; Peters, J. C., *J. Am. Chem. Soc.* **2002**, *125* (2), 322-323; Thomas, C. M.; Mankad, N. P.; Peters, J. C., *J. Am. Chem. Soc.* **2006**, *128* (15), 4956-4957.

49. Brown, S. D.; Peters, J. C., *J. Am. Chem. Soc.* **2004**, *126* (14), 4538-4539.

50. Mankad, N. P.; Whited, M. T.; Peters, J. C., *Angew. Chem., Int. Ed.* **2007**, *46* (30), 5768-5771; Whited, M. T.; Mankad, N. P.; Lee, Y.; Oblad, P. F.; Peters, J. C., *Inorg. Chem.* **2009**, *48* (6), 2507-2517.

51. Harman, W. H.; Peters, J. C., *J. Am. Chem. Soc.* **2012**, *134* (11), 5080-5082.

52. Bertrand, J. A.; Cotton, F. A.; Dollase, W. A., *J. Am. Chem. Soc.* **1963**, *85* (9), 1349-1350; Bertrand, J. A.; Cotton, F. A.; Dollase, W. A., *Inorg. Chem.* **1963**, *2* (6), 1166-1171.

53. Cotton, F. A.; Curtis, N. F.; Johnson, B. F. G.; Mague, J. T.; Wood, J. S.; Harris, C. B.; Robinson, W. R.; Lippard, S. J., *Science* **1964**, *145*, 1305.

54. Bennett, M. J.; Cotton, F. A.; Walton, R. A., *J. Am. Chem. Soc.* **1966**, *88* (16), 3866-3867.

55. Nguyen, T.; Sutton, A. D.; Brynda, M.; Fettinger, J. C.; Long, G. J.; Power, P. P., *Science* **2005**, *310*, 844.

56. Cotton, F. A.; Murillo, C. A.; Walton, R. A., Multiple Bonds Between Metal Atoms; John Wiley: New York, 2005.

57. Collman, J. P.; Boulatov, R., *Angew. Chem., Int. Ed.* **2002**, *41*, 3948.

58. Harisomayajula, N. V. S.; Nair, A. K.; Tsai, Y.-C., *Chem. Commun.* **2014**, *50* (26), 3391-3412; Nair, A. K.; Harisomayajula, N. V. S.; Tsai, Y.-C., *Dalton Trans.* **2014**, *43* (15), 5618-5638.

59. Wolf, R.; Ni, C.; Nguyen, T.; Brynda, M.; Long, G. J.; Sutton, A. D.; Fischer, R. C.; Fettinger, J. C.; Hellman, M.; Pu, L.; Power, P. P., *Inorg. Chem.* **2007**, *46* (26), 11277-11290.

60. Hsu, C. W.; Yu, J. S. K.; Yen, C. H.; Lee, G. H.; Wang, Y.; Tsai, Y. C., *Angew. Chem., Int. Ed.* **2008**, *47*, 9933.

61. Tsai, Y. C.; Hsu, C. W.; Yu, J. S. K.; Lee, G. H.; Wang, Y.; Kuo, T. S., *Angew. Chem., Int. Ed.* **2008**, *47*, 7250.

62. Huang, Y.-L.; Lu, D.-Y.; Yu, H.-C.; Yu, J.-S. K.; Hsu, C.-W.; Kuo, T.-S.; Lee, G.-H.; Wang, Y.; Tsai, Y.-C., *Angew. Chem., Int. Ed.* **2012**, *51* (31), 7781-7785.

63. Kreisel, K. A.; Yap, G. P. A.; Dmitrenko, O.; Landis, C. R.; Theopold, K. H., *J. Am. Chem. Soc.* **2007**, *129*, 14162.

64. Noor, A.; Wagner, F. R.; Kempe, R., *Angew. Chem., Int. Ed.* **2008**, *47*, 7246; Noor, A.; Glatz, G.; Muller, R.; Kaupp, M.; Demeshko, S.; Kempe, n., *Z. Anorg. Allg. Chem.* **2009**, *635*, 1149.

65. Noor, A.; Bauer, T.; Todorova, T. K.; Weber, B.; Gagliardi, L.; Kempe, R., *Chem. Eur. J.* **2013**, *19* (30), 9825-9832.

66. Tsai, Y.-C.; Chen, H.-Z.; Chang, C.-C.; Yu, J.-S. K.; Lee, G.-H.; Wang, Y.; Kuo, T.-S., *J. Am. Chem. Soc.* **2009**, *131* (35), 12534-12535; Liu, S.-C.; Ke, W.-L.; Yu, J.-S. K.; Kuo, T.-S.; Tsai, Y.-C., *Angew. Chem., Int. Ed.* **2012**, *51* (26), 6394-6397.

67. Tsai, Y.-C.; Hsu, C.-W.; Yu, J.-S. K.; Lee, G.-H.; Wang, Y.; Kuo, T.-S., *Angew. Chem., Int. Ed.* **2008**, *47* (38), 7250-7253.

68. Zall, C. M.; Clouston, L. J.; Young, V. G.; Ding, K.; Kim, H. J.; Zherebetskyy, D.; Chen, Y. S.; Bill, E.; Gagliardi, L.; Lu, C. C., *Inorg. Chem.* **2013**, *52*, 9216.

69. Zall, C. M.; Clouston, L. J.; Young, V. G.; Ding, K.; Kim, H. J.; Zherebetskyy, D.; Chen, Y.-S.; Bill, E.; Gagliardi, L.; Lu, C. C., *Inorg. Chem.* **2013**, *52* (16), 9216-9228.

70. Rudd, P. A.; Liu, S.; Gagliardi, L.; Young, V. G.; Lu, C. C., *J. Am. Chem. Soc.* **2011**, *133* (51), 20724-20727.

71. Rudd, P. A.; Liu, S.; Planas, N.; Bill, E.; Gagliardi, L.; Lu, C. C., *Angew. Chem., Int. Ed.* **2013**, *52* (16), 4449-4452.

72. Zall, C. M.; Zherebetskyy, D.; Dzubak, A. L.; Bill, E.; Gagliardi, L.; Lu, C. C., *Inorg. Chem.* **2012**, *51*, 728.

73. Cotton, F. A.; Feng, X.; Murillo, C. A., *Inorg. Chim. Acta* **1997**, *256*, 303; Cotton, F. A.; Daniels, L. M.; Falvello, L. R.; Matonic, J. H.; Murillo, C. A., *Inorg. Chim. Acta* **1997**, *256*, 269; Cotton, F. A.; Daniels, L. M.; Feng, X.; Maloney, D. J.; Matonic, J. H.; Murilio, C. A., *Inorg. Chim. Acta* **1997**, *256*, 291; Cotton, F. A.; Daniels, L. M.; Maloney, D. J.; Matonic, J. H.; Murillo, C. A., *Inorg. Chim. Acta* **1997**, *256*, 283.

74. Wu, L.-C.; Hsu, C.-W.; Chuang, Y.-C.; Lee, G.-H.; Tsai, Y.-C.; Wang, Y., *J. Phys. Chem. A* **2011**, *115* (45), 12602-12615.

75. Cotton, F. A.; Daniels, L. M.; Murillo, C. A.; Pascual, I.; Zhou, H.-C., *J. Am. Chem. Soc.* **1999**, *121* (29), 6856-6861.

76. Ndambuki, S.; Ziegler, T., *Inorg. Chem.* **2012**, *51* (14), 7794-7800; Ndambuki, S.; Ziegler, T., *Inorg. Chem.* **2013**, *52* (7), 3860-3869; La Macchia, G.; Li Manni, G.; Todorova, T. K.; Brynda, M.; Aquilante, F.; Roos, B. O.; Gagliardi, L., *Inorg. Chem.* **2010**, *49*, 5216.

77. Brynda, M.; Gagliardi, L.; Roos, B. O., *Chem. Phys. Lett.* **2009**, *471*, 1.

78. Clouston, L. J.; Siedschlag, R. B.; Rudd, P. A.; Planas, N.; Hu, S.; Miller, A. D.; Gagliardi, L.; Lu, C. C., *J. Am. Chem. Soc.* **2013**, *135* (35), 13142-13148.

79. Dong, H.; Meng, Q.; Chen, B.-Z.; Wu, Y.-B., *J. Organomet. Chem.* **2012**, *717* (0), 108-115.

80. Cotton, F. A.; Koch, S. A.; Millar, M., *Inorg. Chem.* **1978**, *17*, 2084; Cotton, F. A.; Koch, S., *Inorg. Chem.* **1978**, *17*, 2021.

81. Bondybey, V. E.; English, J. H., *Chem. Phys. Lett.* **1983**, *94* (5), 443-447.

82. Collman, J. P.; Barnes, C. E.; Woo, L. K., *Proc. Natl. Acad. Sci. U.S.A.* **1983**, *80*, 7684.

83. Collman, J. P.; Garner, J. M., *J. Am. Chem. Soc.* **1990**, *112* (1), 166-173; Collman, J. P.; Arnold, H. J.; Fitzgerald, J. P.; Weissman, K. J., *J. Am. Chem. Soc.* **1993**, *115* (20), 9309-9310.

84. Collman, J. P.; Harford, S. T.; Franzen, S.; Eberspacher, T. A.; Shoemaker, R. K.; Woodruff, W. H., *J. Am. Chem. Soc.* **1998**, *120* (7), 1456-1465; Collman, J. P.; Harford, S. T.; Franzen, S.; Shreve, A. P.; Woodruff, W. H., *Inorg. Chem.* **1999**, *38* (9), 2093-2097.

85. Collman, J. P.; Harford, S. T.; Franzen, S.; Marchon, J.-C.; Maldivi, P.; Shreve, A. P.; Woodruff, W. H., *Inorg. Chem.* **1999**, *38* (9), 2085-2092.

86. Kuppuswamy, S.; Powers, T. M.; Krogman, J. P.; Bezpalko, M. W.; Foxman, B. M.; Thomas, C. M., *Chem. Sci.* **2013**, *4* (9), 3557-3565.

87. Kuppuswamy, S.; Bezpalko, M. W.; Powers, T. M.; Wilding, M. J. T.; Brozek, C. K.; Foxman, B. M.; Thomas, C. M., *Chem. Sci.* **2014**, *5* (4), 1617-1626.

88. Cotton, F. A.; Fanwick, P. E.; Niswander, R. H.; Sekutowski, J. C., *J. Am. Chem. Soc.* **1978**, *100*, 4725.

89. Clegg, W.; Garner, C. D.; Akhter, L.; Al-Samman, M. H., *Inorg. Chem.* **1983**, *22* (17), 2466-2468.

90. Tauster, S. J.; Fung, S. C.; Garten, R. L., *J. Am. Chem. Soc.* **1978**, *100* (1), 170-175.

91. Baker, R. T. K.; Prestridge, E. B.; Garten, R. L., *J. Catal.* **1979**, *56* (3), 390-406; Baker, R. T. K.; Prestridge, E. B.; Garten, R. L., *J. Catal.* **1979**, *59* (2), 293-302; Haller, G. L.; Resasco, D. E., *Adv. Catal.*, *36*, **1989**, 173-235.

92. Bullock, R. M.; Casey, C. P., *Acc. Chem. Res.* **1987**, *20* (5), 167-173.

93. Stephan, D. W., *Coord. Chem. Rev.* **1989**, *95* (1), 41-107.

94. Gade, L. H., *Angew. Chem., Int. Ed.* **2000**, *39* (15), 2658-2678.

95. Burlitch, J. M.; Leonowicz, M. E.; Petersen, R. B.; Hughes, R. E., *Inorg. Chem.* **1979**, *18* (4), 1097-1105.

96. Tsutsumi, H.; Sunada, Y.; Shiota, Y.; Yoshizawa, K.; Nagashima, H., *Organometallics* **2009**, *28* (7), 1988-1991.

97. Krogman, J. P.; Foxman, B. M.; Thomas, C. M., *J. Am. Chem. Soc.* **2011**, *133* (37), 14582-14585; Krogman, J. P.; Bezpalko, M. W.; Foxman, B. M.; Thomas, C. M., *Inorg. Chem.* **2013**, *52* (6), 3022-3031.

98. Zhou, W.; Napoline, J. W.; Thomas, C. M., *Eur. J. Inorg. Chem.* **2011**, *2011* (13), 2029-2033.

99. Zhou, W.; Marquard, S. L.; Bezpalko, M. W.; Foxman, B. M.; Thomas, C. M., *Organometallics* **2013**, *32* (6), 1766-1772.

100. Jones, M. B.; MacBeth, C. E., *Inorg. Chem.* **2007**, *46*, 8117.

101. Slany, M.; Caminade, A.-M.; Majoral, J. P., *Tetrahedron Lett.* **1996**, *37* (50), 9053-9056.

102. Gade, L. H.; Mahr, N., *Journal of the Chemical Society, Dalton Transactions* **1993**, (4), 489-494; Friedrich, S.; Gade, L. H.; Edwards, A. J.; McPartlin, M., *Chem. Ber.* **1993**, *126* (8), 1797-1805; Friedrich, S.; Memmler, H.; Gade, L. H.; Li, W.-S.; McPartlin, M., *Angew. Chem., Int. Ed. Engl.* **1994**, *33* (6), 676-678; Friedrich, S.; Gade, L. H.; Scowen, I. J.; McPartlin, M., *Organometallics* **1995**, *14* (11), 5344-5349.

103. Clouston, L. J. C., R.C.; Lu, C.C., *Manuscript in prepration*.

104. Ward, A. L.; Lukens, W. W.; Lu, C. C.; Arnold, J., *J. Am. Chem. Soc.* **2014**, *136* (9), 3647-3654.

105. Chakraborty, S.; Chattopadhyay, J.; Guo, W.; Billups, W. E., *Angew. Chem., Int. Ed.* **2007**, *46* (24), 4486-4488.

106. Bontemps, S.; Bouhadir, G.; Dyer, P. W.; Miqueu, K.; Bourissou, D., *Inorg. Chem.* **2007**, *46* (13), 5149-5151.

107. Greenwood, B. P.; Rowe, G. T.; Chen, C.-H.; Foxman, B. M.; Thomas, C. M., *J. Am. Chem. Soc.* **2009**, *132* (1), 44-45.

108. Greenwood, B. P.; Forman, S. I.; Rowe, G. T.; Chen, C. H.; Foxman, B. M.; Thomas, C. M., *Inorg. Chem.* **2009**, *48*, 6251.

109. Pauling, L., *The Nature of the Chemical Bond*; Cornell University Press: Cornell, **1960**.

110. Rudd, P. A.; Planas, N.; Bill, E.; Gagliardi, L.; Lu, C. C., *Eur. J. Inorg. Chem.* **2013**, *2013* (22-23), 3898-3906.

111. Sivasankar, C.; Baskaran, S.; Tamizmani, M.; Ramakrishna, K., *J. Organomet. Chem.* **2014**, *752* (0), 44-58.

112. Allen, A. D.; Senoff, C. V., *Chemical Communications (London)* **1965**, (24), 621-622.

113. Oshita, H.; Mizobe, Y.; Hidai, M., *Organometallics* **1992**, *11* (12), 4116-4123.

114. Miller, D. L., Siedschlag, R.B.; Lu, C.C., *Manuscript in prepration*.

115. Goldberg, D. P.; Telser, J.; Krzystek, J.; Montalban, A. G.; Brunel, L.-C.; Barrett, A. G. M.; Hoffman, B. M., *J. Am. Chem. Soc.* **1997**, *119* (37), 8722-8723.

116. Garribba, E.; Micera, G., *J. Chem. Educ.* **2006**, *83* (8), 1229.

117. Ellis, J. E., *Inorg. Chem.* **2006**, *45* (8), 3167-3186; Brennessel, W. W.; Jilek, R. E.; Ellis, J. E., *Angew. Chem., Int. Ed.* **2007**, *46* (32), 6132-6136.

118. Schnöckelborg, E.-M.; Khusniyarov, M. M.; de Bruin, B.; Hartl, F.; Langer, T.; Eul, M.; Schulz, S.; Pöttgen, R.; Wolf, R., *Inorg. Chem.* **2012**, *51* (12), 6719-6730.

119. Cammarota, R. C., Lu, C.C., *Manuscript in Preparation.*

120. Zhao, Y.; Truhlar, D. G., *Acc. Chem. Res.* **2008**, *41* (2), 157-167; Zhao, Y.; Truhlar, D. G., *The Journal of Chemical Physics* **2006**, *125* (19), 194101-194118.

121. GaussView, Version 6, Dennington, Roy; Keith, Todd A.; Millam, John M. Semichem Inc., Shawnee Mission, KS, 2016.

122. W. J. Hehre, L. R., P. V. R. Schleyer, J. A. Pople, Wiley: New York, **1986**.

123. D. Andrae, U. H., M. Dolg, H. Stoll, H. Preuss, *Theor. Chim. Acta* **1990**, *77*, 123.

124. Cotton, F. A.; Bratton, W. K., *J. Am. Chem. Soc.* **1965**, *87* (4), 921-921.

125. Lawton, D.; Mason, R., *J. Am. Chem. Soc.* **1965**, *87* (4), 921-922.

126. Chisholm, M. H.; Cotton, F. A.; Frenz, B. A.; Reichert, W. W.; Shive, L. W.; Stults, B. R., *J. Am. Chem. Soc.* **1976**, *98* (15), 4469-4476; Chisholm, M. H.; Cotton, F. A.; Extine, M.; Stults, B. R., *J. Am. Chem. Soc.* **1976**, *98* (15), 4477-4485.

127. Cotton, F. A.; James, C. A., *Inorg. Chem.* **1992**, *31* (25), 5298-5307.

128. Cotton, F. A.; Ren, T., *J. Am. Chem. Soc.* **1992**, *114* (6), 2237-2242.

129. Luck, R. L.; Morris, R. H.; Sawyer, J. F., *Inorg. Chem.* **1987**, *26* (15), 2422-2429; Katovic, V.; Templeton, J. L.; Hoxmeier, R. J.; McCarley, R. E., *J. Am. Chem. Soc.* **1975**, *97* (18), 5300-5302.

130. Garner, C. D.; Senior, R. G.; King, T. J., *J. Am. Chem. Soc.* **1976**, *98*, 3526; Menezes, J. C.; Romão, C. C., *Polyhedron* **1990**, *9* (9), 1237-1239; Bursten, B. E.; Cotton, F. A.; Cowley, A. H.; Hanson, B. E.; Lattman, M.; Stanley, G. G., *J. Am. Chem. Soc.* **1979**, *101* (21), 6244-6249; Cotton, F. A.; Hanson, B. E., *Inorg. Chem.* **1978**, *17* (11), 3237-3240.

131. Wheatley, N.; Kalck, P., *Chemical Reviews* **1999**, *99* (12), 3379-3420.

132. Friedrich, S.; Memmler, H.; Gade, L. H.; Li, W.-S.; Scowen, I. J.; McPartlin, M.; Housecroft, C. E., *Inorg. Chem.* **1996**, *35* (9), 2433-2441.

133. Jansen, G.; Schubart, M.; Findeis, B.; Gade, L. H.; Scowen, I. J.; McPartlin, M., *J. Am. Chem. Soc.* **1998**, *120* (29), 7239-7251.

134. Slaughter, L. M.; Wolczanski, P. T., *Chem. Commun.* **1997**, 2109.

135. Mathialagan, R.; Kuppuswamy, S.; De Denko, A. T.; Bezpalko, M. W.; Foxman, B. M.; Thomas, C. M., *Inorg. Chem.* **2013**, *52*, 701.

136. Krogman, J. P.; Thomas, C. M. *Chem. Commun.* **2014**, *50*, 5115-5127

137. Lee, Y.; Peters, J. C., *J. Am. Chem. Soc.* **2011**, *133* (12), 4438-4446.

138. Scepaniak, J. J.; Fulton, M. D.; Bontchev, R. P.; Duesler, E. N.; Kirk, M. L.; Smith, J. M., *J. Am. Chem. Soc.* **2008**, *130* (32), 10515-10517; Scepaniak, J. J.; Vogel, C. S.; Khusniyarov, M. M.; Heinemann, F. W.; Meyer, K.; Smith, J. M., *Science* **2011**, *331* (6020), 1049-1052; Vogel, C.; Heinemann, F. W.; Sutter, J.; Anthon, C.; Meyer, K., *Angew. Chem., Int. Ed.* **2008**, *47* (14), 2681-2684.

139. Tereniak, S. J.; Carlson, R. K.; Clouston, L. J.; Young, V. G.; Bill, E.; Maurice, R. m.; Chen, Y.-S.; Kim, H. J.; Gagliardi, L.; Lu, C. C., *J. Am. Chem. Soc.* **2013**, *136* (5), 1842-1855.

140. Hsu, C.-W.; Yu, J.-S. K.; Yen, C.-H.; Lee, G.-H.; Wang, Y.; Tsai, Y.-C., *Angew. Chem. Int. Ed.* **2008**, *47* (51), 9933-9936.

141. Cotton, F. A.; Hillard, E. A.; Murillo, C. A.; Wang, X., *Inorg. Chem.* **2003**, *42* (19), 6063-6070; Cotton, F. A.; Hillard, E. A.; Murillo, C. A., *J. Am. Chem. Soc.* **2003**, *125* (8), 2026-2027.

142. Sircoglou, M.; Bontemps, S.; Bouhadir, G.; Saffon, N.; Miqueu, K.; Gu, W.; Mercy, M.; Chen, C.-H.; Foxman, B. M.; Maron, L.; Ozerov, O. V.; Bourissou, D., *J. Am. Chem. Soc.* **2008**, *130* (49), 16729-16738.

143. Nguyen, T.; Sutton, A. D.; Brynda, M.; Fettinger, J. C.; Long, G. J.; Power, P. P., *Science* **2005**, *310* (5749), 844-847; Noor, A.; Wagner, F. R.; Kempe, R., *Angew. Chem. Int. Ed.* **2008**, *47* (38), 7246-7249.

144. Noor, A.; Glatz, G.; Müller, R.; Kaupp, M.; Demeshko, S.; Kempe, R., *Z. Anorg. Allg. Chem.* **2009**, *635* (8), 1149-1152.

145. Kreisel, K. A.; Yap, G. P. A.; Dmitrenko, O.; Landis, C. R.; Theopold, K. H., *J. Am. Chem. Soc.* **2007**, *129* (46), 14162-14163.

146. Mashima, K.; Tanaka, M.; Tani, K.; Nakamura, A.; Takeda, S.; Mori, W.; Yamaguchi, K., *J. Am. Chem. Soc.* **1997**, *119* (18), 4307-4308.

147. Nguyen, T.; Merrill, W. A.; Ni, C.; Lei, H.; Fettinger, J. C.; Ellis, B. D.; Long, G. J.; Brynda, M.; Power, P. P., *Angew. Chem., Int. Ed.* **2008**, *47*, 9115; La Macchia, G.; Gagliardi, L.; Power, P. P.; Brynda, M., *J. Am. Chem. Soc.* **2008**, *130* (15), 5104-5114.

148. La Macchia, G.; Aquilante, F.; Veryazov, V.; Roos, B. O.; Gagliardi, L., *Inorg. Chem.* **2008**, *47* (24), 11455-11457.

149. Casey, S. M.; Leopold, D. G., *J. Phys. Chem.* **1993**, *97* (4), 816-830.

150. McGlinchey, M. J., *Inorg. Chem.* **1980**, *19* (5), 1392-1394; San Filippo, J., *Inorg. Chem.* **1972**, *11* (12), 3140-3143.

151. Agaskar, P. A.; Albert Cotton, F., *Polyhedron* **1986**, *5* (3), 899-900; Cotton, F. A.; Kitagawa, S., *Polyhedron* **1988**, *7* (18), 1673-1676.

152. McConnell, H. M.; Holm, C. H., *J. Chem. Phys.* **1957**, *27* (1), 314-315.

153. Cotton, F. A.; Murillo, C. A.; Walton, R. A., Multiple Bonds Between Metal Atoms; John Wiley: New York, 2005.

154. Cotton, F. A.; Eglin, J. L.; James, C. A., *Inorg. Chem.* **1993**, *32* (5), 681-686.

155. Harris, R. K. *Nuclear Magnetic Resonance Spectroscopy*; Longman: London, 1986.

156. Cotton, F. A.; Dunbar, K. R.; Hong, B.; James, C. A.; Matonic, J. H.; Thomas, J. L. C., *Inorg. Chem.* **1993**, *32* (23), 5183-5187.

157. Rudd, P. A.; Liu, S.; Planas, N.; Bill, E.; Gagliardi, L.; Lu, C. C., *Angew. Chem., Int. Ed.* **2013**, *52* (16), 4449-4452.

158. Brynda, M.; Gagliardi, L.; Roos, B. O., *Chem. Phys. Lett.* **2009**, *471* (1-3), 1-10; Brynda, M.; Gagliardi, L.; Widmark, P.-O.; Power, P. P.; Roos, B. O., *Angew. Chem. Int. Ed.* **2006**, *45* (23), 3804-3807; La Macchia, G.; Li Manni, G.; Todorova, T. K.; Brynda, M.; Aquilante, F.; Roos, B. O.; Gagliardi, L., *Inorg. Chem.* **2010**, *49*, 5216-5222.

159. Hsiao, C.-J.; Lai, S.-H.; Chen, I. C.; Wang, W.-Z.; Peng, S.-M., *The Journal of Physical Chemistry A* **2008**, *112* (51), 13528-13534.

160. Manning, M. C.; Trogler, W. C., *J. Am. Chem. Soc.* **1983**, *105* (16), 5311-5320.

161. Da Re, R. E.; Eglin, J. L.; Carlson, C. N.; John, K. D.; Morris, D. E.; Woodruff, W. H.; Bailey, J. A.; Batista, E.; Martin, R. L.; Cotton, F. A.; Hillard, E. A.; Murillo, C. A.; Sattelberger, A. P.; Donohoe, R. J., *J. Am. Chem. Soc.* **2010**, *132* (6), 1839-1847.

162. Cotton, F. A.; Murillo, C. A.; Walton, R. A., Multiple Bonds Between Metal Atoms; John Wiley: New York, 2005.

163. John, K. D.; Miskowski, V. M.; Vance, M. A.; Dallinger, R. F.; Wang, L. C.; Geib, S. J.; Hopkins, M. D., *Inorg. Chem.* **1998**, *37* (26), 6858-6873; Clark, R. J. H.; Firth, S.; Sella, A.; Miskowski, V. M.; Hopkins, M. D., *Journal of the Chemical Society, Dalton Transactions* **2000**, (17), 2928-2932.

164. Berry, J. F.; Bill, E.; Bothe, E.; George, S. D.; Mienert, B.; Neese, F.; Wieghardt, K., *Science* **2006**, *312* (5782), 1937-1941.

165. Hendrich, M. P.; Gunderson, W.; Behan, R. K.; Green, M. T.; Mehn, M. P.; Betley, T. A.; Lu, C. C.; Peters, J. C., *Proc. Natl. Acad. Sci.* **2006**, *103* (46), 17107-17112.

166. Clouston, L. J.; Siedschlag, R. B.; Rudd, P. A.; Planas, N.; Hu, S.; Miller, A. D.; Gagliardi, L.; Lu, C. C., *Journal of the American Chemical Society* **2013**, *135* (35), 13142-13148.

167. Calderazzo, F.; Pampaloni, G.; Rocchi, L.; Englert, U., *Organometallics* **1994**, *13* (7), 2592-2601.

168. Brookhart, M.; Grant, B.; Volpe, A. F., *Organometallics* **1992**, *11* (11), 3920-3922.